# The Detection of Infarcted Stroke Tissue via Localised Sodium Concentration Measurements: A Non-Invasive Approach

**By**

**Friedrich Wetterling**

**(M.Sc., Technical University of Ilmenau, Germany, 2005)**

**SUBMITTED TO THE SCHOOL OF PHYSICS, TRINITY COLLEGE DUBLIN IN PARTIAL FULFILLMENT OF THE REQUIREMENTS FOR THE DEGREE OF DOCTOR OF PHILOSOPHY**

**Presented at**

**The University of Dublin**

**Trinity College**

**Supervised by**

**Dr. Andrew J. Fagan,**

**And**

**Prof. James G. Lunney**

**30th October 2009**

## Summary

Quantitative $^{23}$Na Magnetic Resonance Imaging (qNa-MRI) is a non-invasive technique which has considerable potential for measuring Tissue Sodium Concentration (TSC) changes in pathological brain tissue states such as stroke or tumour. However, the quantification of $^{23}$Na with MRI has been hindered by limitations in Signal-to-Noise Ratio (SNR) within the required spatial and temporal resolution constraints. The aim of the work presented here was to develop a $^{23}$Na MRI resonator system with an optimal compromise between SNR and $B_1$-field homogeneity to allow for accurate qNa-MRI, to adapt an MRI sequence for short Time to Echo (TE) imaging, to apply the technique to an existing *in vivo* model of stroke in the rat brain, and to process the data to gain novel insights into the spatio-temporal TSC evolution after ischaemic stroke.

The design, development, and characterisation of a transceiver (TXRX) and a transmit-only receive-only (TORO) coil system are described. The developed coils were compared to a commercial double-tuned $^{23}$Na/$^{1}$H TXRX surface coil. As a result, the developed double-tuned TXRX surface coil achieved two-fold SNR improvement in the $^{23}$Na channel, while maintaining the high sensitivity in the $^{1}$H channel. Furthermore, the developed double-tuned $^{1}$H/ $^{23}$Na volume resonator achieved a $B_1$-homogeneity better than 5 % across the sample volume. In conjunction with the developed $^{23}$Na receive-only surface coil, up to three-fold better SNR was achieved in sample depths of 12 mm, the depth of interest for rat brain imaging. In a second development phase, a 2D-radial sequence was optimised to shorten the TE after the $^{23}$Na excitation pulse to below 1 ms. A TSC quantification method was developed for the dual resonator system and tested on phantoms containing known $^{23}$Na concentrations. This technique was then applied to the measurement of TSC maps *in vivo* in a rodent model of cerebral ischaemia with a spatial resolution of 1.2 µl and a 10 min image acquisition time. Such high spatio-temporal resolution allowed, for the first time, for the study of regionally dependent TSC change *in vivo* with a quantification accuracy of approximately ± 10 mM for up to eight hours after stroke induction. In contrast to previous studies in this area, it was found that TSC increased immediately in core tissue, but was delayed by up to 4 h in tissue considered to be still-viable but at risk of infarction.

For the first time, the bio-energetic cell failure in infarcted stroke tissue was measured and spatio-temporally resolved. An increase in TSC was hypothesised to indicate infarction, and it is therefore felt that elevated TSC could serve as an irreversible and non-invasive marker for tissue damage after the onset of ischaemic stroke.

**Declaration**

I declare that this thesis has not been submitted as an exercise for a degree in any other university.

This thesis is entirely my own work, except for the advice and assistance in the acknowledgements.

I agree to allow the library of TCD copy or lend a section or this entire thesis on request.

Friedrich Wetterling

**Acknowledgements**

I would like to express my gratitude to those who contributed to the successful running of the $^{23}$Na MRI experiments; without them, I could not have written this thesis.

**Special thanks go to…**

… Dr. Andrew Fagan, for warmly welcoming me to Ireland, which became a new home to me over the past four years, for taking me on as his PhD student, for giving me all the scientific and personal support I needed during the course of my PhD, for facilitating my development as a young scientist in the field of MRI by giving me the opportunity to participate at national and international conferences, and furthermore for contributing to the success of this thesis through setting-up fruitful collaborations with leading MRI groups in Ireland, the UK, and Germany.

…Prof. Mhairi Macrae, and Lindsay Gallagher for supporting MRI scanning of their well-developed *in vivo* intraluminal thread model at Glasgow University/ Scotland, UK.

…Dr. Sven Junge, for supporting MRI scanning at Bruker BioSpin in Ettlingen/ Germany, and for guiding me in the field of RF coil development.

…Martin Tabbert, for supporting the development of the double-tuned volume resonator.

…Dr. Oliviero Gobbo, for supporting MRI scanning at TCIN, Dublin/ Ireland.

…Dr. Jacinta Browne, for an introduction in to the world of tissue-parameter replicating phantoms and their preparation.

… Margaret, my girlfriend who I am inexplicably blessed by, and with who I went through the ups and downs of writing this thesis.

…John, Gerard, Donald, and Paul, my friends who I have shared the same house with and who I enjoyed many good pints of Guinness with.

…Brian, a good friend, who made my stay in Ireland unforgettable.

The research presented in this thesis has been supported by the generosity of the Science Foundation Ireland (SFI).

To my beloved grandmother:

*Ruth Wetterling*.

Without her encouragement this thesis

would have never been written.

# Index

## Abbreviations

| | |
|---|---|
| DC | …direct current |
| *emf* | …electro motive force |
| FA | …flip angle |
| FoV | …field of view |
| FLASH | …fast low angle shot |
| GRE | …gradient echo |
| i.d. | …inner diameter |
| MCAO | …middle cerebral artery occlusion |
| MRI | …magnetic resonance imaging |
| MTX | …matrix |
| NMR | …nuclear magnetic resonance |
| Q-factor | …quality-factor |
| qNa-MRI | …quantitative $^{23}$Na MRI |
| RARE | …rapid acquisition with relaxation enhancement |
| RF | …radio frequency |
| RoI | …region of interest |
| SNR | …signal-to-noise-ratio |
| TA | …acquisition time |
| TE | …echo time |
| TORO | …transmit-only receive-only |
| TR | …repetition time |
| TXRX | …transmit-receive |
| VoI | …volume of interest |
| Voxel | …volume element |
| $^{23}$Na-MRI | …$^{23}$Na magnetic resonance imaging |

# 1 Introduction

Stroke is the third most common cause of death and disability in Ireland [1]. Local $^{23}$Na concentration changes are known, from non-MRI examinations dating back several decades, to directly correlated with pathological changes in stroke tissue [2]. There is as a result a growing interest in investigating whether such pathological changes may be detected using $^{23}$Na Magnetic Resonance Imaging ($^{23}$Na-MRI), for example by measuring regional changes in $^{23}$Na concentration in the acute phase following a stroke [3-11]. However, the exact measurement of Tissue Sodium Concentration (TSC) via quantitative $^{23}$Na-MRI (qNa-MRI) in rat stroke models has been hindered by limitations in Signal-to-Noise Ratio (SNR) within the needed spatial (< 4 µl voxel size) and temporal (< 10 min acquisition time) resolution constraints [12, 13]. In this chapter, the general principles of MRI, possible qNa-MRI resonator systems, the physical properties of the $^{23}$Na nucleus in brain tissue, and the applicability of qNa-MRI to investigate stroke tissue are explained.

## 1.1 The Principles of Magnetic Resonance Imaging

### 1.1.1 The Basic Free Induction Decay (FID) Experiment

In Magnetic Resonance Imaging (MRI) the sample is exposed to a strong externally-applied magnetic field ($B_0$), here 7.05 T. The basic components of the MRI systems used for the work described in this thesis are presented in Figure 1.1. A superconducting electromagnet provides a static magnetic field, which points along the z-direction. A set of shim coils is then used to compensate for $B_0$-field inhomogeneities caused by the magnet itself and susceptibility differences in the sample. A gradient set provides deliberate variations in the static magnetic field strength along the x-, y-, and z-direction. These variations are necessary in order to spatially resolve different sample locations. The radio-frequency resonator completes the MRI system set-up.

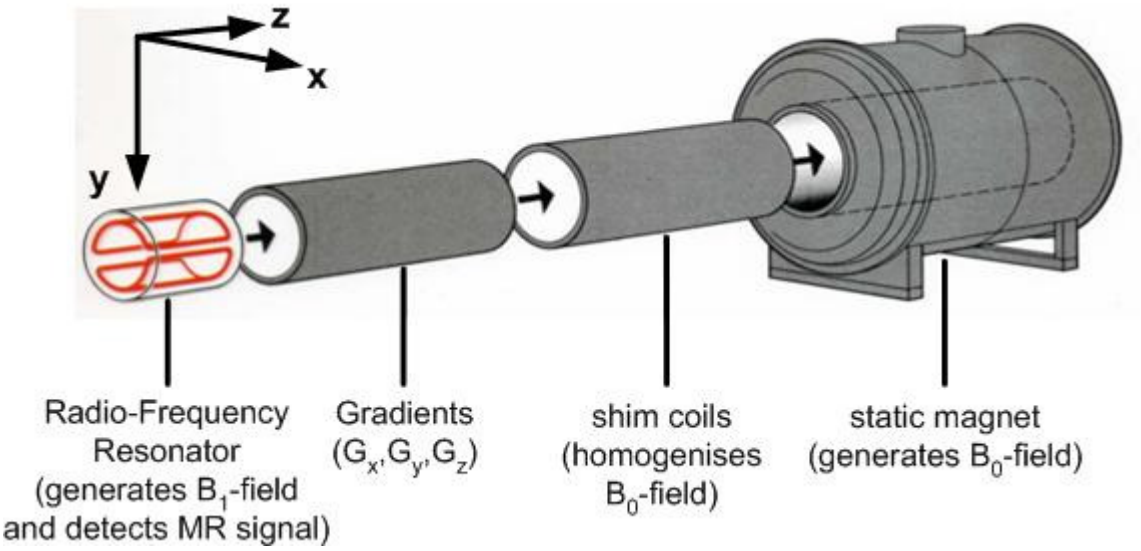


**Figure 1.1: The basic components of an MRI system.**

For the sake of simplicity, the principles of the MRI technique are explained based upon the properties of the $^1$H-nucleus, which is also used in common MRI techniques. The $^1$H spin (½) can occupy two energy levels due to the Zeeman interaction between the $B_0$-field and the proton's magnetic moment ($\mu$). The two energy levels can be interpreted as a parallel ($\uparrow\uparrow$) or antiparallel ($\uparrow\downarrow$) alignment of $\mu$ relative to $B_0$. The occupation of these states reaches a thermal equilibrium, which is described by the Boltzmann distribution:

$$\frac{N_{\uparrow\uparrow}}{N_{\uparrow\downarrow}} = e^{\frac{\Delta E}{kT}} \qquad \text{(Equation 1.1)},$$

where $N_{\uparrow\uparrow}$ / $N_{\uparrow\downarrow}$ are the respective occupancy levels, $\Delta E$ is the Energy difference between the two states, $k$ is the Boltzmann's constant, and $T$ is the temperature. The anti-parallel orientation is energetically less favourable leading to a slight excess of spins in the parallel alignment. The ensemble average of the magnetic moments of these excess spins results in a net magnetisation vector $\vec{m}_0$ with amplitude $M_0$ aligned along the direction of $B_0$, which is usually defined to be the $z$-direction.

A second, time-varying magnetic field, the $B_1$-field, is applied in the $xy$-plane transverse to $B_0$ in the form of a radio-frequency (RF) pulse generated by an RF coil. The applied frequency of this RF-pulse is identical to the precessional frequency $\omega_0$ of the nuclear spins around $B_0$, as described by the Larmor equation:

$$\omega_0 = \gamma B_0 \qquad \text{(Equation 1.2)},$$

where $\gamma$ is the gyromagnetic ratio. This RF pulse tips $\vec{m}_0$ away from the $z$-direction, while the duration and strength of the transmitted RF pulse determines the resultant angular

orientation of $M_0$ relative to $B_0$. An RF pulse which tilts $\vec{m}_0$ from the *z*-axis into the *xy*-plane is called a "$90^\circ$ pulse". After the transmission of a $90^\circ$ pulse, the nuclei precess in the *xy*-plane until the spin population relaxes to its equilibrium state, corresponding to a recovery of the net magnetisation along the *z*-axis. The MRI signal is measured as an induced voltage in a receiving RF coil – the MR signal - as long as there is a net magnetisation precessing in the *xy*-plane.

### 1.1.1 Signal Properties

Two fundamental temporal parameters are used to describe the MR signal. The longitudinal relaxation time, $T_1$, is the time constant describing the rate at which the nuclear spins, once placed in a magnetic field, exponentially approach thermal equilibrium, so that the scalar component in the *z*-direction of the magnetisation vector is described by the formula:

$$M_z(t) = M_0\left(1 - e^{-\frac{t}{T_1}}\right) \qquad \text{(Equation 1.3)},$$

where $M_0$ is the equilibrium magnetisation amplitude. In biological tissues, $T_1$ for the $^1$H-nucleus is long, ranging typically from hundreds of milliseconds to seconds. Differences in the $T_1$ of tissues are one of the primary sources of image contrast in clinical $^1$H-MRI.

A second time constant, $T_2$, describes the transversal net magnetisation decay following RF excitation. Small variations in the local magnetic field, for example those induced by the magnetic moments of neighbouring nuclei, cause the $^1$H spins to precess at slightly different frequencies and consequently to dephase relative to one another. Therefore, the $T_2$-relaxation time relates to the spin-spin interaction. The observed signal decay is described by the parameter $T_2^*$, which is the net transversal relaxation time which is affected in turn by all the dephasing terms [14]:

$$\frac{1}{T_2^*} = \frac{1}{T_2} + \frac{1}{T_2^{inh}} + \frac{1}{T_2^{suscept}} \qquad \text{(Equation 1.4)},$$

where $T_2^{inh}$ represents the dephasing due to magnetic field inhomogeneities and $T_2^{suscept}$ is the susceptibility-related signal loss depending on the sample's magnetic susceptibility. $T_2^*$ generally ranges from a few milliseconds to tens of milliseconds.

Incorporating both $T_1$- and $T_2$-relaxation times, the MR signal, $S(t)$, decays according to the formula:

$$S(t) = S_0\left(1 - e^{-\frac{TR}{T_1}}\right)e^{-\frac{t}{T_2^*}} \qquad \text{(Equation 1.5)},$$

where $S_0$ is the signal strength immediately following the excitation pulse, and $TR$ is the repetition time between two consecutive RF-pulses. In imaging experiments, an additional parameter is used: the Echo Time (TE), which is defined as the time between the RF-pulse application (half pulse length) and the time point at which the maximum signal is acquired (typically of the order of milliseconds). TE has to be chosen appropriately long to let the differences in $T_2^*$ or $T_1$ evolve before detecting the resulting signal. In the case of fast decaying $^{23}$Na signals, TE must be chosen to be below 1 ms. By varying the TR and TE parameters, one can acquire images with contrast weighted by either the $T_1$ or $T_2$ relaxation properties of the tissue under investigation.

### 1.1.1 Spatial Decoding

The MR signal detected originates from the ensemble net magnetisation of the entire sample volume. In order to form an image, the voxel-related net magnetisations must somehow be spatially resolved. This is usually a two-step process: (i) exciting the magnetisation in a single slice within the sample, and (ii) encoding the spatial location of the signal within this slice during data acquisition. This is done by using linearly varying magnetic fields in all three spatial directions to separate the signal from different locations according to a voxel-related frequency and phase difference. With a sample placed within a linear magnetic field gradient, for example, the Fourier Transform of the measured signal shows its strength at each frequency, and thus at each local position. Within the sample, MR imaging systems use three mutually orthogonal sets of gradient coils to generate these three gradient magnetic fields. The different gradients required are: slice selection $G_z$, frequency encoding $G_y$, and phase encoding gradient $G_x$. Timing diagrams, for example that illustrated in Figure 1.2, are used to describe the switching ON and OFF of the gradients, RF pulses and the timing of the data acquisition. These so-called "Pulse Sequences" have many variations leading to different image contrast (e.g. $T_1$ or $T_2$) - Figure 1.2 illustrates a standard Gradient Echo (GRE) sequence as can be used for $^{23}$Na-MRI and which is explained in more detail in Section 2.6.2.1.

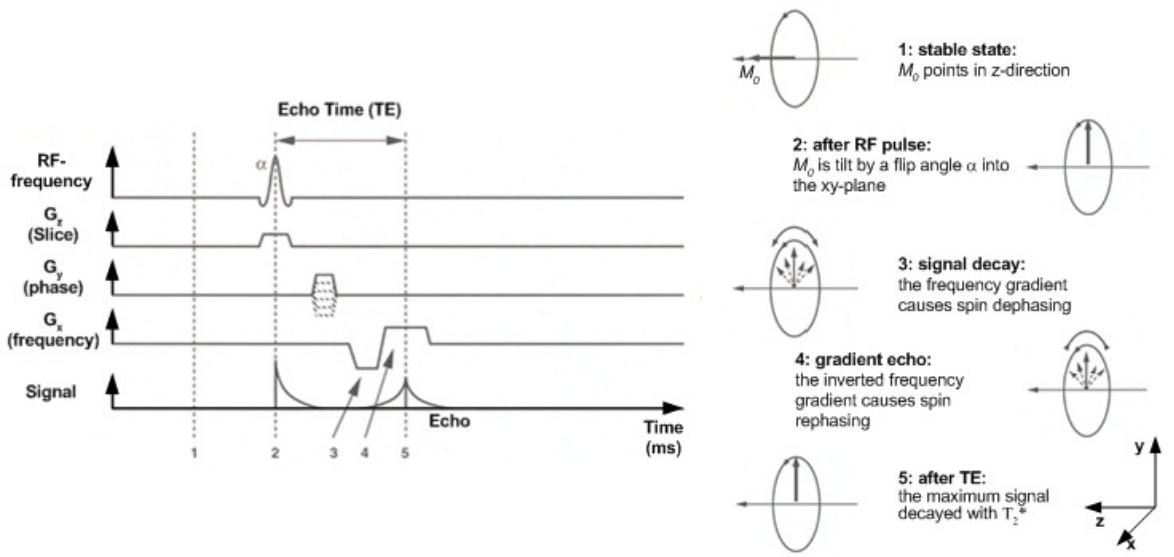


**Figure 1.2: The Gradient Echo pulse sequence (adapted from [15]).**

### 1.1.2 Signal Variations and Noise

Noise is interpreted as increased variance with random amplitude in a measured image. There are two different types of noise in an MR image: low-frequency and wideband noise. The wideband noise is dominant for most MRI systems. It originates in the RF coil and is caused by thermal sources. Low-frequency noise typically exhibits a 1/f characteristic, and is composed of non-periodic, slow variations. In addition, periodic physiological noise can appear as peaks in the frequency spectrum. Any source of fluctuation such as body movements and spontaneous neural and vascular fluctuations contribute to the MRI noise and can decrease the SNR. The noise can effectively be reduced by reducing the coil dimensions, which is a standard design consideration when constructing RF coils, evident for example by choosing a dedicated coil for every part of the subject's body (brain, knee, shoulder, etc.). Considering the sequence parameters, the sequence developer has to carefully choose the Acquisition Time (TA), as the SNR is proportional to the square root of TA and thus leads to the widespread use of signal averaging techniques in MRI.

## 1.2 The NMR Properties of $^{23}$Na in Brain Tissue

From a physics point of view, the sodium nucleus, $^{23}$Na, which has 100 % natural abundance, provides the strongest non-$^{1}$H magnetic resonance signal that can be detected *in vivo*, and thus subtle changes in TSC can potentially be measured using qNa-MRI. The $^{23}$Na nuclei possess a *3/2*-spin, which results in the development of four Zeeman-energy

levels when placed in a static magnetic field. In isotropic environments such as liquid solutions, the energy differences between all four energy levels are identical. The 3/2-spin number indicates that $^{23}$Na-nuclei possess an electric quadrupolar moment, which is due to the asymmetrical charges distribution in the nucleus. The energy differences between the outer Zeeman-energy levels change when sufficiently inhomogeneous electric fields, such as those produced by electron clouds and macro-molecules, exert detectable torques on those electric quadrupolar moments. Both the magnitude and the sign of the energy level shift of the external energy level transitions depend on the angle $\theta$ between the major axis of the quadrupolar tensor and the $z$-axis. If the local environment is isotropic, then averaging across all angles gives zero average energy displacement. In anisotropic environments such as in brain tissue or gels, quantum theory predicts that only 40 % of the total radiated energy contributes to the inner transition, decaying with a slow transversal relaxation time $T_{2s}$, while the remaining 60 % corresponds to the two outer transitions, decaying with a fast transversal relaxation time $T_{2f}$ [16]. This approximation also applies for increasing $^{23}$Na concentrations, since the viscosity of NaCl solutions increases only slightly with increasing concentration; other NMR experiments have also shown that the contribution of electromagnetic field gradients from the $^{23}$Na and $^{35}$Cl ions to the relaxation are smaller compared to those from the electric dipole moments of the water molecules [16]. Thus, the environment in which $^{23}$Na nuclei are located influences the signal properties, with the $^{23}$Na signal detected from anisotropic brain tissue exhibiting bi-exponential decay due to the evolving electrical quadrupolar interaction. Shapiro *et al.* conducted measurements of such bi-exponential $T_2^*$-decay in agar gel phantoms, which replicated the tissue environment of $^{23}$Na ions. As expected, the signal intensity decreased faster with increasing gel concentration in the $^{23}$Na environment [17].

Figure 1.3 shows the simulated transversal $^{23}$Na signal decay for tissue equivalent relaxation times, with $T_{2s}$ = 25 ms and $T_{2f}$ = 5 ms. For standard TEs of 2 ms, the acquired signal strength has already dropped by 25 %. Thus, identical $^{23}$Na concentrations contained in different tissue types may result in different measured MR signal intensity levels depending on the measurement time point after the RF excitation. Consequently, an exact knowledge of the tissue under investigation and its MR relaxation properties is essential for accurately quantifying the TSC. $T_2$-weighting can then be minimised by choosing an appropriately short TE (typically < 1 ms).

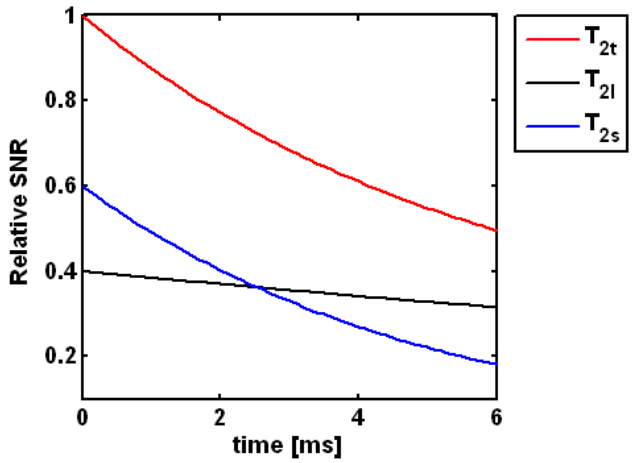


**Figure 1.3: Simulation of the bi-exponential decay in tissue with total transversal relaxation time $T_{2t}$, which is composed of the fast and slow exponential decays with fast $T_{2f}$ = 5 ms and slow $T_{2s}$ = 25 ms transversal relaxation times.**

The NMR relaxation phenomena of spin *3/2*-nuclei are complex for nuclei in aqueous heterogeneous system such as $^{23}$Na-nuclei in tissue. They are strongly affected by local binding and motions, and also by long-range ordering and the arrangements of the macromolecules [16]. Although quadrupolar interactions in biological tissue can be treated as a weak perturbation of the Zeeman interaction, the associated bi-exponential decay makes $^{23}$Na quantification difficult, when TEs longer than 1 ms are used.

## 1.3 Resonator Systems for $^{23}$Na Magnetic Resonance Imaging

The development of a qNa-MRI technique at 7 T is described in this thesis, which was mainly based on the development of an optimised resonator system. The following section gives a brief literature overview about resonators used in previously published $^{23}$Na- and qNa-MRI studies. MRI coils are used to transmit Radio Frequency (RF) pulses into the sample and to receive the RF signal from the sample. Thus, coil systems have a major influence on the acquired Signal-to-Noise Ratio (SNR). MRI coils can be subdivided into two groups: volume and surface coils. Furthermore, coil systems can be distinguished in either single coil or dual coil systems by the way they transmit the RF pulse and receive the MR signal. A single coil system is composed of a single resonator used for both the transmission and the receive modes. A dual coil system is composed of two separate resonators, of which one is used for the transmission and the other for the receiving process. The latter resonator combination can be used to exploit both the transmit advantages of volume coils and the receive advantages of surface coils. The properties of

single coil systems used as transmit-receive (transceiver) surface and volume resonators are discussed in the next paragraph.

The advantage of surface coils is that they can be placed very close to the signal origin on the sample's surface and they thus detect the maximum possible signal strength. Surface coils were used by Thulborn *et al*. to investigate the rat brain [18], by Maril *et al*. to measure the TSC gradient across rat kidneys [19], and by Ouwerkerk *et al*. to image pathological brain and cardiac tissue in humans [20, 21]. Thulborn *et al*. had to compensate for $B_1$-field inhomogeneities caused by the surface coil-dependent sensitivity profile, whereby Ouwerkerk *et al*. and Maril *et al*. employed adiabatic pulses to gain more homogeneous $B_1$-fields. However, the power deposition for such adiabatic RF pulses is higher and the RF pulse lengths are longer compared to standard RF pulses, reducing the possibility of shortening the delay time between the RF-pulse and the data acquisition for qNa-MRI.

Volume resonators, on the other hand, generate a homogeneous $B_1$-field, reducing the need for $B_1$-inhomogeneity compensation. Birdcage coils – a type of volume resonators, have often been used for qNa-MRI, for instance by Constantinides *et al*. who used a single tuned birdcage coil for qNa-MRI on humans [22-24], Thulborn *et al*. who worked with a double tuned $^{23}$Na/$^{1}$H, dual quadrature birdcage coil for qNa-MRI on humans and non-human primates [8], Schepkin *et al*. who used a small birdcage coil (23 mm diameter and 45 mm length) to perform qNa-MRI on tumour in the rat brain [25], and Jones *et al*. who used a small dual quadrature, double tuned birdcage coil (5 cm diameter and 5 cm length) to determine the time of stroke onset in rats [5].

Ideally a transmit-only birdcage coil can be employed as part of a dual coil system, where a surface coil is preferentially used for receiving the MR signal from the sample. Such a dual coil system is technical more sophisticated to build, because both coils must be actively decoupled from each other using an additional Direct Current (DC) circuit incorporated into each coil design. However, good results were achieved using such a system by Bartha *et al*. who used a dual coil system composed of a $^{23}$Na birdcage transmitter and an actively decoupled surface receiver [3]. With this setup, the authors were able to perform $^{23}$Na-MRI on a rabbit model of cerebral ischaemia at 4 T with an acquisition time of 20 min using a 3D GRE sequence. Only a few Phased Array (PA) detector coils have been reported in the literature, all of which were developed for use in clinical MRI systems [26, 27]. Although transceiver PA detectors have been developed for higher field strength and rat brain $^{1}$H/ $^{23}$Na/ $^{31}$P-MRI applications [28], the SNR-benefits of

PAs compared to single receive-only surface coils remains to be verified for pre-clinical investigations on small bore MRI systems.

From reviewing the literature, a double-tuned $^{23}$Na/$^{1}$H transceiver surface coil could provide maximised SNR for $^{23}$Na–MRI assuming one requires the capability to image $^{1}$H to allow for correlation of the $^{23}$Na images with high resolution $^{1}$H anatomical images. On the other hand, for qNa-MRI, a double-tuned $^{23}$Na/$^{1}$H dual coil system composed of a $^{1}$H/$^{23}$Na birdcage and a $^{23}$Na receiver-only surface could enable the TSC quantification in the rat brain, while maintaining a high SNR-efficiency in the $^{23}$Na channel and $^{1}$H imaging capability.

## 1.4 $^{23}$Na Magnetic Resonance Imaging and Stroke

There are two broad categories of stroke, haemorrhage and ischaemia, which reflect diametrically opposite conditions: haemorrhage is characterised by too much blood within the skull, while ischaemia is characterised by a lack of blood and thus a lack of oxygen and nutrients supplied to a part of the brain [29]. The consequence of ischaemic stroke is slow necrosis, the death of tissue, which is also called infarction. The entire underperfused stroke lesion is generally subdivided into core (already infarcted) and penumbra tissue (still-viable and potentially salvageable). The immediate detection of infarcted stroke tissue after ischaemia via localised TSC measurements is the topic of the work presented here.

Brain tissue mainly consists of neurons, where each neuron encapsulates a small volume of intracellular (IC) space. The volume around neurons is referred to as the extracellular (EC) space, which in turn is composed of the EC compartment and the vascular compartment. Although the brain consists of more sophisticated anatomical structures, these are not considered in further explanations, because the physiological $^{23}$Na concentration differs only between the IC and EC spaces (~ 10 mM and ~ 140 mM respectively [30]). The vascular compartment maintains the EC $^{23}$Na concentration at a constant level at all times even in diseased tissue. Thus, changes in cellular $^{23}$Na concentrations levels which for example occur following ischaemic stroke directly influence the overall Tissue Sodium Concentration (TSC).

The $^{23}$Na concentration is functionally important for the neuron's task of conducting electrical potentials along its axons. The different concentration levels of ions within and outside the cell establish a resting potential and polarise the cell membrane. The different concentration gradients ensure a quick equalisation during neuronal

excitation, when the membrane channels open to transmit the action potential along the axon. The *Sodium-Potassium-Pump* (*$Na^+$-$K^+$-pump*) re-establishes the concentration gradients afterwards. The energy for this is obtained from decomposing Adenin-Tri-Phosphate (ATP) into Adenine-Di-Phosphate (ADP). During cerebral ischaemia, the *$Na^+$-$K^+$-pump* function is disrupted leading to an increase of the IC $^{23}$Na concentration. Consequently, the TSC increases, while the EC $^{23}$Na concentration is maintained constant (~ 140 mM) through the vascular compartment and the kidneys.

It is clear from reviewing the literature that a variety of MRI techniques have been used to investigate ischaemic stroke. The vast majority of these are $^{1}$H-MRI-based, with diffusion MRI [10, 31, 32] predominantly used over perfusion MRI [18]. However, $^{23}$Na MRI approaches are beginning to be used, usually accomplished as $T_2^*$-weighted $^{23}$Na-MRI [5, 18, 21, 25, 33, 34], while $T_1$-weighted $^{23}$Na-MRI may also prove useful for the detection of $^{23}$Na concentration changes [35].

A study comparing Diffusion-Weighted $^{1}$H-MRI (DWI), Perfusion-Weighted $^{1}$H-MRI (PWI), and $^{23}$Na-MRI demonstrated that PWI is lacking in its ability to indicate disruptions in cell functionality [34]. The other two techniques demonstrated similar accuracies in localising areas of infarcted tissue. However, the temporal evolution of the abnormalities in ischaemic brain tissue detected by $^{23}$Na-MRI is different from that detected by $T_2^*$-weighted $^{1}$H-MRI and DWI related Apparent Diffusion Coefficient (ADC) maps [11]. Jones *et al*. demonstrated that the increase of $^{23}$Na concentration which occurs during focal cerebral ischaemia can be measured with $^{23}$Na-MRI in the rat brain [5] and they went so far as to estimate an onset time of ischaemia, which has proved impossible to estimate using DWI. The aim of this project was to develop $^{23}$Na-MRI on a 7 T small bore MRI system in order to investigate the evolution of functional parameters during cerebral ischaemia in the rodent's brain.

There are two different approaches using qNa-MRI to detect stroke in brain tissue:

1. Measuring the mean $^{23}$Na concentration, which is the Tissue Sodium Concentration (TSC), and
2. Separately measuring the EC and IC $^{23}$Na concentration separately (using Chemical Shift Imaging or Multiple Quantum Coherences Weighting).

The first approach, which is used in the current work, will be explained more extensively in Section 7.3 (The Quantification of TSC). The second approach is based on splitting the detected $^{23}$Na signal into separate EC and IC signal components. Invasive methods, such as Chemical Shift Imaging (CSI), which use Shift Reagents (SRs) and non-invasive

methods such as the Multiple Quantum Coherence (MQC) filters, allow for such splitting of the $^{23}$Na signals.

In CSI, the SR used is a paramagnetic anion, which cannot pass through the cell membrane, and hence does not enter the IC space. Once the SR reaches a certain compartment, it shifts the resonance frequency of only the $^{23}$Na ions contained in that compartment. It appears that the SR enters the EC-interstitial-space in every organ except the healthy brain, where it is constrained to the plasma space by the intact blood-brain-barrier [36]. CSI was used by Winter and Bansal, who used TmDOTP$^{5-}$ as the SR to mark the EC $^{23}$Na ions and to detect the IC $^{23}$Na signal in a brain tumour (9L gliasarcoma) [37]. The $^{23}$Na concentration was not quantified by MRI measurements, but rather transversal relaxation times of the EC $^{23}$Na ions were calculated by subtracting the measured IC $^{23}$Na signal in the presence of the SR from the measured total $^{23}$Na signal in the absence of the SR. They found that fast transversal relaxation with a time $T_{2f}$ occurs extracellularly as well as intracellularly, with almost equally fast relaxation times at 9.4 T (IC: $T_{2f}$ = 2.0 ± 0.8 ms and EC: $T_{2f}$ = 3.4 ± 0.3 ms). Therefore, it cannot be assumed that fast relaxation times of $^{23}$Na-nuclei occur only in the IC space, since they were also measured in the EC space, which exacerbates applying the MQC approach (see below). Neuberger *et al*. found the major disadvantage of CSI to be the inherently long data acquisition times required to acquire the 4-dimensional data sets that contain one spectral dimension and three spatial dimensions [38]. This meant that only a relatively sparse three-dimensional k-space matrix could be sampled. In conclusion, CSI can be used to shift the EC $^{23}$Na signal and thus can be used to measure the IC $^{23}$Na signal directly. In addition to the toxicity of all SRs used to date, applying CSI for brain *in vivo* investigations is practically difficult, because they do not pass the blood brain barrier and would only reach their target if directly injected into the brain tissue.

The other method of splitting $^{23}$Na signals from the EC space and the IC space is to use MQC filters, which exploit the quadrupolar moment of $^{23}$Na to distinguish between $^{23}$Na-nuclei in the EC and IC spaces. Due to the $^{23}$Na-nucleus's inherently different relaxation properties in spatially restricted environments, it is assumed that $^{23}$Na in the IC space interacts stronger with adjacent macro-molecules and therefore exhibits a stronger bi-exponential decay compared to $^{23}$Na-nuclei in the EC space, which are assumed to be less influenced by macro-molecular interactions. Three single quantum coherences, two double quantum coherences and one triple quantum coherence arise between the four non-degenerated energy levels of the $^{23}$Na nucleus.

Pekar *et al*. suggested that multiple quantum filtration could be used to selectively observe the resonance from intracellular *3/2*-spin metal ions [39]. Later, Kline *et al*. formulated that the presence of an MQC-signal could be used to identify populations of $^{23}$Na nuclei by their molecular environment and could be used to detect changes in the IC space as they occur during cerebral ischaemia [40]. However, the signal intensity following a multiple-quantum spin sequence is only a small fraction of the signal intensity following a single, ideal, 90˚ excitation pulse (*in vivo* values of 10 % to 15 % have been reported [41]). This technique has also proven to be only partially successful, since it was found that EC ions also exhibit bi-exponential relaxation [42]. Nevertheless, MQC filters were successfully applied in imaging cartilage. Cartilage is strongly anisotropic compared to brain tissue and therefore possesses very short transversal relaxation time, which in turn result in strong MQC effects [43, 44]. Hancu *et al*. demonstrated the diagnostic applicability to image the normal human brain *in vivo* within 20 min using a three dimensional triple quantum filtered $^{23}$Na imaging sequence [45]. However, $B_1$-inhomogeneities [46], and $B_0$-inhomogeneities [47] cause problems in MQC-MRI, and the fast transverse relaxation times could not sufficiently be studied with currently available methods [16]. Practical complications were also mentioned by Goodman *et al*., who were unable to observe even-ordered $^{23}$Na coherences in rat brain tissue under optimised experimental conditions [48].

The measurement of MQC is still difficult due to a lack of conclusive results and a ten-fold lower SNR compared to TSC measurements. Thus, an SNR-optimised $^{23}$Na-MRI coil system may also contribute to novel insights in future MQC filtering experiments.

## 1.5 Hypothesis

1. The geometry and dimensions of a double-tuned transceiver surface coil can be optimised in a way that the detected SNR increases by more than 50 %, when compared to a commercially available planar surface coil (optimised for the $^{23}$Na/$^{1}$H-MRI rat brain application).
2. A dual coil system can be built, which generates a homogeneous $B_1$-field at the $^{23}$Na frequency and therefore allows the quantification of TSC *in vivo*. At the same time such a system can be built in such a way that it improves the detected SNR at the $^{23}$Na frequency in the RoI, when compared to a commercially available double-tuned transceiver surface coil (optimised for the $^{23}$Na/$^{1}$H MRI rat brain application).

3. The TSC can be measured in a permanent *in vivo* rodent stroke model with a quantification accuracy and spatio-temporal resolution sufficient to detect subtle regional variations in TSC during the acute phase of cerebral stroke, using an optimised resonator system, sequence, and high static magnetic field strength (7 T).

## 1.6 Document Structure

The document is structured into 9 chapters. The theory and basic methods used in MRI resonator design and characterisation are described in Chapter 2. The practical influences of different design parameters, such as coil dimensions and geometry, inductance, and loading on signal related bench test parameters are investigated and the development of a bench testing method is described in Chapter 3. The design, development, and characterisation of a double-tuned transceiver surface coil, as an improvement on a commercially available double-tuned transceiver surface coil is described in Chapter 4. The benefits of using such an optimised coil for achieving the maximum SNR per unit time together with a 2D Fast Low Angle Shot (FLASH) sequence are demonstrated. The development of a double-tuned birdcage resonator for quantitative qNa-MRI is described in Chapter 5. The development of a receive-only surface coil is described in Chapter 6. The best performing coil system was used to quantitatively measure TSC in *in vivo* stroke model as described in Chapter 7. In a final development Chapter 8, a novel delayed-exponential model was employed to analyse the TSC time courses in various spatial locations of the stroke lesion. This thesis ends with a discussion and conclusion in Chapter 9.

# 2 MRI Resonator Theory and Characterisation

$^{23}$Na Magnetic Resonance Imaging ($^{23}$Na-MRI) suffers from low SNR caused by the $^{23}$Na-nuclei's low gyromagnetic ratio, low concentration in tissue and fast MR signal decay. The detectable $^{23}$Na SNR in the rat brain is furthermore restricted by the small voxel size ($< 4\ \mu l$) which is required to spatially resolve structures such as the caudate-putamen and the cortex in the rat brain. Careful design of the detector systems with the specific sample dimensions and transmit pulse requirements in mind can therefore maximise the available SNR. The origins of the measured RF signal in the Nuclear Magnetic Resonance (NMR) experiment, the theory of RF circuit and resonator element design, and common characterisation techniques for room temperature MRI resonators are described in this chapter.

## 2.1 NMR Signal Theory

As described in Section 1.1, the RF resonance coil is used to apply a 90˚-pulse in order to tip the *z*-directed net magnetisation vector $\overrightarrow{m_0}$ into the orthogonal *xy*-plane, where it precesses while returning to its equilibrium orientation (along the *z*-direction). The induced electro motive force (*emf*) for a given geometric relationship between the detector coil and the sample location (see Figure 2.1) may be described as follows:

To enable the computation of the magnetic field strength originating from a sample location $\vec{r_0}$, the magnetic dipole moment must be converted to the equivalent magnetic dipole moment, which is defined by a current flowing in a closed loop with surface area $\vec{A}$:

$$\overrightarrow{m_0} = I \cdot \vec{A} \qquad \text{(Equation 2.1).}$$

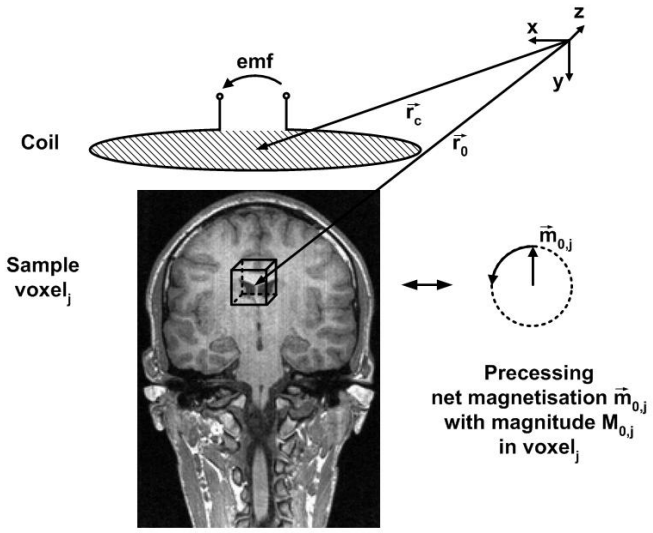


**Figure 2.1: The geometric relationship between the detector coil and the sample, where the sample is placed underneath the coil. The precessing net magnetisation vector in a particular sample voxel (illustrated at the right side of the image) induces an *emf* in the detector coil, which can be measured as a voltage drop-off across the coil terminals.**

From this definition, the magnetic field strength at an arbitrary location on the coil's detector surface having a distance $r$ to the voxel position $\vec{r_0}$ can be determined via the Bio-Savart Law:

$$d\vec{B} = \frac{\mu_0 I d\vec{L} \times \vec{r_0}}{4\pi r^3} \qquad \text{(Equation 2.2)},$$

where $\mu_0$ is the permeability of free space, and $I$ is the current in $dL$ - the current flowing in the loop formed by the equivalent magnetic dipole moment. The solution to this equation can be found elsewhere [49].

The final computation of the induced *emf* is based upon Faraday's Law of electromagnetic induction. It states that the induced *emf* in a conductive loop equals the rate of change of magnetic flux through the loop [50], revealing that a time varying magnetic field strength threading through the conductive loop acts as a source of electric field and vice versa:

$$E = -\frac{d\Phi_B}{dt} \qquad \text{(Equation 2.3)},$$

where $E$ is the induced *emf* and $\Phi_B$ is the magnetic flux threading through the conductive loop at various time points $t$.

To compute the magnetic flux $\Phi_B$ for the net magnetisation vector at one time point, it is necessary to integrate over the magnetic field strength components ($B_y$), which thread through the surface coil in parallel orientation to the surface coil's normal vector.

Thus, when the magnetic flux threading through the detector coil varies over time, as it does in MRI, a measurable *emf* is induced in the detector loop (Figure 2.2).

## 2.2 Electro-Magnetic Resonance Theory

The task of the MRI detector is to pick-up the induced *emf* during the MRI experiment and to transmit it as a voltage to the system preamplifier before further analogue-to-digital conversion and data acquisition. Careful design of this first element in the receiver chain is important to reduce signal losses during the measurements. Signal reflection for example can occur for cable lengths $> \lambda/10$ (where $\lambda$ is the wavelength of the RF signal, which is related to the Larmor frequency and the velocity factor in the coaxial cable), when the cable and preamplifier impedances are mismatched. The detector impedance possesses complex impedance, which varies according to the coil environment, especially when placed inside the magnet on a variable load such as a rat's head. Two main strategies exist to match the detector coil to the expected input impedance at the preamplifier (typically 50 Ω). The first option is to use another preamplifier directly at the coil terminals. The second and more commonly used approach is to exploit the electro-magnetic resonance effect at the desired Larmor frequency. The latter approach served for the development of various coil systems for $^{23}$Na- and qNa-MRI in this work and is described in the next paragraph.

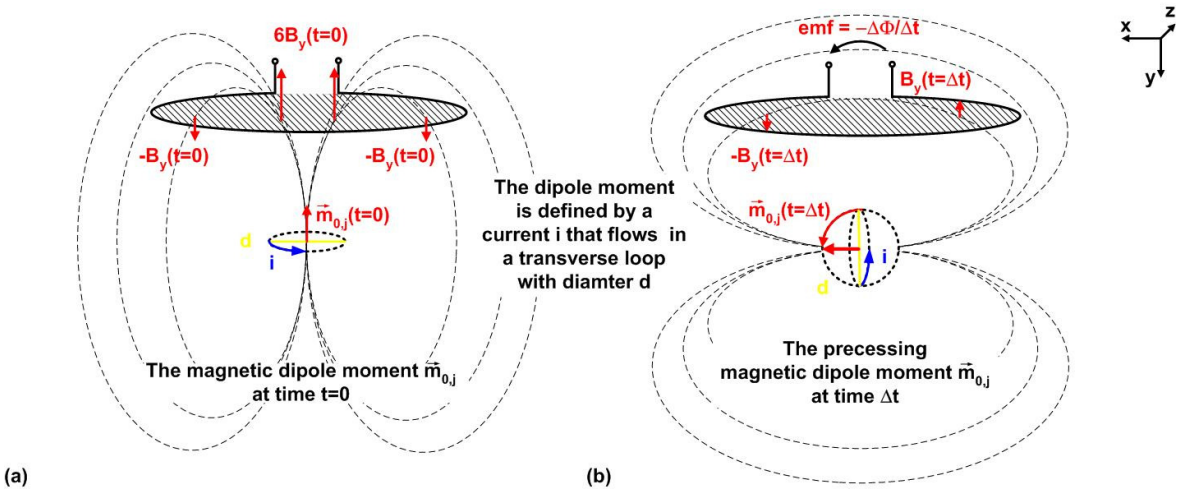


**Figure 2.2: Sketch of the NMR signal calculation of (a) a magnetic dipole moment modelled by an equivalent current flowing in a transverse loop, representing the situation immediately after the application of a 90°-pulse, and (b) the induced *emf* at time *Δt* later, when the magnetic dipole moment has precessed to a point along the *x*-direction.**

The basic idea behind the electro-magnetic resonance circuit is to simplify the complex impedance by cancelling out the imaginary parts of the impedance of the resonance circuit, namely the inductance and capacitance. The real impedance can then be easily transformed to the cable and preamplifier input impedance, as described in Section 2.5.2 ('Matching') below. The impedance of a parallel *LC* resonator is composed of the complex capacitive and inductive impedances. The inductive impedance of the coil wire is

$$Z_L = j\omega L \qquad \text{(Equation 2.4)},$$

with the angular frequency $\omega$, and the conductor inductance *L*. The capacitive impedance with parallel capacitance *C* is defined as:

$$Z_C = \frac{1}{j\omega C} \qquad \text{(Equation 2.5)},$$

Neglecting loss mechanisms, the frequency of such a resonance circuit is given by:

$$\omega_0 = \frac{1}{\sqrt{LC}} \qquad \text{(Equation 2.6)}.$$

This resonance equation demonstrates that the commonly employed parallel *LC* resonance circuit oscillates at one single frequency for which the magnetic energy stored in the inductor is exchanged for electric energy to be stored in the capacitor and vice versa. The resonance frequency is hence solely determined by the values of *L* and *C*, which can in practice be composed of several capacitive and inductive components, including parasitic capacitance between the coil and the sample.

The loss mechanisms, neglected above, are the reason why the resonance circuit inductance and capacitance for a desired Larmor frequency is difficult to be theoretically determined. Especially at high frequencies (> 1 MHz), the various loss mechanisms and interactions of the resonator with its conductive environment make it difficult to apply the loss-free resonance circuit approach. Therefore, the resonance frequency for the chosen element parameters must, in practice, be tuned through an iterative optimisation process, with the result monitored using a network analyser, which is explained in Section 2.4.2. Nevertheless, the knowledge of the loss mechanisms and their origin is of importance for the design of a well performing resonator. The loss mechanisms are explained in more theoretical detail in the next section.

## 2.3 Loss Mechanisms

The loss mechanisms in room-temperature resonators are predominantly determined by the Brownian motion of the electrons in the inductive loop leading to a potential difference,

which adds to the NMR signal-related *emf*. The effective noise signal magnitude $\sigma_n$ in the NMR experiment is mathematically expressed as:

$$\sigma_n = \sqrt{4 \cdot R_{eff} \cdot k_B \cdot T \cdot \Delta f} \qquad \text{(Equation 2.7)},$$

where $k_B$ is the Boltzmann constant, $T$ is temperature of the probe and $\Delta f$ the bandwidth of the detected NMR signal. The equivalent circuit diagram of the MRI resonance coil includes the losses as one effective loss resistance $R_{eff}$ in series with the coil inductance $L_{coil}$. An optimum room-temperature resonator is thus characterised by its very low effective noise resistance and its ability to pick-up the highest possible *emf*.

Four different loss mechanisms contribute to the effective loss resistance, which are due to the antenna effect (radiation losses), the wire length (resistive losses), magnetic field carrying currents in the sample (magnetic losses), and parasitic capacitors arising between sample and coil (electric losses) [49]. The effective resistance representing the four loss mechanisms is computed additively:

$$R_{eff} = R_R + R_\Omega + R_M + R_E \qquad \text{(Equation 2.8)}.$$

The theoretical equations for the computation of the effective loss resistance are given in the next paragraphs.

The resistive resistance for a resonator made of conductive wire of length $l_{wire}$, circumference $c_{wire}$, conductivity $\kappa_{coil}$, and skin depth $\delta_{coil}$ is calculated via:

$$R_\Omega = \frac{l_{wire}}{\kappa_{coil} \cdot \delta_{coil} \cdot c_{wire}} \qquad \text{(Equation 2.9)},$$

The skin depth $\delta_{coil}$ describes the frequency dependent penetration property of the electric current in metallic conductors and is computed as:

$$\delta_{coil} = \sqrt{\frac{2}{\mu_0 \cdot \mu_R \cdot \omega \cdot \kappa_{coil}}} \qquad \text{(Equation 2.10)}.$$

where $\mu_0$ is the permeability constant in vacuum, $\mu_R$ is the permeability constant of the material, and $\omega$ corresponds to the angular frequency.

Magnetic losses occur during the transmit phase and the application of a high current (typically in the range of 1 A) to the coil, which is driven by the high power amplifier. The transmitted $B_1$-field generated by the resonance coil induces eddy currents in the conductive sample. These eddy currents contribute to additive local magnetic fields within the sample with considerable influences on the total local magnetic field and thus the local flip angle. For a spherical sample of radius $b$, the calculation leads to

$$R_M = M_G \cdot \sigma \cdot N^2 \cdot \omega^2 \cdot b^5 \qquad \text{(Equation 2.11)},$$

where $M_G$ is a coil geometry-related factor, $N$ is the number of turns, and $\sigma$ is the electric conductivity of the media used in the sphere.

An unbalanced coil starts to radiate some of the electromagnetic energy stored in the resonator to its environment. Such radiation losses occur due to the development of two resonance modes, one corresponding to the loop resonance and the other corresponding to an antenna of small dimensions. This effect is also known as the antenna effect. It becomes more evident for resonators with conductor lengths > λ/10, where λ is the RF wavelength in the conductor material. Thus splitting the conductor into multiple segments, as well as symmetrically arranging the circuit capacitors, can suppress the radiation losses [49].

Electric losses occur due to the close proximity of the resonance structure to the conductive sample environment. The electric field build up in capacitors penetrates in to the surrounding space and the conductive sample. Those electric fields drive currents through the sample and thus contribute to the electric loss mechanisms with:

$$R_E = \quad E_G \cdot \omega^3 \cdot L^2 \cdot C_d \qquad \text{(Equation 2.12)},$$

where $E_G$ is the geometry factor of the coil, and the coil is characterised by an inductive value $L$ and a capacitive value $C_d$. Considering that the radiation and magnetic losses are very small during the receive period, the optimisation of receiver surface coils must focus on the minimisation of the resistive and electric losses, which is discussed in more detail below.

The resistive losses could potentially be reduced by the use of highly conducting materials such as silver or carbon nanowires [51]. However, the magnetic susceptibility of silver is very different from tissue and can cause MR signal distortions when brought near the sample. On the other hand, the highly conducting carbon nanowires could provide the ideal resonator material. Admittedly, the properties and macroscopic access to this novel material are still restricted. For this reason copper was preferred over silver or nanowires to develop MRI resonators for this project.

Varying the coil geometry and number of windings also has some potential with regards to increasing the detectable SNR. The measurable SNR benefit from the use of multiple inductor windings highly depends on the frequency and the dimensions-related loss mechanisms. As an example, one may express the increase in SNR obtained by doubling the number of windings as:

$$\frac{emf(2N)}{\sigma(2N)} = \quad c(2N)\frac{emf(N)}{\sigma(N)} \qquad \text{(Equation 2.13)}.$$

where $N$ is the original number of windings, and $c$ is the factor by which the SNR is increased. The induced *emf* doubles according to Faraday's Law:

$$emf(2N) = 2 \cdot emf(N) \qquad \text{(Equation 2.14).}$$

The measured noise voltage level at the coil terminals is related to the effective resistance (Equation 2.8) as follows:

$$\sigma_n \propto \sqrt{R_{eff}} \qquad \text{(Equation 2.15).}$$

Since, the electric losses are proportionally to $L^2$ (Equation 2.12), they increase by a factor of four, because $L$ was doubled by the doubled number of windings $N$. However, the resistive losses are only directly proportional to $N$, resulting in an effective noise signal increase of:

$$R_{eff}(2N) = 2^2 \cdot R_E + 2 \cdot R_\Omega \qquad \text{(Equation 2.16).}$$

Considering that the electric losses are negligible for small detector dimensions and low resonance frequencies, it becomes evident that the effective noise levels for a doubled number of windings increases by approximately 40 %:

$$\sigma(2N) = \sqrt{2} \cdot \sigma(N) \qquad \text{(Equation 2.17).}$$

Thus as long as the resistive losses dominate the electric losses and the conductor length is smaller than $\lambda/10$, doubling the number of windings can result in a SNR increasing factor:

$$c(2N) = \frac{2 \cdot emf(N)}{emf(N)} \cdot \frac{\sigma(N)}{\sqrt{2} \cdot \sigma(N)} = \sqrt{2} \qquad \text{(Equation 2.18).}$$

In the case of larger coil geometries (e.g. for human MRI), dielectric losses dominate the effective resistance and therefore multi-winding results in no effective SNR gain.

However, for small surface coils and low resonance frequencies, multi-winding must be considered to achieve the highest possible SNR. The fact of dominating resistive losses could furthermore be exploited through cooling the resonator coil and by these means limiting the temperature-dependent losses [52]. The fact that multiple winding coils for rat brain MRI at 79 MHz results in higher SNR was practically tested in this work (Chapter 3), exploited for the development of a transceiver surface coil (Chapter 4) and also used to develop a receive-only surface coil (Chapter 6).

## 2.4 Resonator Development Tools and Test Methods

Designing and developing RF resonators is a challenging task and requires the careful use of expensive equipment such as a network analyser to exactly tune and match the MRI resonator. The development of such high performance resonators is based upon the 4-port

network theory, where the developed *LC* resonator is treated as a black box with four connectors, which then is assessed by its ability to reflect and absorb electro-magnetic waves. The actual resonance frequency, the resonator's quality-factor, and resonator coupling effects can thus be accurately characterised. The scattering parameter theory, the laboratory equipment used to characterise resonators, and the essential measurement methods for designing MRI resonators are described in this section.

### 2.4.1 The Scattering Parameters (s-Parameters)

Any electronic unit can be described by its frequency-dependent complex *s*-parameter set $s_{ab}$, when contemplating that the electronic unit is a black box with four connectors - an electric 4-port network (see Table 2.1). The *s*-parameter matrix is designed in a way that it relates the incident (-) and reflected (+) wave amplitudes at each port of the network. For the 4-port network shown in Figure 2.3, the *s*-parameters are defined as follows:

$$\begin{bmatrix} V_1^- \\ V_2^- \end{bmatrix} = \begin{bmatrix} s_{11} & s_{12} \\ s_{21} & s_{22} \end{bmatrix} \cdot \begin{bmatrix} V_1^+ \\ V_2^+ \end{bmatrix} \qquad \text{(Equation 2.19),}$$

where $V_1$ and $V_2$ are the voltage amplitudes measured in port 1 and 2, respectively. The reflected or output wave at each port is a function of the input waves at all ports:

$$s_{ab} = \left. \frac{V_a^-}{V_b^+} \right|_{V_a^+=0} \qquad \text{(Equation 2.20).}$$

Out of the four *s*-parameters, the input reflection coefficient $s_{11}$ and the transmission coefficient $s_{21}$ are the most useful *s*-parameters for determining the resonance frequency and the matching properties of the *LC* resonator.

### 2.4.2 The Network Analyser

A network analyser is composed of a multi-frequency power signal generator, generating sinusoidal signals with temporally increasing frequency, an oscilloscope for measuring the reflected and transmitted voltage levels of an investigated circuit, and a processor for coordinating the interaction of both the generator and the oscilloscope.

**Table 2.1: The terminology used to characterise 4-port networks by four s-parameters.**

| *scattering parameter* | *Notation* |
|---|---|
| **$s_{11}$** | **input reflection** |
| **$s_{12}$** | **reverse transmission** |
| **$s_{21}$** | **Transmission** |
| **$s_{22}$** | **output reflection** |

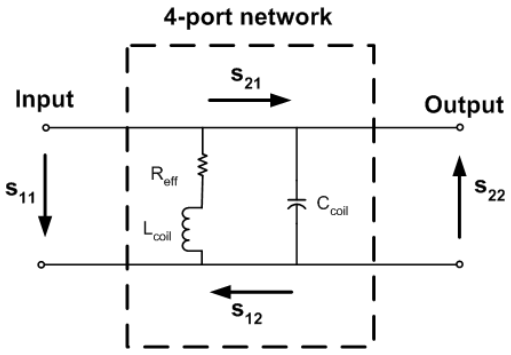


**Figure 2.3: The graphical interpretation of the scattering parameters in a 4-port network. The 4-port network circuit represents the equivalent parallel LC resonance circuit, which was used for this work.**

Test objects with one or two ports can be connected to the network analyser. The scattering parameters can then be measured based upon the electric 4-port network theory. To measure the reflection and transmission, hybrids or diplexers are integrated into the test ports of the network analyser to separately detect the emitted and reflected waves. The attenuation between voltages is calculated using the formula derived from the decibel scale of power attenuation [50]:

$$A(s_{ab}) = \quad -20 \cdot \log_{10}\left(\frac{V_a^-}{V_b^+}\right) \quad [db] \qquad \text{(Equation 2.21).}$$

A network analyser can be used to measure the resonance frequency of an MR detector coil. Other coil characterising parameters, among them the Quality-factor (Q-factor), coil impedance, and transmission attenuation can also be measured. The network analyser used for this study was model E5061A (Agilent Technologies, USA). The following subsections describe how to measure the $s_{11}$-reflection curve and Q-factor, and the $s_{21}$-transmission curve of a resonance coil.

### 2.4.3 Pick-up Loops

Pick-up loops are used to test resonance circuits without physically connecting the resonator to a coaxial cable, which would require capacitive impedance matching. They allow for a quick measurement of the resonance frequency for the chosen inductor loop and its capacitance in conjunction with a network analyser. Different size pick-up coils are needed for the analysis of resonance circuits of varying sizes, such as volume resonators (70 mm inner diameter (i.d.)), surface coils (25 mm i.d.) or trap circuit inductors (5 mm i.d.) in the case of *in vivo* MRI. The pick-up coil holder consists of a coaxial cable (RG316), a BNC plug (for connecting to the network analyser), a quick-release connector (SMB, Huber and Suhner, Switzerland), and a plastic rod to which the cable was fixed

(Figure 2.4). Pick-up coils were soldered to a corresponding SMB jack. The connections were insulated using heat shrink. Such an arrangement allows the coil designer to change pick-up coils easily without having too many wires on the work bench.

### 2.4.4 The Reflection Measurement

The reflection measurement is one of the most basic network analyser measurements, which allows for the determination of the resonance frequency and matching properties among other parameters of a *LC* resonator. In order to measure the $s_{11}$-reflection attenuation, the *LC* resonator is connected to port 1 of the network analyser. By defining the centre frequency and the frequency span, the attenuation curve can be recorded as shown in Figure 2.5 for a 79.4 MHz surface coil; the centre frequency and span were chosen 79.4 MHz and 20 MHz, respectively. At the resonance frequency nearly all of the electromagnetic wave was absorbed by the resonator, which resulted in less than -30 dB $s_{11}$-reflection attenuation at 79.4 MHz, representing very good signal absorption. Almost no signal was absorbed at other frequencies, as indicated by the complete reflection of the incident wave at these frequencies (> -1.5 dB). This measurement allowed for the accurate determination of the resonance frequency of any *LC* resonator under real world influences such as resistive losses and loading effects (electric losses).

### 2.4.5 The Transmission Measurements

For an $s_{21}$-transmission measurement two network analyser ports are used simultaneously. The input channel 2 is used for measuring the transmitted wave parameters of the electromagnetic wave, which is transmitted from output channel 1 through the 4-port test network.

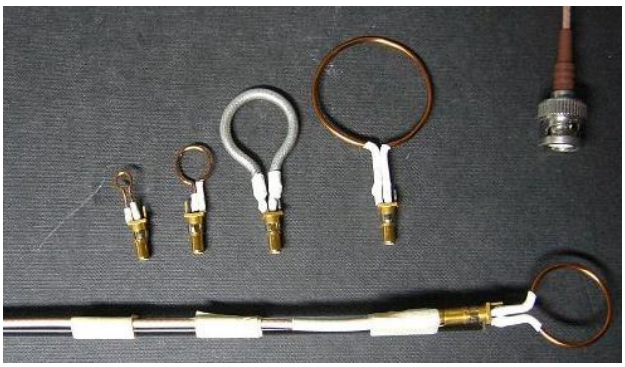

**Figure 2.4: Different size pick-up coils, and pick-up coil holder.**

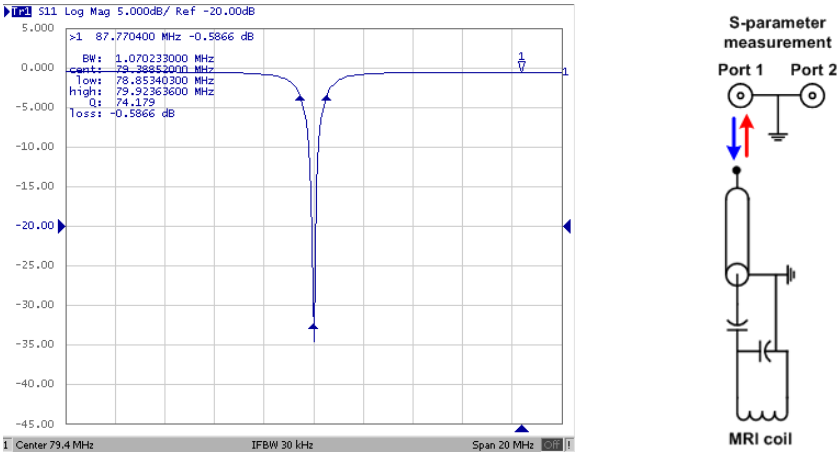


**Figure 2.5: The $s_{11}$-reflection measurement using the network analyser port 1 to emit electromagnetic waves of a certain frequency range (span) and measure the reflected waves in the same port 1.**

A pick-up coil is generally connected to channel 1 to detect the incident and transmitted wave, while the coil under test is connected to channel 2 (see Figure 2.6). In cases with multiple element coils, where the transmission isolation between coil elements must be tested, the pick-up coil can be substituted by the second resonance coil. A typical $s_{21}$-transmission attenuation curve for a well-designed parallel LC resonance circuit results in optimum transmission (> -15 dB) at the resonance frequency and little wave transmission (< -30 dB) at other frequencies. This measurement is useful for measuring the SNR-related coil performance, as described in Chapter 3 ('Empirical Evaluation of Shaped Surface Coil Sensitivities at 79.4 MHz') and also to test the coil insulation in multiple resonator compositions and multiple-frequency-tuned resonators.

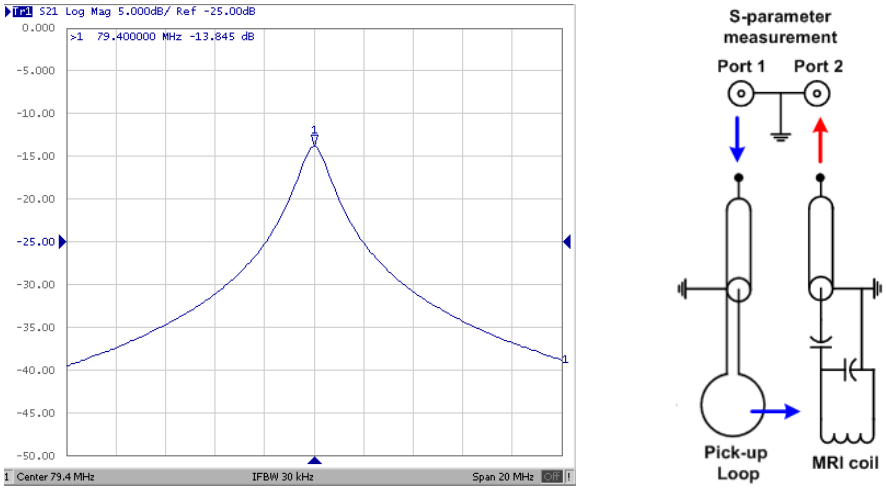


**Figure 2.6: The $s_{21}$-transmission measurement using the network analyser port 1 to emit electromagnetic waves of a certain frequency range (span) and measure the transmitted waves in port 2.**

### 2.4.6 The Q-Factor Measurement

For a preliminary evaluation of the performance of a resonance coil, one usually measures the coil's quality factor (Q-factor). The inductor-related Q-factor is defined as the ratio of the stored magnetic energy in the inductor to the energy lost per unit cycle, and may be expressed by:

$$Q_L = \frac{L\omega}{R_\Omega} \qquad \text{(Equation 2.22).}$$

where $R_\Omega$ represents the resistive losses due to the skin effect and conductor length. The capacitor-related Q-factor is defined as the ratio of stored electric energy in the capacitor C to the energy lost per unit cycle:

$$Q_C = \frac{1}{\omega C \cdot R_E} \qquad \text{(Equation 2.23).}$$

where $R_E$ represents the electric losses in the capacitive resonator components. The total Q-factor of the resistive *LC* circuit is then defined as:

$$Q = \sqrt{\frac{L}{C}} \cdot \frac{1}{R_{eff}} \qquad \text{(Equation 2.24).}$$

The Q-factor can be measured and computed in various ways, of which the two main approaches are explained in the next paragraph.

The $s_{11}$-reflection based approach can serve to compute the Q-factor from the measured peak width and resonance frequency. Loss mechanisms lead to a peak widening and a decrease in Q-factor. From the frequency difference between the -3dB attenuation values relative to zero attenuation and the centre frequency, the Q-factor can be computed as follows:

$$Q = 2 \cdot \frac{\omega_0}{\Delta\omega_{-3dB}(s_{11})} \qquad \text{(Equation 2.25).}$$

In this case, the matched resonator is damped by the characteristic load impedance $Z_0$ to which the circuit is connected. Hence, only half of the energy is dissipated in the matched impedance of the resonator and the other half in the source load. Therefore, the measured Q-factor must be corrected by a factor of two for the reflection-based Q-factor measurement approach.

The second option is based upon a transmission measurement with two loosely coupling probes. The Q-factor is computed from the -3 dB peak width and the centre frequency:

$$Q = \frac{\omega_0}{\Delta\omega_{-3dB}(s_{21})} \qquad \text{(Equation 2.26).}$$

This method is more difficult to set up, because the two pick-up coils must be well isolated from each other, so that each of them only interacts with the resonance circuit and they effectively do not 'see' each other. The maximum $s_{21}$-transmission attenuation should be measured below -20 dB, the maximum-to-minimum $s_{21}$-attenuation difference should be larger than 20 dB across the set-up frequency span, and cable wave-related losses need to be suppressed by cable traps. Cable waves occur on the coaxial cable shield in unbalanced resonator designs, when the ground conductor is connected to a non-ground part of the resonator, which in turn leads to propagating cable waves over the RF shield of the coaxial cable.

## 2.5 Resonance Circuit Design

The design of MRI resonators is non-trivial, because many components contribute to the performance of the resonance coil. The main problem is that the complex impedances of inductors and capacitors are frequency-dependent. Hence, the accurate component choice can become difficult when dealing with a small number of circuit components. The basic design principles used later in this thesis for the development of surface and volume resonators are described in this chapter pertaining to the example of surface coils.

### 2.5.1 Tuning

An MRI surface detector coil is composed of a loop of wire connected to a parallel capacitor $C$ forming an $LC$ resonance circuit. The circuit's resonance frequency is set to match the Larmor frequency and can be calculated according to (Equation 2.6). Tuning to the Larmor frequency is achieved by varying either $L$ or $C$. Since the inductor value is fixed by the geometric loop size, the capacitor's value is generally used to tune to the target resonance frequency. A similar size pick-up loop connected to the network analyser and matching the surface coil geometry may be used to inductively couple into the coil to determine the resonance frequency from the recorded reflection attenuation values. The target frequency $f_2$ is then iteratively approached by measuring the resonance frequency $f_1$ achieved using the soldered-in capacitance $C_1$ and computing the necessary capacitance $C_2$ as follows:

$$C_2 = \frac{f_1^2}{f_2^2} \cdot C_1 \qquad \text{(Equation 2.27).}$$

The final frequency should be approximately 1 % above the target frequency to allow for the parallel insertion of a variable tuning capacitor and to guarantee a reasonable dynamic

tuning range, when presenting various sample loads to the coil. The tune capacitance should be designed to be partly variable by adding in a parallel trimmer capacitor, $C_{tune,var}$, which modifies the total tune capacitance according to (see Figure 2.7):

$$C_{tune,tot} = \quad C_{tune} + C_{tune,\mathrm{var}} \qquad \text{(Equation 2.28).}$$

### 2.5.2 Matching

Measuring the induced MR signal as a voltage at the detector terminals requires a matching network to transform the coil impedance to the required cable impedance. A common matching network chosen for MRI detector coils is the series impedance transformation network, which is described in more detail in this section.

The cable connecting the resonator to the preamplifier of the MRI system must have 50 Ω impedance to reduce power losses through electromagnetic wave reflection that occur in conductors longer than $\lambda/10$ (equal to 9.5 cm @300 MHz in copper wire). The simplest approach is to match the resonator impedance via a single reactive element in series with the RF cable (Figure 2.8). The matching capacitor also needs to be designed variable in order to compensate for variations in the tuning capacitance value in different experiments with different sample loads. From the tuned resonance circuit component values, one can mathematically compute the required matching capacitance value. Assuming the total capacitance $C_t$ and the resonance frequency are known, the resonator's inductance can be computed via the resonance equation given earlier (Equation 2.6).

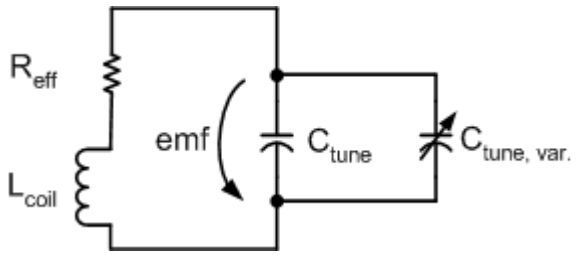


**Figure 2.7: Parallel LC circuit with variable tuning capacitor. The induced *emf* drop-off can be measured across the capacitors.**

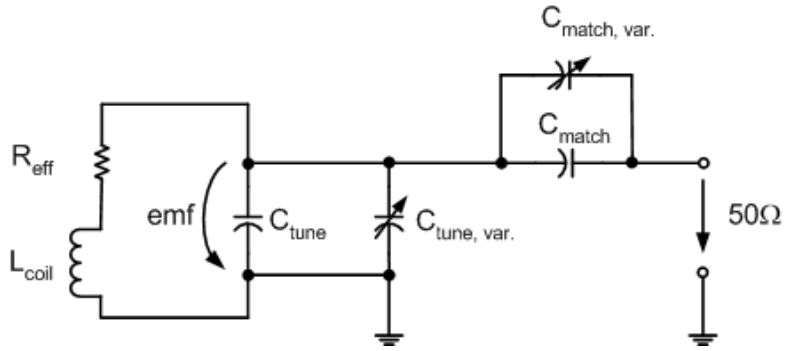


**Figure 2.8: Impedance transformation at the coil terminals using a series matching capacitor adjustable by a variable trimmer capacitor to match the output impedance to 50 Ω.**

In the next step, the effective loss resistance is determined from the Q-factor measurement (Equation 2.4), and thus the impedance without the RF cable connected to the coil can be written as:

$$Z = \frac{1}{\frac{1}{Z_L + R_{eff}} + \frac{1}{Z_{C_t}}} + Z_{C_m} \qquad \text{(Equation 2.29).}$$

The inductive and capacitive impedances can be substituted using Equation 2.4, and 2.5, which leads to an impedance equation illustrating the rising complexity for resonator designs, even with only three reactive elements:

$$Z = \frac{R_{eff}}{\omega^2 C_t^2 \left( R_{eff}^2 + \left( \omega L - \frac{1}{\omega C_t} \right)^2 \right)} - j \frac{1}{\omega C_t} \left( \frac{\omega^2 L^2 - \frac{L}{C_t} + R^2}{R^2 + \left( \omega L - \frac{1}{\omega C_t} \right)^2} + \frac{C_t}{C_m} \right) \qquad \text{(Equation 2.30).}$$

In order to match the coil impedance to the 50 Ω coaxial cable impedance, the real part of the coil impedance must equal $R_i$ = 50 Ω and the imaginary part of Z must equal to zero:

$$\mathrm{Re}\{Z\} = R_i \qquad \text{(Equation 2.31),}$$

and

$$\mathrm{Im}\{Z\} = 0 \qquad \text{(Equation 2.32).}$$

Following Equation 2.31, one can express the real impedance as:

$$R_i = \frac{R_{eff}}{\omega^2 C_t^2 \left( R_{eff}^2 + \left( \omega L - \frac{1}{\omega C_t} \right)^2 \right)} \qquad \text{(Equation 2.33).}$$

which can be converted into a quadratic equation to solve for the tune capacitor value:

$$C_{t_{1/2}} = \frac{L}{R_{eff}^2 + \omega^2 L^2} \pm \frac{L}{R_{eff}^2 + \omega^2 L^2} \sqrt{L^2 - \frac{\left(R_i - R_{eff}\right) \cdot \left(R_{eff}^2 + \omega^2 L^2\right)}{\omega^2 R_i}} \qquad \text{(Equation 2.34).}$$

To satisfy Equation 2.32, the factors in parenthesis relating to the imaginary component of Equation 2.30 must sum to zero, and hence we can write for the matching capacitance:

$$C_m = -C_t \frac{{R_{eff}}^2 + \left(\omega L - \frac{1}{\omega C_t}\right)^2}{\omega^2 L^2 - \frac{L}{C_t} + R_{eff}^2} \qquad \text{(Equation 2.35).}$$

The value of $C_t$ and the nominator in Equation 2.35 are positive, and hence the divisor must be negative, to result in a positive matching capacitance. This is expressed by the following boundary condition:

$$C_t < \frac{L}{\omega^2 L^2 + {R_{eff}}^2} \qquad \text{(Equation 2.36).}$$

Equations 2.35 and 2.36 can then serve to mathematically determine the necessary capacitance values for known coil inductance, resistance, and target resonance frequency. If the boundary condition of Equation 2.36 turns out false for the chosen resonator design, capacitive impedance transformation is impossible and other means of matching must be implemented (e.g. inductive matching).

### 2.5.3 Symmetric Resonator Design

The connection of the ground conductor to the resonator circuit is crucially important for a well performing resonator and also for the suppression of radiation losses. The ground conductor should ideally be connected to a point with zero voltage, which subsequently serves as a constant reference point for the induced *emf*. In the resonator structures discussed previously, only one such zero voltage point existed, located at half the inductor length. By splitting the tuning capacitor into two capacitors, additional joints can be created (Figure 2.9). The ground connector can thus be connected to a position near the circuit board rather than to the more distant and less accessible site of the resonator. The substituted series capacitor values may be determined by the following equation:

$$\frac{1}{C_{t1}} + \frac{1}{C_{t2}} = \frac{1}{C_t} \qquad \text{(Equation 2.37).}$$

Assuming that both series capacitors are of equal value, the latter equation simplifies to:

$$C_{t1/t2} = 2C_t \qquad \text{(Equation 2.38).}$$

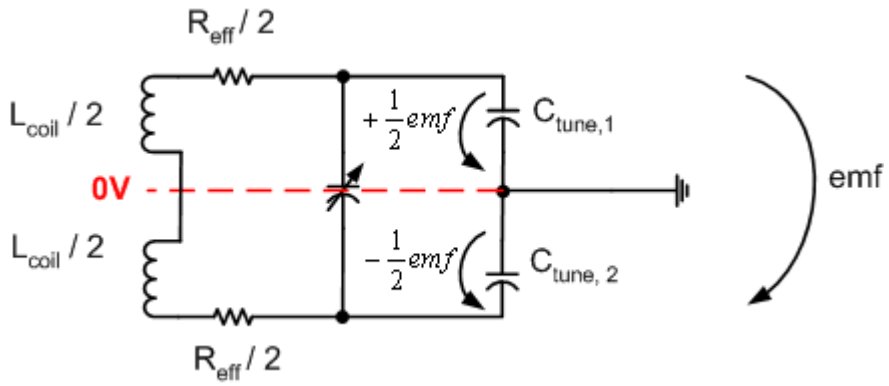


**Figure 2.9: The symmetry line (dashed, red) marks the zero voltage level on the RF circuit after an *emf* is induced in the detector coil. Splitting the capacitors creates an additional symmetric access point for the ground connector between them and thus ensures balanced coil design.**

Consequently, twice the capacitance value is needed for two series capacitors in order to maintain the same resonance frequency that was achieved with just one capacitor. Practical retuning may be necessary, because the inductor length decreases with an additionally introduced capacitor gap in the resonator.

### 2.5.4 Trap Circuits

Trap circuits are parallel resonators, which are used as building blocks in resonance circuit design to achieve multiple resonance frequency properties. For the case of a trap circuit introduced into a parallel resonator, the trap circuit causes a peak split and thus a double resonance effect; the resulting structure will then resonate at both a Low Frequency (LF) and a High Frequency (HF) with the single resonance frequency being in between the LF and the HF. This peak split effect can be exploited to either block one frequency between both the LF and HF, or to use the two peaks to detect the NMR signal in multi-nuclei MRI at different LF and HF Larmor frequencies (e.g. the $^{23}$Na 79.4 MHz and $^{1}$H 300.3 MHz frequencies at 7 T).

#### 2.5.4.1 Double-Tuning

The trap circuit capacitance serves as a capacitive reactance influencing the HF, whereas high impedance is presented to the LF. Similarly, the trap circuit inductor exhibits high impedance to the HF, but behaves inductively at the LF (Figure 2.10).

Computational methods for determining the component (i.e. capacitance) values were given by Shen *et al*. [53]. Nevertheless, it proved more practical to work out the circuit component values empirically using the coil structure in single resonance mode.

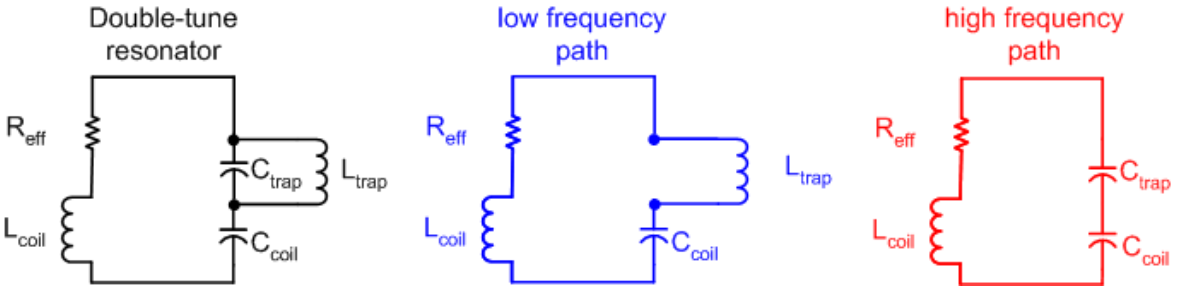


**Figure 2.10: Double tuned parallel resonance circuit design via a series trap circuit. The low and high frequency current paths are sketched separately in blue and red.**

For a given resonator inductance $L_c$, the coil capacitance $C_c$, the trap circuit capacitance $C_t$, and the trap circuit inductance $L_t$ were determined using the following procedure:

1. An arbitrary inductor was wound to form $L_t$ ensuring it was far smaller than the coil inductor $L_c$. Two windings of a 1 mm copper wire (a 5 mm drill bit) were suitable for small surface coil detectors (i.d. < 40 mm).
2. The low target frequency was tuned by varying $C_c$, according to the procedure explained in Section 2.5.1 ('Tuning').
3. The high target frequency was tuned by varying $C_t$, according to the procedure explained in Section 2.5.1 ('Tuning').
4. The trap circuit inductance $L_t$ was varied by physically deforming the windings of the inductor (stretching or compressing), so that the trap circuit parameters could be varied to achieve more practical trap circuit capacitance values.

Ideally the trap circuit inductance should exhibit high impedance at the HF and therefore remains 'invisible' to the higher resonance:

$$Z_{L_t}(@\,HF) \quad > 800\Omega \qquad \text{(Equation 2.39).}$$

In the same way, the trap circuit capacitance should exhibit high impedance at the LF to remain 'invisible' to the lower resonance frequency:

$$Z_{C_t}(@\,LF) \quad > 800\Omega \qquad \text{(Equation 2.40).}$$

The latter requirement is achieved in practice by using trap capacitor values with far smaller values than the value of the LF tuning capacitor.

### 2.5.4.2 Frequency Blocking

In cases where it is desirable that the resonator cannot resonate at a specific frequency, the trap circuit can be used as a frequency blocking element. When tuned to the same frequency as the resonator frequency, the trap-to-resonator circuit interaction results in a

peak split and subsequently high impedance at the resonance frequency arises. This principle can be used to block cable currents being fed into the ground conductor for asymmetrical resonator designs, to block the induction of an unwanted frequency in a resonance structure, and to actively decouple a resonator during inactive sequence periods. The active decoupling was achieved by inserting a DC voltage-controlled PIN diode switch into the trap circuit inductor path. By forward-biasing the PIN diode, the trap circuit is activated, which causes a double resonance peak split at frequencies below and above the blocked-off centre frequency (Figure 2.11). In this way, the RF coil could be switched either on- or off-resonance. The challenge imposed on the design of such a circuit was the DC circuit, which needed to be incorporated into the RF circuitry. It was essential to isolate the DC potential from the RF terminals through the use of high value blocking capacitors (1 nF). To avoid RF signal drain through the DC terminals, non-magnetic RF chokes (> 2 μH) were also employed.

### 2.5.5 Inductance Calculations

The coil dimensions were mostly determined by the field of view to be imaged. Hence to tune the coil to the target resonance frequency, the empirical capacitance value determination procedure was chosen from which in turn the approximate coil inductance was computed. However for double-tuning and active decoupling applications, trap circuit inductors with well defined inductance had to be wound. The inductance for given geometrical parameters was computed from the straight wire and single layered inductance approximations explained below.

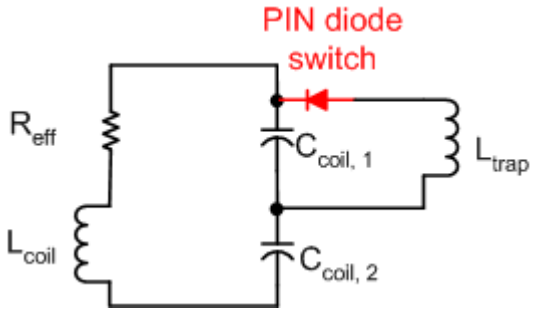


**Figure 2.11: Frequency blocking via an actively switched PIN diode using an external DC voltage supply (not shown). The resonance frequency of the trap circuit must coincide with the coil resonance frequency to achieve sufficient suppression of the unwanted resonance property.**

#### 2.5.5.1 Straight Wire

The inductance of a straight wire is simply computed by [49]:

$$L[nH] = \quad 0.2 \cdot l \cdot \left[ \ln\left( \frac{4 \cdot l}{\phi} \right) - 0.75 \right] \qquad \text{(Equation 2.41),}$$

where ϕ is the diameter and $l$ is the wire length in mm. For instance, two 5 mm long straight wire leads as part of a solenoid coil correspond to an inductance of 6 nH.

#### 2.5.5.2 Single Layered Solenoid

The computation of the inductance for a single layered solenoid is not trivial at higher frequencies, due to the skin effect which limits the current flow inside the conductor, and also due to the proximity effect between two loop windings, which restricts the current flow further in a sophisticated and difficult-to-predict way. An exact solution of the inductance via the elliptical integrals *K(k)* and *E(k)* can be achieved numerically and is described elsewhere [49]. Such exact inductance calculations were not needed for this work, but rather a rough guidance of how much inductance could be achieved with certain geometric inductor parameters (i.e. diameter, wire width, and pitch) to for instance wind trap circuit inductors for double-tuned coils or active decoupling circuits.

An inductor with length $l$ larger than 0.4 times the diameter $d$ in mm and with an air core can be approximated using the following equation [54]:

$$L = \quad 4 \cdot \pi \cdot 10^{-7} \frac{H}{m} \cdot \frac{d^2 N^2}{(18 \cdot d + 40 \cdot l) \cdot 25.4} \qquad \text{(Equation 2.42),}$$

From this approximation the required number of windings can be estimated for a desired inductance:

$$N = \quad \sqrt{\frac{L}{\left( 4 \cdot \pi \cdot 10^{-7} \frac{H}{m} \right)} \cdot \frac{(18 \cdot d + 40 \cdot l) \cdot 25.4}{d^2}} \qquad \text{(Equation 2.43),}$$

For an inductor dimension of 3.0 mm length, and 7.6 mm diameter, the number of necessary windings to achieve a 29 nH inductance was computed to be 1.6.

For a more accurate inductance calculation, an online inductance calculator (http://hamwaves.com/antennas/inductance.html) can be used, which incorporates the wire thickness, and frequency-dependent skin depth and the proximity effect.

### 2.5.6 Geometric Decoupling

The decoupling of two separate LC circuits tuned to identical frequencies is important to achieve high performance of both resonators. Because high $B_1$-homogeneity is desired over the sample field of view, rather large resonators are preferred for RF transmission. On the other hand, to maximise the SNR, the receiver coil geometry must be chosen to be small and its location must be very close to the NMR signal origin. Thus, the geometric decoupling of the two separate coils, which form a dual resonator system, is essential for methods such as qNa-MRI or when using multiple receive-only coils (phased arrays). The oscillating resonator generates a magnetic field, which according to Faraday's Law would induce an *emf* in a neighbouring coil. Such 'cross-talk' must be prevented if one is to acquire solely NMR-related signals in a dual resonator set-up. It is possible to geometrically decouple two resonators from each other, such that the temporal magnetic flux changes generated by one coil through the surface area of the second coil are zero. There are two options to achieve this using two surface coils, either by arranging the two coils with a 10 % overlap ([55], Figure 2.12(a)) or arranging them orthogonally to each other with arbitrary positioning options of the one coil along the central axis of the second coil (Figure 2.12(b)). There exist other non-geometrical methods to decouple two resonance coils, such as active decoupling, preamplifier decoupling, and filtering. However, from experience such techniques are not as effective when used alone, but rather serve as a complimentary option to geometrical decoupling using either of the methods described above.

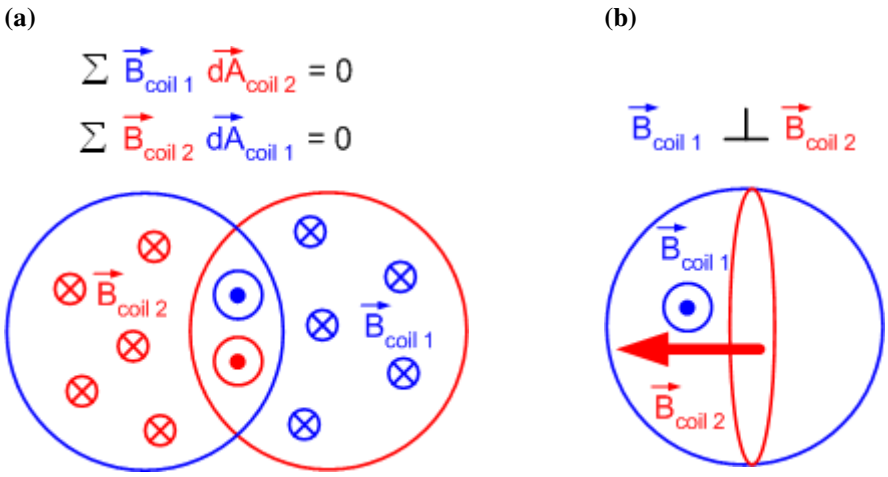


**Figure 2.12: Geometric decoupling of two resonance loops (blue and red) by (a) 10 % geometric overlap and (b) orthogonal coil arrangement. The magnetic flux generated by each coil threading through the surface area of the other cancel each other out, which therefore ensures complete independence of both coils with no current being induced by the coil current flow in adjacent coils.**

## 2.6 MRI Resonator Characterisation

The characterisation of the resonators developed during the course of this work was an important procedure to ensure they were working optimally from the point of view of SNR and $B_1$—homogeneity, prior to using them for *in vivo* MRI studies. The resonators were first characterised on the bench, before being tested on physiological tissue-replicating phantoms in the MRI scanner. These two characterisation methods are described in the next two sections.

### 2.6.1 On-Bench Characterisation

The evaluation of MRI resonators starts at the work bench by conducting simple network analyser measurements. The Q-factor should be measured continuously after tuning, splitting the capacitors, introducing trimmer capacitors, and introducing the matching circuitry in order to detect possible circuit-related errors (e.g. cold solder joints) which manifest as a diminished Q-factor. The measurement of the loaded and unloaded Q-factors also serves as a test of the electric losses and can also serve to verify that a sufficient dynamic matching and tuning range was chosen. The load should mimic physiological tissue, and as such can comprise of a hand, forearm, thigh, or a jar with physiological NaCl solution.

#### 2.6.1.1 The Unloaded and Loaded Q-factor Measurement

When a conductive sample is brought near the resonance coil, parasitic capacitances occur near the detector element (Figure 2.13). These parasitic capacitors possess low Q-factors and create a parasitic current path through the sample.

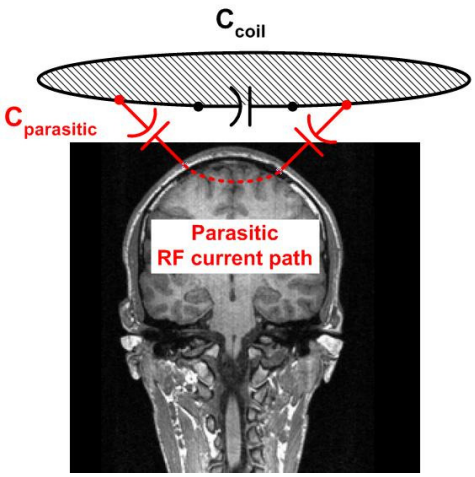


**Figure 2.13: The parasitic current path through the conductive sample (e.g. human head) resulting in dielectric losses and lowered Q-factor.**

Since, the parasitic capacitances are situated in parallel with respect to the coil capacitor, they add to the tuning capacitance in a way that the intrinsic LC resonance frequency decreases [49], which can be easily observed in a $s_{11}$-reflection measurement using the network analyser. The resulting electric losses depend on the parasitic resistance (earlier referred to as the electric loss resistance $R_E$) at the investigated frequency and can be evaluated by comparing the Q-factors obtained for different loads. For large resonators, for example those developed for human imaging, the unloaded to loaded Q-factor ratio is believed to characterise the real resonator quality, providing a useful qualitative indicator of performance [49]. This technique is valid since, for large coil geometries, the electric losses generally dominate the resistive losses for well-designed coils. However, for small resonators developed for rodent imaging which generally have low electric losses, this approximation proves to be inappropriate, especially at the low $^{23}$Na resonance frequency of 79.4 MHz used in the current work. As a result, a sensitivity profile based approach to characterise receiver surface coils was developed in Chapter 3.

### 2.6.1.2 The $B_1$-Homogeneity Measurement

The $B_1$-Homogeneity characterisation of the volume resonator developed in this work was an important consideration, given the importance of achieving a uniform flip angle excitation across the sample in order to achieve high quantification accuracy of the TSC measurement. The $B_1$-homogeneity measurement method described in the following paragraph was developed by Dieter Depner under supervision of Martin Tabbert in Bruker BioSpin GmbH, Ettlingen, Germany (Figure 2.14).

To determine the relative $B_1$-field strength generated within the sample region inside the volume resonator, its RF input was supplied with the RF sweep signal emitted

from the network analyser output port 1. A small (12 mm diameter) tuned sensor loop (bandwidth 20 to 30 MHz) was used to measure the magnetic field strength-related *emf* induced in the pick-up loop at all spatial locations inside the volume resonator. The RF voltage signal was directly rectified on the sensor by a pair of Schottky diodes and a low-pass filter. Thus signal losses and distortions due to sensor-resonator-interactions could be prevented. The sensor was automatically positioned via a PC-controlled three dimensional stage. The filtered signal was fed into the DC input at the rear of the network analyser, from where it was digitised before the $B_1$-field strength-related DC potential magnitude was transferred to the PC for data acquisition and analysis.

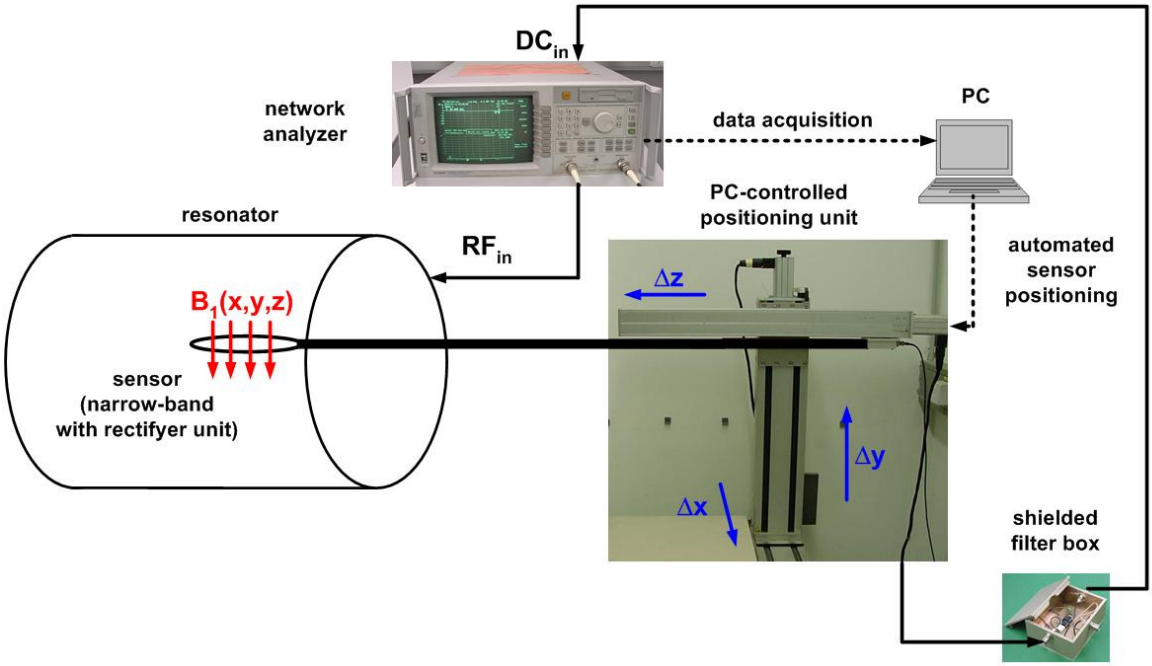


**Figure 2.14: Set-up used in Bruker BioSpin GmbH, Ettlingen, Germany for $B_1$-homogeneity measurements.**

### 2.6.2 On-Site Characterisation Using MRI

All MRI scanning was performed on Bruker 70/30 BioSpec systems (7 T, 30 cm bore diameter) equipped with either AV1 (at University of Glasgow) or AV3 (at Bruker BioSpin GmbH, Ettlingen) electronics. Together with the medium size gradient inset (BGA-12, 400 mT/m), an inner diameter of 120 mm remained for the sample and the resonator positioning.

#### 2.6.2.1 The Fast Low Angle Shot Sequence (FLASH)

The FLASH sequence is a Gradient Echo Sequence (see Section 1.1.1) which was used to compare coil systems using high $^{23}$Na concentration solutions (hence no short $T_2$ components were present). This sequence allows for the use of short Repetition Times (TR) due to the establishment of a steady state condition at the flip angle, which is generally smaller than 90°. The flip angle, also referred to as the Ernst angle, which maximises the measured signal is given by the following equation:

$$\alpha = \cos^{-1}\left( e^{-\frac{TR}{T_1}} \right) \qquad \text{(Equation 2.44).}$$

This equation is valid as long as $T_1 > TR$. Because TXRX surface coils possess a coil profile dependent flip angle distribution, it was chosen to adjust the 90° flip angle to approximately 12 mm sample depth. For receive-only surface coils, on the other hand, the flip angle distribution is considerably more homogeneous due to the use of a volume resonator for RF transmission. To prevent flip angle-related signal improvements for small TRs, a long TR of 200 ms was used. In this way, a fair comparison of the receive performance of transceiver and receive-only surface coils could be achieved.

The following sequence parameters produced sufficient SNR to allow for coil comparisons: 10 min Acquisition Time (TA), with 5 ms TE, Gaussian RF pulse of 600 µs pulse length, matrix size (MTX 80 x 80), Field of View (FoV 80 x 80 mm$^2$), low bandwidth (5 kHz), and 20 % partial echo positioning.

#### 2.6.2.2 Adjustments

Several system parameters must be adjusted before beginning any MRI scanning experiment, including the centre of the spectrometer frequency, the $B_0$-shimming, and the determination of the optimal RF pulse power. These adjustments differ depending on whether transceiver volume coils or transceiver surface coils are being used, as well as for the nuclei investigated (e.g. different adjustments for $^1$H- and X (non-$^1$H)-nuclei -resonators). The scanner performs these adjustments automatically when using $^1$H transceiver volume coils. However, for X-nuclei imaging, it is necessary to adjust these parameters manually, since the automatic procedure invariably fails because the detected MR signal is generally too low.

As a result, for X-nuclei imaging, these important parameters were manually adjusted for each experiment. Shimming was performed using a single pulse experiment (started with the 'GSP' button) employing the shim tool provided by ParaVision 5.0. By

adjusting the sliders for the *x, y, z,* and $z^2$ shim coils, the Free Induction Decay (FID) curve and the Fast Fourier Transformed (FFT) peak shape were monitored. This was best conducted using an off-centre excitation frequency to observe the sinusoidal-exponential FID curve changes while varying the shimming. Optimal $B_0$-homogeneity resulted in a long FID with a mono-exponential decay, and a thin-shaped FFT peak. This procedure was performed for the $^{23}$Na nuclei adjustments, using the receive-only $^{23}$Na surface coil. For double-tuned $^{23}$Na/$^{1}$H transceiver surface coil experiments, shimming was performed with the $^{1}$H MR signal.

The centre frequency adjustment was necessary to guarantee a proper *k*-space acquisition and adjustments were performed for the $^{23}$Na receive-only and the double-tuned $^{1}$H/$^{23}$Na transceiver surface coils during the previously explained single-pulse experiment.

The Reference Pulse Power required for achieving a 90° flip angle with a 1 ms long block pulse had to be manually determined for all transceiver surface coils. This reference power value was then used by Bruker's pulse sequence software environment, ParaVision 5.0, to compute the RF pulse power for various other pulse shapes, pulse lengths, and flip angles. The following paragraph explains the procedure for determining the reference pulse power using the Bruker 7 T MRI system.

Determining the RF pulse power for the $^{1}$H measurements is explained in the Bruker manual. The $^{23}$Na-signal is much lower than the $^{1}$H-signal, so using the same procedure for $^{23}$Na as for $^{1}$H would not measure enough signal within the chosen image slice to optimise the RF pulse power. Thus, a simple spectroscopy experiment was run. The pulse power was then adjusted by assessing the maximum signal magnitude of the FID. By changing the RF transmit power attenuation, the latter maximum FID value changes. The optimal 90°-pulse power attenuation was reached, when the FID value was maximal - increasing the RF pulse power further reduced the amplitude of the FID signal. The pulse reference gain was ~ 27 dB for the 2 cm diameter planar transmit-receive surface coil (Bruker BioSpin, Ettlingen, Germany). For a better understanding of the pulse power attenuation definition employed by ParaVision 5.0, the dB scale definition of input-to-output-power-ratio, $P_1/P_2$, and input-to-output-voltage-ratio, $V_1/V_2$ may be used:

$$dB = \quad 10 \cdot \log \frac{P_1}{P_2} = 20 \cdot \log \frac{V_1}{V_2} \qquad \text{(Equation 2.45).}$$

To double the flip angle, the local $B_1$-field must be doubled. The $B_1$-field is directly proportional to the current flowing in the coil and the voltage applied to the coil terminals. Thus, to double the voltage applied to the coil terminals, a four-fold power increase is

necessary. Hence, the difference between a 90° and a 180°-pulse corresponds to a change in attenuation of 6 dB on the MRI scanner control. This flip angle and in turn power difference can serve to confirm an accurate 90° pulse power by increasing the 90° power level by 6 dB, which should result in an elimination of the FID signal, due to the application of a 180° flip angle and the concomitant signal saturation effect.

#### 2.6.2.3 The Reference Pulse Power Measure

The power needed to generate a $B_1$-field, which tips the net magnetisation vector by 90° is often used as a criteria for characterising resonator performance. The higher pulse power needed to achieve a 90°-pulse, the more power losses occur in the resonator itself. Considering that 500 W (corresponding to -6 dB on the PV5.0 pulse power attenuation scheme) is the maximum applicable power that can be delivered to the coil terminals, the reference pulse power can be converted into a coil-specific reference pulse power. Hence, the 90°-reference pulse power needed for small surface coils and rat brain $^{23}$Na MRI was far smaller (30 dB / ~ 0.1 W) than for larger volume resonators (12 dB / ~ 8 W).

#### 2.6.2.4 The Signal-to-Noise-Ratio Measure

The SNR was measured as the ratio between the mean value of a Region of Interest (RoI) placed in the sample region of the image, and the standard deviation of a RoI placed in an area of the image containing only noise. The SNR values achieved for physiological tissue-replicating samples can give a good indication of the expected *in vivo* SNR. Different resonators are often compared on their achieved SNR in the MR images. However, a fair comparison of coils under those measurement conditions is difficult due to the sophisticated adjustments needed and the differences in NMR signal generation between single and dual coil systems. Descriptions of specific comparisons of coils developed during the course of this work are provided in the following chapters.

# 3 Empirical Evaluation of Shaped Surface Coil Sensitivities at 79.4 MHz

To design an SNR-efficient MRI detector, one must carefully adjust the resonator geometry and dimension to the Larmor frequency and the sample's Volume of Interest (VoI), respectively. The aim of the work presented in this chapter was to optimise the surface coil detector element for *in vivo* rat brain MRI at 7 T (79 MHz) in order to maximise the measurable SNR during the $^{23}$Na-MRI experiment. However, the SNR in $^{23}$Na MR images of homogeneous test samples containing solutions with physiological $^{23}$Na concentration is low. This hinders the fast acquisition of highly resolved images for the comparison of different coil designs. Therefore, a novel bench-level evaluation method was developed, which allowed for the optimisation of the coil parameters on the work bench with regards to SNR-efficiency for the desired sample geometry (i.e. the rat brain).

## 3.1 Introduction

Surface coils demonstrate superior SNR behaviour over volume resonators leading to a widespread use of these detectors for an extensive range of MRI examinations [56]. The maximal axial signal sensitivity can be found in the centre of a planar surface coil. However, shaping the coil onto a cylindrical surface displaces the maximal signal location towards the centre of the shaping radius, consequently improving the sensitivity at depth within the sample [57]. Several computer simulations are described in the literature, which aimed to optimise the detector element for single or multi-element surface coils [57-59]. However, the results were solely based on the geometrical relationship between signal origin and detector coil, whereby electric circuit design-related sensitivity differences such as those caused by component-dependant Q-factors, were neglected. Therefore, a practical optimisation process was required to determine the best coil geometry [60], material [61],

and circuit design [62]. Moreover, a simple resonator sensitivity assessment based upon the loaded and unloaded Q-factor is not suitable for the assessment of the resonator's SNR-efficiency [63], although it is common practice in coil laboratories around the world. The reason suggested for this is that an increasing Q-factor does not directly translate to improvements in SNR, because both the detected signal and noise can be equally increased by a rise in Q-factor under certain circumstances.

In this chapter, it is described how shaped surface coils with different geometries (circular, square, or multi-winding), dimensions (14 to 50 mm side length of square coils), materials (wire or foil), and Q-factors were empirically evaluated on the work bench by measuring the $s_{21}$-attenuation-based sensitivity profiles in order to find the optimum detector design for rat brain $^{23}$Na-MRI at 7T. Furthermore, the setting-up of sample load-replicating NaCl phantoms is described and the accuracy of the concentration set-up method was determined using a conductivity meter. For the later assessment of the qNa-MRI quantification accuracy, the measurement accuracy for the conductivity meter method was also determined.

## 3.2 Methods

Firstly, a bench level test method was developed to measure coil-dependant signal sensitivity profiles using a network analyser rather than using the time-consuming and expensive MRI scanning method. In addition to the time and cost penalty, the SNR efficiency comparison of various detectors with MRI is difficult due to the complex experimental setup composed of the magnet, gradients, and acquisition chain each contributing to a large experimental error. Various resonators were designed and tested on the work bench with the method developed and the optimum detector element parameters were determined. In a final test, the coil profile measured with the bench-level test was compared with profiles measured using the MRI system and profiles computed with a theoretical sensitivity approach.

### 3.2.1 The Development of a Bench-Level Test Method for Surface Coil Detector Elements

To assess *LC* resonator elements for MRI, one usually characterises the signal sensitivity fall-off along an axis (say the *y*-axis) perpendicularly-oriented to the coil surface, thereby describing the coil sensitivity for various sample depths. Using the Biot-Savart law (Equation 2.2), it can be shown that along the *y*-axis, the magnetic field, $B_y$, is strongest at the centre of the surface coil and falls off with distance, *y*, from the centre according to:

$$B_y = \frac{\mu_0 \cdot I \cdot r^2}{2 \cdot \sqrt{\left(y^2 + r^2\right)^3}} \qquad \text{(Equation 3.1)},$$

where $\mu_0$ is the permeability of free space, $I$ is the current and $r$ is the radius of the resonance loop. Applying both the Biot-Savart law and the principle of reciprocity to a detector loop with diameter $r$, it can be shown that the detected signal $S$, along the $y$-axis is the strongest at the centre of the loop and falls off with distance $y$, from the centre according to [49]:

$$S \propto \frac{r^2}{2\sqrt{\left(y^2 + r^2\right)^3}} \qquad \text{(Equation 3.2)},$$

This equation allows for a theoretical computation of the optimum surface coil dimensions. The maximum SNR for a volume element (voxel) at a sample depth $y$ is theoretically realised when the circular and planar surface coil radius, $r$, is adjusted such that

$$r = \frac{y}{\sqrt{5}} \qquad \text{(Equation 3.3)},$$

and the coil is oriented with its central axis intersecting the voxel [57]. This approximation results in a radius of ~ 5 mm and a circular surface area of ~ 80 mm$^2$ for a sample depth of 12 mm. Considering that rectangular and circularly-shaped surface coils with equal detector areas achieve similar sensitivities [59], one can convert the circular coil radius to the side length of a square coil with identical surface area. Thus, the theoretically-derived optimum side length for a square-shaped surface coil giving optimum SNR at 12 mm sample depth is approximately 9 mm long. However, one might anticipate that this approximation would prove inaccurate for non-planar and very small surface coils, since coil dimension-dependent loss mechanisms were neglected in the approximation. Therefore, to empirically test resonators with a variety of coil designs, a bench test method was developed. In this way, the sensitivity measurements for various coil dimensions could reveal whether the theoretically-derived coil dimensions were suitable for the required rat brain MRI application and desired $^{23}$Na resonance frequency.

The experiment was set-up as shown in Figure 3.1. A small loop of copper wire (0.8 mm thick, 3 mm i.d.) was oriented in the $xz$-plane and was fed with an alternating current via a twisted wire from the network analyser port 1. The twisted wires minimised any additional magnetic field components arising from the leads.

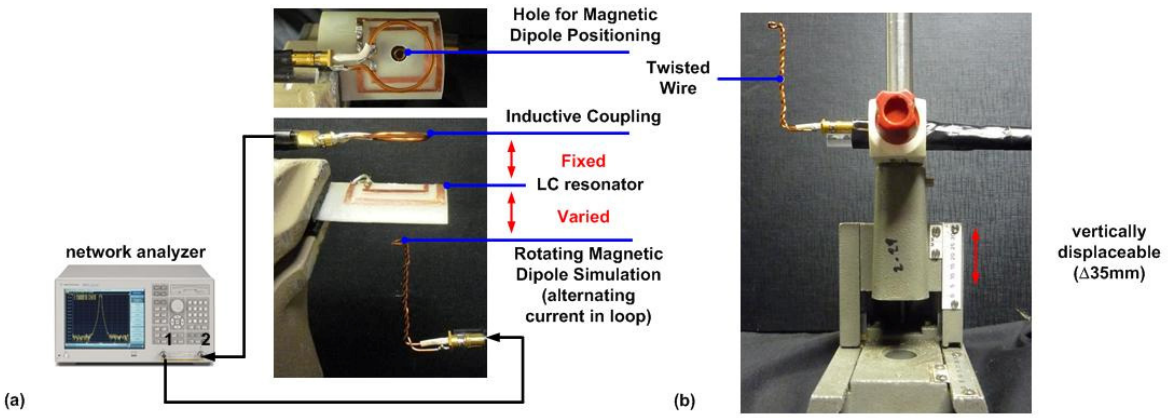


**Figure 3.1: (a) The set-up of the sensitivity measurement using the *s21*-transmission measurement on the network analyser and (b) a two-way stage to displace the magnetic dipole generating pick-up loop with respect to the LC resonator.**

A current flowing in the small horizontal circular coil generates a vertical magnetic dipole moment. By orientating the loop surface in parallel to the LC resonator surface area and supplying the loop with an alternating current, a precessing net magnetisation was simulated, which induced a measurable *emf* in the resonance coil as theoretically described in Section 2.1 ('NMR Signal Theory'). The loop was attached to a two-way stage fixed to the bench, which permitted an exact coil displacement (± 0.25 mm) of the loop vertically along the *y*-axis by up to 35 mm. Thus the coil-dependent sensitivity profile could be acquired. To enable an accurate comparison between different detector coils and coil elements, identical inductive coupling was used in each case and only the LC resonator loop itself was changed for each experiment. The inductive coupling was adjusted by varying the distance between the LC resonator and the coupling loop until 50 Ω matching was achieved. Using the identical coupling circuit avoided unnecessary uncertainty arising from differential matching facilities.

### 3.2.2 The Development of Physiological Load Replicating Phantoms

The optimisation of the *LC* resonator for *in vivo* applications requires the consideration of sample losses, which are usually simulated through the use of phantoms. These typically consist of vials containing physiological concentrations of NaCl. Reference phantoms with known $^{23}$Na concentration are also necessary for the accurate quantification of TSC via $^{23}$Na MRI, which will be explained in Chapter 7. The procedure, which was used to setup the NaCl solutions, is described in this section, together with a description of the achievable accuracy of the resultant $^{23}$Na concentration in solution.

The required mass of NaCl to set-up a desired molar concentration $c_m$ for a given volume $V$ of distilled water is:

$$m = \quad M \cdot V \cdot c_m \qquad \text{(Equation 3.4)},$$

where $M$ is the molar weight of the ionic NaCl compound, which is 58.443 g $mol^{-1}l^{-1}$. Using a volumetric flask (1 l with ± 0.01 l accuracy) and a balance (Adam, AQT-200 with ± 0.01 g accuracy), NaCl solutions with molar concentrations from 10 to 150 mM in 10 mM concentration steps were set-up. The conductivity of the resultant solutions was measured using a conductivity meter (Wissenschaftlich Technische Werkstätten, Cond 315i) and graphed versus molar mass (Figure 3.2). The experiment was repeated ten times to measure the systematic error in setting-up the $^{23}$Na concentration solutions. The linear regression of the measured data resulted in a well-fitting linear curve describing the relationship between the measured conductivity $\sigma(c_m)$ and molar NaCl concentration $c_m$ which is:

$$\sigma(c_m) = \quad 0.095\frac{mS}{cm \cdot mM} \cdot c_m + 0.372\frac{mS}{cm} \qquad \text{(Equation 3.5)}.$$

The standard deviation of the measured conductivities was converted using Equation 3.5 in order to obtain a molarity value, which represented the NaCl solution set up error encompassing the measurement accuracy for the conductivity meter. The experiment was also influenced by a systematic error resulting from the volumetric and mass inaccuracies of the set up process.

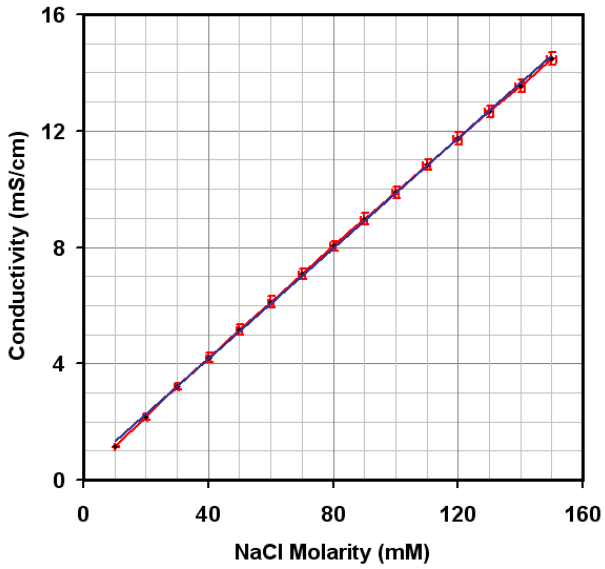


**Figure 3.2: Conductivity measurement of the NaCl solution as a function of the set up NaCl molarity.**

The Gaussian error $\Delta M$ for setting up molarity $M$ was computationally determined by the following equation:

$$\frac{\Delta M}{M} = \sqrt{\left(\frac{\Delta m}{m}\right)^2 + \left(\frac{\Delta V}{V}\right)^2} \qquad \text{(Equation 3.6)},$$

The computed Gaussian error for the weighing of the constituents that were mixed and the measurement uncertainty for the conductivity measurement method are graphed in Figure 3.3. It was found that the conductivity meter accuracy was approximately ± 1 mM NaCl – measured as the difference between the computed set-up error and the measurement uncertainty. The overall error in $^{23}$Na concentration by weighing of the constituents that were mixed and the volumetric error varied between 0.7 and 1.8 mM in dependency of the molarities.

For the detector element optimisation three phantoms were set up, containing 45 mM (physiological $^{23}$Na concentration), 145 mM (maximum physiological $^{23}$Na concentration), and 1 M NaCl solutions in vials of the same type as shown in Figure 3.4. The conductivity calibration curve served to check that the solution was mixed correctly and achieved the desired $^{23}$Na concentration. The development of air bubbles within the image range was avoided either by inbuilt bubble traps (see Figure 3.4) or by employing gel carriers, such as agarose or agar. A 500 mM NaCl agarose gel phantom (2 %) was also set-up for MRI-based 3D coil profile measurements.

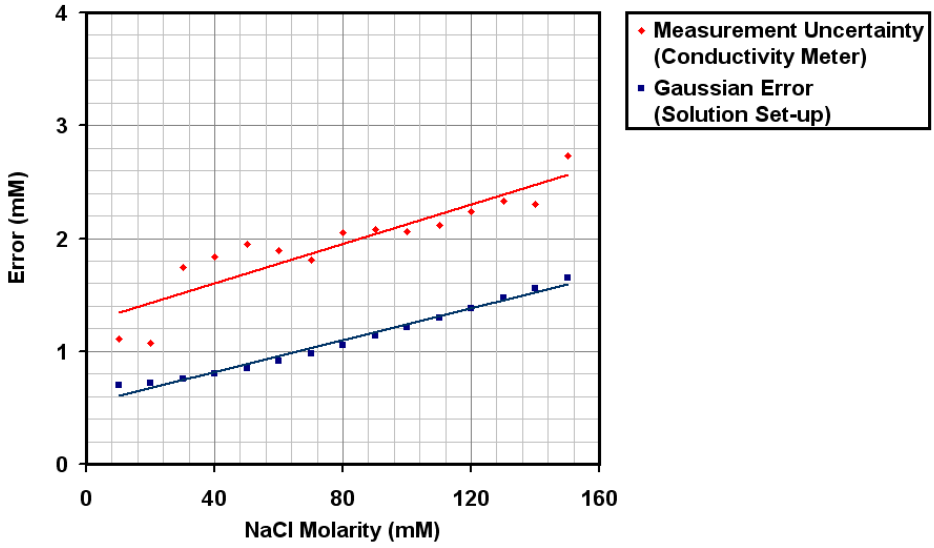


**Figure 3.3: The set up error measured via conductivity measurement method (red line) and estimated via Gaussian error calculation (blue line). Lines are results of a linear fit to the data. The difference between the offset of each line was taken as an indicator for the systematic conductivity meter measurement error.**

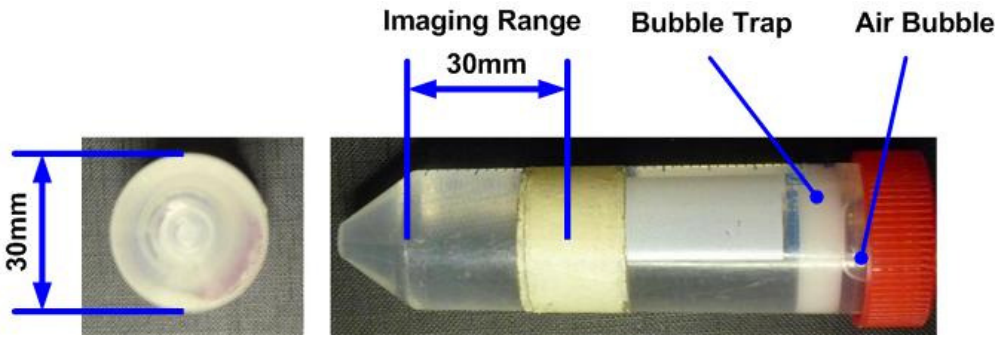


**Figure 3.4: Cylindrical vial of diameter similar to a rat's head filled with a solution with defined NaCl concentration to model the loading effects and to test for the coil performance via MRI scanning.**

A slightly larger cylindrical jar (40 mm i.d.) was used for this purpose, which fit exactly to the cylindrical surface shape of the detector coil carrier material (fibreglass former, 42 mm i.d.). The gel phantoms were set up by boiling the gel/ NaCl-solution in a microwave for approximately 1 minute. Observation of the boiling procedure ensured that no solution spilled out of the container. Afterwards, the solution was stirred and left to cool down for up to one hour, during which time the solution gradually solidified to a gel-like carrier.

### 3.2.3 Test Circuit Development

Theoretically, the optimum signal sensitivity for a surface detector coil can be achieved by matching the coil dimensions to the required sample depths, and by minimising signal losses as arising from resistive, electric, radiation, and magnetic loss mechanisms. Two resonators (included tuning and matching facilities) were designed; one to test for the influence of different coil dimensions and a second to test for the influence of the electronic circuit design on the signal sensitivity. A third study was conducted on different coil geometries using the inductive coupling scheme, which was described in Section 3.2.1.

#### 3.2.3.1 The Influence of Various Coil Dimensions on the Relative Signal Sensitivity

Square detector elements were developed with side length *s*, and with the element surface area wrapped around a cylindrical fibreglass former (42 mm i.d.) as shown in Figure 3.5. When varying the side lengths, both the curved and linear sides were changed by the same amount, maintaining the square aspect ratio. This experiment was designed to investigate how varying the detector coil side length ($s$ = 14 mm to 50 mm in 4 mm steps) influenced the detector coil output voltage (relative sensitivity) along the $y$-axis of the coil over a 20 mm range (typically the deepest depth for rat brain imaging).

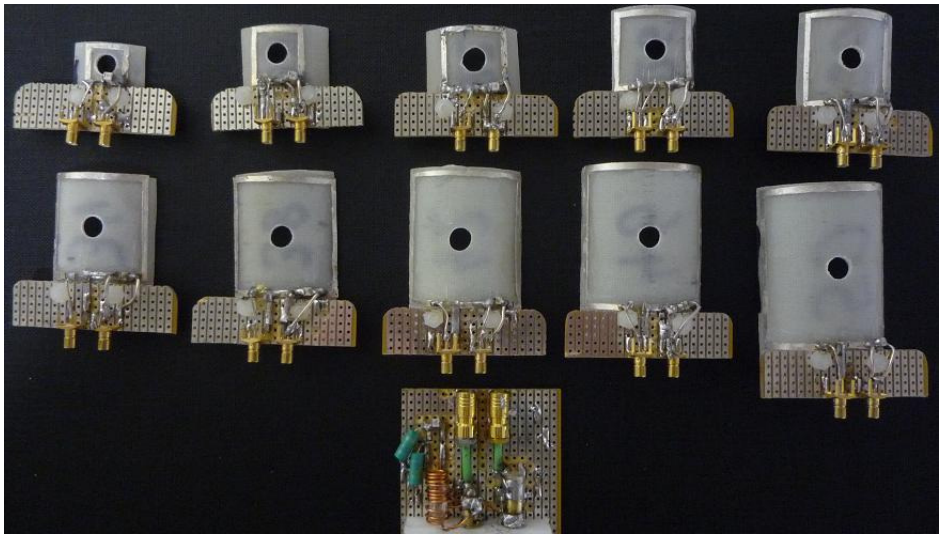

**Figure 3.5: Variable side length detector elements and the base circuit (bottom) to which every element could be connected for the transmission measurements.**

To facilitate an accurate comparison between different side length detector coils, the same matching and tuning 'base' circuit was used and only the pre-tuned 79.4 MHz coil loops themselves were changed between each measurement. Inductive coupling was used for the base circuit, which allowed for remote matching and tuning when the coil was placed inside the MRI scanner. The remote tuning and matching also enabled testing of this coil arrangement using MRI scanning. Remote tuning and matching capability is useful if such an arrangement were to be used for MRI experiments in the scanner, although this was not done in the current study.

The $s_{21}$-transmission attenuation was recorded for various magnetic dipole generating loop positions along the line perpendicular to the tangent at the centre of the detector coil. To position the loop precisely within each detector's centre, a hole was drilled into the fibreglass former. The resonator circuit is shown in Figure 3.6. Using Equation 2.21, the measured $s_{21}$-attenuation value may be converted to an output voltage at the coil terminals, assuming a unitary (i.e. 1 V) input voltage:

$$S_{rel} = 1V \cdot 10^{-\frac{A(s_{21})}{20}} \qquad \text{(Equation 3.7).}$$

As a result, one obtains a relative as opposed to an absolute measurement of (i.e. the relative signal sensitivity $S_{rel}$). The maximum relative output voltage measured was 0.118 V. All calculated relative output voltages were then normalised to this value in order to allow for straightforward comparison between coil sizes.

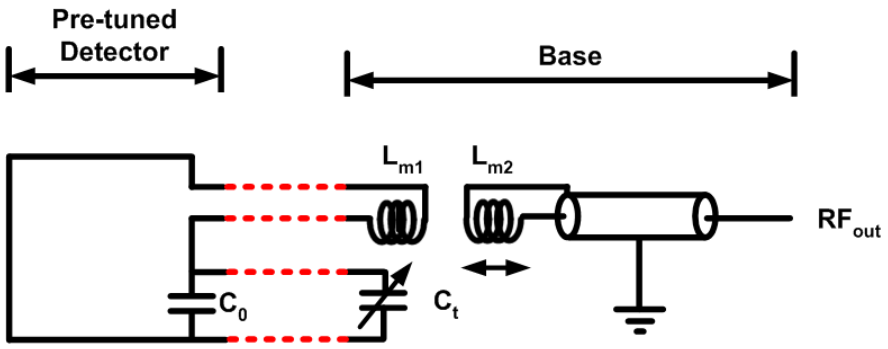


**Figure 3.6: The circuit used for the variable coil dimensions experiment. Each detector loop was pre-tuned to > 79.4 MHz and connected via two SMB connectors to the tuning capacitor $C_t$ and coupling loop $L_{m1}$ (red dashed lines). The position of the inductive coupling loop $L_{m2}$ could be remotely adjusted to match the coil impedance to 50 Ω.**

The measurements were repeated five times and the standard deviation was calculated to determine the repeatability of the measurements. In addition to measuring the sensitivity profiles for different detector coils, the effects of loading the various side length detector coils with two sample vials (containing 145 mM and 1 M NaCl solutions) were tested, and the signal sensitivity and Q-factor were also measured at 0 mm depth for the loaded conditions (by placing the transmit loop in the centre of the detector coil elements from above). Loading affected the circuits' resonance frequency and impedance. For this reason, the coils were tuned and matched both before and after loading. The $s_{21}$-attenuation and Q-factor were recorded for the unloaded, 145 mM and 1 M loaded coil. The attenuation was converted to relative signal sensitivity. The relative sensitivity and Q-factor were calculated for each of the ten different sized detector coils. The experiment was repeated three times and a standard deviation calculated to demonstrate the repeatability of the measurements.

#### 3.2.3.2 The Influence of Passive Inductance on the Relative Signal Sensitivity

Engineers and physicists strive to design and manufacture high Q-factor detector coils with the assumption that it leads to greater signal sensitivities. For example the incorporation of a trap circuit inductance into the resonator circuit, which is necessary for double-tuned coils, was reported to decrease the Q-factor by up to 20 % [64]. Nevertheless, the absolute relationship between Q-factor and detector coil sensitivity is difficult to establish. The aim of this experiment was to verify that an increase in Q-factor yields an increase in relative signal sensitivity and if possible to establish the exact relationship between both for one specific coil arrangement. To this end, a coil whose Q-factor could be varied was developed, as discussed below.

A square-shaped surface coil ($s$ = 26 mm) was mounted on a cylindrical fibreglass tube (42 mm i.d.) and tuned to 79.4 MHz by a variable capacitor (2 to 120 pF, NMTM120CE, Voltronics) and a inductor (home-made, with 20 windings wrapped around a 6 mm drill bit using 0.8 mm diameter wire). A threaded brass rod was mounted to the coil base, which could be screwed into the inductor $L_{m1}$ in order to vary the inductance. The circuit diagram is shown in Figure 3.7. The variable inductor built into the coil's circuit allowed the Q-factor to be varied from approximately 38 to 50. The detector coil was tuned and matched after each Q-factor variation. Matching of the coil was performed inductively, using a 3-winding loop (home-built, with 3 windings wrapped around a 10 mm drill bit using 1.5 mm diameter wire), which could be varied in position relative to the variable coil inductor. The signal sensitivity at the 0 mm position was recorded for various Q-factors and loading conditions. The measurements were repeated four times for each of the three loading conditions. A standard deviation was calculated to determine the experimental uncertainty in Q-factor and relative signal sensitivity.

#### 3.2.3.3 The Influence of Various Coil Geometries on the Relative Signal Sensitivity

The inductive coupling method described in Section 3.2.1 was used to investigate the relative signal sensitivity profiles for six different coil detectors constructed using different geometries (square, circular, multi-winding) and different material shapes (thin/ thick wire, foil). A photograph of the six detector elements can be found in Figure 3.8. The signal sensitivities were measured once for every detector. The sensitivity at the resonator centre was determined when loaded with a vial containing physiological 45 mM NaCl solution.

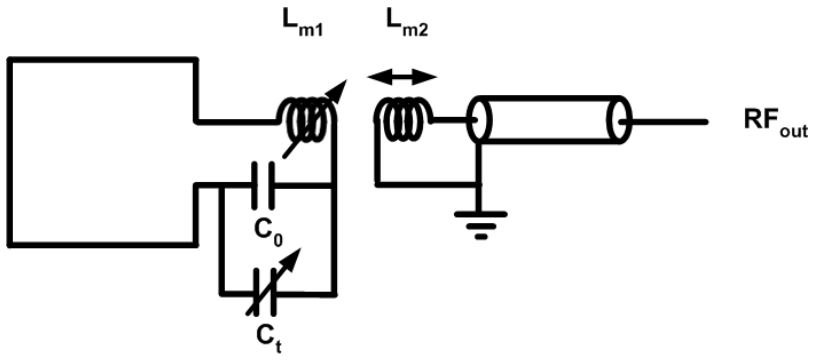


**Figure 3.7: Electronic circuit design used for the measurement of relative signal sensitivity as a function of Q-factor. The circuit used for the previous variable aspect-ratio experiment was modified by replacing the fixed inductor ($L_{m1}$ in Figure 3.6) with a variable inductor. The surface coil was tuneable to 79.4 MHz via a large variable trimmer capacitor in order to compensate for a varied coil inductance $L_{m1}$. The position of the inductive coupling loop $L_{m2}$ could be remotely adjusted to match the coil impedance to 50 Ω.**

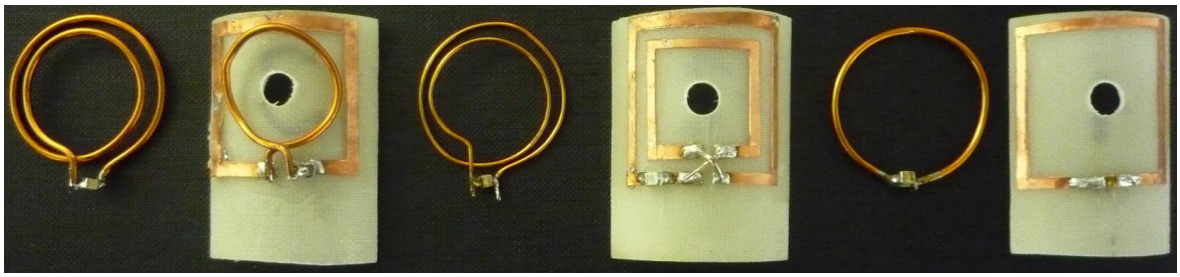

**Figure 3.8: Resonator elements with various coil geometries.**

Using the difference between loaded and unloaded sensitivities at 0 mm depth, a correction factor could be computed and applied to correct the unloaded sensitivity measurements made at the other positions along the *y*-axis.

### 3.2.4 Comparison of Theoretical Calculations with Bench and MRI System Measurements

The aim of this final experiment was to verify whether the bench level test is a reliable method to compare coil profiles on the work bench. The accuracy of the measured coil profiles (i.e. the measured relative signal sensitivity along the central *y*-axis) was compared with theoretical predictions and coil profiles measured using the Bruker 7 T MRI scanner. A $^{23}$Na receive-only surface coil (described in Chapter 6) served as the test surface coil for this comparison. The coil profile was extracted from the acquired MR image set of a 500 mM NaCl/ 2 % gel concentration phantom (cylindrical jar with 40 mm i.d. and 60 mm height). The profile line extracted from the MRI measurement which is identical to the profile line measured relative to the surface coil detector element using the bench test method is marked in the axial, coronal, and sagittal MR images presented in Figure 3.9. The three images are representative orthogonal cross sections through a 3D dataset.

For comparison, the MR signal sensitivity along the central *y*-axis was extracted in 1 mm steps and averaged across a circular region in the *xz*-plane, which had a 5 mm diameter. The sensitivity profiles along the same profile line were also measured on the work bench for the same surface coil. Finally, the theoretical coil profile was computed for a single winding circular loop with radius of 13mm (using Equation 3.2).

## 3.3 Results

The results in Figure 3.10, 3.11, and 3.12 are based upon data acquired by physics undergraduate student Laura Shields and are presented in similar form elsewhere [65].

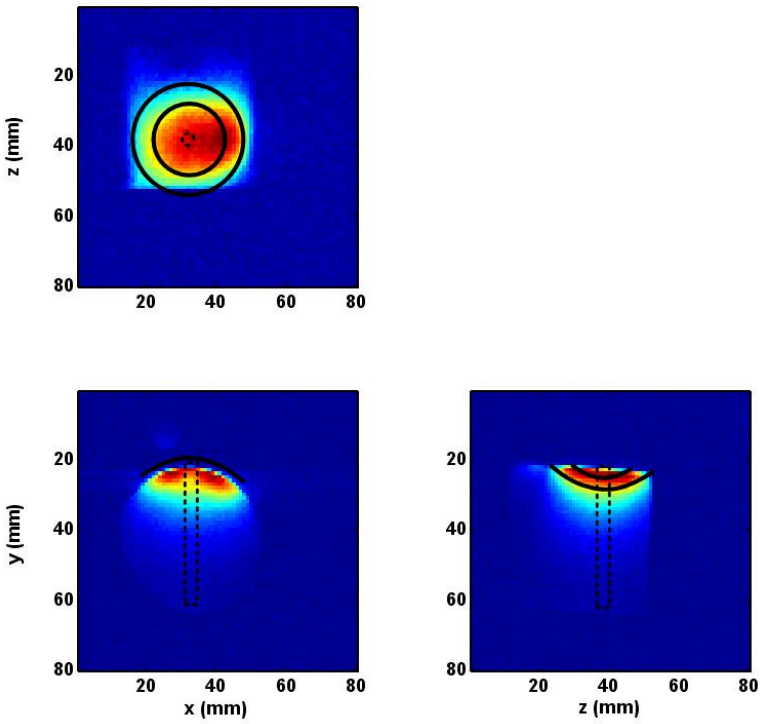


**Figure 3.9: Representative axial, sagittal, and coronal $^{23}$Na MR images through a 500 mM NaCl gel phantom; the images were acquired using a 2-winding receive-only surface coil (with coil element positions indicated by the solid black lines in each image). The extracted coil profile along the *y*-axis is marked with a dotted rectangle or circle in the respective cross sections.**

### 3.3.1 The Influence of Various Resonator Dimensions on the Relative Sensitivity

A graph of relative sensitivity, normalised to the maximum output voltage measured in the centre of the smallest side length detector coil was plotted against distance for each detector coil, and is illustrated in Figure 3.10. The graph shows that smaller detector coils (14-22 mm) are more sensitive at depths of ~ 0-10 mm, while larger detector coils (26-50 mm) are more sensitive at depths of ~ 10-20 mm. As can be seen from the graph, the relative signal sensitivity falls off with increasing depth. The fall-off is more rapid with smaller compared to larger detector coils. For large detector coils (26-50 mm), the measured relative sensitivity was observed to peak prior to the fall-off. The distance at which the peak occurred increased with increasing detector coil size. The error bars for the 26 mm coil element profile were included in Figure 3.10 to demonstrate the accuracy and repeatability of the bench test measurement method. The errors determined from the standard deviation of five measurements were below 5 % for all coil elements and sample depths and are not shown for the other profiles in Figure 3.10 for clarity.

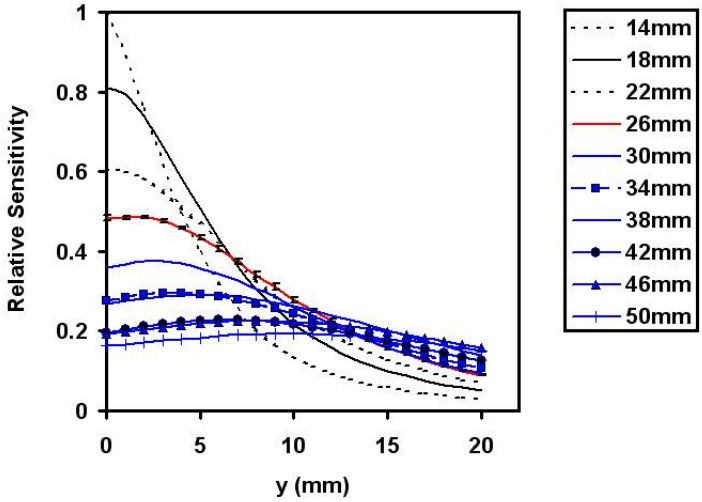


**Figure 3.10: Relative sensitivity profiles measured as a function of sample depth along the vertical *y*-axis perpendicular to the coil surface for various detector element side lengths. The standard deviation over five measurements per sample point for the 26 mm side length detector element profile is included (< 5 %) – the errors were similarly small for the other profiles and are omitted for clarity.**

A graph of Q-factor as a function of detector coil side length for three different loading conditions is presented in Figure 3.11. From this graph, three different observations can be made: Firstly, it was noticed that the Q-factor was nearly constant and averaged 47 ± 1 for the unloaded condition. Secondly, when loaded with the 145 mM phantom, the Q-factor decreased only for larger side length detectors (30 to 50 mm), with no significant changes observed for smaller side lengths detectors (14 to 26 mm). Thirdly, the higher concentration load of 1 M NaCl caused significant Q-factor decrease for nearly all investigated side length detectors except the smallest detector with 14 mm side length.

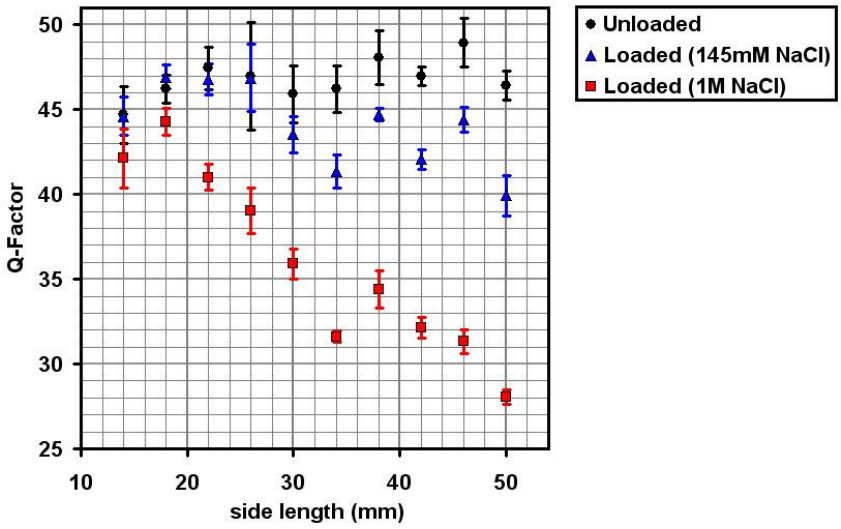


**Figure 3.11: Measured Q-factors as a function of element side lengths for three different loading conditions.**

### 3.3.2 The Influence of Passive Coil Inductance on the Resonator Sensitivity

A graph of the relative signal sensitivity measured as a function of Q-factor for three loading conditions is presented in Figure 3.12. It was found that by varying the Q-factor of a specifically-designed coil, the signal sensitivity decreased linearly with Q-factor as expected. The slope was the highest for the unloaded coil, and the smallest for the highest 1 M NaCl load. However, a significant non-zero offset in normalised sensitivity (extrapolated via linear regression) was noted, averaging at 63 ± 4 % of the maximum relative signal sensitivity for the three loading conditions tested. Furthermore, the relationship between Q-factor and relative signal sensitivity was investigated. Independently of the coil loading, the Q-factor was reduced by 25 % through the inductor variation. Thus, a 25 % decrease in relative signal sensitivity was expected. However, the relative signal sensitivity drop was measured to be lower than 25 % and decreased with higher concentration loading: 10 % for the unloaded, 8.5 % for 145 mM NaCl load, and 6.7 % for 1 M NaCl load.

### 3.3.3 The Influence of Various Geometries on the Resonator Sensitivity

A graph of relative sensitivity, normalised to the maximum output voltage measured in the centre of the two-winding circular thick wire coil was plotted against distance for LC resonators with different coil geometries, and is illustrated in Figure 3.13. The two-winding coil, which was wound from thick 1.5 mm diameter copper wire, clearly outperformed all other geometries.

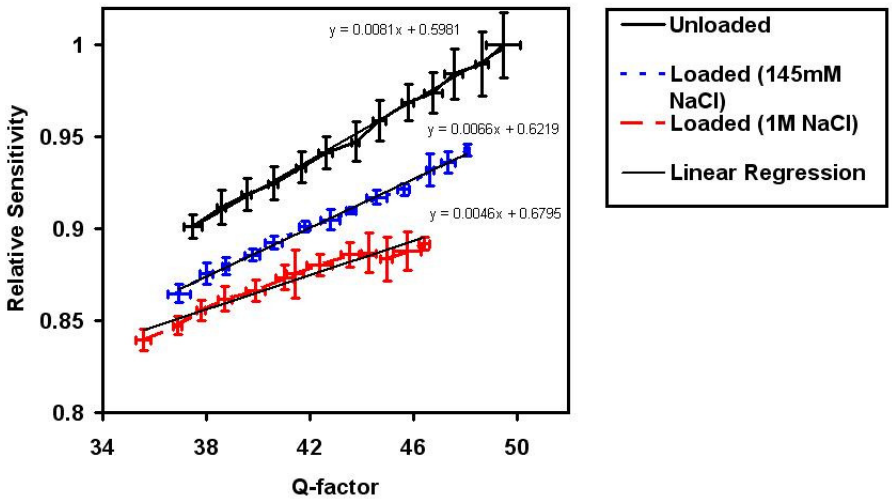


**Figure 3.12: Measured relative signal sensitivity as a function of Q-factor for three different loading conditions.**

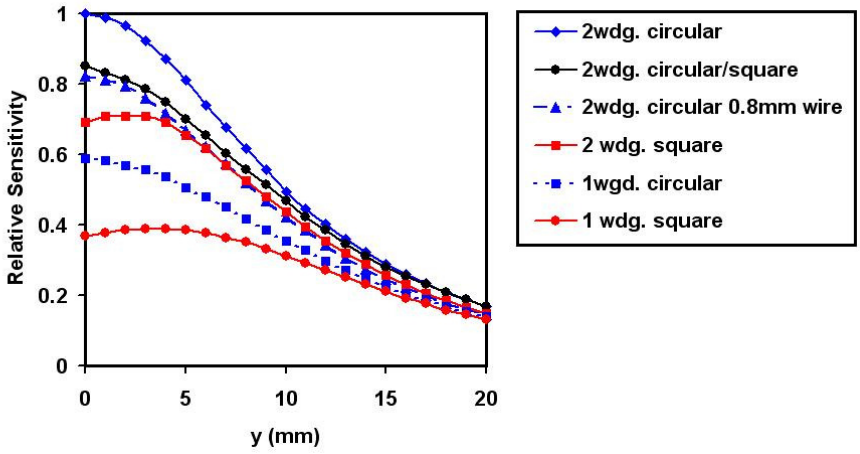


**Figure 3.13: Measured relative signal sensitivity profiles as a function of sample depth for six different coil geometries. The two-winding circular thick wire coil performed best across the desired sample depth of 20mm.**

The square coils, which were anatomically-shaped and fixed to a cylindrical fibreglass former, all exhibited a peak in the measured sensitivity prior to the fall-off with depth into the sample, which resulted in slightly different coil profiles in comparison to the planar circular coils. The circular wire coil elements were held in place by two planar plastic sheets with a hole drilled into the centre of the coil element, which served as the exact magnetic dipole generating coil positioning. For a better analysis, the loaded and unloaded Q-factors as well as the relative signal sensitivity at 10 mm sample depth under physiological loading conditions were extracted and graphed in Figure 3.14.

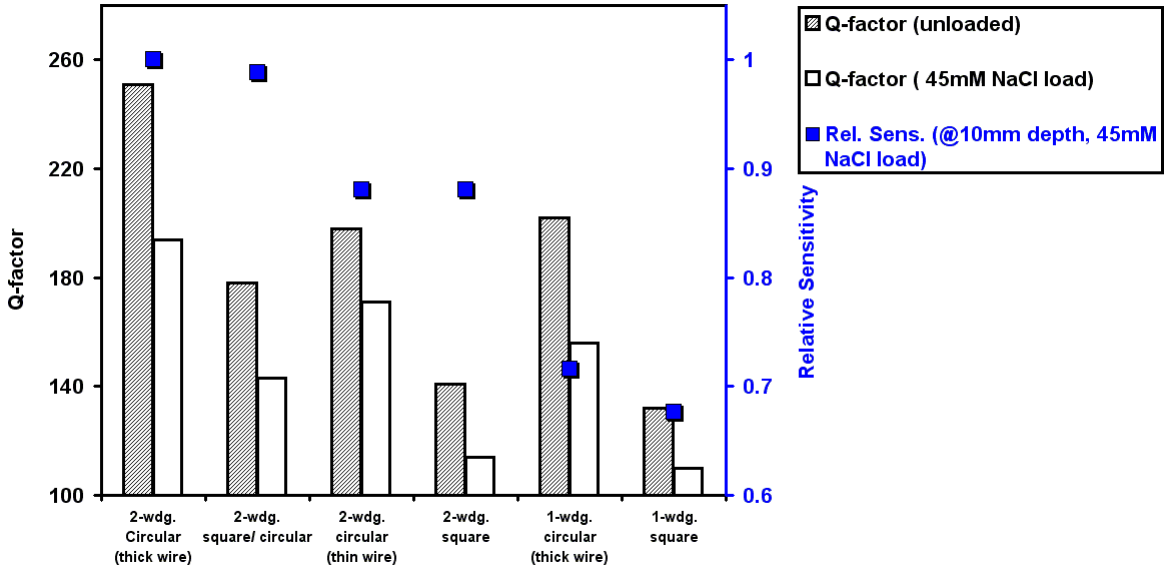


**Figure 3.14: The effective sensitivity at 10 mm depth, together with the loaded and unloaded Q-factor values measured for various coil geometries.**

Square coils and thin wire circular coils performed approximately 10 % worse than their circular thick wire counterparts. Although the Q-factor was higher (170) for the two-winding circular thin wire coil compared to that measured for the two-winding square coil geometry (110), the relative signal sensitivity was similar for both resonators.

### 3.3.4 Comparison of Theoretical Calculations with Bench and MRI System Measurements

A jar containing 500 mM NaCl solution in 2 % agarose gel was imaged at the 7 T MRI facility at Glasgow University, UK, using the receive-only surface coil (two-windings, $^{23}$Na) described in Chapter 6. A profile was extracted from the MR image and compared to the theoretically computed and bench-measured profiles (Figure 3.15). The data from the $^{23}$Na MRI scanner and the bench-test method were compared as follows: The intensity value, at 2 mm sample depth (starting at the detector centre) served to normalise the extracted MRI coil profile. The relative signal sensitivity values along the coil profile line were normalised to the relative signal sensitivity value at 0 mm depth for the bench measurements and theoretical computations. The theoretical signal fall-off at a distance along the axis perpendicular to a 26 mm diameter planar loop of wire was computed with Equation 3.2.

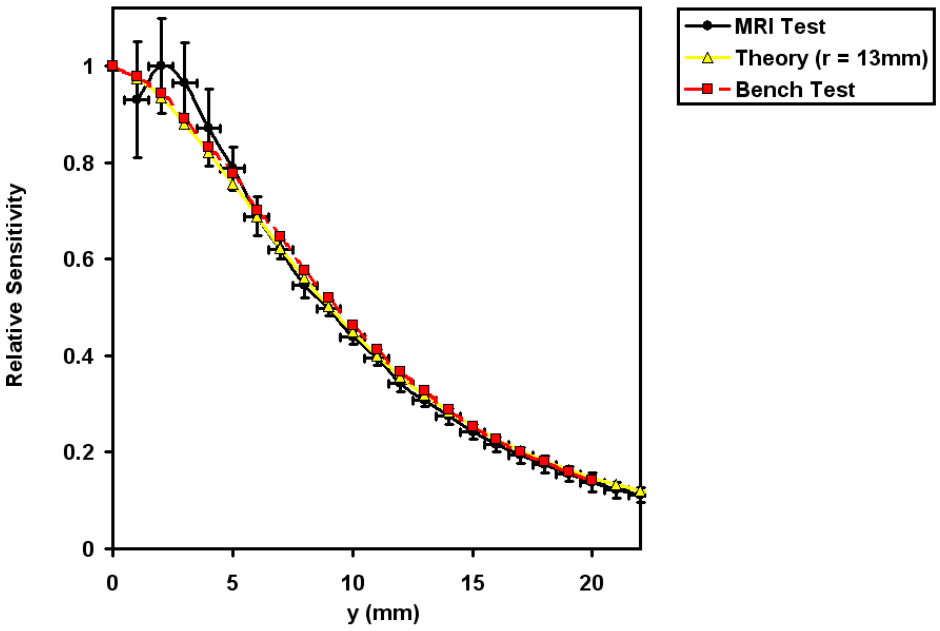


**Figure 3.15: Profiles measured for the two-winding (20 and 30 mm) receive-only surface coil using MRI and bench tests. Also shown is the theoretically-derived profile for a 26 mm diameter circular loop. The coincidence between MRI, bench test and theoretically simulated profiles is clearly noticeable.**

The profiles of relative signal versus distance were plotted. The uncertainty in distance was half the voxel size: 0.5 mm. The bench-level and theoretical profiles displayed a

strong agreement. The MRI profile measurement demonstrated a large sensitivity variation near the detector surface (0 to 4 mm), most likely due to systematic errors related to the MRI measurement technique. However, the bench test and theoretical results were within one standard deviation of the MRI measurement results.

## 3.4 Discussion

A practical approach to the optimisation of MRI surface coil elements was developed and tested to derive the optimum coil dimension and geometry for a given VoI and resonance frequency. A common approach described in the literature uses a theoretically-derived coil geometry to match the desired VoI in the sample, which is generally presumed to provide the optimum coil sensitivity [59]. However, such approaches based exclusively on geometrical considerations invariably omit losses incorporated by the circuit design and other loss mechanisms which may be different in their importance at various frequencies and for different coil dimensions. Therefore, it was believed that a practical measurement of the surface coil profiles on the work bench would better reflect on the surface coil receive-capabilities with respect to its dimension, geometry and electric circuit design. A similar experimental setup was used by Fitzsimmons *et al*. to test double-tuned resonators, although without the possibility of acquiring the coil profiles [66]. Tomanek *et al*. employed the same bench test principle to assess the axial sensitivity of various birdcage resonators [67].

### 3.4.1 Empirical versus Theoretical Coil Dimension Optimisation

The theoretically derived side length for a square planar coil to provide maximum signal sensitivity at 12 mm sample depth was computed to be $s \sim 9$ mm [57], while the empirically found optimum side length in the current study was far higher at between 26 and 30 mm. The theoretical approximation was designed for planar coils; whereby the coils used for this experiment were wrapped around a cylindrical fibreglass former with 40 mm i.d. to better fit the anatomy of the rat's head. This led to the better performance of larger dimension surface coils because the sensitivity maximum was moved towards the cylindrical 20 mm radius with larger than 20 mm side lengths of the square resonators. Given the wide variety of possible detector element designs, a universal mathematical equation to describe the optimal coil dimensions for a greater variety than only planar single loop coils would be useful. In the absence of such a theoretical approach, the empirical method described here offers a quick and practical way of optimising the parameters for a variety of coil dimensions and geometries.

### 3.4.2 Electric Losses

From the practical measurements of different side length detector coils, it was found that electric losses were negligible at 79.4 MHz for maximal physiological sample loads (145 mM NaCl) and detector side lengths < 30mm. Electric losses could also be neglected for coil dimensions smaller than 18 mm, when load concentrations as high as 1 M NaCl were used. Electric losses arise due to parasitic capacitances, which build up between the coil and the sample depending on the dielectric constant (permittivity) of the material between them and also on the conductivity of the sample. The parasitic capacitance can be estimated from the known dielectric material parameters and the coil dimensions. Epoxy resin bonded fibreglass was used for the coil support, which had very low permittivity (~ 5). Assuming a 2 mm epoxy resin layer between the NaCl solution and the silver of the coil element, the parasitic capacitance for a 14 mm side length and 2 mm foil width coil was theoretically computed to be 2.5 pF, which corresponds to a 800 Ω capacitive impedance at the 79 MHz resonance frequency. Consequently, this particular coil remained relatively unaffected by the parasitic capacitance, because the coil capacitance was high at 85 pF (23 Ω), and thus all losses resulted entirely from the coil's resistive paths. The conductivity of the sample was also significant. The Q-factor dropped significantly for coils with side length > 18 mm and high concentration loads of 1 M NaCl with this effect, increasing to lengths > 30 mm for loads of 145 mM. The electric losses thus depend on the coil dimensions, sample conductivity, permittivity of the material used between coil and sample as well as the employed frequency. In general, the loss mechanisms in small detector coils (< 30 mm side length) are negligibly small, and hence such coils tend to be dominated by resistive losses. Resistive losses in turn could be minimised by cooling the detector element, for example to liquid $N_2$-temperatures (77 K), thereby reducing the Brownian motion in the detector coil [68]. The use of larger capacitor values with higher permittivity could further reduce the electric losses [69].

### 3.4.3 The Q-factor and the Signal Sensitivity

The relative signal sensitivity was measured as a function of various Q-factors for three different loading conditions, which allowed for testing the influences of electric losses occurring with different sample loads and the resistive losses added by increasing a variable inductor. The relative signal sensitivity increased linearly with increasing Q-factor. However, a non-zero offset of the linear regression curves was noticed at approximately 60 % of the maximal measured signal sensitivity. The slope of the linear regression curve furthermore decreased with increased sample load. The decrease in the

resonator Q-factor was identical for all sample loads (25 %), although the relative signal sensitivity reduction was sample load-dependent. The increased sample load added electric losses to the resonance structure and thus reduced the effect of increased resistive losses in the variable inductor on the detected relative signal sensitivity. The offset indicates that by reducing the coil Q-factor through the variable inductor, the relative signal sensitivity can not drop by more than 40 % (~ 60 % offset at extrapolated zero Q-factor). This suggests that if there would be a possibility to reduce the Q-factor of the variable inductance to near zero by introducing more core material into the variable inductor, the coil would still detect 60 % of the induced signal.

Consequently, a direct linear relationship between Q-factor and relative signal sensitivity could not be established, without the consideration of all of the loss mechanisms. These occur in various resonator parts and vary with the loading conditions. This further supports the idea of using the bench-level test introduced in the current work to evaluate the surface coils' performance, since it enables the spatial sensitivity measurement rather than a derivation of the sensitivity properties from a Q-factor value, which is difficult to exactly link to the relative signal sensitivity profile.

### 3.4.4 The Optimum Surface Coil Geometry for Rat Brain MRI at 79 MHz

The two-winding circular coil wound with thick wire outperformed all other tested coil geometries at 79 MHz and small < 30 mm coil diameter. Bottomley *et al*. similarly found that circularly-shaped coils achieved 92 % of the theoretical maximum SNR - better than any other shape [57]. In addition to the coil material, the theoretical rationale behind multi-winding and the resultant SNR increase has already been discussed in Section 2.3 ('Loss Mechanisms). The low electric losses in small resonators at 79 MHz justify reducing the resistive losses by cooling down the resonator in order to achieve higher SNR. At room-temperature, the only option available is to multi-wind in order to increase the SNR. In this way, the induced *emf* could be improved by a factor *N*, where N is the number of windings. Thus as long as the resistive losses dominate the effective noise resistance of the resonance circuit, the SNR could be improved by approximately $\sqrt{N}$. This has been proven theoretically in Section 2.3. Care must be taken to not exceed the $\lambda/10$ conductor length and limit the parasitic capacitance values in between windings by choosing sufficiently large gaps between the loops and thereby reducing the proximity effect. Furthermore, the dielectric losses increase with multiple windings and consequently there is a limit of windings for a certain sample geometry and resonance

frequency. This limit seemed to have been achieved by two multi windings for the rat head sample geometry at 79.4 MHz. The gap between the windings had to be chosen larger than 3 mm to observe the Q-factor increase. This gap ought to be larger for more than two windings, while the dielectric losses increase further. Up to four winding resonance loops were tested. The relative signal sensitivity benefits were minor for more than two winding coils, because the dielectric losses increased with these coils.

### 3.4.5 Resonator Sensitivity Comparison using MRI and Bench Level Tests

The profiles measured with MRI revealed an excellent agreement with bench test and theoretically-derived profiles. The bench test and theoretical profiles coincided perfectly from the beginning to the end of the profile measurement range with marginal errors below 5 %. The 0 to 4 mm profile range measured with MRI revealed larger variations of ~ 10 % and exhibited a maximum sensitivity at 2 mm sample depth. This MR sensitivity maximum was believed to be related to Gibb's ringing and partial volume effects at the sample's edges. Discrete Fourier approximation is used in the reconstruction of images in MRI. The accuracy of the Fourier reconstruction depends on the smoothness (continuity) of the underlying function. When imaging a circular vial, discontinuities occur at the edges. Such discontinuities contain high frequencies that are not included in the discrete Fourier reconstruction and hence they appear as spurious intensity oscillations in the reconstructed images. These spurious oscillations are known as the Gibbs ringing artefact [70] and partially explain the slight over- and underestimation of the initial profile points. In addition to this, when a voxel covers both sample and sample-free areas, partial volume effects occur and signal sensitivity is reduced according to the ratio of sample and sample-free volume. Measuring the SNR in centre coil positions was difficult, because the samples, invariable contained in a plastic container with finite wall thickness (typically 1 mm) could only be positioned below the detector coil and hence the resulting distance between sample and coil acted as an artificial spacer between the coil and the first data point acquired along the *y*-axis. As a result, the first data point in the MRI profile may have been influenced by this partial volume effect.

The bench test method described herein was reliable and compared well to the MRI results with fewer sources of error, potentially allowing for the assessment of smaller signal sensitivity differences between coils in the RF laboratory. The bench experiment employed a magnetic dipole generating coil, which was identical for every surface coil that was tested, and thus the coil sensitivity profiles could be directly compared independently of the surface coil mode (i.e. transceive or receive-only). The bench-testing method as

suggested is limited to power-matched coils, but could be extended to preamplifier matched coils by incorporating theoretical considerations suggested by Wang *et al*. [58]. A future comparison of different surface coils is required in order to establish if sensitivity differences measured in bench level and MRI measurements concur. Consequently, the final MRI coil integration tests are still necessary to confirm a correct coil performance. Nevertheless, coil dimensions, geometry and circuit design can now be optimised on the work bench using the measurement technique described here. This technique could prove useful for the development of non-proton MRI coils in particular, since the assessment of such coils using MRI is difficult due to the inherently low SNR in non-proton MR images.

# 4 The Development of a Double-Tuned $^{23}Na/^{1}H$ Transceiver Surface Coil

$^{23}$Na-MRI of small laboratory animals is challenging due to the high spatial resolution requirements (voxel size < 4 µl). Thus, to achieve sufficient spatial resolution within acceptable acquisition time, a careful design of the Radio-Frequency (RF) resonator was necessary. To increase the $^{23}$Na SNR efficiency, the detector geometry was wavelength-optimised to the $^{23}$Na Larmor frequency at 7 T (see Chapter 3). Initially, a double-tuned $^{23}$Na/$^{1}$H transceiver surface coil was considered for $^{23}$Na-MRI, with the desired requirement that it allow for in-bore adjustments such as variable tuning and matching. In this chapter, the design and development of such a double-tuned $^{23}$Na/$^{1}$H transceiver surface coil is described. The coil performance was compared to an optimised commercial transceiver surface coil. A two-fold SNR improvement was achieved, which allowed for the acquisition of $^{23}$Na rat brain MR images with unsurpassed spatio-temporal resolution.

## 4.1 Introduction

A transceiver surface coil for MRI consists of an *LC* resonance loop that serves the dual purpose of transmitting RF power to the sample and receiving the induced signal from the sample. Double-tuning a "transceiver" coil to the $^{23}$Na and $^{1}$H frequencies is difficult, especially when two separate and independently tuneable channels are required. Nevertheless, double-tuning is necessary if one wishes to acquire high resolution anatomical $^{1}$H images to register with the lower resolution $^{23}$Na images without the need to exchange or in any way disturb the coil system during the experiment. Furthermore, such a single structure coil system allows for most of the optimisation and adjustment procedures (shimming, RF pulse power, centre frequency) to be performed using the

higher $^{1}H$ signal. Three main approaches have been described in the literature for double-tuning a MRI resonator:

1. Two geometrically-decoupled resonance coils with different resonance frequencies,
2. Two identically tuned resonance coils with a peak split achieved through geometric coupling, and
3. One single double-tuned coil employing the trap-circuit approach.

The first design idea is based on the design of two single resonance loops. Two geometrically decoupled coils, one resonating at the lower and the other at the higher frequency, can be designed in such a way that each is a single resonance coil yet both are completely decoupled from each other. However, this comes with limitations in possible coil arrangements towards each other and subsequent SNR trade-offs, because the MR sensitive field of views are different. Moreover, for surface coils in particular, this design prevents the arrangement of each coil in its optimum position relative to the source of the MR signal, resulting in decreased SNR performance. As a result, the geometrically decoupled coil approach is predominantly employed for volume coils such as birdcage coils, where orthogonal coil arrangement is relatively simple [53].

The second approach is based on the transformer-coupled design [66], which achieves the double-tuned state through two physically separated, but strongly coupled resonance loops. Both coils are tuned to the same resonance frequency before bringing them close to each other. In this case, blocking circuits and specific distance adjustments are required to achieve the required single resonance performances. Volotkovsky *et al.* built a double ring coil with a single inductive coupling loop [71], which required spacing between loops and thus reduced the available volume within the MR scanner. A capacitively coupled version of this two-surface coil design was developed by Alecci *et al.* [64]. It was demonstrated that the decoupling circuit reduced the available SNR at the $^{23}Na$ frequency by 28 %. The design of such a coupled resonator arrangement is limited due to the additionally needed electronic decoupling circuits such as trap circuits to block the unwanted second resonance frequency in each loop.

The third approach is the trap circuit design, which achieves double-tuning via the insertion of a second resonance circuit (the trap circuit) into the original resonance loop. The trap circuit consists of a parallel *LC* combination composed of a trap circuit inductor, which picks-up no MR-signal and thus only adds to the conductor losses [72]. As a result, the trap circuit coil design suffers from signal losses due to the additionally inserted inductor. Nevertheless, only one resonance structure is necessary for both frequencies,

which may therefore be arranged in an optimum position near the sample under investigation without trading-off sensitivity of one or the other channel due to restricted resonator positioning as it is the case for the double-resonator approaches.

A study carried out by Fitzsimons *et al.* to compare various double-tuned surface coils, found that, transformer-coupled probes (similar to the double-resonator design) perform with similar efficiency compared to trap circuit probes [66]. Therefore, in view of these findings and the additional benefits afforded by the use of one resonance structure, the trap circuit design was chosen for the design of herein presented double-tuned surface coil. Furthermore, the identical coil sensitivity profiles which resulted from tuning a single loop to both frequencies using the trap circuit design may allow for the quantification of the TSC [33]. However, difficulties in designing such a coil arise from the desire to have two separate cable connections, and also from the necessary independent but variable tuning as well as matching circuits. Consequently, a sophisticated design had to be developed to decouple the low frequency ($^{23}$Na) components from the high frequency ($^{1}$H) components in such a way that the tuning and matching of one frequency left that of the other frequency unchanged. Balancing the steady ground connection of the two-port double-tuned resonator was also a major problem. All these issues were resolved during a research visit to the coil development department at Bruker BioSpin GmbH, Ettlingen, Germany, where an existing circuit design of a two-port double-tuned surface coil was studied. The Bruker $^{1}$H/$^{23}$Na transceiver surface coil design comprised a planar detector shape. This commercial coil served as a reference for SNR-performance comparisons of the $^{23}$Na resonator systems described in this thesis.

As elucidated in Chapter 3, the SNR at the $^{23}$Na frequency can be increased by employing two windings with an appropriate distance between each other, and by anatomically shaping the surface coil detector element. Thus the two-winding detector element design was incorporated into the surface coil design in an attempt to improve the overall $^{23}$Na SNR capabilities of the resonator. The principle of this double-tuned circuit, and how it was adapted to the optimised two-winding surface coil detector element, is described in the following sections.

## 4.2 Resonator Design and Development

The electronic circuit was designed in such a way that the surface coil resonated at 79.4 and 300 MHz, the respective $^{23}$Na and $^{1}$H resonance frequencies at 7 T. Furthermore, two coaxial cables were connected to this resonator in order to transmit the induced

MR-signal from the surface coil to the preamplifier of the MRI system. The physical location of the connection of these cables to the resonator was chosen carefully in order to prevent leakage currents of one frequency going through the coaxial cable of the other frequency.

The electronic design principle of the double-tuned resonator is illustrated in Figure 4.1 described with its basic RF circuit components, which comprised the detector inductance ($L_{Det}$), the trap circuit inductance ($L_{Tr}$), the trap circuit capacitance ($C_{Tr}$), the $^{23}$Na-resonance frequency-determining capacitor ($C_{Na}$), and the $^{1}$H-resonance frequency-determining capacitor ($C_H$). The chosen double-tuning design is somewhat more complex than the trap-circuit method described in Section 2.5.4. This higher level of complexity introduced by the parallel capacitor $C_H$ was necessary to achieve a balanced ground connection and two frequency-dependent live connection paths on the resonance circuit.

To understand the double-tuning capability of this circuit, one must find the frequency-dependent current paths determined by the capacitive and inductive impedances 'seen' at 79.4 and 300 MHz, respectively. For instance at 300 MHz, the impedance of the $^{23}$Na capacitor ($C_{Na}$ = 20.4 pF) is low at 26 Ω compared to that of $C_{Tr}$ (4.7 pF) at 113 Ω and $L_{Tr}$ (40 nH) at 75 Ω. The $^{23}$Na-resonance frequency determining capacitor $C_{Na}$ thus acts as a short-cut at the higher $^{1}$H-resonance frequency. Therefore, the electronic circuit at 300 MHz can be simplified as shown in Figure 4.2. From the simplified circuit diagram, one can determine the resonance condition at 300 MHz following Equation 2.6:

$$\omega_0 = \frac{1}{2\pi\sqrt{\left(L_{Det} \parallel L_{Tr}\right)\cdot\left(C_H \parallel C_{Tr}\right)}} \qquad \text{(Equation 4.1).}$$

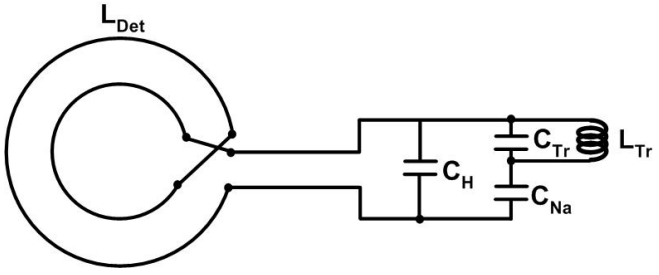


**Figure 4.1: The principle electronic circuit of the double-tuned resonator.**

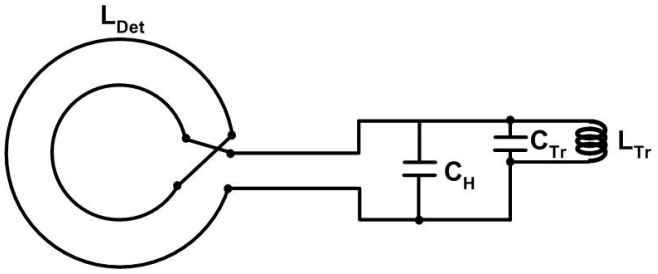


**Figure 4.2: The principle electronic circuit 'seen' by the $^{1}$H resonance frequency.**

At the $^{23}$Na resonance frequency of 79.4 MHz, the impedance of $C_H$ ( 5 pF) and $C_{Tr}$ ( 4.7 pF) are high at 428 Ω compared to 20 Ω for the trap circuit inductor $L_{Tr}$ (~ 40 nH). Consequently, the $C_H$ and $C_{Tr}$ remain 'unseen' by the low $^{23}$Na-resonance frequency. Therefore, the electronic circuit at 79.4 MHz simplifies as shown in Figure 4.3. Thus the resonance condition at this frequency can be noted as:

$$\omega_0 = \frac{1}{2\pi\sqrt{(L_{Det} + L_{Tr})\cdot(C_{Na})}} \qquad \text{(Equation 4.2).}$$

Bearing these design principles in mind, the surface coil was practically developed as described in the next few paragraphs.

The developed surface coil was optimised to image a volume measuring 20 x 20 x 20 mm$^3$ below the coil surface, for which the optimum shaped-surface coil dimensions at 79.4 MHz were derived in Chapter 3. The detector part of the coil was manufactured using copper wire (1.5 mm diameter) wound to two windings of 20 mm and 30 mm inner diameter (i.d.) and shaped over a semi- cylindrical fibreglass tube (42 mm i.d.). The coil was tuned to approximately 180 MHz by a 4.7 pF capacitance; the 180 MHz was chosen as it is the approximate mean value of the two target frequencies. To facilitate a balanced ground connection, the 4.7 pF capacitance was split effectively into two 10 pF (CHB series, TEMEX, France) series capacitance values ($C_{H1}$ and $C_{H2}$).

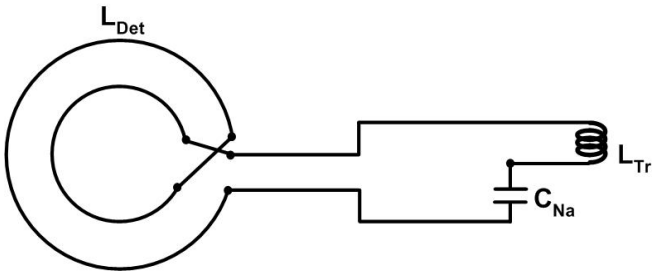


**Figure 4.3: The principle electronic circuit 'seen' by the $^{23}$Na resonance frequency.**

The inductance of the detector loop was measured to be 166 nH. Parallel to the series capacitors, a second capacitor ($C_{Na}$) and a trap circuit composed of the trap inductance ($L_{Tr}$) and capacitance ($C_{Tr}$) were inserted and the conductor path was extended to the circuit board. The trap circuit inductor was composed of a 60 mm long, 1 mm diameter copper-beryllium wire, wound on 6 mm diameter drill bit (1.5 windings, resulting in an inductance of approximately 40 nH). The value of the inductor used in the commercial coil design served as a rough guide. The trap circuit capacitor was chosen in such a way that 300 MHz was achieved in conjunction with the capacitors $C_{H1}$ and $C_{H2}$. The final trap circuit capacitance was determined to be 4.7 pF ($C_{Tr}$) and resulted in a trap circuit resonance of 360 MHz. One resonance peak thus resulted at approximately 300 MHz due to the total coil capacitance of 10 pF ($C_H$ of 5 pF in parallel to $C_{Tr}$ of 4.7 pF) and the total coil inductance of 32 nH ($L_{Det}$ of 166 nH in parallel to $L_{Tr}$ of 40 nH). The lower resonance frequency of approximately 79 MHz was achieved via the series detector and trap circuit inductance and the $^{23}$Na frequency determining capacitance. The resulting structure with approximately 206 nH inductance and 20 pF capacitance resonated at 80 MHz, because the capacitors $C_{H1}$ and $C_{H2}$ had only minor influence on the lower resonance frequency due to their low capacitive value (~ 5 pF) and subsequent high impedance at 79.4 MHz. The $C_{Na}$ capacitor was also split into capacitors $C_{Na1}$ and $C_{Na2}$. They were placed symmetrically with respect to the originally inserted tuning capacitors $C_{H1}$ and $C_{H2}$ for reasons explained in the next paragraph.

The importance of symmetry was to generate ‘cold joints’ on the circuit board side: joints at which the measurable potential variation was zero when an *emf* was induced in the coil. One such cold joint exists for every tuned *LC* parallel resonator at half of the inductor length. The cold joint can be empirically found by tapping along the inductor with a metal screw driver and simultaneously observing the $s_{11}$-reflection measurement on the network analyser screen. The resonance curve will remain unchanged if the resonator is tapped at a cold joint and a decrease in frequency will be observed in case of touching a “hot” spot. To generate additional cold joints, the principle of split capacitors was employed, as it has been discussed in Chapter 2. The connection of ground to a cold joint is beneficial since it guarantees optimised resonator stability with regards to matching and tuning.

The cold joints can be located at frequency-dependent physical positions on the resonance circuit. This fact was exploited when connecting the RF signal cables to the double-tuned resonator. By attaching the low frequency output cable to a high frequency cold joint, a drain of high frequency signal through that additional conductor path could be minimised. This splitting of the cold joints is sketched in Figure 4.4 (a) and (b). The $^{23}$Na

capacitors $C_{Na1}$ and $C_{Na2}$ possess low impedance (26 Ω) at the higher frequency. Thus, at high frequency these capacitors behave like a short cut and therefore do not change the higher frequency's cold joint position, which was located at half the trap circuit's inductance – i.e. in between the trap circuit capacitor's electrodes ($C_{Tr}$).

Care must also be taken of were to mount the trap circuit inductance and low capacitance values. When mounted near the active resonator part, the electric field surrounding the capacitor and the magnetic field in the inductor can interfere with the local magnetic field on the sample, particularly problematic when fed with high power. Therefore, it was necessary to mount those components at a distance of at least one coil diameter distance from the detector element. It is also important to block remaining components of the undesired second frequency in the respective RF coaxial cable path to limit signal losses. The final coil and circuit design is shown in Figure 4.5. A $^{1}H$ trap circuit was inserted in between the $^{23}Na$ terminal point in series with a trimmer capacitor (0.5 to 6 pF, Voltronics, NMQM6GE) for matching purposes and the coaxial cable for transmitting the measured $^{23}Na$ MR signal to the preamplifier.

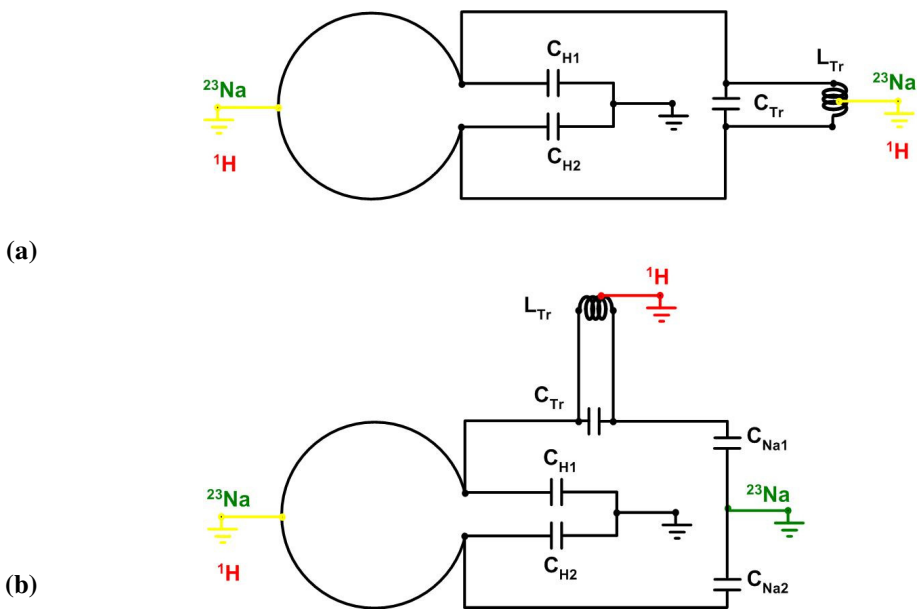


**Figure 4.4: Circuit design of the double-tuned two port surface coil demonstrating the double-tuning and "cold joint" splitting within the circuitry loop. Coloured ground connectors represent the available virtual ground positions for the respective $^{23}Na$ and $^{1}H$ frequencies. (a) Addition of the trap circuit inductance $L_{Trap}$. Virtual ground exists at half the inductor length of the detector element. (b) The trap circuit is moved away from the cold joint and split $^{23}Na$ tuning capacitors are added into the trap circuit path. $C_{Na1}$ and $C_{Na1}$ are effectively short circuits for the $^{1}H$ frequency and therefore the virtual ground for $^{1}H$ and $^{23}Na$ splits.**

The trap circuit was tuned to 300 MHz by a 0.3 to 3.5 pF trimmer capacitor (AT5800, TEMEX, France), a 3.3 pF fixed value capacitor, and a 1.5 winding 0.8 mm diameter copper wire wound on 6 mm drill bit (approximately 40 nH). For $^{23}$Na tuning purposes, a tuning trimmer capacitor (0.5 to 6 pF, Voltronics NMQM6GE) was mounted in parallel to the $C_{Na1}$ and $C_{Na2}$. Tuning of the $^{1}$H frequency was achieved via a custom-designed variable inductor, which worked by inserting a brass tuning rod into the windings of the trap circuit inductance, which could be screwed in and out remotely in order to tune to the 300 MHz resonance frequency. This mechanism was manufactured by the mechanical workshop in the School of Physics, TCD. $^{1}$H matching was achieved through a trimmer capacitor (0.5 to 6 pF, Voltronics, NMQM6GE). Once all coil components were mounted, the optimisation process started.

First the $^{1}$H frequency was tuned by varying the fixed capacitors $C_{H1}$ and $C_{H2}$ (i.e. by alternately swapping in different-valued capacitors) and monitoring the result using a pick-up loop. The RF cables for $^{1}$H and $^{23}$Na were then connected to the respective matching capacitors. In a second step, the inter-channel decoupling was adjusted by inserting the 300 MHz trap circuit into the $^{23}$Na cable connection point path. The $s_{21}$-transmission measurement had to be below -30 dB in order to achieve maximum $^{23}$Na Q-factor through acceptable $^{1}$H/$^{23}$Na inter-channel decoupling. The decoupling at the 79 MHz frequency was then adjusted by varying the $C_{Na1}$-to-$C_{Na2}$-ratio, whereby the condition $C_{Na1} > C_{Na2}$ had to be fulfilled ($C_{Na1}$ = 64 pF and $C_{Na2}$ = 30 pF).

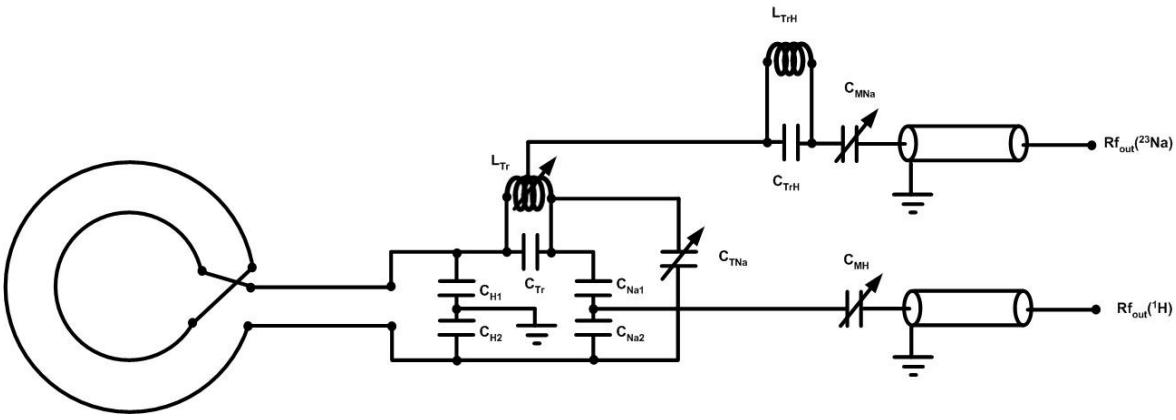


**Figure 4.5: Circuit Design of the double-tuned $^{23}$Na/$^{1}$H transceiver surface coil. $C_{H1}$ = 10 pF, $C_{H2}$ = 10 pF, $C_{Tr}$ = 4.7 pF, $C_{Na1}$ = 64 pF, $C_{Na2}$ = 30 pF, $C_{TrH}$ = 3.3 pF + (0.8 to 3.2 pF), $C_{TNa}$ / $C_{MH}$ / $C_{MNa}$ = 0.5 to 6pF. The trap circuit inductance was made variable for $^{1}$H tuning. Also note the added in $^{1}$H-blocking circuit to the $^{23}$Na matching path.**

This compensation was necessary, because insertion of the trap circuit inductance and connection of the coaxial cables to the resonator lead to a shift of the cold joint for the $^{23}$Na frequency (was no longer located between $C_{Na1}$ and $C_{Na2}$, but rather was below $C_{Na2}$). The ratio was deemed to be adequately adjusted when the dip in the $s_{21}$-transmission curve was measured below -30 dB at 79 MHz. To measure the resonance properties of the final coil design, both RF cables were connected to the network analyser and the $s_{11}$-reflection and transmission curves were acquired (Figure 4.6).

The mechanical stability of the coil is an important factor in the coil design to ensure optimum performance under *in vivo* measurement conditions. Once the resonator is placed on top of the sample and moved into the magnet bore, the resonance properties change due to interactions with the scanner environment (for example with the gradients) and with the sample itself. Therefore, variable tuning and matching capacitors were mechanically stably inbuilt into each channel of the transceiver coil in order to restore the optimum resonance properties at the site of the MRI experiment. Accessing one of the small 6 mm diameter trimmer capacitors from a distance > 1 m was difficult due to a lack of space and light in the magnet. Thus, it was important that those capacitors could be remotely varied from outside the magnet bore. To do this, 30 cm long fibreglass rods were attached to the variable components via custom-made plastic supports that prevented breakage of the brittle glass capacitors (Figure 4.7).

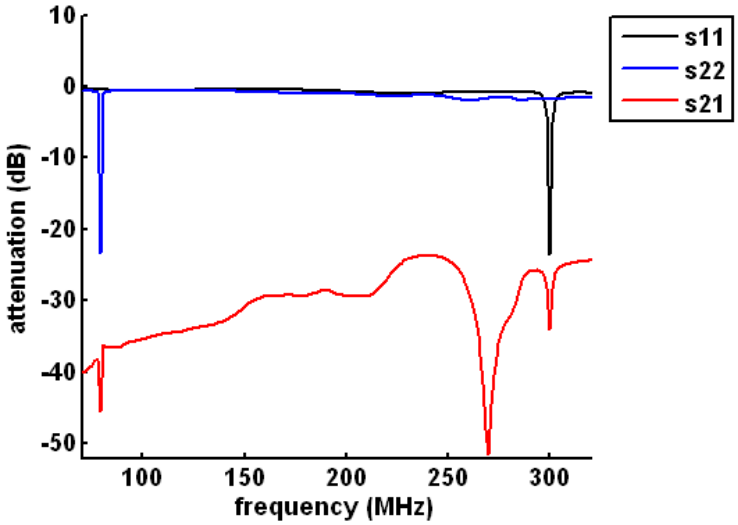


**Figure 4.6: Network analyser measurements for the developed transceiver surface coil for the $^{23}$Na channel connected to port 1 and the $^{1}$H channel connected to port 2 ($s_{11}$- and $s_{22}$-measurements for the $^{1}$H and $^{23}$Na channels respectively). Note the lack of resonance peak at the undesired resonance frequency, which was characterised by a perfect channel isolation of < -30 dB in the $s_{21}$-transmission curve in each case.**

(a)

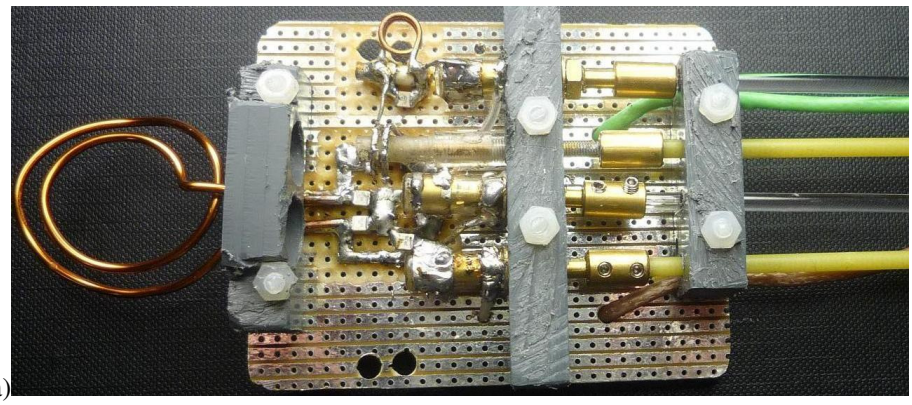

(b)

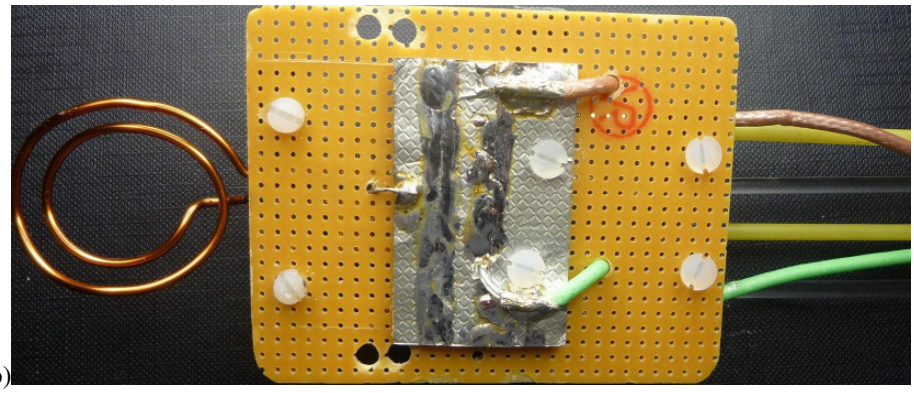

(c)

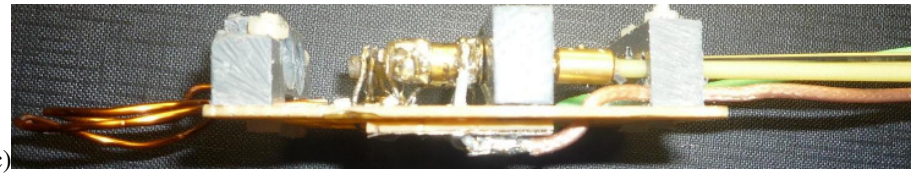

**Figure 4.7: Photographs of the finished $^{23}$Na/$^{1}$H double-tuned transceiver surface coil in different views: (a) top, (b) bottom, and (c) side.**

## 4.3 Coil Characterisation Results

The newly-developed coil was compared to a commercially available Bruker-built $^{23}$Na/$^{1}$H surface transceiver coil for several reasons. Firstly, although a single-resonance surface coil would have performed better from an SNR perspective, the double-tuning was a requirement for the surface coil developed here. Secondly, maximum SNR can be achieved with surface coils compared to volume resonators and also flip angle variations can be assessed easier with transceiver surface coils due to a regionally dependant coil profile. Thus a fair comparison of both the newly-developed and the reference coil system was guaranteed. Thirdly this coil is commercially available for a moderate price and could therefore be used as a general reference in inter MRI centre comparison studies by other research groups. The sensitivity profiles for each coil were also measured using the $s_{21}$-transmission based bench test method (described in Chapter 3), and the results illustrated in Figure 4.8. The $s_{21}$-transmission attenuation was comparatively measured at

12 mm depth and was corrected for the sample losses as described in Chapter 3. The measured coil systems' parameters are tabulated in Table 4.1. It can be seen from both Table 4.1 and Figure 4.6 that the newly-developed coil performs significantly better than the Bruker-built coil, particularly at the $^{23}$Na frequency. The $^{23}$Na sensitivity was 35 % better at the coil centre for the newly-developed transceiver coil compared to the $^{23}$Na channel of the commercial coil, whereas no sensitivity benefits were measured for the $^{1}$H channel at this position. At 12 mm sample depth, the $^{23}$Na sensitivity was 100 % better for the newly-developed transceiver coil compared to the $^{23}$Na channel of the commercial coil. A 20 % sensitivity improvement was also measured for the $^{1}$H channel at this depth. These improvements for both $^{23}$Na and $^{1}$H channels at 12 mm depth compared to the improvement measured at 0 mm depth most likely resulted from the non-planar shaped surface coil geometry of the newly-developed coil.

## 4.4 MR Imaging Experiments

### 4.4.1 Phantom $^{23}$Na MR Imaging

The coils were compared under MRI measurement conditions using a non-physiological 1 M NaCl concentration phantom.

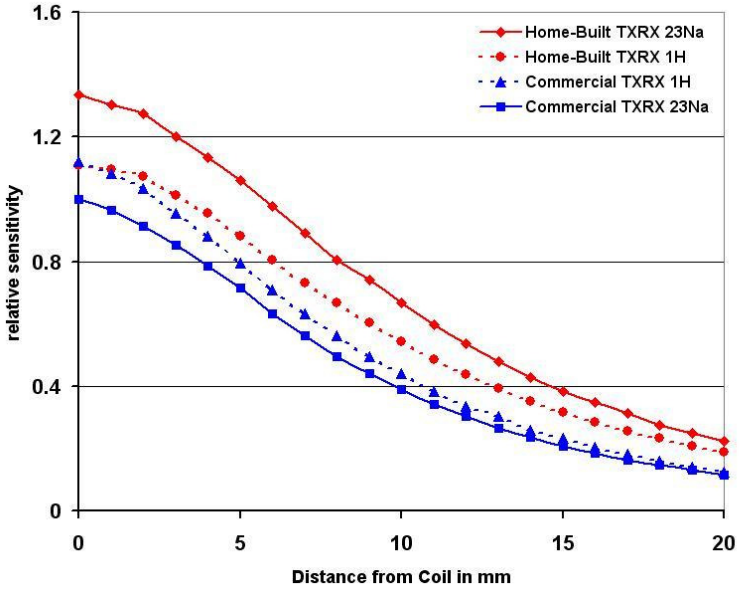


**Figure 4.8: Relative signal sensitivity for the newly-developed transceiver surface coil and a commercial transceiver surface coil as measured on the work bench.**

**Table 4.1: System parameters of the newly-developed double-tuned surface coil and the commercial reference coil.**

| Channel/ Coil | $Q_{unloaded}$ | $Q_{loaded}$ | $P_{Ref}$ Atten. (dB) | Rel. Sens. Loaded s21 @12 mm | Dynamic Range (in MHz) | Decoupling from $^{23}$Na (in dB) | Decoupling from $^{1}$H (in dB) |
|---|---|---|---|---|---|---|---|
| $^{23}$Na/ developed | *140* | *117* | *33* | *0.6* | *76.8..84.6* | *x* | *-35* |
| $^{23}$Na/ reference | *80* | *76* | *27* | *0.3* | *77.8..81.3* | *x* | *-32* |
| $^{1}$H/ developed | *84* | *75* | *x* | *0.5* | *299..303* | *-34* | *x* |
| $^{1}$H/ reference | *78* | *75* | *x* | *0.4* | *296..309* | *-37* | *x* |

In each case, the flip angle was adjusted to 90° at approximately 12 mm sample depth for both coils. As a result, lower flip angles occurred in volumes with larger and smaller than 12 mm sample-coil distance, because inherently less net magnetisation precessed in the *xy*-plane at those distances. Usually, transceiver surface coils are employed in such a way that the 90° flip angle adjustment is set to an area near the surface coil, which in turn causes a coil sensitivity profile dependent flip angle drop-off with distance from the coil surface. Consequently, the magnetisation component contributing to the measurable MRI signal in depth larger than 0 mm is lowered. However, when transceiver coil systems are compared with specific regard to their receive capability at a certain depth, as is the case here, identical transmit conditions must be ensured.

For rat brain MRI, the signal detected at a depth of 12 mm into the head (corresponding to the mid –brain region) should be compared for different coils under the assumption that identical net magnetisation contributes to the measured signal so that differences in the detected SNR arise entirely from losses occurring in the respective coils. Therefore, the 90° flip angle was adjusted to approximately 12 mm sample depth for both transceiver coils. This resulted in an unusual saturation feature in the MR images of the homogeneous phantom at depths < 10 mm, due to a flip angle > 90° in this region, which leads to signal saturation, as demonstrated in Figure 4.9. The transmit sensitivity profile-related flip angle distribution resulted in a 180° flip angle and thus zero precessing net magnetisation component at approximately 5 mm into the sample for the chosen coil configurations. Due to the non-existent MR signal in those regions, a saturation line occurred, which possessed different line shapes depending on the coil geometry, being either convex for the planar or concave for the anatomically-shaped surface coil.

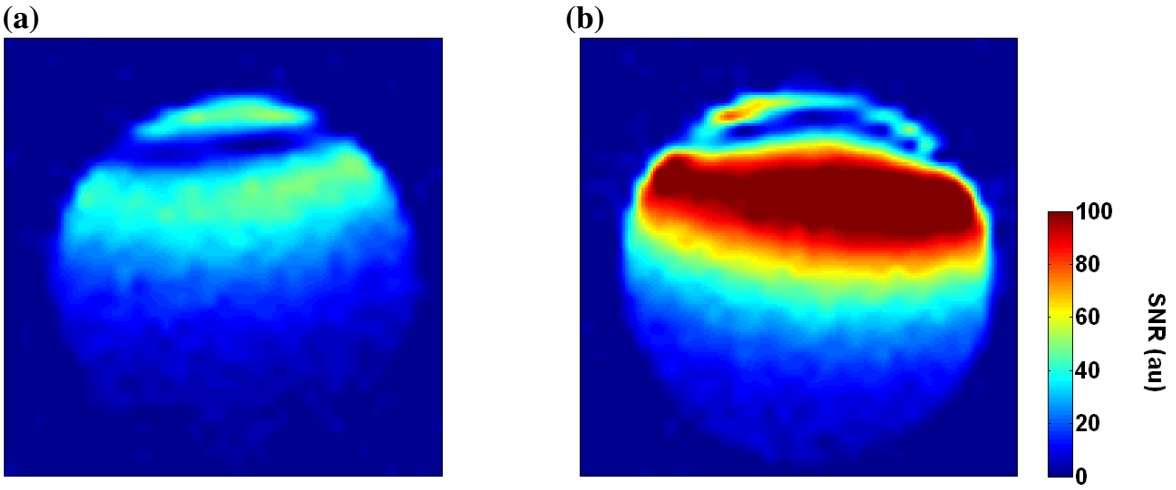


**Figure 4.9: SNR maps computed from $^{23}$Na MR images of a homogeneous phantom (1 M NaCl, 30 mm i.d.) acquired with (a) commercial $^{23}$Na/$^{1}$H surface coil and (b): newly-developed $^{1}$H/$^{23}$Na surface coil. Note the significantly increased SNR and the more homogeneous signal profile, particularly noticeable in deeper sample areas due to the bigger and anatomically-shaped coil surface used. The colourbar indicates arbitrary units (au) of SNR.**

In this study, the sequence parameters used to acquire the images were as follows: 2D FLASH, 5 ms TE, 250 ms TR, 30 % echo position, 10 min TA, 7 kHz BW, 80 x 80 MTX, 80 x 80 mm FOV, 2 mm ST, 13 slices. A doubling of the SNR at 12 mm sample depth was measured in the MR image acquired with the newly-developed transceiver surface coil.

### 4.4.2 *In vivo* $^{1}$H and $^{23}$Na MRI

A 1.5 year old Sprague Dawley rat (400 g) was scanned using the newly-developed $^{1}$H/$^{23}$Na transceiver surface coil. The sequence parameters were chosen to maximise the SNR following a 40 min acquisition time. In general, short echo times are desirable for $^{23}$Na-MRI to minimise signal losses due to the short $T_{2s}^{*}$-decay. Furthermore, short repetition times can be used to image in the steady state due to the short $T_1$ (< 46 ms) of $^{23}$Na nuclei *in vivo*, and hence the detectable MR signal per unit scan time can be maximised. Repetition times in the region of 20 ms are common in SNR optimised $^{23}$Na-MRI using 3D GRE sequences [3, 34, 64]. The relatively long TE of 5 ms used in the current study was selected to allow for the use of a low bandwidth of 5 kHz again to maximise the SNR, which consequently resulted in an increased time before the central k-space point was sampled after the RF pulse, where an asymmetric echo was chosen (20 % partial echo). Choosing a bigger field of view reduced the maximum gradient strength without decreasing SNR per unit scan time. The 3D FLASH sequence parameters that were used were: TE 5.1 ms, TR 22.1 ms, 17 Av, 40 min 10 s TA, 45˚ flip angle at

2 mm sample depth, 125 ms block pulse, 5 kHz BW, 80 x 80 x 20 MTX, 80 x 80 x 80 $mm^3$ FOV. $^{23}Na$ images were acquired with a spatial resolution of 1 x 1 x 4 $mm^3$ (corresponding to a voxel size of 4 μl, compared for example, 8 μl in a similar study [64]). The series of axial $^{23}Na$ images thus acquired are shown with additional zero-filling to 0.5 x 0.5 x 2 $mm^3$ voxel sizes in Figure 4.10. Notice the strong $^{23}Na$ signal from vessels and suppressed $^{23}Na$ signal from tissue with shorter $T_{2s}$ (for example, gray and white matter regions of the brain) and the consequently increased signal loss due to use of relatively long TE of 5 ms. SNRs measured for the transceiver coil were 15 for brain and 45 for ventricular cerebrospinal fluid.

$^{1}H$ images were acquired using a RARE (Rapid Acquisition with Relaxation Enhancement) sequence with RARE factor 8, 234 x 234$\mu m^2$ in-plane resolution and 2 mm slice thickness in 5 min 20 s acquisition time, 33 ms $TE_{eff}$, 2500 ms TR. The axial $^{1}H$-MRI slices are presented in Figure 4.11.

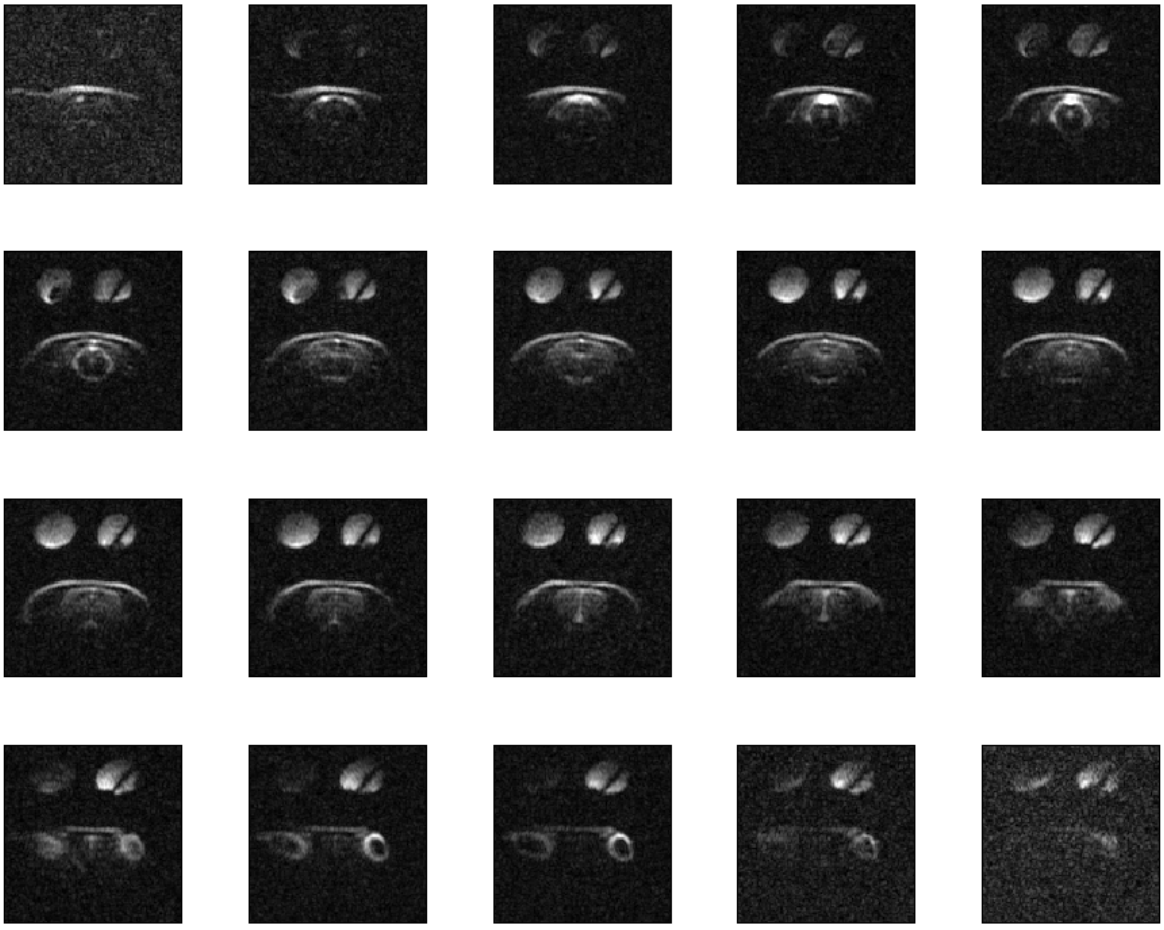

**Figure 4.10: Axial $^{23}Na$ MR images through the rat brain acquired with 3D FLASH sequence in 40 min, with 0.5 x 0.5 $mm^2$ in-plane resolution, and 2 mm slice thickness (after 3D zero-filling by factor 2). Notice the two fiducial vials (8 mm i.d.), which were mounted above the coil for quantification purposes. High $^{23}Na$ signal resulted from the fat layer above the brain which lay in near proximity to the surface detector element.**

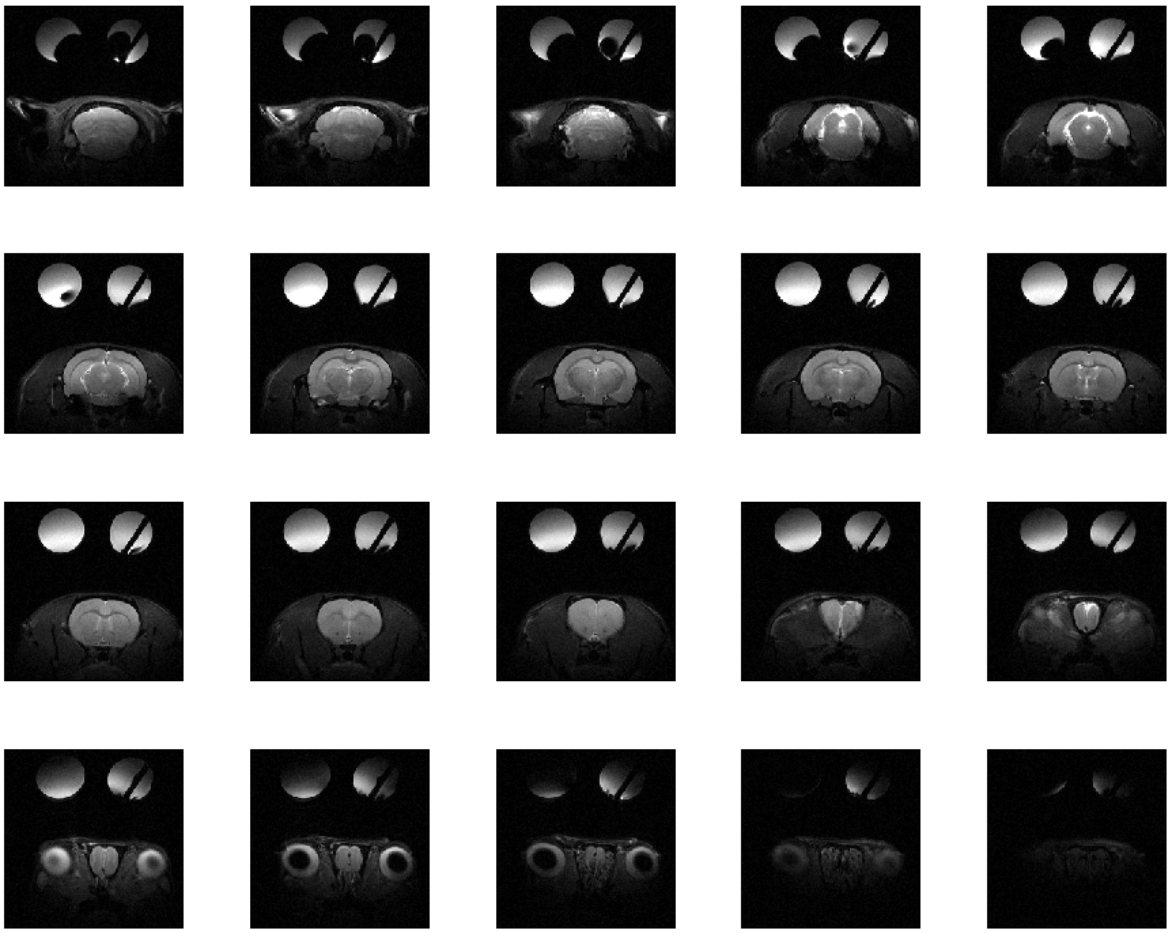

**Figure 4.11: Axial $^{1}$H MR images through the rat brain acquired within 5 min 20 s, with 0.2 x 0.2 mm$^2$ in-plane resolution, and 2 mm slice thickness.**

Notice the homogeneous signal intensities measured across the rat brain, although signal drop-off can be observed with larger coil-sample distances – lower parts of the rat head remained invisible. The chosen coil geometry was thus well suited for rat brain MRI.

## 4.5 Discussion

A transceiver surface coil was developed, which allowed for SNR efficient $^{23}$Na MR image acquisition. The SNR was doubled compared to the commercial transceiver surface coil proving that the RF circuit theory and design methods were applied in a practically correct way. However, as is the case for all transceiver surface coils, the SNR efficiency came at the expense of strong sensitivity profile-related signal variations. A resonator system solving this problem is described in Chapters 5 and 6. The development of the transceiver surface coil was thus a first stage before developing the more complex volume resonator. Trap circuits were practically designed for double tuning and variable tuning and matching was integrated into the detector coil with emphasis placed on resonator stability and balance.

The circuit design principle employed the cold joint method rather than the use of balancing units. The commercial surface coil was constructed using the same circuit design principles; however this coil used a planar shape, with the detector element constructed with 4 mm wide foil and an i.d. of 20 mm. The SNR benefits measured for the newly-developed coil when compared to the commercial transceiver surface coil arose entirely from for the $^{23}$Na frequency-optimised detector geometry, achieved through the use of two windings. The developed detector coil was optimised for the $^{23}$Na frequency, as opposed to the commercial coil detector element, which was optimised to the $^{1}$H channel. Employing a two winding loop of thick copper wire doubled the detector element inductance.

Because an identical trap circuit inductance was maintained on going from one to two windings, the ratio between detector and trap circuit inductance rose with less relative resistive losses occurring in the trap circuit. Consequently, the double tuning of the newly-developed coil had less influence on the resonator losses than it had on the losses in the commercial coil, which had only one detector element winding. At the same time doubling the number of detector windings increased the detected *emf* by approximately 50 %. As a limitation of the small trap circuit inductance, the $^{1}$H tuning range was reduced from 14 to 4 MHz - this was tuned via the variable trap circuit inductor. Nevertheless, a variable tuning range of 4 MHz proved to be dynamically sufficient for the range of possible applications. To increase the range of $^{23}$Na applications to which the developed transceiver surface coil could be potentially employed, variable matching was integrated into the $^{23}$Na channel, resulting in a broader tuning range compared to the commercial coil.

Some studies base the assessment of coil performance on the consumed reference-pulse power [64], that is the power needed to generate a 90° pulse. The power consumption reduces with reduced resonator losses, and could therefore be used as an indicator of a coil's performance. Under certain circumstances, for example with nearly identical surface coil dimensions and flip angle calibration at an identical sample location (e.g. at the surface or at 12 mm sample depth), a comparison of the power levels required by two transceiver coils is possible. The reference pulse attenuation needed in the current study was approximately 6 dB less for the developed surface coil compared to the commercial coil, which translates to approximately four times less power needed to achieve a 90° pulse with the developed coil, which further translates to a two-fold voltage drop. The principle of reciprocity would therefore lead one to expect a two-fold increase in SNR, which was indeed confirmed in the MR images of the phantom. Moreover, the loaded Q-factor was only 35 % better compared to the commercial coil - equivalent to a

35 % relative sensitivity improvement measured at the resonator centre. The sensitivity thus improved with sample depth, which may be attributed to the anatomical shape of the developed surface coil. Consequently, all three measures (pulse power, relative sensitivity, and SNR) compared favourably and combined to deliver a 100 % better SNR performance of the developed coil over the commercial transceiver coil at the $^{23}$Na frequency and at 12 mm sample depth.

The newly-developed coil also demonstrated excellent performance from the point of view of both coil stability and on-site flexibility in its usage (i.e. tuning, matching, inter-channel decoupling). Table 4.2 summarises the current state-of-the-art in rat brain $^{23}$Na imaging, comparing voxel sizes, image acquisition times, field strengths used, and SNR values achieved. In order to compare the ventricular SNR values measured in the current study with those measured elsewhere, the SNR values measured in the ventricles in the brain in these studies were converted to an 'equivalent SNR', correcting for field strength, acquisition time and voxel resolution (i.e. commensurate with all images being acquired at 7 T in 40 minutes with 4 µl voxel resolution, respectively).

**Table 4.2: Comparison of current state-of-the-art rat brain $^{23}$Na-MRI studies.**

| | Bartha *et al. [3]* | Christensen *et al. [33]* | Lin *et al. [34]* | Alecci *et al. [64]* | Augath *et al. [73]* | Jones *et al [5],* Yushmanov *et al. [13]* | This study |
|---|---|---|---|---|---|---|---|
| voxel resolution (µl) | *27* | *15.5* | *0.76* | *8* | *16* | *0.48* | *4* |
| Acquisition Time (min) | *20* | *180* | *85* | *35* | *7* | *5* | *40* |
| $B_0$-field strength (T) | 4 | *1.5* | *4.7* | *4* | *9.4* | *3* | *7* |
| Ventricular SNR (au) | *40±16* | *x* | *2* | *25* | *6* | *x* | *45* |
| Equivalent Ventricular SNR (au) | *15* | *x* | *10* | *21* | *2* | *x* | *45* |
| Comments | | *no SNR derivation possible* | *Derived from time course* | | *Triple Reson. Coil* | *no images/ no SNR derivation possible* | |

The significant improvement achieved in the current study is clear from this comparison. Apart from the current work, the recent work by Alecci *et al*. achieved the best equivalent SNR [64] . This study used a coil with a Q-factor of 64, and a square loop, planar detector element which, taken together may have reduced the achievable SNR in the $^{23}$Na MR images by upwards of 30 % for reasons elucidated in Chapter 3. The doubled SNR measured in the current study compared to the next best reflects the improved coil design, which exhibited a loaded Q-factor in excess of twice that of the next best coil design (117 versus 64 in [64]). Three-fold better equivalent SNR was measured compared to Bartha *et al*., who used a similar dual coil system and identical 3D GRE sequence [3]. Ten-fold better equivalent SNR was achieved compared to a recently published 2009 study [73], where a novel triple $^{1}$H/ $^{23}$Na/ $^{39}$K coil was employed. In this paper, it is likely that the $^{23}$Na channel lacked some degree of SNR efficiency to improve the $^{39}$K SNR efficiency, with the $^{39}$K MR signal being the least NMR sensitive of all three nuclei in living brain tissue. A difficulty in performing a SNR comparison is that many studies in the literature do not present raw data nor do they quote SNR values. For example, Christensen *et al*. acquired images with four times larger voxels at four times less field strength in four times longer acquisition times [33]. The comparison of their SNRs (unspecified) with the SNRs achieved in this study where thus rendered difficult.

Limitations of the newly-developed transceiver coil arise, however, when quantitative measurements are required, because transceiver coils generate an inherently inhomogeneous $B_1$-field corresponding to the coil sensitivity profile. To overcome this problem, adiabatic pulses could be employed with the newly-developed coil described herein, with no restrictions due to the coil's pulse power efficiency. Another possibility to quantify TSC is to use the $^{1}$H sensitivity profile to compensate the $^{23}$Na coil sensitivity, as has been demonstrated by others [33]. However, this method may prove inapplicable to investigate stroke models *in vivo*, since the $T_2$-weighted $^{1}$H MR signal in infarcted stroke tissue changes with no correlation to the $^{23}$Na signal changes.

In conclusion, a significant improvement in SNR values was measured for the newly-developed coil, relative to the current state-of-the-art rat brain imaging studies. Thus, this newly-developed coil could prove useful to acquire high SNR $^{23}$Na brain images *in vivo* with high resolution and within reasonable acquisition times. Additionally, the high SNR efficiency of the $^{1}$H channel could be used to measure diffusion, as well as $T_1$- or $T_2$-weighted $^{23}$Na MR images *in vivo*. The progress of tumour tissue treatment, the evolution of ischaemic stroke tissue as well as the study of Alzheimer's disease tissue could thus be studied non-invasively over time based upon a relative, but nevertheless

localised $^{23}$Na concentration measurement. However, since quantification accuracy was deemed of paramount importance for the stroke imaging experiments described in Chapters 7 and 8, it was decided to develop a dual-resonator system involving a volume resonator for RF transmission and a receive-only surface coil for signal detection. This work is described in the following chapters.

# 5 The Development of a Double-Tuned $^{23}$Na/$^{1}$H Birdcage Resonator

The design, construction and characterisation of a double-tuned birdcage resonator for $^{23}$Na and $^{1}$H MRI is described in this chapter. A $B_1$-homogeneity of less than 5 % was achieved for both $^{23}$Na and $^{1}$H channel across the rat head. The newly-developed resonator allows for channel-independent balanced tuning and matching on site within the MRI scanner. Furthermore, active decoupling enabling its use as a $^{23}$Na transmit-only resonator was incorporated into the coil design, making it a versatile tool for qNa-MRI of small laboratory animals.

## 5.1 Introduction

During the transmit phase of a quantitative MRI experiment, identical flip angle distribution resulting from a homogeneous excitation of the entire Volume of Interest (VoI) is desirable. The flip angle is directly proportional to the transmitted $B_1$-field strength, which is generated by the current flowing in the resonator. Surface coils, as opposed to volume resonators, suffer from magnetic field strength drop-off with increasing sample distances from the coil. The use of adiabatic RF pulses can achieve an approximation of a homogeneous $B_1$-field distribution to overcome this problem with surface coils. However, a major drawback of such RF pulses is the longer excitation pulse length required and the higher RF-power delivered to the sample, which are of concern considering the desire to use short TE pulse sequences for qNa-MRI, and considering the Specific Absorption Rate (SAR) issues at the high $B_0$-field strength used in the current study. Therefore, the most practical solution for qNa-MRI was to develop a coil, which produced an inherently homogeneous $B_1$-field across the sample volume. Solenoid coils fulfil this requirement with maximum efficiency. However, the $B_1$-field of a solenoid coil

is oriented in parallel to the coil's axis, and hence when placed in the bore of a magnet, access in and out of the coil is severely limited since the $B_1$-field (and hence the coil's axis) must be orientated perpendicular to the $B_0$-field. Indeed, for practical purposes, a suitable coil design must allow easy and open access to its interior, which invariably necessitates that its $B_1$-field be perpendicular to its symmetry axis. A coil which fulfils this practical criteria is the birdcage resonator, originally suggested by Hayes *et al*. in 1985 [74].

A birdcage resonator is a volume resonator, which is composed of two end rings joined by an even number ($N$) of rungs (Figure 5.1), where a single saddle element is formed by two rungs and two end-ring segments. The coil structure resonates at a frequency determined by the saddle capacitances $C$ and inductances $L$. The RF signal is coupled into and out of the system via a matching capacitor, which matches the coil impedance to the 50 Ω cable impedance similar to the principle described in Chapter 2 (2.5.2 Matching). The birdcage structure must be tuned on-resonance by additional variable tune capacitors. Tuning and matching capability is necessary to compensate for various sample load influences on the coil's resonance parameters. When the coil is correctly tuned, the currents flowing along adjacent straight conductors produce an approximation to a sinusoidal current magnitude distribution around the surface of the cylinder. This generates a highly uniform transverse magnetic RF field (the $B_1$-field) across the sample volume inside the birdcage coil.

The $B_1$-homogeneity is directly linked to the flip angle distribution across the sample and is thus required to be homogeneous for qNa-MRI in order to achieve adequate quantification accuracy. To summarise, the design targets for the birdcage resonator were:

1. double-tuned for $^{23}$Na and $^{1}$H,
2. optimised for $^{23}$Na $B_1$-homogeneity,
3. independent $^{1}$H and $^{23}$Na channels (achieved via orthogonal geometric decoupling through an orthogonal $B_1$-field arrangement),

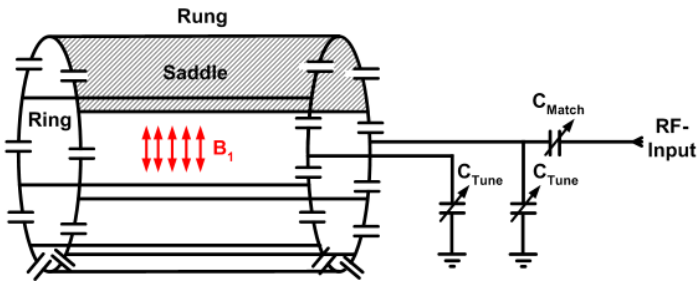


**Figure 5.1: A single-tuned high-pass birdcage coil composed of two end rings and eight rungs, where two rungs and two end-ring segments form one saddle. The direction of the homogeneous alternating $B_1$-field is indicated by red parallel arrows in the sample region.**

4. capability to vary the tuning in a balanced way, thereby maintaining the symmetry of the birdcage structure and consequently the $B_1$-homogeneity for the widest range of loading conditions,
5. capability to vary the matching on both channels, and
6. active decoupling in the $^{23}$Na channel in excess of -30 dB, to prevent SNR losses for cases of an imperfect geometrically decoupled receive-only surface coil.

## 5.2 Resonator Design and Development

The design of birdcage resonators to ensure efficient and homogeneous $B_1$-field generation, while also ensuring high detection SNR and stable operation, is further complicated by a desire to double-tune the device to allow for imaging at frequencies which may be far apart from each other. A number of approaches have been used to design double-tuned birdcage coils. These included:

1. A single birdcage structure with interleaved legs for each of the two frequencies, where interleaved legs where designed in such a way that only the one or the other frequency could pass through them,
2. two single tuned birdcage structures with different diameters, which can be merged in order to achieve images of the same sample (merged two-birdcages design), and
3. A single birdcage structure with common legs and trap circuits in each saddle for double-tuning purposes.

The interleaved design was chosen by Matson *et al*. to develop a birdcage for phosphorus and hydrogen MRI [75]. However, the $^{1}$H frequency blocking circuit inserted in the respective interleaved phosphorus legs may have decreased the birdcage efficiency. Moreover, the residual current flow in the interleaved legs of the 'unseen' resonator path may have contributed to further signal losses. In a more recent publication, the merged birdcage design was used to build a $^{129}$X/$^{1}$H volume resonator [76]. However, difficulties

in inter-channel decoupling were still encountered with this design, although they were minimised by orthogonally arranging the two coils via a rotational shift of 90°. Shen *et al*. employed the trap circuit design to develop a double-tuned $^{23}$Na/$^{1}$H birdcage coil composed of a single resonance structure [53]. The difficulty of decoupling the $^{1}$H from the $^{23}$Na channel was mentioned for this birdcage design strategy, which was only partly achieved via inductive coupling, the use of narrow band balancing units, and by open-circuiting the particular channel not being used during coil operation.

The design goal in the current work was to develop a double-tuned birdcage resonator for use at 7 T exhibiting high $B_1$-homogeneity at the $^{23}$Na frequency, with the ability to actively decouple the $^{23}$Na resonance from a $^{23}$Na receive-only surface coil, and to maintain as high $^{1}$H sensitivity as possible. The resonance frequencies at 7 T are between 2.3 and 4.7 times higher than at 3 and 1.5 T, the frequencies for which Shen *et al*. designed their double-tuned low-pass birdcage coils [77], which imposes additional considerations. For instance, the value of the tuning capacitors required for a low-pass 300 MHz resonator with the dimensions required for rat imaging are < 2 pF, a very low capacitance which renders it difficult to fine tune every saddle to the identical resonance frequency given the available chip capacitor range from 0.5 pF to 180 pF and the inherent errors in accuracy of even the highest specification chip capacitors which are commercially available, which is particularly acute for the lower end of the capacitance range (typically ± 5%, equivalent to 2 ± 0.1 pF). Therefore, the high-pass birdcage design was selected for developing the double-tuned $^{23}$Na/$^{1}$H birdcage coil at 7 T, because the need for such low capacitance values is not so extreme for high-pass birdcage designs. The double-frequency mode was achieved by inserting additional trap circuits into each saddle, as shown in Figure 5.2 and the inter-channel decoupling was achieved by driving both channels at an end-ring position, which corresponded to a cold joint for the other frequency (similar as explained in previous Chapter 4). Two tuning and one matching trimmer capacitor were incorporated into the coil design for each channel, where the tuning trimmers were mechanically linked for balanced tuning and matching purposes.

### 5.2.1 Geometric Resonator Design

When deciding upon the dimensions of the birdcage resonator, the sample Volume of Interest (VoI) identified as the region encompassing the rat brain (approximately 12 ×15 × 20mm$^3$ for an average adult weighing 300 g), was used. Considering sample movements and variable sample positioning in height, the dimensions of the VoI within the birdcage was defined as a 30 mm diameter spherical region centred in the volume resonator.

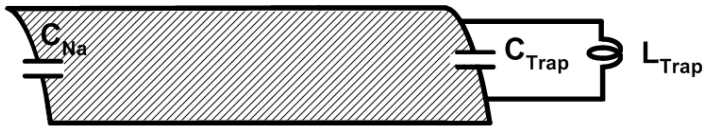


**Figure 5.2: The Trap Circuit as used in each saddle of the double-tuned birdcage resonator.**

The outer coil diameter was chosen to be 112 mm, in order to fit into the BGA-12 gradient coil set, which has an inner diameter of 120 mm. The inner diameter was chosen to be 72 mm in order to accommodate the rat cradle and maximise the variable sample volume, while also leaving enough space for the resonator components inside the RF shielding (108 mm i.d.). To achieve the maximum sensitivity and homogeneity, a resonator length to diameter ratio of 0.7 was chosen as recommended elsewhere [78]. Thus, the selected 75 mm coil diameter translated to a 105 mm birdcage length.

### 5.2.2 Resonator Component Value Calculation

For simple birdcage designs, the capacitor values can be calculated using the freely available BirdcageBuilder Software developed and provided by Chin *et al.* [79]. Although this simplified approach does not cater for the use of trap circuits used for dual-tuned coils, it can be employed to approximately determine the necessary tune capacitance for a given birdcage structure and resonance frequency. This single tune capacitor value can serve for a further computation of the trap circuit components needed to double-tune the resonance circuit. An eigenvalue-based approach to computationally predict the resonance frequency for a chosen set of coil capacitor, trap inductor and trap capacitor values was suggested and verified by Shen *et al.* [77]. However, the capacitances and inductance cannot be computed directly using this approach, because it only allows for an empirical determination of the circuit components by computing the achieved double-resonance frequencies for a given set of component values. The approach was furthermore restricted to low-pass birdcage resonator designs. For the high-pass design in the current work, a different approach had to be developed to find the starting component values for the birdcage structure.

From the derived resonator dimensions, the single resonance coil capacitor value was computed for a 10.5 cm leg length, 0.6 cm leg width, 1 cm end-ring width, 3.7 cm coil radius, and 5.6 cm RF shield radius using the BirdcageBuilder Software. For a high pass single resonance birdcage resonator, the capacitance values were computed to be

$C_{79.4}$ = 210 pF and $C_{300.3}$ = 15 pF for the frequencies of 79.4 and 300.3 MHz for $^{23}$Na and $^{1}$H respectively. For the final coil design, only one capacitor was used per saddle, whereas typical high-pass designs employed one capacitor in both end-ring segments. Consequently, the estimated capacitance value had to be divided by a factor of two, resulting in the pre-estimated capacitances of $C_{79.4}$ = 105 pF and $C_{300.3}$ = 7.5 pF for the $^{23}$Na and $^{1}$H frequencies, respectively.

To predict the trap circuit component values, one must recall the trap circuit idea from Section 2.5.4.1 (Double-tuning). The idea of the trap circuit was to lower the tune capacitance by the inclusion of a series trap circuit capacitor, which is only 'seen' by the higher frequency currents. For the lower frequency, this series capacitor is bridged by the trap circuit inductor, which is arranged in series with the detector inductance and hence increases the coil inductance. Together with the coil capacitance and the coil inductance, the lower resonance frequency is achieved.

From the required single resonance capacitances, the trap circuit components could be calculated by the following procedure. Firstly, the trap circuit capacitance was computed as:

$$C_t = \frac{C_{Na} \cdot C_H}{(C_{Na} - C_H)} \qquad \text{(Equation 5.1).}$$

from which the trap circuit capacitance was estimated to be 8 pF. Secondly, the trap circuit inductance $L_t$ was calculated as suggested by Shen *et al*. [53] by considering the impedance ($Z$) of the trap circuit:

$$Z = \frac{j\omega L_t}{(1 - \omega^2 L_t C_t)} \qquad \text{(Equation 5.2).}$$

With respect to the boundary conditions at the lower frequency (79.4MHz), one requires:

$$L_t < \frac{1}{\omega_{LF}^2 C_t} \qquad \text{(Equation 5.3),}$$

and at the higher frequency (300.3MHz):

$$L_t > \frac{1}{\omega_{HF}^2 C_t} \qquad \text{(Equation 5.4),}$$

Using these considerations, the trap circuit inductance range was calculated to be 35 nH < $L_t$ < 500 nH for the double-tuned 79.4/ 300 MHz 12-leg birdcage coil. Using Equations 2.41 and 2.42 for a straight and solenoid wire inductance respectively, it was found that 1.5 windings of 1 mm thick copper-beryllium wire wound on a 0.6 mm drill bit with straight legs of length 5 mm achieved an inductance of 40 nH. It was desirable to keep the trap inductance as small as possible to reduce cross-talk between the eight

integrated trap circuits. It was then necessary to re-compute the low frequency capacitance $C_{Na}$ again, by integrating the additional trap circuit inductance measures into the birdcage dimensions and computing the single resonance capacitors using the BirdcageBuilder software. The revised coil capacitance was pre-estimated to be 70 pF. The trap circuit capacitance was computed to be 8.5 pF. Those values were approximations and had to be empirically fine tuned on the work bench using the network analyser as described in Section 2.5.1. The final chosen capacitors were $C_{trap}$ = 15 pF and $C_{23Na}$ = 62.8 pF. At the $^{1}$H cable connection point, no $^{1}$H tuning was required and the $^{23}$Na tuning was maintained by inserting a 140 pF capacitor. At the $^{23}$Na cable connection point, no $^{23}$Na tuning was required and the $^{1}$H tuning was maintained by inserting a 5.6 pF capacitor. The circuit diagram is shown in Figure 5.3.

### 5.2.3 Resonator Construction

The volume resonator was partly developed during a 6 week research visit at Bruker BioSpin GmbH, Ettlingen in collaboration with Dr. Sven Junge and Martin Tabbert. Some parts were directly purchased from Bruker, with suppliers quoted for other components as listed below.

The conducting rungs were etched from a tin-coated copper substrate (35 µm thick), which was wrapped onto the surface of a 72 mm diameter fibreglass tube. The birdcage was covered with a second fibreglass tube of 112 mm diameter, which had a copper foil on its inner surface, separated into strips interconnected by 1 nF capacitors to shield the birdcage structure from external sources of RF. The RF shield prevented interactions of nearby gradient coils with the resonator, for example by preventing eddy currents from forming, and in this way stabilised the resonance frequency properties of the newly-developed resonator. The substrate holding the birdcage conductor structure was positioned 38 mm from the bottom of the cylinder and wrapped around the cylinder and soldered together at the joining edge. To hold the substrate in place, it was fixed with two cable straps. The various capacitors and inductors were soldered onto the end ring sections. The resonator was inserted into the shield to measure the resonance frequency with a pick-up coil (with 30 mm i.d.), using the $s_{11}$-reflection measurement as described in Section 2.4.4. It was important to position the pick-up coil centrally with respect to the birdcage structure. Through rotating the resonator around the fixed pick-up coil, the homogeneous $^{23}$Na and $^{1}$H coil modes were determined as the peaks in the $s_{11}$-reflection measurement, which roughly maintained constant attenuation during the resonator rotation.

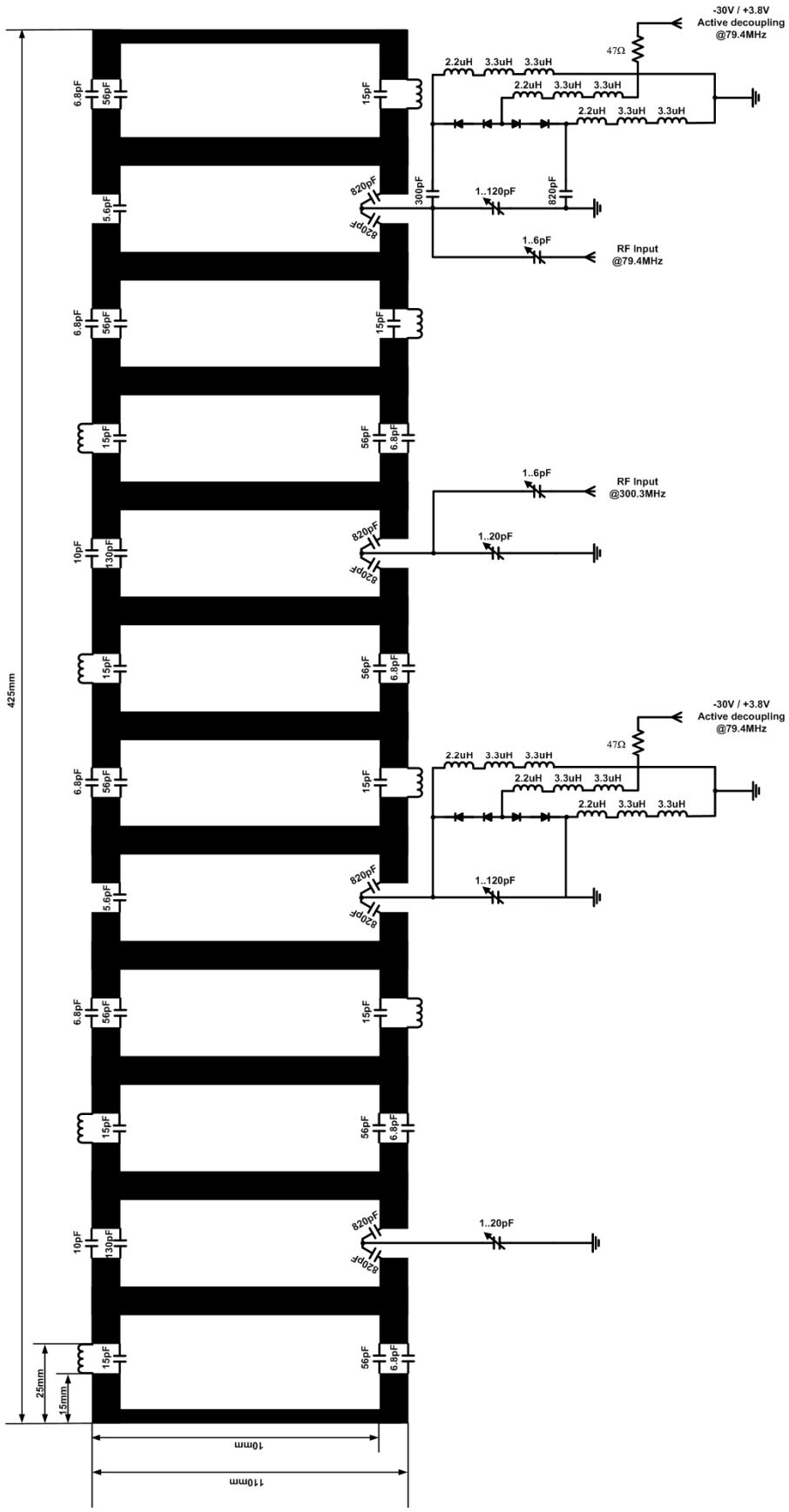


**Figure 5.3: Circuit diagram for double-tuned $^{1}H/^{23}Na$ birdcage resonator.**

To get closer to the desired frequencies of 300.3 and 79.4 MHz, the capacitors were replaced, using Equation 2.27 to approximate the required capacitance values. Since the total coil capacitance, which determines the resonance frequency, is further increased through the introduction of match, tune, and active decoupling circuit capacitances, the target frequencies were set to be 310 MHz and 85 MHz.

Tuning of the trap circuits was complicated by strong interactions between the implemented trap circuit inductors on adjacent saddle elements. Each trap inductor was adjusted separately. To do this, it was first necessary to modify the inductance of all the trap inductors, except the particular one under test, by introducing metal screws into their respective trap circuit inductors. As a result, the trap circuit under test resonated at a different frequency compared to the surrounding trap circuits, and as a consequence cross talk between them was minimised. Using a small pick-up loop (with 6 mm i.d.) the $s_{11}$-reflection measurement was performed via coupling into the tested trap circuit inductor. Initially the resonance frequency for every trap circuit was determined by this procedure, which averaged 257.0 ± 1.1 MHz. Each trap circuit was then tuned by physically skewing and stretching its inductor's windings or repositioning it further or closer to the corresponding trap circuit capacitance. Every inductance was modified in this way, until all trap circuits resonated within ± 0.25 MHz of the mean resonance frequency value.

To enable tuning to the resonance frequency when loaded by various loads and placed inside the magnet, two tuning trimmer capacitors were integrated into the resonator circuit, as shown for one trimmer capacitor in Figure 5.4. These trimmers were inserted into saddles located at 180° from each other, and connected between the saddles and the RF shield.

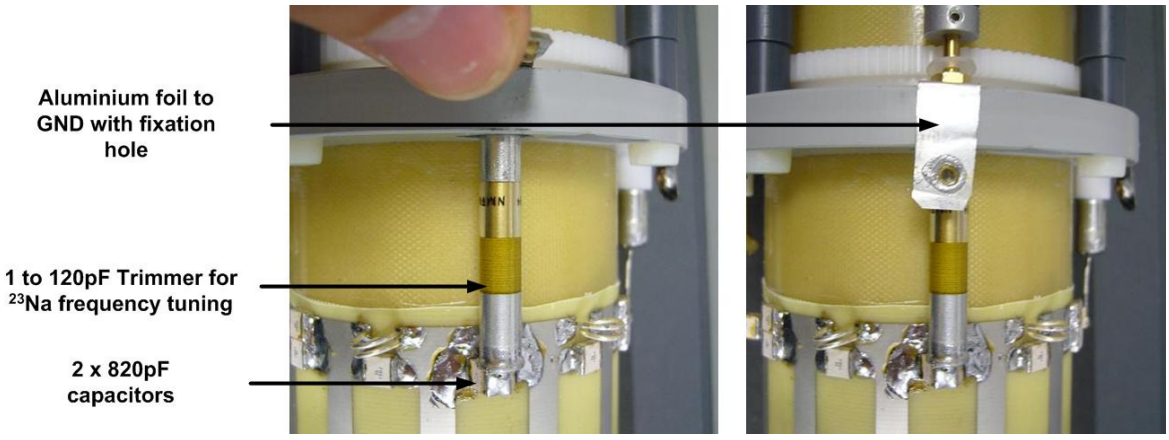


**Figure 5.4: Trimmer capacitor used for tuning to the $^{23}$Na frequency at a saddle conducting zero $^{1}$H potential at this $^{23}$Na RF cable connection point. Note the aluminium foil to connect ground to the RF-shield.**

In order to sufficiently decouple the $^{1}H$, from the $^{23}Na$ coaxial cable connection point, their connection points on the resonator were located at positions of zero potential for the other frequency. The maximum potentials occurred at the feeding/ tapping points and on the opposite side of the resonator, while zero-potential points were located at 90° shifted saddle positions on the resonator with respect to the feeding point. Consequently, the $^{1}H$ and $^{23}Na$ RF cable connection points were designed to be at 90° shifted positions on the resonator. Thus the $^{23}Na$ $B_1$-field generated by the coil was oriented orthogonally to the $^{1}H$ $B_1$-field components. This inherent geometric decoupling principle prevented the $^{23}Na$ RF power from being dissipated in the $^{1}H$ channel and vice versa.

The capacitive and inductive components in the respective cable connection points were removed from the saddle segment and replaced by the single tuning capacitor. Therefore, the capacitance had to be re-adjusted to the frequency which 'saw' zero potential at this saddle. Hence, the saddle to which the $^{23}Na$ trimmer was connected was re-tuned to the $^{1}H$ frequency, and saddles which were connected to the $^{1}H$ trimmer were re-tuned to the $^{23}Na$ resonance frequency. To prevent DC short cuts, an important consideration given the requirement to incorporate DC-driven active decoupling circuits, two high value 820 pF capacitors were integrated into the upper saddle segment near the tuning trimmer. To mechanically hold the tuning trimmer capacitor in place, a plastic ring (labelled 'number two' in Figure 5.5) was glued on to the fibreglass cylinder. The positioning of rings three and four are also shown in Figure 5.5, which were also used for physical support.

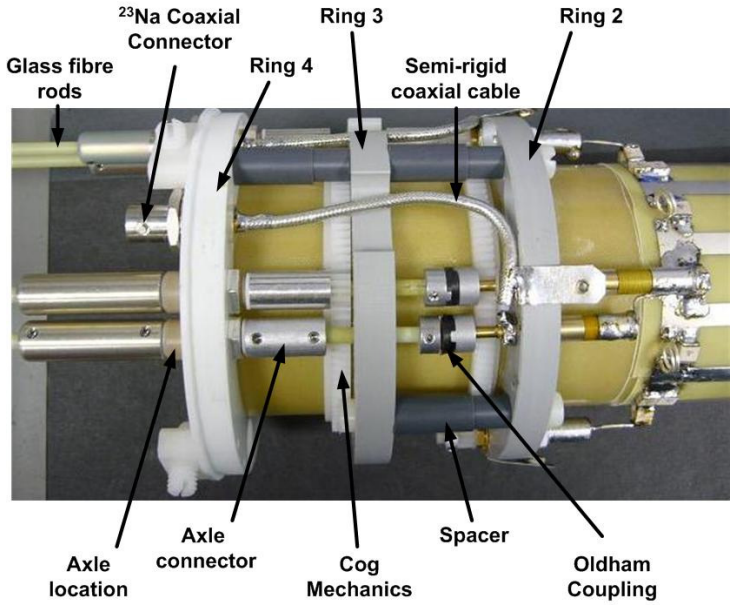


**Figure 5.5: Mechanics of the birdcage resonator.**

It was necessary to leave sufficient space between these rings to accommodate tuning and matching rods and a cog system to interlink the respective tuning trimmer capacitor pairs. To connect the tuning trimmer to the shield, an aluminium strip was prepared with two punched holes, through one of which the trimmer capacitor could be adjusted using the tuning rod, and another small one to which an M3 nut was soldered. The aluminium strip was subsequently fixed to the RF shield using a very short M3 screw inserted from the outside through a hole drilled in the shield. The positioning of the hole in the shielding was determined by the positioning of the nut on the aluminium strip.

Both tuning trimmers were mechanically coupled through a Bruker-designed coupling mechanism comprising a circular cog ring wrapped around the resonator's inner fibreglass former. To latch to this, small cogs were fitted onto the trimmer capacitor shafts in such a way to prevent them from moving from their desired position, and also to avoid twisting the shafts of the brittle glass trimmer capacitors.

Matching capacitors were connected to each tuning trimmer capacitor. Because the matching capacitor and the RF-cable added impedance to the resonance structure, the resonator symmetry had to be restored which was achieved by the symmetric trimmer capacitors connected via the cog system. To restore balance, the trimmer capacitor to which the matching capacitor was connected was decreased in its value accordingly. This adjustment was achieved empirically through a network analyser $s_{11}$-reflection measurement as follows:

1. The resonator was loaded with a phantom simulating the geometry and conductivity of a rat body,
2. The tuning trimmer capacitors were turned to their maximal value.
3. With identical number of turns on each tuning trimmer capacitor, the resonance frequency was adjusted, as measured with a pick-up loop in $s_{11}$-reflection measurement mode (with the resonator loosely positioned within but electrically connected to the shield).
4. The matching capacitor was connected to the RF cable.
5. The RF shield was connected to the resonator,
6. The RF coaxial cable was connected to the network analyser instead of the pick-up loop so that the resonator could be matched to 50 Ω via the trimmer capacitor, as determined from a $s_{11}$-reflection measurement,
7. The resonator was tuned on resonance by varying only one trimmer capacitor - the tuning trimmer capacitor, closest to the matching trimmer,

8. The two tuning trimmer capacitors were connected with the cog system.

As a result, the resonator could be tuned and matched at both the 300.3 and 79.4 MHz resonance frequencies. The inter-channel isolation, as measured by connecting the $^{23}$Na and $^{1}$H coaxial cables to the two network analyser ports and measuring the $s_{21}$-transmission was measured to be less than -30 dB. The transmission and reflection curves measured for a 10 MHz sweep range around the respective resonance frequencies are illustrated in Figure 5.6, demonstrating the isolation achieved on each channel.

### 5.2.4 Active decoupling

The double-tuned $^{23}$Na/$^{1}$H volume resonator was designed to generate an optimally homogeneous $^{23}$Na $B_1$-field while also allowing for the acquisition of $^{1}$H images, which could be accurately co-registered.

To enable the use of a $^{23}$Na receive-only surface coil in conjunction with the birdcage resonator, the latter must be switched off-resonance during the reception period and on-resonance during RF transmission. Although there are possibilities to geometrically decouple coils (for example, by arranging the orientation of the surface coil parallel to the $B_1$-field of the birdcage), the accurate geometric decoupling of similarly tuned resonators is difficult to set-up without the use of a network analyser, and thus is impractical for *in vivo* experiments in the MRI system. Consequently, in addition to geometric decoupling, both coils had to be actively decoupled through the use of an active decoupling circuit in order to suppress surface-birdcage coil cross-talk. The task of the active decoupling circuit did not only comprise the switching of the coil resonance to an arbitrary off-resonance frequency, but rather to convert the low impedance at the resonance frequency into high impedance during the inactive period.

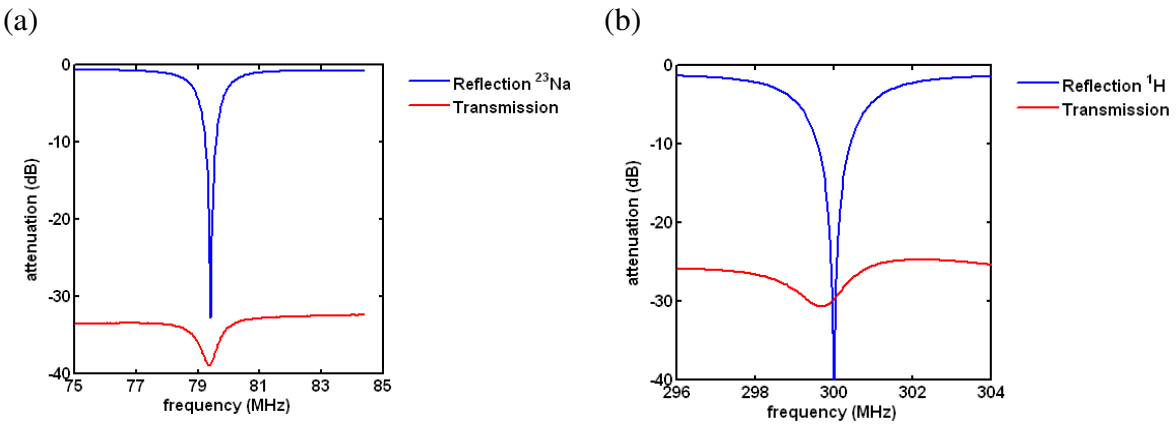


**Figure 5.6: $s_{11}$-/$s_{22}$-reflection measurements and $s_{21}$-transmission measurements for (a) the $^{23}$Na and (b) the $^{1}$H channel of the newly-developed birdcage resonator.**

As already mentioned in Section 2.5.4.2, active decoupling can be achieved through the integration of a PIN-diode switched trap-circuit into the resonance structure, which allows for the RF coil to be switched either on- or off-resonance. The coil was designed to be switched off-resonance, that is, the coil was on-resonance frequency as long as the PIN-diode was reverse-biased, which is the default situation. The challenge imposed on the design of such a circuit, is that the DC circuit supplying the bias control voltage must be incorporated into the RF circuit. The following design rules must be considered when incorporating active decoupling:

1. Separate DC potential from RF ground by high value capacitors (> 0.5 nF),
2. Separate RF potential from DC potential/ ground by RF chokes (> 1 µH),

The decoupling was measured with a 30 mm i.d pick-up loop and the $s_{21}$-transmission measurement using the network analyser (Figure 5.7). The decoupling was then computed as the difference between the attenuation at 79.4 MHz during on- and off-resonance mode, which was measured to be -35 dB for the $^{23}$Na channel. A ground ring was additionally introduced near ring four to equalise the RF and DC ground via 1 nF chip capacitors. A photograph of the final birdcage coil together with the RF shield is presented in Figure 5.8.

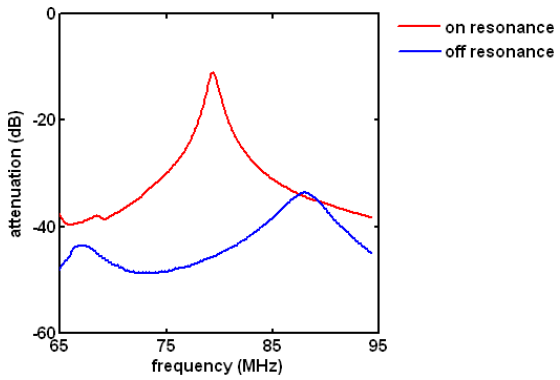


**Figure 5.7: *s21*-transmission measurement for $^{23}$Na channel using a geometrically coupled pick-up loop to test the $^{23}$Na active decoupling performance.**

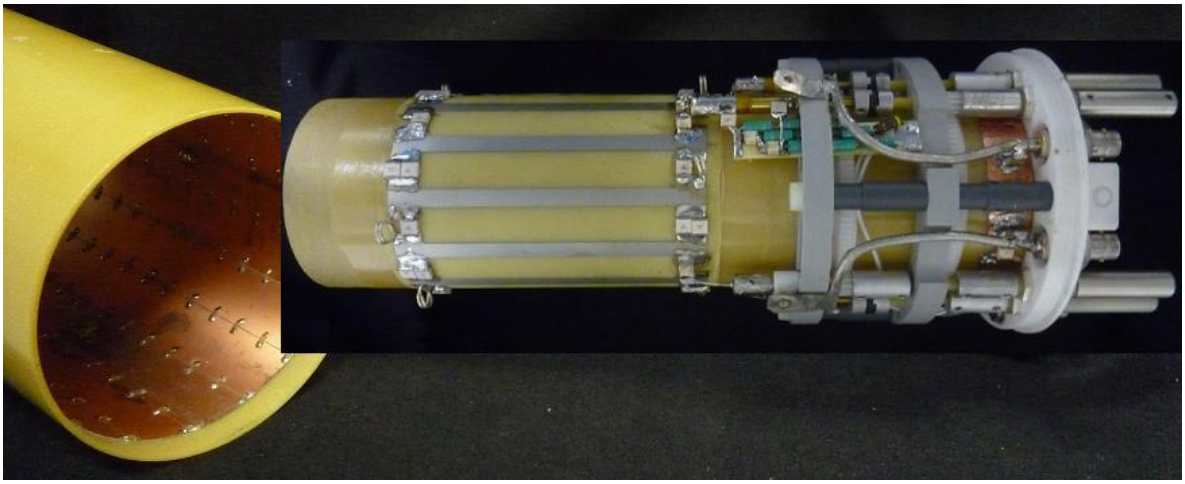

**Figure 5.8: The newly-developed resonator system composed of the RF-shield and the $^{1}H/^{23}Na$ birdcage coil (inset).**

## 5.3 Coil Characterisation Results

Birdcage resonators are generally characterised by their $B_1$-field homogeneity, pulse power consumed to generate a 90° flip angle, and their Q-factor. The birdcage was developed to generate a homogeneous $B_1$-field at the $^{23}Na$ frequency and to allow for $^{1}H$ MR image acquisition for co-registration purposes. In this section, the developed birdcage coil was characterised by its system parameters and generated $B_1$-homogeneity.

### 5.3.1 System Parameters

The system parameters which were used to characterise the performance of the birdcage resonator included Q-factor, channel isolation, active decoupling performance and dynamic tuning range. The results are tabulated in Table 5.1. Note the decreased loaded Q-factor, which demonstrated the strong dielectric interaction between the resonator and the sample load. The necessary RF reference pulse power for the birdcage coil was higher (14 dB) compared to the developed surface coils (27 dB).

**Table 5.1: System parameter of the developed double-tuned $^{23}Na/^{1}H$ birdcage coil.**

| | $Q_{unloaded}$ | $Q_{loaded}$ | $P_{Ref}$ (dB) | Dynamic Range (in MHz) | Decoupling from $^{23}Na$ (in dB) | Decoupling from $^{1}H$ (in dB) | $^{23}Na$ Active Decoupling (in dB) |
|---|---|---|---|---|---|---|---|
| $^{23}Na$ channel | *82* | *64* | *14* | *78.8..79.9* | *x* | *-40.4* | *-34.4* |
| $^{1}H$ channel | *142* | *56* | *15.2* | *294..306* | *-31.1* | *x* | *x* |

### 5.3.2 $B_1$-field Homogeneity

The $B_1$-field was measured using an automated positioning system, where every position within the resonator was tested with a small and weakly coupling pick-up loop, which was specifically designed for this bench test method (see Section 2.6.1.2 'The $B_1$-homogeneity measurement'). The relative $B_1$-field strength was measured for a 2D slice volume in the central coil region (Figure 5.9). The sample-related $B_1$-homogeneity was assessed for a circular RoI with 3 cm diameter covering the central coil region. The resulting $B_1$-field strength varied by ± 3.8 % for the $^{1}$H and ± 4.5 % for the $^{23}$Na channel across the 7 cm$^2$ circular coil region. Across a bigger 5 cm diameter circle, the $B_1$-field strength varied by ± 6.8 % for the $^{1}$H and ± 7.8 % for the $^{23}$Na channel. The latter $B_1$-homogeneity value may be of importance for future applications other than brain imaging (e.g. whole body MRI).

## 5.4 MR Imaging Experiments

The performance of the developed birdcage resonator when integrated into the rest of the Bruker MRI system was tested in both phantom experiments and *in vivo* imaging. Both channels were assessed using phantoms; however *in vivo* MR images were only acquired for the $^{1}$H channel due to the inherently low *in vivo* $^{23}$Na MR signal for such resonators. Besides, the $^{23}$Na channel was designed to be used in conjunction with a receive-only $^{23}$Na surface coil.

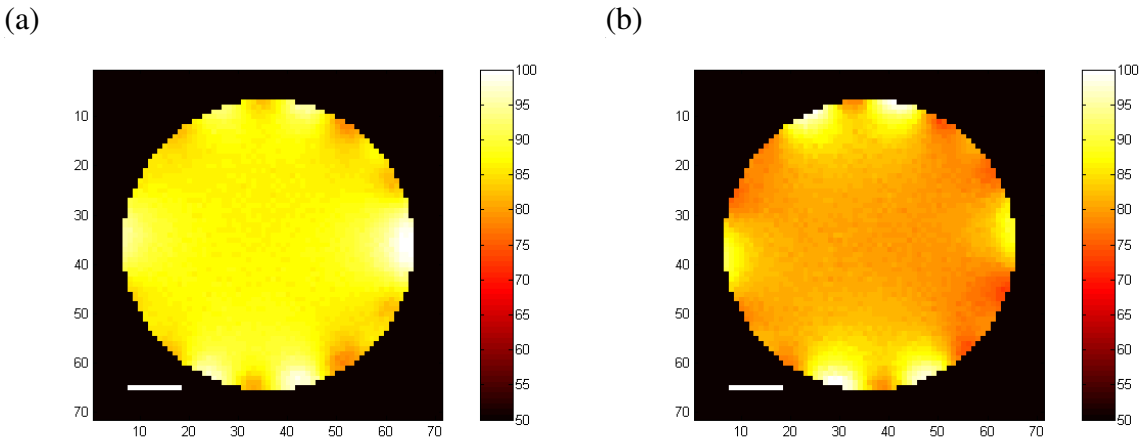


**Figure 5.9: (a) $^{1}$H- and (b) $^{23}$Na-$B_1$-homogeneity for the newly-developed $^{1}$H/$^{23}$Na birdcage coil. The diameter of the measured circular area was 6.5 cm, the white bar represents 1 cm length. $B_1$-homogeneity was measured over a circle of diameter 3 cm located at the centre: $^{1}$H ± 3.8 % $^{23}$Na ± 4.5 %; and over a 5 cm diameter $^{1}$H ± 6.8 % $^{23}$Na ± 7.8 %.**

### 5.4.1 Phantom $^{23}$Na MR Imaging

The $^{23}$Na MR sensitivity was tested on a 1 M NaCl solution phantom and compared to the MR images acquired with the commercial $^{23}$Na/$^{1}$H transceiver surface coil (Figure 5.10). The imaging sequence parameters were as follows: 2D FLASH, TE/ TR = 5 ms/ 250 ms, 30 % echo position,10 min TA, 7 kHz BW, 80 x 80 MTX, 80 x 80 mm$^2$ FOV, 2 mm ST, 13 slices. The SNR achieved with the volume resonator was four times less at 10 mm sample depth compared to that achieved in the transceiver surface coil. Nevertheless, the $B_1$-homogeneity and sensitivity-homogeneity resulted in an ideal homogeneous MR image perfectly corresponding to the homogeneous sample distribution of the saline solution phantom.

### 5.4.2 In Vivo $^{1}$H MR Imaging

The resonator $B_1$-homogeneity was furthermore demonstrated in *in vivo* $^{1}$H MR image experiments (Figure 5.11). The following imaging sequence parameters were used: 2D RARE sequence, TR/ $TE_{eff}$ = 3262 / 64 ms, RARE factor 8, 5 min 13 sec TA, 256 MTX, 50 kHz BW, 80 x 80 mm$^2$ FOV, 2mm slice thickness, 0.3 x 0.3 mm$^2$ in-plane resolution. No signal drop-off was evident across the extent of the rat head, so that the entire rat head was visible in the MR images (the lower part of the rat head remained invisible in the transceiver surface coil MR images).

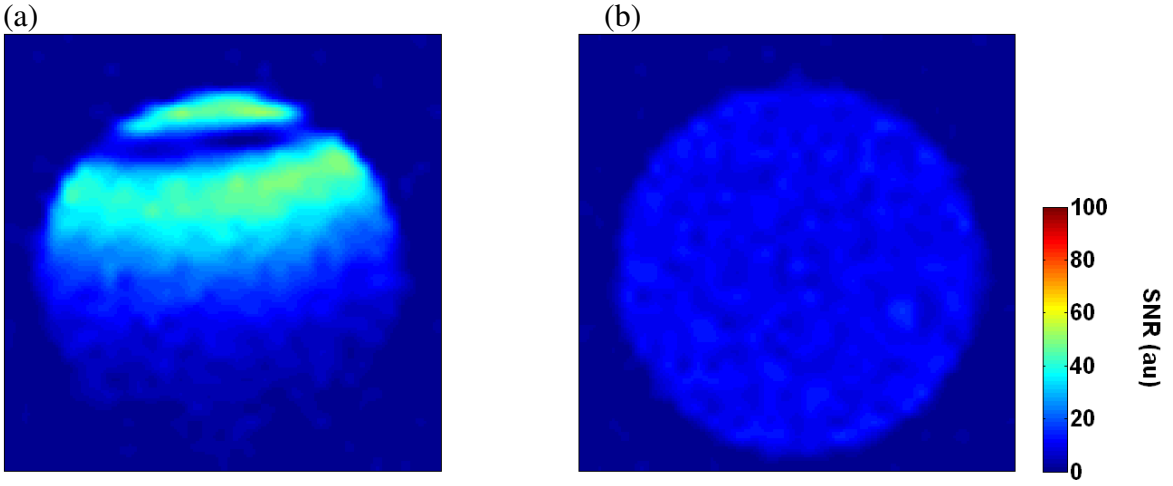


**Figure 5.10: SNR maps computed from $^{23}$Na MR images of a homogeneous phantom (1 M NaCl, 28 mm i.D.) acquired with (a) commercial $^{23}$Na/$^{1}$H surface coil and (b) $^{1}$H/$^{23}$Na birdcage coil. Note the homogeneous birdcage intensity across the sample that comes at the expense of reduced SNR compared to surface coils. The colourbar indicates arbitrary units of SNR.**

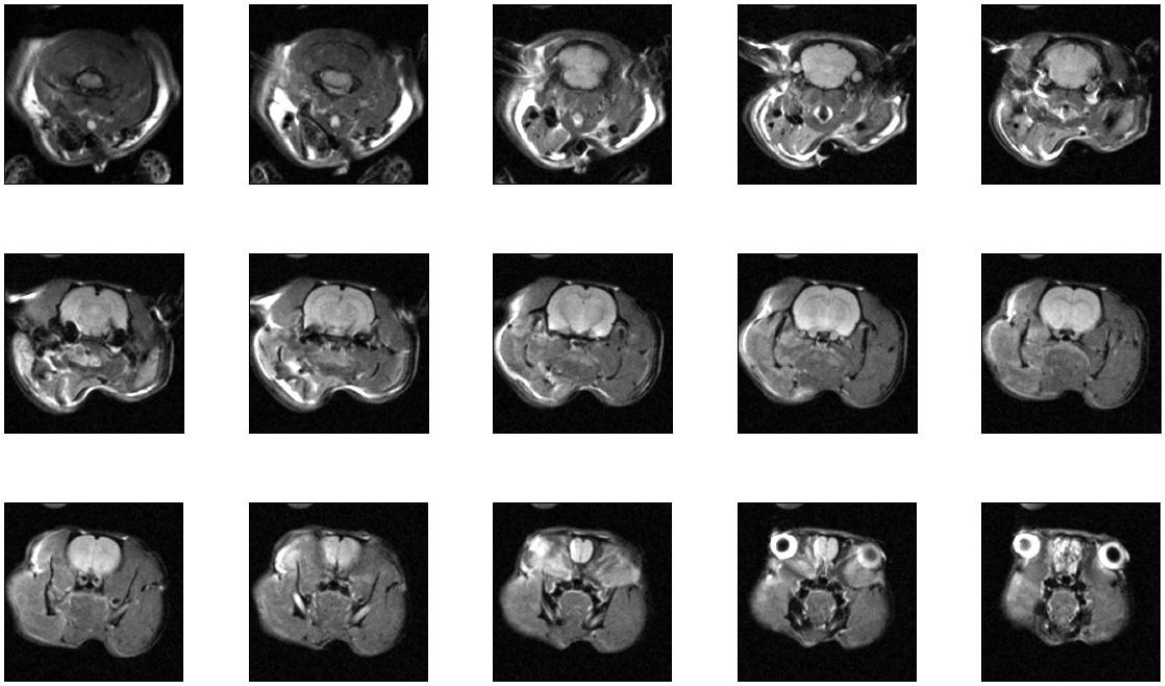

**Figure 5.11: $^{1}$H MR images of the rat head acquired during the first sham surgical operation at Glasgow University ('sham 1' data set). The images were acquired with 0.3 x 0.3 mm$^{2}$ in-plane resolution, 2 mm slice thickness, and 5 min 13 sec acquisition time.**

## 5.5 Discussion

A novel high-pass $^{23}$Na/$^{1}$H birdcage coil structure was developed. Driving the coil in the linear mode and connecting the $^{23}$Na and $^{1}$H RF cables at its quadrature access points allowed for the construction of a birdcage resonator with excellent stability performance. Low pass birdcage resonator designs have been described in the literature, with their inter-channel isolation typically achieved through narrow-band balancing units [53, 77] or simply using a 90° rotational shift between two interleaved birdcages [76]. Badly isolated channels cause signal dissipation through the secondary frequency channel ultimately leading to decreased SNR performance and unstable or unbalanced resonator properties. The inter-channel isolation values were not quoted in these studies. Hudson *et al*. build an interleaved microscopy birdcage coil for $^{1}$H and $^{13}$C MRI at 11.7 T, with a 16 mm coil diameter [80]. The inter-channel-isolation was moderate with values of -23 and -16 dB for 125 and 500 MHz, respectively. The inter-channel isolation measured for the developed birdcage coil was significantly better with -35 and -30 dB measured for the 79.4 and 300.3 MHz channels, respectively. This high degree of inter-channel isolation was further demonstrated by the minor frequency changes of one frequency peak, typically < 50 kHz, which were measured while the other channel was tuned or matched. Furthermore, the

single structure coil design used in the current design allowed for the full use of the available space in an optimum manner, as opposed to interleaved coil designs which necessarily require more space due to the nestling of their inner and outer birdcage structures.

The active decoupling of the current resonator was measured to be less than -35 dB, an improvement on the -30 dB value measured for a birdcage coil developed for mouse imaging at 7 T which, it should be noted, was only single-tuned for $^{1}$H-MRI [81]. In a separate study, Asfour *et al*. did not characterise the active decoupling of their developed coil system [76].

With regard to $B_1$-field homogeneity measurements quoted in the literature, Streif *et al*. reported a 10 % $B_1$-homogeneity for a slightly smaller (35 mm diameter) single resonance $^{1}$H birdcage coil (300 MHz) [81]. Shen *et al*. reported a $B_1$-homogeneity over the head volume of ± 20 % for a double-tuned human birdcage coil [53]. Tomanek *et al*. found a ± 6 % $B_1$-homogeneity over the 3 cm inner range along the *z*-axis for $^{31}$P/$^{1}$H interleaved birdcage design at 7 T and 70 mm (i.d.) [67]. For the birdcage resonator described in the current study, the $^{1}$H $B_1$-homogeneity was found to be slightly better than the $^{23}$Na $B_1$-field homogeneity, which was most likely due to variations caused by the trap circuit inductors. These had less influences on the $^{1}$H current distribution around the resonator than on the $^{23}$Na current distribution, since at the higher $^{1}$H frequency the trap inductors are effectively shorted by the trap circuit capacitors. Overall, the $B_1$-homogeneity that was achieved is a significant improvement on corresponding values quoted in the literature. Furthermore, the single resonance structure design proved to be stable and practical for *in vivo* rat brain $^{23}$Na and $^{1}$H MRI at 7 T.

Identical flip angle distribution across the VoI was necessary for a straight forward and accurate quantification of $^{23}$Na concentration *in vivo*. Since the $B_1$-field strength directly translates to the locally generated flip angle, a homogeneous $B_1$-field distribution was desired. The newly-developed resonator showed excellent $B_1$-homogeneity across the VoI and thus allowed for the quantification of Tissue Sodium Concentration in conjunction with an SNR-optimised receive-only surface coil, as described in Chapters 7 and 8.

# 6 The Development of a $^{23}$Na Receive-Only Surface Coil

The design, development and performance of an SNR-optimised receive-only surface coil for $^{23}$Na rat brain MRI is described in this chapter. This resonator allowed for balanced tuning and matching in situ within the MRI scanner. Active decoupling was integrated into the coil circuit to enable dual resonator operation for quantitative $^{23}$Na MRI (qNa-MRI) at 7 T.

## 6.1 Introduction

A dual coil system for MRI is usually composed of a surface coil and a volume resonator, where the volume coil (e.g. that described in Chapter 5) is used to transmit the RF pulse to the sample location (transmit-only mode) and the surface coil is used to detect the NMR signal from this location (receive-only mode). In this way, the optimum $B_1$-field homogeneity generated by the transmit-only volume coil and the high SNR detected by the receive-only surface coil can be exploited to maximise the overall SNR in the MR images [82]. Dual resonator systems are commonly used in clinical MRI, where the body transmit coil is inbuilt into the gradient set and separate receive-only surface coils are used to detect the MR signal. However, in pre-clinical MRI, the standard scanner system comprises no transmit body coil and thus transmit resonators need to be developed separately for dual coil systems. Furthermore, the small dimensions of resonators dedicated to small laboratory animal MRI cause stronger interactions between each other and therefore require that the receive-only resonator, such as the surface coil developed in this chapter, needs to be electro-magnetically decoupled from the transmit-only coil. Inappropriate resonator decoupling inevitably leads to SNR losses and thus adequate resonator decoupling imposes an extra degree of difficulty on the surface coil's design.

The fact that the coil operates in receive-only mode, on the other hand, allows for a coil design without the need to consider the sample-to-capacitor positioning on the resonator as necessary for transceiver surface coils, because no high power is conducted through the coil, and thus capacitors with low capacitance values may be placed close to the conductive sample volume. This stands in contrast to transceiver surface coils, where the capacitors must be located farther from the sample volume in order to avoid magnetic losses arising from stray electric fields, which occur near low value capacitors.

To develop the receive-only surface coil, the principle design of a single-tuned surface coil which was explained in Section 2.5 was extended by an active decoupling circuit. The advantage of receive-only coils have been described previously as part of single-tuned $^{1}$H [81], $^{23}$Na [82], and double-tuned $^{1}$H/$^{129}$Xe TORO coil systems [76]. The performance of those coils was tested in comparison to a similar size transceiver surface coil using identical RF pulses for the TORO and the TXRX system comparison. The 90˚ flip angle was adjusted to the sample surface for the TXRX coil system in each case, whereas a homogeneous 90˚ flip angle distribution across the entire sample was ensured by the TORO system. Hence, TORO systems exhibited better penetration depth than TXRX surface coils of identical dimensions, because the surface coil sensitivity was affecting the image sensitivity only once during the receive mode, whereas the coil sensitivity affected the image sensitivity twice during the transmit and the receive mode for the TXRX coil. It remained unclear from these papers, however, whether the TORO systems achieve an overall better SNR sensitivity compared to TXRX surface coils of identical dimensions, when both coil sensitivities are compared in areas of identical flip angles. Nevertheless, when homogeneous $B_1$-fields and maximised SNR are required, as in the case of Perfusion Weighted Imaging (PWI) and qNa-MRI, the receive-only surface coil as part of the transmit-only volume resonator increases the detectable SNR considerably, compared to the SNR achieved with a stand-alone birdcage coil [81].

## 6.2 Resonator Design and Development

### 6.2.1 Practical Resonator Design

The electronic circuit design, which has been extensively described in Section 2.5 was used to design the receive-only surface coil. In addition to the common resonance circuit design, an active switchable decoupling circuit was incorporated into the standard coil design. The circuit design is presented in Figure 6.1.

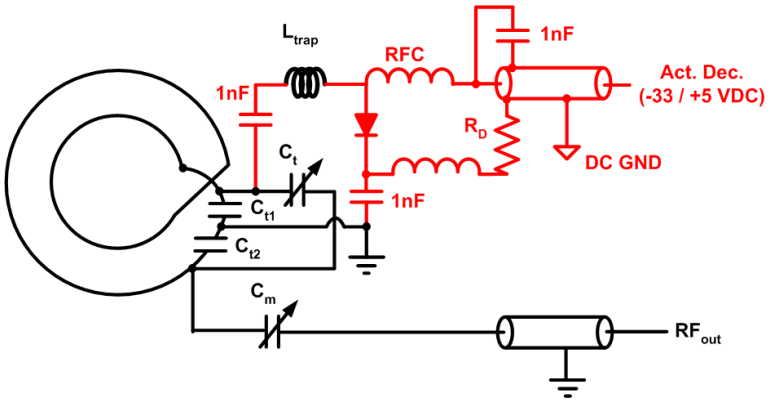


**Figure 6.1: Circuit diagram of the receive-only $^{23}$Na surface coil with the active decoupling circuit indicated in red (RFC is Radio Frequency Choke, $R_D$ is Diode Resistance (50 Ω) , and 1 nF capacitors are DC blocking capacitors).**

The optimum surface coil dimensions were derived from practical experiments of using different surface coil geometries and dimensions, described in Chapter 3. Copper wire (1.5 mm diameter) was wound around a 20 mm and 30 mm diameter vial to form the two winding detector coil element. The detector was then bent over a 42 mm diameter cylindrical fibreglass tube to move the coil sensitivity maximum from its geometric centre along its axis into the investigated sample volume. Care had to be taken to ensure a big enough gap between the two windings to limit the proximity effect with particular care required at the position of the crossing of the two coil terminals, where a generous loop arc was chosen to limit dielectric cross talk between the two wire endings. A decreased Q-factor (< 160) resulted, if the wire spacing was too small. Thus the Q-factor was carefully observed during the design process.

In a first design step of the electronic circuit board, the coil was equipped with two series capacitors $C_{t1}$ and $C_{t2}$ (2 x 56 pF, CHB series, TEMEX, France), which resulted in a resonance frequency of 81 MHz, as measured using the network analyser. Thus, the chosen detector element had an inductance of approximately 140 nH. The resonator was variably tuneable via a trimmer capacitor, $C_t$ (0.5 to 6 pF, NMQM6GE, Voltronics, USA).

The matching and tuning circuit was mounted on a strip board (42 x 120 mm$^2$, AJB16, Farnell) to which the resonance loop was soldered. Non-magnetic coaxial cable with matching BNC connectors (RG316 and 11BNC50-2-13-133NE respectively, Huber and Suhner, Switzerland) were used to transmit the RF signal from the receiver coil to the preamplifier of the Bruker MRI system.

The connection of the matching capacitor required a re-adjustment of the split capacitor values. The cold joint was shifted into $C_{t2}$, the tuning capacitor between the ground and the live RF terminal connection points. Thus, to move the cold joint back to

between the two tuning capacitors, the capacitance value of $C_{t2}$ had to be decreased. The empirical optimisation of the resonance frequency was achieved via the $s_{11}$-measurement and a concomitant capacitor exchange until the target resonance frequency was achieved and the cold joint was found between $C_{t1}$ and $C_{t2}$. The final tuning capacitor values were $C_{t1}$ = 56 pF and $C_{t2}$ = 47 pF. A photograph of the surface coil is presented in Figure 6.2.

### 6.2.2 Active decoupling

To enable the surface coil to be used in conjunction with the birdcage resonator, active decoupling had to be incorporated in the resonance circuit. The trap circuit resonance frequency had to be tuned to 79.4 MHz when designed, as discussed in Section 2.5.4.2. It was decided to connect the trap circuit inductor across $C_{t1}$, which ultimately acted as the trap circuit capacitor in case of a forward-biased PIN-diode. Hence, the required trap circuit inductance was determined to be 72 nH (resulting in the 79.4 MHz resonance frequency). This was achieved by an inductor wound with the number of turns and inductor leg length computed from Equations 2.42 and 2.41. The straight conductor leading to and coming from the inductor element location was 40 mm long with 2 mm conductor width, resulting in approximately 29 nH inductance. The other 43 nH was made up of a single layer solenoid with three windings (5 mm coil diameter, 5 mm wire length). A PIN diode was used as the trap circuit switch (UM9401SM, Microsemi). RG58 cable and matching coaxial connectors (Radionics, Ireland) were used for the DC supply cable connection of the PIN diode.

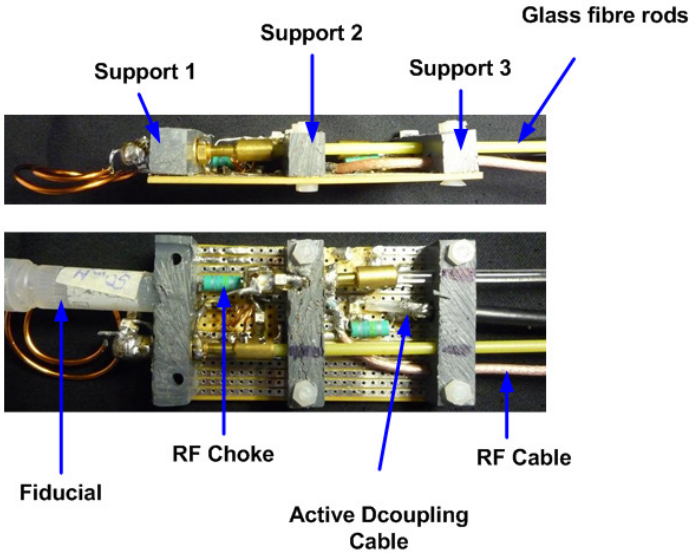


**Figure 6.2: Photograph of the receive-only $^{23}$Na surface coil.**

To block the RF from dissipating in the DC supply cable, 4.7 µH RF Chokes (IM4, Vishay) were introduced to the DC path, which acted as low impedance for the DC current, but high impedance for the RF current. Attention was drawn to avoid RF short cuts that by-passed the RF Chokes (RFCs), and vice versa to avoid DC short cuts by-passing the diode resistance to RF ground. The separation of the DC and RF ground was achieved via two blocking capacitors (1 nF, CHB, TEMEX) inserted into the trap circuit in series with the trap circuit inductor. The remaining RF power at the other end of the RFCs was shortened by another 1 nF capacitor. A 105 pF capacitor was introduced by Streif *et al*. [81] for the same purpose at 300 MHz. However, at the 79.4 MHz, higher 1 nF capacitance value was necessary to exhibit sufficiently low impedance to the RF at the lower frequency used.

The active decoupling was fit to the surface detector element while disconnected to enable perfect tuning of the trap circuit. The trap circuit was tuned using a small pick-up loop (6 mm i.d.), which was coupled into the trap circuit inductor, while the PIN diode was shortcut with a short piece of wire. The trap circuit was tuned by physically stretching and compressing its inductor's windings until the resonance frequency of 79.4 MHz was achieved. The diode shortcut was removed and the detector coil connected to the network analyser. The RF chokes were connected and the trap circuit tested under active switching conditions, using an external signal generator to supply the bias voltage (+ 5 V/ -36 V).

The $s_{21}$-attenuation was measured for the on- and off-resonance coil modes using a 20 mm (i.d.) pick-up loop. The difference in transmission attenuation at the 79.4 MHz resonance frequency was used as a measure of active decoupling. The measured 79.4 MHz current coupled into the pick-up loop was suppressed by -36 dB during the off-resonance coil mode (Figure 6.3). The typical trap circuit decoupling curve was characterised by a splitting of the central peak, resulting in two peaks; one at a lower and the other at a higher frequency. A symmetric peak split in excess of 30 MHz measured using the $s_{11}$-reflection measurement (Figure 6.4) is usually considered a good indicator for a properly designed active decoupling circuit.

Other methods exist to measure the active decoupling performance, which include two geometrically decoupled pick-up loops and an $s_{21}$-transmission measurement. When the resonator is brought close to the two pick-up loops, signal transmission occurs from one pick-up loop via the resonator to the other pick-up loop. During the active decoupling phase, no signal is transmitted through the resonator and thus, the degree of decoupling between the two pick-up loops can be measured.

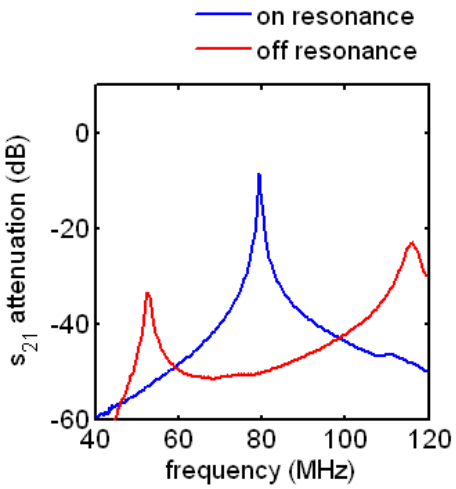


**Figure 6.3: $s_{21}$-transmission measurement for the $^{23}$Na receive-only surface coil connected to port 1 and the 20 mm pick-up loop positioned in parallel to the surface coil surface detector with a distance of 40 mm connected to port 2.**

This method is often used to characterise phased array resonator decoupling [49, 83], but due to the indirect measurement set-up, coupling between the two pick-up loops rather than the coupling between the receive-only surface coil with the transmit-only volume resonator is invariably measured. Consequently, the single pick-up coil method used to measure the resonator decoupling in this study replicated the measurement conditions more realistically. The single pick-up coil method was also applied by Streif *et al.* to characterise their TORO coil system [81], whereas the active decoupling performance has not been measured in the other two coil development studies [76, 82].

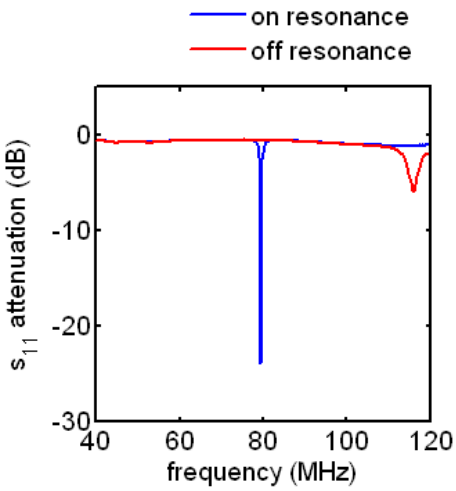


**Figure 6.4: $s_{11}$-reflection measurement acquired by connecting the $^{23}$Na receive-only surface coil BNC connector to the network analyser port 1. The 79.4 MHz resonance peak occurs during the on-resonance coil mode (blue line) and a 30 MHz peak-split occurs during the off-resonance coil mode (red line).**

## 6.3 Coil Characterisation Results

The surface coil was characterised and compared to the transceiver $^{23}Na/^{1}H$ commercial surface coil with respect to the Q-factor, active decoupling performance, and relative signal sensitivity. The results are given in Table 6.1. The loaded Q-factor measured for the developed surface coil was 42 % higher than for the commercial transceiver surface coil. The active decoupling between the receive-only surface coil and the volume resonator was measured for the worst case scenario of complete geometric coupling between the two coils, i.e. the $B_1$-field from the volume resonator oriented orthogonally to the plane of the surface coil. The decoupling was better than -23 dB during the transmit period, when the surface coil was switched off-resonance.

The relative signal sensitivity profiles (Figure 6.5) were measured for the newly-developed and the commercial surface coils using the bench-level measurement technique described in Section 3.2.1, showing an increase in relative signal sensitivity of the order of 45 % compared to the transceiver surface coil at the coils' centre and an approximately 100 % sensitivity increase at a 12 mm sample depth. The latter increase is most likely due to the anatomical shaping of the receive-only coil, compared to the planar geometry of the transceiver coil.

## 6.4 MR Imaging Experiments

### 6.4.1 Phantom $^{23}$Na MR Imaging

The $^{23}$Na MR sensitivity of the receive-only coil was tested on a 1 M NaCl phantom and compared to the MR images acquired with the $^{23}Na/^{1}H$ transceiver surface coil using the same phantom, as previously shown in Figure 5.10.

**Table 6.1: System parameter of the developed double-tuned $^{23}Na/^{1}H$ birdcage coil.**

| | $Q_{unloaded}$ | $Q_{loaded}$ | $Q_{loaded}/Q_{unloaded}$ | Loaded $s_{21}$-sensitivity @12 mm | Pick-up coil decoupling (in dB) | Receive active decoupling (in dB) | Transmit active decoupling (in dB) |
|---|---|---|---|---|---|---|---|
| RO (developed) $^{23}Na/^{1}H$ | *142* | *125* | *1.14* | *0.68* | *-36* | *-25* | *-23* |
| TXRX (commercial) $^{23}$Na-channel | *76* | *72* | *1.06* | *0.35* | *x* | *x* | *X* |

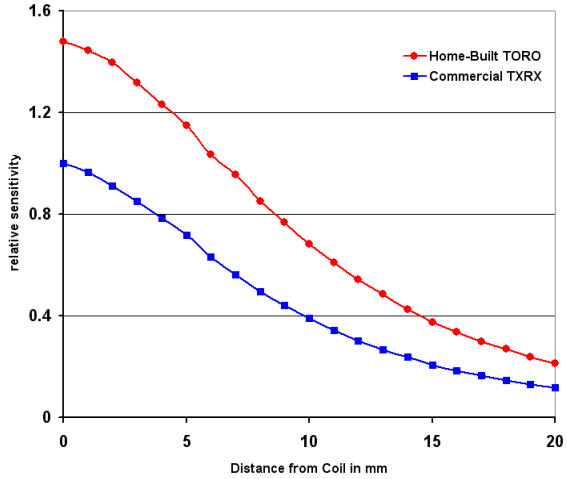


**Figure 6.5: Relative signal sensitivity of the newly-developed receive-only surface coil (red line) as a function of distance from the coil surface compared to the commercial transceiver surface coil sensitivity (blue line).**

The 90° flip angle was adjusted to approximately 12 mm detector-sample depth for the commercial transceiver surface coil. The SNR achieved with the surface coil was nearly identical at this depth compared to the transceiver surface coil SNR (Figure 6.6). Note the smoother receive-only surface coil profile, which was solely dependent on the surface coil sensitivity profile during the receive-mode, whereas a homogeneous flip angle distribution was ensured by the transmit-only birdcage coil.

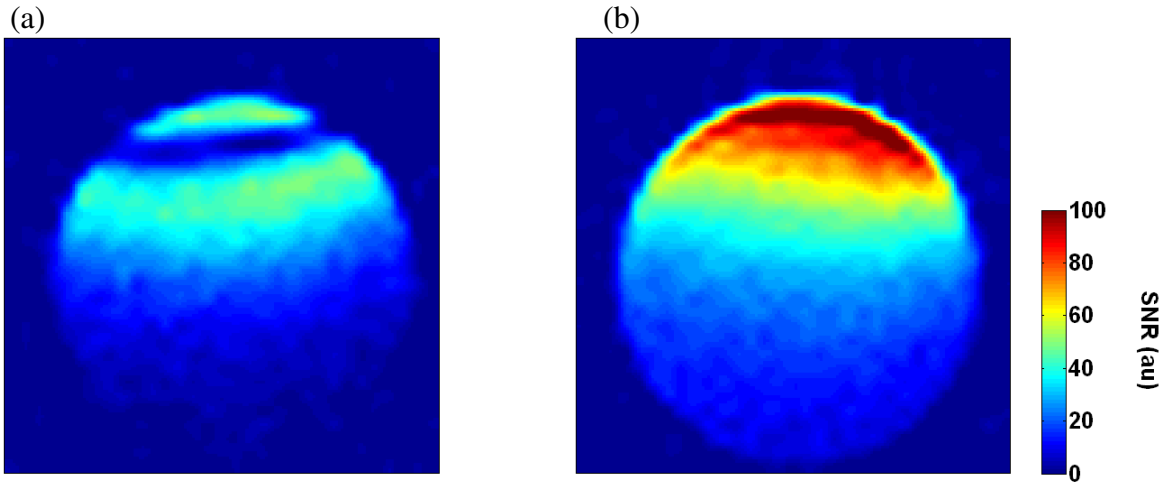


**Figure 6.6: SNR maps computed from $^{23}$Na MR images of a homogeneous phantom (1 M NaCl, 28 mm i.D.) acquired with (a) commercial $^{23}$Na/$^{1}$H transceiver surface coil and (b) developed $^{23}$Na receive-only surface coil. Note the deeper penetration depth and the improved coil profile arising from the homogeneous excitation using the birdcage resonator. The colorbar indicates arbitrary units of SNR.**

However, transceiver coils are rarely used with these adjustments, rather their 90° flip angle would normally be positioned close to or immediately at the surface to avoid such saturation bands at depth in the sample, so the approach of Barberi *et al*. [82] is justified.

Figure 6.7 illustrates the resulting coil profiles measured in a different coil comparison experiment on a 4 M NaCl solution phantom using identical 2D FLASH sequence parameters for the commercial $^{23}$Na/$^{1}$H TXRX surface coil compared to the newly-developed $^{23}$Na receive-only surface coil. However, in this case the TXRX flip angle was adjusted to 90˚ at the sample surface. The SNR differences in deeper sample regions then simply resulted from a decrease in penetration depth for the transceiver surface coil, which was influenced by twice the surface coil-dependent sensitivity profile in the TXRX case compared to the TORO mode. A 3-fold SNR increase at 12 mm sample depth was demonstrated in favour of the newly-developed receive-only coil system.

### 6.4.2 *In vivo* $^{23}$Na MRI

*In vivo* $^{23}$Na MR images were acquired for a 300 g Sprague Dawley rat with the dual resonator system developed here. The chosen imaging parameters were as follows: 160 x 80 x 20 MTX, 5kHz BW, 8 x 8 x 8 cm$^3$ FOV, FA 90, TE/TR = 2.6/ 23.0 ms, block pulse length 0.15 ms, 39 min 12 sec TA, 10 % echo position, 1 x 1 x 4 mm$^3$ voxel (0.5 x 0.5 x 2 mm$^3$ after 3D zero-filling by factor 2). The results are presented in Figure 6.8.

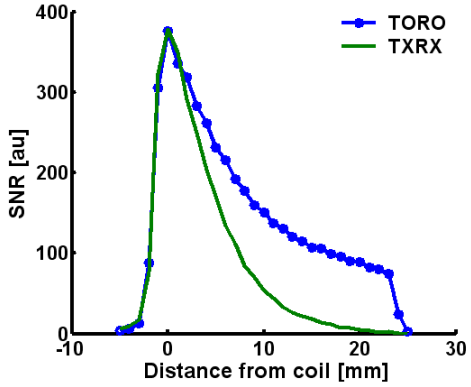


**Figure 6.7: Comparison of the SNR profiles measured in a 4 M NaCl solution phantom using the $^{23}$Na receive-only coil and commercial $^{23}$Na/$^{1}$H transceiver surface coil. The flip angle was adjusted at approximately 90˚ across the entire sample for the transmit-only receive-only (TORO) system and to the sample surface for the transceiver (TXRX) system.**

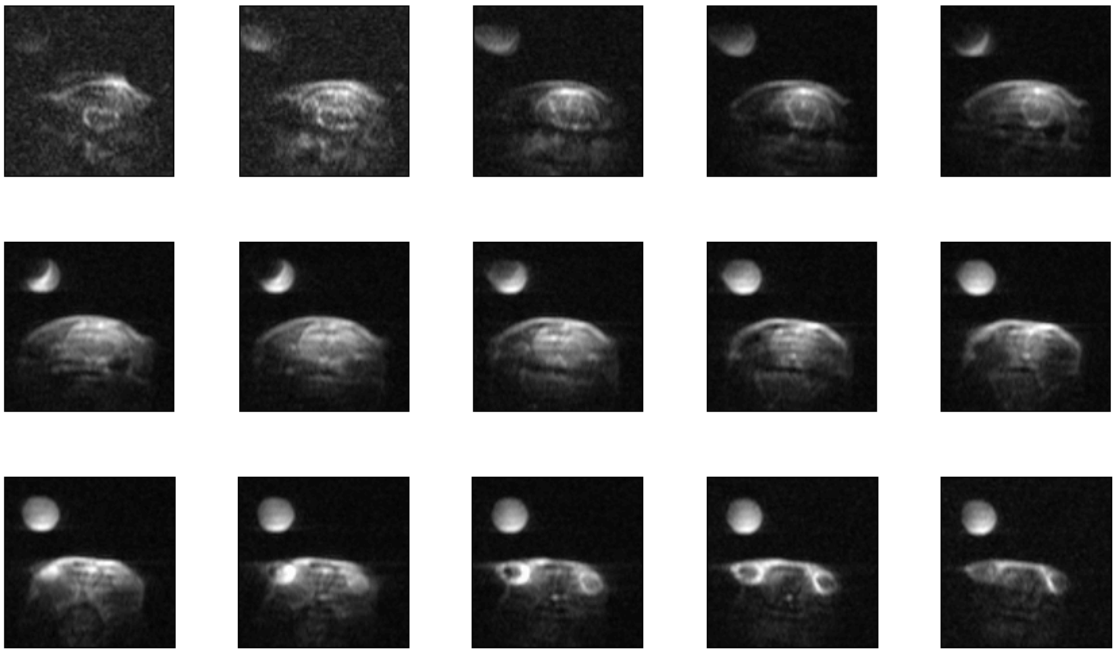

**Figure 6.8: $^{23}$Na MR images of rat brain acquired in ~ 40 min with the newly-developed dual resonator system. The fiducial vial had an inner diameter of 8 mm.**

## 6.5 Discussion

The design of an optimised surface coil detector element was employed to develop a $^{23}$Na receive-only surface coil with advantages regarding the penetration depth and SNR performance for *in vivo* qNa-MRI at 7 T. The quantification accuracy in the qNa-MRI experiment benefits from a homogeneous flip angle distribution generated by the transmit-only volume resonator, because measuring and compensating for flip angle variations generated by transceiver surface coils is difficult and error-prone. However, standard sensitivity profile compensation algorithms exist to correct for the receive-only coil sensitivity, which enable the quantification of TSC with such a dual coil system as explained in the next Chapter.

The relative sensitivity benefits measured using the bench level test could not be confirmed with the MRI test method. Although, from results of the bench-test comparison, the developed receive-only surface coil could have been expected to achieve 100 % more SNR than the commercial $^{1}$H/$^{23}$Na transceiver surface coil, comparing the two coils under MRI conditions with identical flip angles in the analysed RoIs, only a modest SNR increase (< 10 %) was measured for the receive-only coil in the MR images at 12 mm sample depth. As a reason one can assume that the bench-measurement omitted the birdcage-to-surface coil interaction and the quality of the active decoupling circuit, both of which would be expected to degrade the SNR. Due to the close proximity of the birdcage

and surface coil circuits (within 15 mm distance from each other), a further reduction in the overall SNR may also have occurred. A solution to this problem could be to detune every single saddle on the birdcage coil during the off-resonance mode of this coil. Nevertheless, the origins of the surface-to-birdcage coil interactions are difficult to assess in terms of SNR loss using either work bench or MRI measurements.

Results presented by others in peer-reviewed journals gave the impression that the SNR achieved with dual coil systems is higher than for similar sized surface transceiver coils [82]. Streif *et al*. compared their receive-only surface coil to a transceiver surface coil with identical coil dimension while still placed inside the off-resonant transmit volume resonator [81]. Thus identical surface-to-birdcage coil interactions occurred for both the TXRX and the TORO mode, although TXRX surface coils are usually employed in free space without being surrounded by a volume resonator. The dual coil system developed by Barberi *et al*. was also compared to an similar size transceiver surface coil - this time in free space [82]. However, the 90˚ flip angle was applied to the sample surface rather than the RoI and thus the flip angles dropped off with distance from the coil for the TXRX coil, whereas 90˚ flip angles were achieved everywhere in the sample with the TORO system. This resulted in less precessing net magnetisation for RoIs in farther sample-coil distances (in deeper sample regions). However, since transceiver coils are used in this configuration, this is perhaps a justifiable comparison between the two coils and thus decreased the detected SNR.

Although maximum SNR could have been achieved with a single-tuned $^{23}$Na transceiver surface coil, it was legitimate to compare the single-tuned $^{23}$Na receive-only surface coil to the double-tuned $^{23}$Na/$^{1}$H transceiver surface coil, because the target application was to acquire $^{1}$H and $^{23}$Na MR images with the same coil system and with maximum $^{23}$Na SNR. In the case of the dual coil system developed herein, the birdcage resonator fulfilled the double-tuning $^{1}$H and $^{23}$Na resonator function. For comparison purposes with other studies, the newly-developed receive-only surface coil was compared to the commercial TXRX surface coil by adjusting the flip angle to 90˚ at the sample surface. The SNR differences in deeper sample regions was then simply influenced by a decrease in the transmit penetration depth for the TXRX surface coil. The sensitivity profile was influenced by twice the surface coil-dependent sensitivity profile in this case. Thus a three-fold SNR increase at 12 mm sample depth in favour of the developed receive-only coil system was measured, although the effective SNR achieved with the receive-only coil was measured approximately identical, when RoIs which experienced identical flip

angles were compared. SNR losses were expected to be measured for the dual coil system due to the surface-to-birdcage coil interaction. Such losses had been measured by Barberi *et al*. [82] and Streif *et al*. [81], although those SNR differences were not explicitly discussed in their papers.

The active decoupling performance of the receive-only surface coil was -23 dB during the transmit period, when the coil was geometrically coupled to the birdcage coil. Streif *et al*. measured a decoupling of -46 dB for the receive-only surface coil [81]. It is assumed that the coil was geometrically decoupled from the birdcage coil, when this value was measured. A similar degree of decoupling could have been achieved for the developed coil system here, by geometrically decoupling it from the birdcage resonator. However, the active decoupling capability is unnecessary in case of a perfect geometric decoupling. Therefore, the active decoupling was measured to be -23 dB for the worst case scenario in this study, which is the geometrically coupled coil positioning. The active decoupling tested via the pick-up coil method was measured to be -35 dB and compared well with the value measured by Streif *et al*. (-36 dB) [81]. Therefore, it can be concluded that the performance of the developed dual resonator system compared well with dual coil system performances published by others.

The development of a double-tuned $^{23}$Na/$^{1}$H dual resonator system was challenging and it was found that the system design as selected in the work presented herein was limited by the decoupling of the $^{23}$Na receive-only surface coil from the $^{1}$H birdcage resonator channel. This limitation remained unmentioned by Asfour *et al*. who may have encountered similar problems with the double-tuned $^{1}$H/$^{129}$Xe coil system [76]. In the case of a $^{23}$Na surface coil being geometrically decoupled from the $^{23}$Na birdcage channel, the $^{1}$H $B_1$-field generated by the volume resonator would fully penetrate through the surface coil – so that the surface coil would be geometrically coupled with the $^{1}$H birdcage channel (because the $^{23}$Na and $^{1}$H $B_1$-field were orthogonally arranged on the birdcage resonator). As a result, the receiver detector coil would effectively act as a closed conductor structure during transmission of the high power 300 MHz RF pulse. This $B_1$-field would induce sufficiently high current in the surface coil, which in turn would generate a magnetic field around the surface coil. Such a secondary magnetic field would degrade the local $B_1$-homogeneity in close proximity of the surface coil detector element.

Decoupling the surface coil electronically with $^{1}$H trap circuits [64] remained unsuccessful, because the surface-to-birdcage coil positioning was variable and thus no one circuit design would satisfy all possible coil configurations. This was problematic, because the $^{1}$H trap circuit inductor on the surface coil was penetrated by the $B_1$-field in

strong dependency of the surface-to-birdcage coil positioning. Furthermore, the $^{1}H$ trap circuit would degrade the detectable SNR in the $^{23}Na$ channel [64]. Since the image artefacts were negligible for the animal positioning procedure using the $^{1}H$ TriPilot sequence, it was decided to rotate the birdcage coil by 90° for the high resolution $^{1}H$ anatomical scanning performed after the $^{23}Na$ MRI experiments (in such a way that the $^{23}Na$ surface coil was geometrically decoupled from the $^{1}H$ birdcage coil channel).

The MRI system setup, completed with the animal holding cradle and air gases supply tubing hindered the fixation of the surface-to-birdcage coil positioning for the targeted $^{23}Na$ MRI application. Nevertheless, by fixing the surface coil in one location relative to the birdcage coil, the decoupling can be improved to < -35 dB, which should be considered for future coil system developments. This approach was for example used to develop a phased array coil, which was mounted on the shell of the volume coil [84]. Similar principle was employed by Lanz *et al*. to develop a cardiac phased array together with transmit surface coil, where both coils where in fixed positions relative to each other [27].

In conclusion, a dual coil system for qNa-MRI was developed with excellent $B_1$-homogeneity and adequate SNR performance compared to similar coil systems. The stability of the developed coil system was ensured by incorporating variable and balanced tuning and matching facilities both at the two birdcage channels and at the $^{23}Na$ receiver coil. The quality of the dual coil system was demonstrated by the highly spatial- and temporally-resolved *in vivo* $^{23}Na$ imaging of a rat's head. This opens up the possibility to use this coil system to facilitate quantitative measurements of the total, intracellular, and extracellular $^{23}Na$ concentration in a wide range of *in vivo* models of common human diseases such as stroke, tumour, Alzheimer's disease, aging, and paramyotonia.

The dual coil system was used to study the evolution of the TSC in a rat model of cerebral ischaemia, where the ability to quantify the TSC values accurately was of paramount importance. These measurements are described in Chapter 7.

# 7 The Measurement of Tissue Sodium Concentration (TSC) after Stroke

Tissue Sodium Concentration (TSC) increases in ischaemic stroke tissue for several hours after stroke onset [2]. The hypothesis in the current work is that the spatio-temporally resolved measurement of the TSC after stroke could provide a diagnostic parameter upon which still-viable stroke tissue could be distinguished from infarcted tissue non-invasively. However, the low Signal-to-Noise Ratio (SNR) resulting from the low TSC, low gyro-magnetic ratio, small sample volume and relatively fast signal decay in tissue makes $^{23}$Na Magnetic Resonance Imaging ($^{23}$Na-MRI) difficult in the living rat brain. In this chapter, an SNR-optimised resonator system, described in Chapter 5 and 6, was used to quantify the TSC *in vivo* in the rat brain with unsurpassed spatio-temporal resolution. Furthermore, in this chapter the short TE sequence and raw data reconstruction technique used for *in vivo* imaging are described together with a description of the developed quantification method, and the *in vivo* stroke model. The results are discussed in the context of previous studies on similar *in vivo* stroke models.

## 7.1 Introduction

Several $^{23}$Na-MRI approaches have been explored by other groups over recent years; with practical limitations encountered for most (see Section 1.4). Considering the toxicity of shift reagents [38] and the difficulties in applying multiple quantum coherence filters *in vivo* [4, 6], the approach adopted here relies on the direct measurement of the TSC.

Thulborn *et al*. developed a compartment model for a better understanding of the stroke-related TSC changes [18]. The authors divided the tissue volume $V_t$ into three distinct compartments: an intracellular compartment (IC) with volume $V_i$ (~ 85%), an extracellular compartment (EC) with volume $V_e$ (~ 12%), and a vascular compartment with volume $V_v$ (~ 3%), such that:

$$V_t = V_i + V_e + V_v \qquad \text{(Equation 7.1)},$$

with the intracellular $^{23}$Na concentration differing from the extracellular and vascular $^{23}$Na concentrations. Among several other metabolites in our body, the vascular $^{23}$Na concentration is maintained constant at ~ 140 mM by the corticomedullary $^{23}$Na gradient in the kidneys [85]. The major role of the kidneys is to maintain cell homeostasis[1] of body fluids and electrolytes, which is highly dependent on the extracellular $^{23}$Na concentration. The extracellular $^{23}$Na concentration in brain tissue is identical to the vascular $^{23}$Na concentration and is buffered from the space of the entire body with minimal perfusion and the high permeability of $^{23}$Na ions through the vessel walls. Locally, intracellular $^{23}$Na concentration is maintained by the $Na^+/K^+$ pump that establishes negative $^{23}$Na and positive $^{39}$K concentration gradients, directed from the extracellular to the intracellular space. As a result, the intracellular $^{23}$Na concentration is maintained low at ~ 10mM. From the difference in intra- and extracellular $^{23}$Na concentrations in the intra- and extracellular compartments, an overall TSC can be derived – for instance, in rodent brain tissue, a typical value of ~ 45 mM has been reported [33]. Pathological tissue changes may then relate directly to changes in local TSC.

Ischaemic stroke is a catastrophic event after which the arterial blood flow to one part of the brain is pathologically restricted and thus oxygen supply to cells within this part is limited. The limitation in oxygen supply to the cells in turn degrades the energy metabolism of cells within the stroke area leading to a diminished efficiency in the $Na^+/K^+$-pump function. As described earlier, the $Na^+/K^+$-pump's task is to maintain ion concentration gradients between both sides of the cell membrane. Hence, the limitation of this function leads to changes in local ion concentrations, which is referred to as a change in cellular homeostasis [86].

The ion concentration itself depends not only on the amount of ions in a certain compartment, but also on the volumetric compartment size. For example as a result of increased $^{23}$Na concentration inside cells and degraded $Na^+/K^+$-pump function, water molecules are attracted into the cell. The influx of water dilutes the intra-cellular $^{23}$Na concentration, but also increases the intracellular compartment volume, a change which is biologically referred to as cellular oedema. Initially, an imbalance in the cellular homeostasis causes oedema and a resultant shift in the relative compartmental volumes. This cell swelling can be measured non-invasively as an immediate change of signal

[1] **Homeostasis** is the property of tissue to regulate its metabolic environment (i.e. ion levels) constant.

intensity in Diffusion Weighted Imaging (DWI), reflecting changes in the measured Apparent Diffusion Coefficient (ADC) [8, 34, 87].

The permanent deprivation of vital nutrients from cells caused by the stroke ultimately leads to cell membrane rupture and the accumulation of extracellular fluids in these areas. This second stage is called infarction; the tissue is damaged and cannot be salvaged anymore. Areas with loss of membrane integrity can be identified in *ex vivo* sliced brain samples using a histochemical method based on staining the slices with haematoxylin and eosin, a double stain used to identify ischaemic neurons. Delineating the exact infarction area is more difficult and requires the assessment of neurons by their shrunken, retracted, and triangulated appearance under a microscope.

The subsequent formation of vasogenic oedema changes the molecular environment for water. Thus the $^{1}$H NMR relaxation parameters change in a way that the $T_2$-weighted signal intensity increases. Although, this change cannot be measured directly after membrane integrity loss, the regions of vasogenic oedema are fully developed and detectable by 24 h after Middle Cerebral Artery Occlusion (MCAO) [88]. Due to the correlation between infarcted tissue and $T_2$-weighted signal increase, $^{1}$H $T_2$-weighted MRI is currently regarded as the gold standard for infarcted stroke tissue detection. However, the delay of 24 h (in humans) before stroke-related signal changes are detectable complicates the early detection of still-viable stroke tissue, tissue that could be salvaged by pharmacological treatment or surgical intervention.

In addition, the increased $T_2$-weighted signal intensities, as well as the acute ADC decline, can transiently normalise in the subacute phase after ischaemia. This $T_2$-weighted signal normalisation most likely occurs because of a brain watercontent normalisation, which increases again during the chronic phase, when cavitation formation begins [89]. The reasons for ADC normalisation during the subacute phase remain to be investigated in future studies. It is known that these changes are uncorrelated with the histology during the normalisation phase [90, 91], which suggests that ADC cannot serve to mark infarcted stroke tissue. The variability of the $T_2$ and ADC values hamper the accurate assessment of stroke tissue in humans. Thus, other imaging modalities must be developed to enable the direct and non-invasive identification of infarcted tissue after stroke.

The vital role of $^{23}$Na concentrations in cell homeostasis led to the hypothesis that small changes in TSC relate to changes in tissue viability after stroke. Such changes in TSC may either relate to cell swelling and the subsequent increase in intra-cellular $^{23}$Na concentration [92, 93] or cell death, i.e. infarction, due to a replacement of intra- by

extra-cellular fluids, which must inevitably result in an increased TSC. Several studies have measured an increase in TSC for up to 3 days after stroke induction in rats [2, 5, 10, 12, 13, 34] . However, significant differences were reported in the specific time course of the TSC after cerebral ischaemia in animal and in human studies. The measurements varied between a direct increase [5, 13, 94], and a delayed increase with either an initial decrease [3] or with only a slightly varying TSC [8, 86] during the early phase. The early phase up to 4 h after stroke onset time remains the most interesting, because it is believed that tissue can be salvaged during this stage. Nevertheless it has not been explored adequately, primarily due to the required setup time of the *in vivo* model on the laboratory bench. Typically, the animal transfer from the bench to the MRI scanner and the time-consuming setup of the physiological control units has hindered data acquisition earlier than 60 min after stroke onset time in recent $^{23}$Na MRI studies of rodent MCAO models.

Despite such difficulties in exploring the acute phase of stroke in experimental animal models, the measurement of TSC is nevertheless regarded as a possible method to characterise viable or infarcted tissue after ischaemic stroke. Significant differences in TSC levels have been found in tissue with risk of infarction and already infarcted tissue [86]. Indeed, such differences have led to the hypothesis that there is a viability threshold, separating viable from non-viable tissue.

Others hypothesised that the temporal rate of TSC increase, the TSC slope, could vary differently in still-viable compared to infarcted tissue due to the tissue-dependent collateral blood supply [12]. Thus, tissue with increased collateral blood supply may exhibit an increased TSC slope, assuming that firstly TSC increases immediately after stroke onset time and secondly that the additional amount of $^{23}$Na-ions are delivered via the increased collateral blood supply paths. If the TSC is linearly increasing after stroke, it has also been hypothesised that one may retrospectively determine stroke onset time, a highly significant parameter for the diagnosis and treatment decision after stroke [5]. In this particular study, the stroke onset time was determined by fitting data acquired between 2 to 7 h after Middle Cerebral Artery Occlusion (MCAO) in four rats to a linear increase in TSC. As a result, the authors reported that stroke onset time could be determined with an onset time error of 1 min ± 4 min. However, this approach may prove very unreliable in humans, since in practice it would not be possible to acquire more than two temporally-spaced data points, since the patient management must be decided upon quickly, and consequently the amount of data from which to accurately fit a TSC increase would be insufficient. Furthermore, it is unclear whether a linear fit to the data is

appropriate; Chapter 8 ("The Development of a Non-Linear Model for TSC Increase after MCAO") describes an exponential fit to the data, which may inevitably lead to a different stroke onset time result to that reported by groups using a simple linear fit. Although stroke onset time may not be accurately deducible from TSC measurements, the accurate quantification of the TSC and the rate of TSC increase could potentially reveal a reliable parameter for the assessment of stroke tissue viability.

The aim of the work described in this chapter was to measure regional and temporal differences in the evolution of the TSC with high spatio-temporal resolution from as early as 0.5 up to 8 h after MCAO in five rat brains.

## 7.2 Short Echo Time Acquisition and Data Reconstruction

To allow for the quantification of TSC, it was necessary to acquire $^{23}$Na images using a specially adapted pulse sequence, which was suited to the fast $^{23}$Na signal decay [95], and specifically allowed for a short Time to Echo (TE). Back Projection Imaging (PI) for example achieves sufficiently short TE values, where TE is characterised by the time delay between the time of the RF pulse application, and the time of the central k-space acquisition. Standard gradient echo sequences suffer from longer TEs (typically TE > 2 ms), which arises from sampling an echo signal, usually starting at the edge of *k*-space, before the central *k*-space point is sampled. When a Free Induction Decay (FID) sampling scheme is chosen, each PI acquisition starts in the centre of *k*-space, reducing the achievable TE by an immediate *k*-space centre acquisition.

The *in vivo* experiments described at the end of this chapter involved the acquisition of 2D radial *k*-space trajectories with short TE < 1 ms. The SNR per unit time advantages of the 2D- over the 3D-acquisition technique is derived in the next section. The Ultra-Short TE (UTE) sequence, the detailed parameter optimisation, and the 2D radial reconstruction method are described in the following sections.

### 7.2.1 2D- versus 3D-Data Acquisition

Common MRI acquisition techniques can be divided into two groups, the so-called 2D-and 3D-techniques. The excitation of both techniques is fundamentally different; with global excitation for 3D-techniques and local slice selective excitation for 2D-techniques. Thus, for 3D-techniques, the entire volume, which is within the sensitivity range of the probe, contributes to the measured NMR signal. On the other hand, only net magnetisation located in a selected slice volume contribute to the measured signal in 2D-techniques.

3D-sequences have typically been employed due to their inherently larger SNR per unit scan time, when used with short repetition times and small flip angles in the steady state spin condition [11, 34]. However, the steady state spin condition can only be exploited for quantitative $^{23}$Na MRI (qNa-MRI) in conjunction with sophisticated $T_1$-compensation methods. To measure density-weighted rather than relaxation time-weighted $^{23}$Na signal, tissue with highly differing spin-lattice relaxation times ($T_1$) must reach the complete equilibrium state before the consecutive excitation pulse application. For the given $T_1$ of dissolved $^{23}$Na ions at 7 T, the repetition time $T_R$ above which $T_1$-weighting is negligible is approximated as follows:

$$T_R = \quad 5 \cdot T_1\left(^{23}Na \ \ in \ \ solution \,@\, 7T\right) \qquad \text{(Equation 7.2).}$$

*In vivo*, the highest $T_1$-relaxation time occurs in blood and cerebral spinal fluid with $T_1$ of approximately 40 ms at 7 T. Thus, to prevent any relaxation dependent signal differences and to enable the quantification of the TSC, the $T_R$ must be chosen to be approximately 200 ms. The SNR differences between 3D- and 2D-sequences will be derived for a 90 °-flip angle, 200 ms $T_R$, and a complete 2D-multi-slice acquisition within one $T_R$.

The mathematical relationship between SNR of an MRI experiment and voxel size $\Delta x \Delta y \Delta z$, sampling time $t_{sam}$, number of averages $Av$, and number of phase encoding steps $N_p$ [96] can be formulated as:

$$SNR \propto \quad \Delta x \cdot \Delta y \cdot \Delta z \cdot \sqrt{Av} \cdot \sqrt{N_p}\sqrt{t_{sam}} \qquad \text{(Equation 7.3).}$$

Where $Av$ is the number of signal averages, and Np is the number of phase encoding steps. In the case of long $T_R$, the repetition time increases by a dead time $t_{dead}$, which is assumed to have no effect on the SNR, as long as $T_R$ is chosen ≥ 200 ms. The sampling time can then be substituted as follows:

$$t_{sam} = \quad T_R - t_{dead} \qquad \text{(Equation 7.4).}$$

The SNR relationship with the chosen acquisition parameters (Equation 7.3) can thus be rewritten as:

$$SNR \propto \quad \Delta x \cdot \Delta y \cdot \Delta z \cdot \sqrt{Av} \cdot \sqrt{N_p}\sqrt{T_R - t_{dead}} \qquad \text{(Equation 7.5).}$$

If the SNR per unit time is of interest, one must consider the total acquisition time ($T_{aqu}$) needed for the acquisition of one full data set:

$$T_{acq} = \quad Av \cdot N_p \cdot T_R \qquad \text{(Equation 7.6).}$$

For 2D-sequences, the total acquisition time for one data set then depends on the number of phase encoding steps in the say $y$-direction $N_y$:

$$T_{acq,2D} = \quad Av_{2D} \cdot N_y \cdot \left(t_{sam} + t_{dead}\right) \qquad \text{(Equation 7.7).}$$

for 3D-sequences, this acquisition time depends on the number of phase encoding steps in both *y*- and *z*-directions $N_y$ and $N_z$:

$$T_{acq,3D} = \quad Av_{3D} \cdot N_y \cdot N_z \cdot (t_{sam} + t_{dead}) \qquad \text{(Equation 7.8).}$$

The time to acquire one full 3D data set is subsequently longer than for one 2D slice, because of the increased number of phase encoding steps ($N_z$) in slice direction. Although a 2D slice can be acquired $N_z$ times faster, the SNR in the same slice acquired with a 3D-technique is exactly $\sqrt{N_z}$ times higher. However, when the time penalty between the two sequences is compensated by an $N_z$-fold increase in the number of 2D-averages $Av_{2D}$, identical SNR ought to be achieved in identical acquisition times for both 2D and 3D approaches.

In the above discussion, the acquisition of only one slice was considered, whereas in normal MRI several slices through the brain are desirable. Due to the slice selective RF-excitation employed for 2D-sequences, multiple slices can be acquired within one $T_R$ without breaching the original requirement, which was a full relaxation of the spin system. In other words, the SNR per unit time in a certain voxel can be acquired as part of a 3D-sample volume and an increased number of phase-encoding steps or alternatively as a 2D-slice volume and an increased number of averages. This holds true for $^{23}$Na-MRI at 7 T as long as identical TE is employed and all slices can be acquired within one $T_R$ of 200 ms.

Admittedly, the 3D-technique benefits a shorter TE due to the applicability of shorter RF pulses and the unnecessary slice re-phase gradient application time (see Section 7.2.2). However, shorter RF-pulses also require higher RF-pulse power which must be taken into account particularly when volume resonators, rather than transceiver surface coils, are used. For instance, the $^{23}$Na/$^{1}$H birdcage coil required 8 W (12 dB reference pulse power) to achieve a 90°-flip angle in the rat brain for a 1 ms block pulse. The theoretically achievable minimum RF-pulse length was then restricted to 0.125 ms by the maximum deliverable power from the amplifier (500 W, -6 dB). However, no shorter than 0.5 ms pulses should be applied with the used Bruker birdcage coil to stay below the 50 W maximum power specification for which the coil components were designed. A slice selective pulse with 0.6 ms length was used for the 2D-sequence. Hence, similar SNR was expected for the 2D and 3D techniques, justifying the use of the 2D-technique for rat brain qNa-MRI at 7T. When the dead time is negligible, for example in steady state sequences such as FLASH, where smaller flip angles are used and $T_R$ is smaller than $T_1$,

the 3D-sequence develops clear SNR benefits over the 2D-sequence, especially for a larger number of slices [96].

Thus, the 2D- and 3D-SNR is identical for 90˚ flip angle excitations, a fully relaxed spin system ($T_R$ = 200 ms), and under the assumption that all slices are acquired within one $T_R$. This has also been confirmed by a similar proof published elsewhere [97].

### 7.2.2 The 2D Ultra Short TE Acquisition Scheme

Projection Imaging (PI) was the data acquisition method of choice in the early years of MRI. The 2D UTE sequence used in the current study is a modern variant of the original PI sequence, which acquires radial trajectories starting from the *k*-space centre by applying two gradients simultaneously. By applying the two gradients simultaneously, the orientation of these trajectories can be varied by the radial trajectory angle $\theta$, depending on the gradient magnitude-ratio. Hence, when the two gradients are switched on, the signal contains as many frequency components as there are points sampled during the gradient switching period. Through a Fourier Transformation (FT) the multi-frequency signal can be decomposed into its separate frequency components, where the FT of the trajectory acquired in the frequency domain gives the projection of the object with beams perpendicular to the line in the image domain (Figure 7.1). By changing the angle $\theta$, as many linearly independent projections can be acquired as required to solve the Gaussian system of equations for a desired resolution in the image domain.

At least as many projections as sample points per trajectory should be scanned, however, as a rule of thumb claims to overcome significant image artefacts, 1.5 times the amount of sample points per line should be acquired [96]. These artefacts occur as streaks in the outer image areas, which become more prominent in under-sampled projection images. A back-projection algorithm is typically used to solve for the system of equations composed of at least as many equations as the amount of elements contained along one projection. The image quality can further be improved by filtering the trajectories before reconstruction (filtered back-projection).

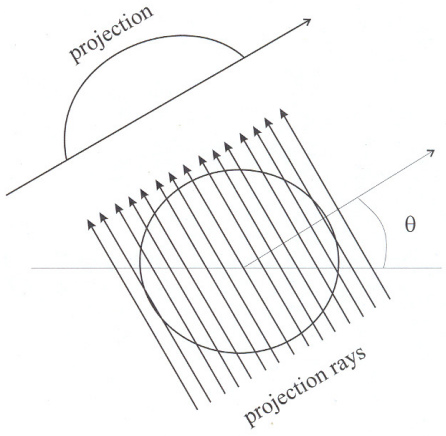


**Figure 7.1: The PI sampling scheme. The projection angle $\theta$, defines the trajectory direction in the frequency domain and the perpendicular beams indicate the projection direction in the image domain [98].**

The 2D Ultra Short TE (UTE) sequence that was chosen for this *in vivo* study was designed to start with a narrow-band RF-pulse (600 μs) and a slice selective gradient. The sequence diagram is illustrated in Figure 7.2. Shortly after the RF-pulse, a slice selection re-phase gradient was applied to compensate for the dephasing caused during half of the RF-pulse width. The application of the slice re-phase gradient was time-costly (approximately twice the gradient-dependent ramp time) and increased TE by approximately 500 μs. The signal was then read out from the *k*-space centre in a radial manner by simultaneously applying the two non-slice gradients, as opposed to Cartesian sequences, where the two gradients are switched consecutively.

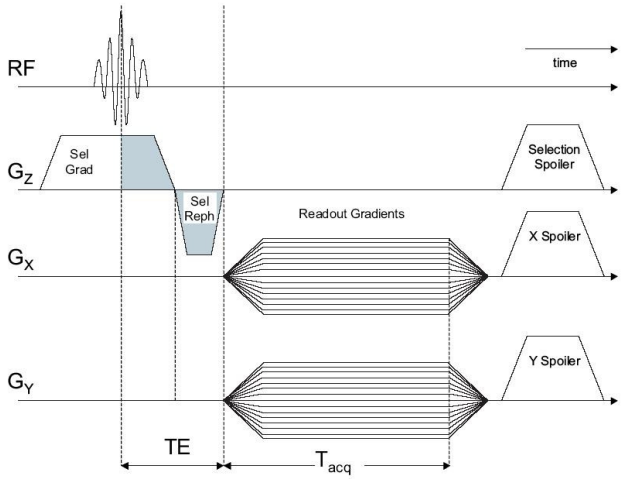


**Figure 7.2: The 2D-Radial sequence describing the timing of the gradient, and RF-pulse switching, together with the relative start time of the acquisition. Notice the characteristic radial gradient switching of two gradients simultaneously in order to read out the MR signal (adapted from the Bruker PV5.0 manual).**

A slice spoiler at the end of the acquisition was then applied to spoil the remaining net magnetisation. A filtered back-projection algorithm served as reconstruction method by the Bruker PV5.0 software to form the image, for example the one shown in Figure 7.3. The chosen sequence parameters and their optimisation are described in the next section.

### 7.2.3 *In Vivo* Acquisition Parameters

The 2D UTE sequence was optimised to achieve maximal SNR, minimal TE, and to allow for $^{23}$Na density measurements. It was further optimised for gradient duty cycle to allow for the acquisition of *in vivo* $^{23}$Na images with high spatio-temporal resolution for up to 7 h without overheating the system (Table 7.1). The $^{23}$Na/$^{1}$H birdcage coil described in Chapter 5 was used for transmit-receive $^{1}$H imaging and transmit-only $^{23}$Na imaging. The $^{23}$Na receive-only coil as described in Chapter 6 was used to receive the $^{23}$Na MR-signal. Both coils were geometrically decoupled during $^{1}$H and $^{23}$Na imaging.

For pulse sequences, which use TEs greater than 1 ms, the different relaxation times in reference solutions and tissue can lead to TSC underestimation. For instance, with a TE of 2 ms and using a solution rather than a gel as a reference, $^{23}$Na concentrations were underestimated by up to 20 % in test phantoms made of 10% agarose gel [99]. For $^{23}$Na imaging, a TE of 853 µs was achieved in the current study, which minimised such $T_2$-weighting effects on the measured signal intensity.

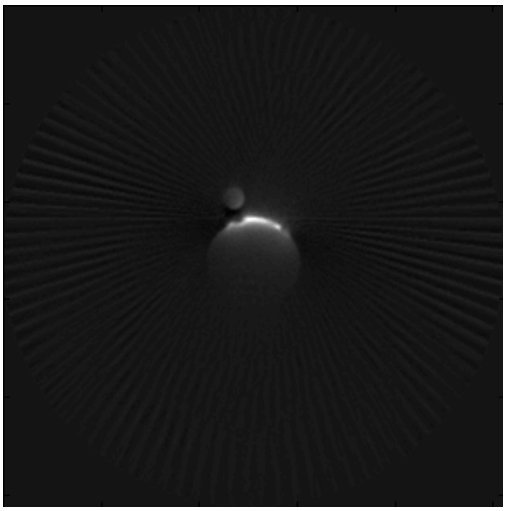

**Figure 7.3: Reconstructed image of a homogeneous phantom with a fiducial vial positioned above the coil. Notice the streaking artefacts in the outer image areas resulting from the back-projection algorithm and the under-sampling scheme. The circular area covered by the small vial had a diameter of 8 mm.**

**Table 7.1: Sequence parameters used for *in vivo* $^{23}$Na and $^{1}$H MRI of the brain. The following parameters are listed: Field of View (FoV), Matrix Size (MTX), Slice Thickness (ST), Acquisition Time (TA), Echo Time (TE), Repetition Time (TR), Flip Angle (FA).**

| | $^{23}Na$ | $^{1}H$ |
|---|---|---|
| *Sequence* | 2D UTE | 2D RARE |
| *FoV* | 20 cm x 20 cm | 8 cm x 8 cm |
| *MTX* | 256 x 256 | |
| *(read x phase)* | (100 projections) | 256 x 256 |
| *ST* | 2 mm | 2 mm |
| *TA* | 10 min | 5 min |
| | | 64 ms |
| *TE* | 853 µs | (RARE-factor 8) |
| *TR* | 200 ms | 3262 ms |
| *FA* | 90° | 90°/ 180° |
| *BW* | 15 kHz | 50 kHz |

$T_1$-weighting effects were reduced by using long $T_R$ of 200 ms. Typically $T_R$ values quoted in the literature range from 100 to 120 ms [21, 100]. Through the use of such low $T_R$ values, which are typically < 2 - 3 times $T_1$, signal from fluid-like compartments (e.g. blood and CSF) were deliberately suppressed in order to gain higher SNR from tissue. Stronger quadrupolar effects are assumed to cause faster transverse magnetisation loss in tissue compared to solutions and thus faster recovery to the equilibrium spin state [16]. In brain tissue, $T_1$ was measured to be 44 ± 1 ms at 7 T [97]. Thus the gain in tissue SNR from the use of relatively low $T_R$ value might justify the incorporation of $T_1$-weighting effects. However, $T_1$-weighting effects make TSC quantification difficult when stroke models are investigated, where the relaxation times can change over the time course of the experiment. The aims of the current study were to accurately quantify the TSC during the acute phase of a stroke, and thus any $T_1$-related problem were avoided altogether by using a $T_R$ of 200 ms, thereby deliberately reducing the maximal achievable SNR with qNa-MRI compared to steady-state $^{23}$Na-MRI.

The bandwidth was set to 15 kHz, the lowest value possible with the AV1 electronics on the 7 T Bruker system at the Glasgow MRI facility where the *in vivo* experiments were performed. The bandwidth was minimised in order to maximise the SNR per unit time.

A large FOV of 20 x 20 cm was chosen for the $^{23}$Na imaging to prevent gradient overheating and minimise gradient delay - related artefacts, which occur in the *k*-space centre due to temporal deviations in the gradient delay times (within 50 µs). The *k*-space data was eight times undersampled to reduce the acquisition time and compensate for the larger acquired FOV. The undersampling-related streaking artefacts were only visible in the outer regions (> 60 mm diameter) of the reconstructed images.

Theoretically, 2D-multi-slice imaging results in identical SNR compared to 3D-acquisition for identical repetition times. The number of multiple slices that could be acquired within the $T_R$ of 200 ms was restricted to five and hence accurate slice positioning was required in each rat in order to cover the entire stroke lesion. The accurate slice positioning was achieved by positioning the $^{23}$Na slice stack at the middle of the frontal cortex using the $^{1}$H pilot scan. The availability of good quality $^{1}$H pilot images demonstrates the necessity of using the double-tuned resonator system described in Chapter 5 and 6 for *in vivo* qNa-MRI.

### 7.2.4 The 2D Radial Reconstruction Method

Filtered back-projection was the default reconstruction algorithm as implemented in the Bruker PV5.0 software. However, reconstruction-related artefacts were noticed in the image that resulted from temporal inaccuracies in the gradient delay times. These artefacts appeared as smearing and are typical for images reconstructed using a filtered back-projection method.

Alternative approaches to back-projection reconstruction exist. The radially acquired *k*-space data can be regridded from the radial grid to the Cartesian grid. The Cartesian *k*-space data can then be inversely Fourier transformed to convert the data from the frequency to the image domain. It has been demonstrated that radial *k*-space data processed by inverse Fourier transformation results in improved image quality by O'Sullivan *et al*. in 1985 [101].

Although the 2D radial reconstruction approach was theoretically straightforward, regridding the radial *k*-space data poses some practical computational challenges. Two different methods for radial-to-Cartesian *k*-space regridding were found in the literature. The first relies on nearest-neighbour interpolation and the second on a convolution based algorithm. The nearest-neighbour interpolation approach is based upon the computation of the nearest Cartesian grid point to which the radial-discretely sampled signal intensity is assigned, as illustrated in Figure 7.4. As a result, the second nearest *k*-space points in the over-sampled radial *k*-space centre location remains unassigned in some cases; whereas radial *k*-space coordinates in the outer *k*-space areas are repeatedly assigned to the nearby Cartesian grid points.

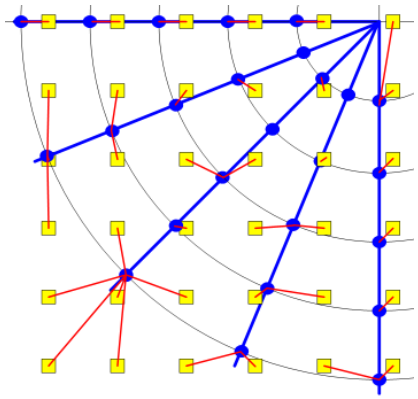

**Figure 7.4: Graphical example of the nearest neighbour interpolation principle for radial (blue circles) and Cartesian (yellow squares) *k*-space grids. The interpolation distance is marked with red lines. Notice that externally located *k*-space points contribute to the signal intensity of several Cartesian grid locations, whereas other more centrally located k-space points remain unused by the regridding procedure.**

Convolution regridding is based upon a distance-weighted accumulation of several radial *k*-space points to reconstruct the discrete Cartesian *k*-space intensities. A convolution window defines the amount of radial *k*-space points that contribute to the regular Cartesian *k*-space signal intensity. Depending on the distance between radial and Cartesian *k*-space coordinates, the radial signal intensity is weighted by a window function. Jackson [102] and Beatty [103] described numerical approaches to compute the Kaiser-Bessel window parameters in dependence of the grid and the window width. A comprehensive description of the convolution based regridding algorithm for $^{23}$Na MRI was given in a more recently published PhD thesis by Nagel [97]. Despite the improvement in the accuracy of *k*-space data transformation using the convolution approach, it comes at the price of an oversampled *k*-space centre that requires considerable computational post-processing involving sophisticated parameter optimisation, which was beyond the scope of the current work. As a result, the nearest neighbour interpolation method was chosen to reconstruct the *in vivo* radial data sets acquired here, with the algorithm implemented in Matlab®.

Filter functions are generally applied to increase the SNR by weighting the outer *k*-space, which commonly contains components with low SNR compared to the SNR measured in the central *k*-space. Hence noise originating from the peripheral *k*-space areas can be suppressed, while trading-off some resolution. A commonly employed filter is the Hanning filter:

$$F_{Hanning} = \cos^2\left(\frac{2\pi k}{W_H}\right) \qquad \text{(Equation 7.9),}$$

where $k$ refers to the radial distance from the $k$-space centre and $W_H$ characterises the filter width. The application of $k$-space filtering algorithms was also referred to as apodisation and was extensively discussed elsewhere [104, 105]. The unfiltered and Hanning-filtered regridded Cartesian $k$-space data is compared in Figure 7.5. The 2D-radial reconstruction procedure was implemented as follows:

1. The radial FID data was loaded into Matlab®.
2. The polar coordinates $r$ and $\varphi$ for the $s$th radial sample position on the $p$th radial projection were converted to Cartesian coordinates:

$$x(p,s) = r(p,s) \cdot \cos(\varphi(p,s)) \qquad \text{(Equation 7.10)},$$

and

$$y(p,s) = r(p,s) \cdot \sin(\varphi(p,s)) \qquad \text{(Equation 7.11)}.$$

3. Square Cartesian coordinate matrices $X_c$ and $Y_c$ were generated with side length equal to twice the amount of samples along one radial k-space line.
4. The Hanning filter was applied to the radial trajectories.
5. The nearest neighbour interpolation was computed.
6. The inverse Fast Fourier Transformation was performed to convert the interpolated $k$-space data into image space.

A comparison of the 2D regridding versus filtered back-projection reconstruction approaches is shown in Figure 7.6, demonstrating the significant improvement in image quality achieved with the regridding approach.

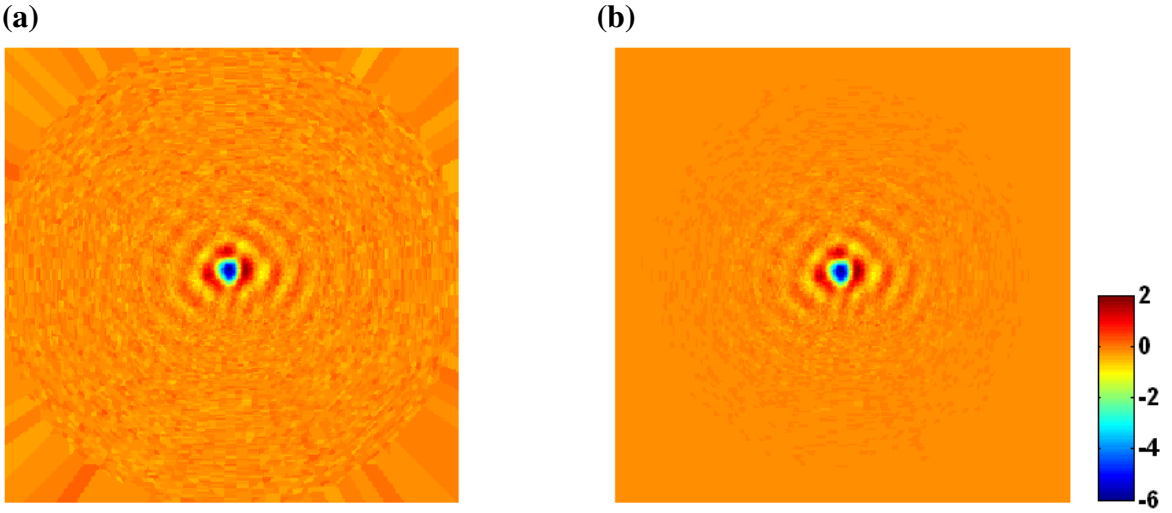


**Figure 7.5: Amplitude matrices of the reconstructed $k$-space using (a) the next neighbour interpolation without and (b) with applied Hanning-filtering. The colourbar labels are in arbitrary units.**

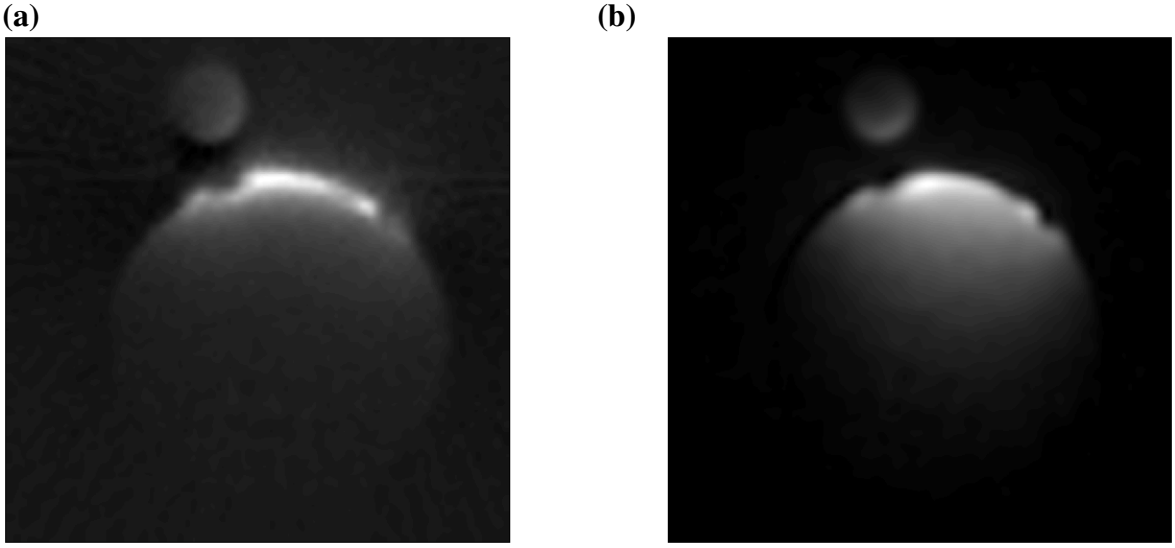


**Figure 7.6: Reconstructed $^{23}$Na images of a uniform phantom (40 mm i.d.) reconstructed with (a) back-projection as default in PV5.0 and (b) self-implemented regridding algorithm. The inner diameter of the small fiducial vial was 8 mm.**

The inherent surface detector coil profile characterised by a half-spherical signal intensity drop with distance from the coil surface, is more evident in the image which was reconstructed by regridding. Overall, this image was less affected by hardware-related artefacts than the image reconstructed by filtered back-projection, as evidenced by less shadowing artefacts at the edges of the fiducial vial and cylindrical jar. Furthermore, the regridding image was free from streaking artefacts common to back-projection images.

## 7.3 The Quantification of TSC

In MRI, static, quasi-static and rapidly changing magnetic fields are employed to measure the $^{23}$Na-MR signal, which is linearly linked to the $^{23}$Na nuclei concentration in samples with identical MR relaxation behaviour. Nevertheless, a standard technique for the calibration of the absolute $^{23}$Na concentration is difficult, because the measured MR signal underlies strong spatio-temporal variations with different detector coil loads and indeed different detector systems. Therefore, references of known $^{23}$Na concentration must be measured simultaneously within every image. The $^{23}$Na signal can then be quantified based upon linear regression, where a calibration curve serves to convert the acquired $^{23}$Na signal intensity image into a $^{23}$Na concentration map. A mathematical relationship between the Tissue Sodium Concentration (TSC) and the MRI signal intensity was derived by Thulborn and Ackerman [106]. Their dual tuned coil approach used the ratio of the signal intensity in a $^{23}$Na image to that in a $^{1}$H image to calibrate the MR system for a certain range of biological $^{23}$Na concentrations. Based upon the assumption that the

current distribution within the detector coil was identical for both the $^{23}$Na and the $^{1}$H frequency, the spatially constant $^{23}$Na/ $^{1}$H-ratio intensity served to eliminate the detector sensitivity from the measured $^{23}$Na image. A linear relationship between the $^{23}$Na/ $^{1}$H-ratio intensities and the respective $^{23}$Na concentration was established by computing the slope *a* and the offset *b* of the linearly linked $^{23}$Na signal and the actual $^{23}$Na concentration. These two parameters were computed from the measurement of two reference $^{23}$Na signal intensities ($I_{r1}$ and $I_{r2}$) in the area of two known reference $^{23}$Na concentrations ($C_{r1}$ and $C_{r2}$), where the slope was calculated as:

$$a = \frac{C_{r1} - C_{r2}}{I_{r1} - I_{r2}} \qquad \text{(Equation 7.12),}$$

and the offset was computed as:

$$b = I_{r1} - a \cdot C_{r1} \qquad \text{(Equation 7.13).}$$

Once the calibration curve was determined, the TSC in voxel *j*, $TSC_j$, could be estimated for a given intensity $I_j$ via:

$$TSC_j = a \cdot I_j + b \qquad \text{(Equation 7.14).}$$

However, this method relies on a homogeneous $^{1}$H density in the entire sample, which may hold true for solutions of various $^{23}$Na concentrations, but will inevitably fail for *in vivo* samples. To compensate for the $^{1}$H concentration variations between tissue and solution, a correction factor of 0.8 (assuming 80% $H_2O$ abundance in tissue) was introduced by Christensen *et al*. to quantify TSC in non-pathological rat brain tissue [33]. The same group later expanded on their quantification technique, employing a three-reference-vial calibration method to map TSC in human cerebral tumours [18]. In this case, they compensated for $B_1$-inhomogeneities by using a dual-tuned coil approach similar to that described in Chapter 6. In pathological condition such as stroke, however, the $^{1}$H tissue concentration changes independently from the $^{23}$Na tissue concentration, and thus quantification approaches which use a unique correction factor are not applicable to quantify TSC in *in vivo* stroke models.

Nevertheless, the reference vial approach proved useful for studies where no coil sensitivity correction was necessary. For instance, it was applied to images acquired with a single-tuned $^{23}$Na birdcage coil to study brain tumours [21]. The remaining receive- and transmit sensitivity was measured on healthy volunteers through the acquisition of three $^{23}$Na data sets with 45°, 90°, and 135° flip angles. The $B_1$-sensitivity maps were then determined and allowed for compensating these after the tumour study.

An approach that did not use reference vials was developed by Schepkin *et al*. [25], who used 24 measurements in healthy rat brain tissue to obtain an average signal intensity value, which was compared to the average signal intensity in tumour tissue at day zero of their measurements. The healthy brain $^{23}$Na concentration was assumed to be 45 mM - a value which has been well established in the literature as an average across the healthy rodent brain [18, 33]. The day zero TSC served as a reference concentration for the determination of spatio-temporal tumour growth after treatment in ten rats. The use of a reference vial to normalise the signal intensities in each image was not mentioned; however, it is likely that coil loading would have changed during the experiment, for example due to $^{23}$Na concentration changes in the tumour. Consequently, the accuracy of the data may be compromised by the lack of signal normalisation due to the different coil loading conditions, resulting in varying $^{23}$Na signal intensities and hence TSC values. Moreover, this method required highly accurate image co-registration and may therefore be prone to high errors in TSC quantification due to the inherent difficulty in co-registering poor quality sodium images.

Another quantification approach was employed by Ouwerkerk *et al*. [107], who measured TSC in human breast cancer using a solenoid transceiver coil, which generated a reasonably homogeneous $B_1$-field. The quantification was based upon two scans: a sample scan and a reference scan. To enable the compensation for different coil loading, a fiducial ring-shaped jar was scanned simultaneously with both the reference and the sample. As a result, any difference in reference and sample image signal intensities measured in the fiducial vial position could be attributed to coil loading variations and corrected for by a simple normalisation procedure. The reference phantom comprised a bag filled with a known 40 mM NaCl solution that covered the coil's inner field of view. Hence, by dividing the signal intensity of the sample image by that of the reference, and multiplying it by the known reference $^{23}$Na concentration and loading correction factor, the TSC was quantified.

For the current work (i.e. quantifying TSC in rat brain tissue), the latter approach of Ouwerkerk *et al*. was adapted [107]. Using a separate scan of a homogeneous reference phantom and a fiducial, which was fixed to the receiver coil, the sensitivity profile could be compensated and TSC could be simultaneously quantified. The following sections describe the quantification processing as it was implemented in a programm written in Matlab®. The quantification procedure will be explained using the example of a NaCl

concentration phantom that was composed of five different $^{23}$Na concentrations, which is described in the next section.

### 7.3.1 Phantoms Replicating *in vivo* $^{23}$Na Concentration- and Relaxation Properties

Phantoms, which replicate the physiological brain TSC and relaxation time range, are described in this section. Besides the phantoms described in Section 3.2.2 ("The Development of Physiological Load Replicating Phantoms"), $^{23}$Na concentration phantoms were required as standards for (a) the quantification of the TSC, and (b) the assessment of the TSC quantification accuracy.

For the quantification of the TSC, two kinds of phantoms were necessary; one phantom filling the sample Field of View (FoV), and another phantom, the fiducial, which was fixed above the coil for co-registration purposes. The reference phantom had to accurately replicate the physiological range of the relaxation times at known $^{23}$Na concentration (120 mM NaCl, 1 % gel, 40 mm i.d.). The fiducial was a small (8 mm i.d.) vial with 50 mM NaCl and set up as agarose gel (1 %) to avoid the movement of air bubbles. Air bubbles were an undesired side product of the setting up process.

For the assessment of the quantification accuracy, two phantoms were necessary, one replicating various $^{23}$Na concentrations across the physiological TSC range, and another replicating the various physiological NMR relaxation properties of the brain tissue. The TSC-replicating phantom was composed of five different $^{23}$Na concentrations covering the physiological possible TSC range. Four vials (i.d. 8 mm) each containing 40, 70, 100, and 160 mM NaCl solutions were placed inside a 35 mm (i.d.) cylindrical jar that was filled with 130 mM NaCl solution. To avoid moving air bubbles during the experiment, gels were used (1 % agarose). The $T_2$-relaxation time-replicating phantom was similarly composed of four vials in a cylindrical jar (35 mm i.d.). The $^{23}$Na concentration was chosen high at 500 mM NaCl to achieve better SNR per acquisition time. The gel concentration however varied from 0, 1, 2, to 3 % agarose gel concentrations in the vials and 5 % agarose gel in the cylindrical jar. Thus, the expected $T_2$-relaxation times in tissues were approximately replicated and TE-related $T_2$-weighting effects could be tested by scanning this phantom.

### 7.3.2 Image Co-registration and Coil Sensitivity Correction

The dual resonator system that was described in Chapters 5 and 6 was used for all experiments presented in this Chapter. The homogeneous $B_1$-field generated by the birdcage coil guaranteed a relatively homogeneous flip angle distribution across the entire

sample. The receive-only surface coil was then employed to maximise the detectable signal, an important consideration given the extremely low $^{23}$Na signal. As a result our system allowed for the quantification of TSC with high SNR.

Besides $B_0$-inhomogeneities, quantification of the $^{23}$Na concentration using MRI was challenging due to the inherent signal sensitivity profile, which depended on the surface coil detector. Assuming a relatively homogeneous $B_1$-field generated by the birdcage resonator (measured $\pm 4.5$ % across the 3 cm inner diameter), the sensitivity profile was solely dependent on the surface coil dimension. By scanning a homogeneous phantom in a reference scan, the sensitivity profile was measured. The phantom comprised a cylindrical jar with 40 mm diameter and was filled with 120 mM NaCl dissolved in distilled water and 1 % agarose gel. Before compensation, both the reference and the sample images were co-registered in terms of the surface coil positioning. A fiducial vial was permanently fixed above the surface coil, and hence was scanned with both sample and reference. The fiducial vial has an inner diameter of 8 mm and was filled with 50 mM NaCl dissolved in distilled water and 1 % agarose gel. The image of the homogeneous fiducial also exhibited the sensitivity profile of the detector coil, which allowed for the use of a semi-automated three dimensional procedure for co-registering the sample and reference images, as follows:

1. The RoI of the fiducial vial was determined manually from the $^{23}$Na reference and sample scans.
2. The two-dimensional cross correlation coefficient was then computed for the chosen sample slice and various reference slice RoIs.
3. The reference slice RoIs were varied by three-dimensional translational shifts ($\pm 5$ mm) and two-dimensional in-plane rotations ($\pm 10^{\circ}$) automatically derived from the cross correlation analysis.
4. The translational and rotational offsets were applied to co-register the sample and reference images for later quantification procedure.

After co-registering the reference image ($R$) to the sample image ($S$), the quotient image ($Q$) was computed as:

$$Q_j = \frac{S - \overline{N_S}}{\sigma(N_S)} \cdot \frac{\sigma(N_R)}{R - \overline{N_R}} \qquad \text{(Equation 7.15)},$$

where $N_S$ and $N_R$ were the RoIs representing sample and reference noise, chosen as square regions at the upper left corner in each image (250 pixel), and $\sigma$ was the respective

standard deviation of the noise. The averaged noise magnitudes were usually different in sample and reference images and lead to a $^{23}$Na concentration offset when they were not taken into account, as has also been observed by Romanzetti *et al*. [108]. Therefore, it was necessary to divide the SNR values by each other rather than dividing pure image intensities.

The sample, reference, and quotient images are presented in Figure 7.7. Notice the increased noise intensities outside the sample, resulting from amplification following the division procedure. Also notice the sensitivity compensated signal distribution at depth in the sample; the different $^{23}$Na concentrations can clearly be made out in the four vials and the surrounding gel.

### 7.3.3 The Quantification Method

To compensate for sample-dependent loading of the detector coil, the quotient image was compensated by the signal differences measured in an area of known $^{23}$Na concentration. Initially, it was planned to use the fiducial vial on top of the surface coil for this purpose. However, this approach resulted in inconsistent quantification results, the reasons for which were hypothesised as follows:

Firstly, the fiducial vial was positioned very closely to the birdcage resonator structure, almost touching the inside wall of the resonator's tube. The $B_1$-inhomogeneities were highly spatially dependent in these areas, and hence even minor rotational and/or translational differences in the surface coil positioning with respect to the birdcage coil may have resulted in highly variable sample and reference signal intensities, which would be impossible to reproduce in practice and would be expected to vary from experiment to experiment, as indeed was observed.

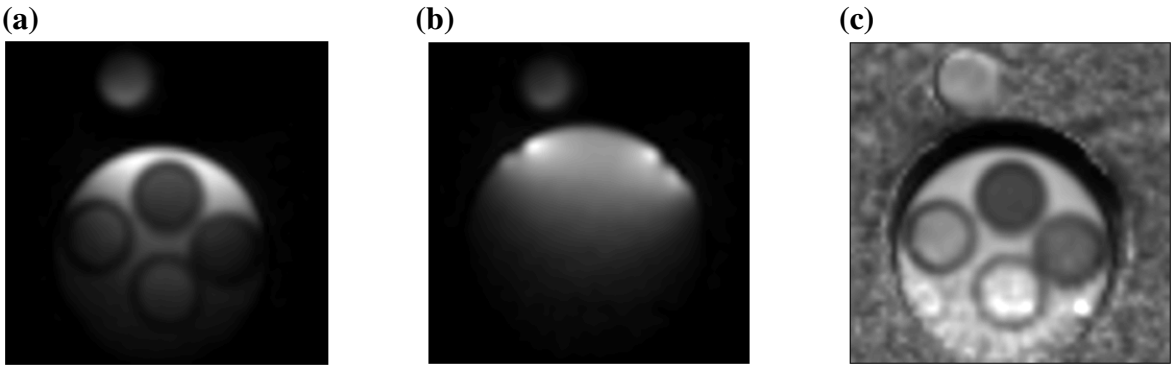


**Figure 7.7: (a) The sample SNR map was divided by (b) the co-registered reference SNR map to compute (c) the sensitivity corrected quotient image.**

Secondly, the shimming was performed using the sensitivity dependent $^{23}$Na receiver surface coil signal. In general, first order shimming was performed as described in Section 2.6.2.2 (Adjustments). Nevertheless, it is likely that the shimming routine may have performed differently in different regions surrounding the coil, for example correcting for $B_0$-inhomogeneities differently near the high NaCl concentration (120 mM) reference phantom compared to near the lower NaCl concentration (50 mM) fiducial vial. This in turn may have resulted in the detection of spatially-dependent signals, which subsequently would be expected to vary differently between the sample and reference images, independently of other coil loading considerations. Therefore, it was decided to use the fiducial vial as a control point marker for image co-registration purposes only, and use an internally known $^{23}$Na concentration reference for loading correction purposes. The TSC of the healthy rat brain was used to this end which, as mentioned in the previous section, has been well established in the literature as measuring ~ 45 mM averaged across the brain. For example, Christensen *et al.* measured the TSC in the rat brain at 45 ± 4 mM using MRI which was validated using the gold standard *ex vivo* $^{22}$Na radionuclide method [33]. For the stroke experiments in the current study, the contra-lateral side of the rats' brain was used for the purpose of loading compensation, as it was known to remain completely unaffected by the stroke model that was used [109].

The ratio of the mean signal magnitudes in the reference and the sample image, $F_S$ and $F_R$, respectively, were computed from the manually chosen RoI in the computed quotient image. The respective sample and reference concentrations ($c(F_R)$ and $c(F_S)$) must be known for the chosen RoI. The sample RoI was chosen to be the contra-lateral normal brain region (~ 45 mM) in the *in vivo* experiments and to be the 130 mM $^{23}$Na concentration RoI in the phantom experiment. The reference $^{23}$Na concentration was 120 mM. The correction factor for variable loading was computed as:

$$cor = \frac{\overline{F_R} - \overline{N_R}}{\sigma(N_R)} \cdot \frac{\sigma(N_S)}{\overline{F_S} - \overline{N_S}} \qquad \text{(Equation 7.16).}$$

A second correction factor for the quantification of the $^{23}$Na concentration (*conc*) in the quotient image was computed from the known $^{23}$Na concentration in the sample and the reference RoI chosen for loading compensation, as well as a factor for quantification - the reference phantom $^{23}$Na concentration (120 mM):

$$conc = 120mM \cdot \frac{c(F_S)}{c(F_R)} \qquad \text{(Equation 7.17).}$$

These values served as correction factors for the previously computed quotient image. $TSC_j$, the TSC in voxel *j,* could then be quantified by following equation:

$$TSC_j = Q_j \cdot cor \cdot conc \qquad \text{(Equation 7.18).}$$

A graph of the calculated $^{23}$Na concentration for the five set $^{23}$Na concentrations in the phantom is shown in Figure 7.8. A linear relationship between set and estimated $^{23}$Na concentrations was established.

### 7.3.4 The Quantification Accuracy

The quantification error in images acquired with a 10 minute acquisition time and a voxel resolution of 1.2 µl was computed for the five different $^{23}$Na concentrations in the test phantom. The phantom was imaged 45 times consecutively; the quantification error was calculated in the compounded images, which consisted of the first image added to the second, then to the third added, out to the addition of the 45$^{th}$ image. In all cases it was found that the quantification error was below 10 mM for the chosen sequence parameters and the physiological $^{23}$Na concentration range of 40 to 160 mM. The accuracy was improved to $< 8$ mM by averaging data acquired over two hours, although further averaging did not improve the quantification accuracy.

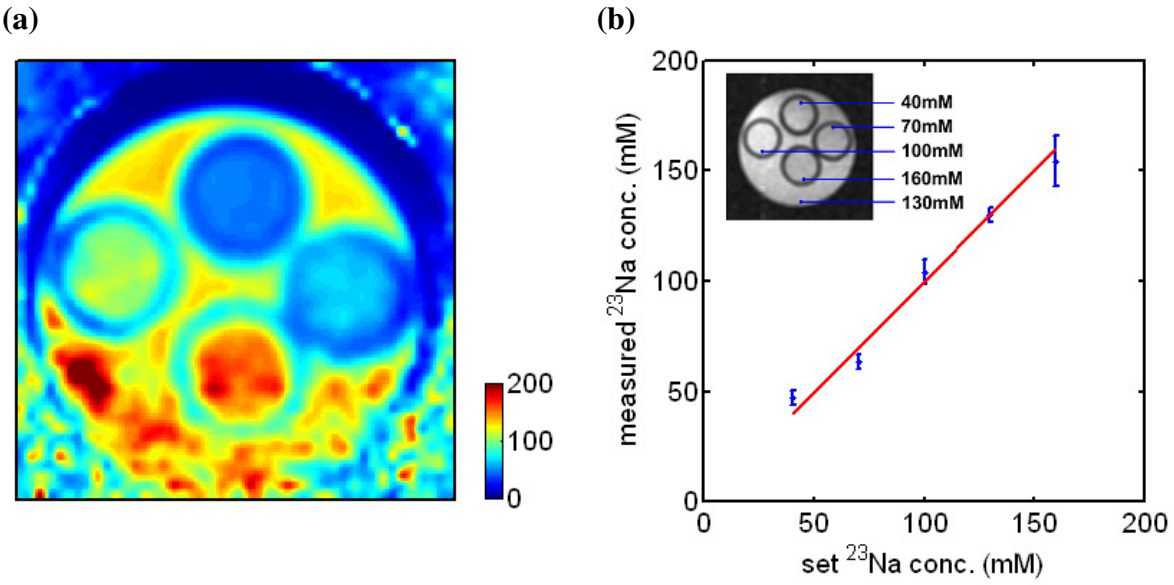


**Figure 7.8: (a) Quantitative $^{23}$Na concentration map of the $^{23}$Na concentration test phantom (colourbar in units of mM). (b) The quantified $^{23}$Na concentrations as a function of set $^{23}$Na concentrations.**

This may be due to the fact that the quantification error was dependent on the co-registration accuracy: since the signal intensity dropped by 63 % at a distance of 12 mm from the surface coil, variations in image co-registration (between sample and reference scan) would exert a large effect on the quantification accuracy and were thus considered as the major cause of quantification error. The accuracy of setting up NaCl solutions quantifying $^{23}$Na concentration via the conductivity meter method was found to be < 3 mM, as described in Section 3.2.2 ('The Development of Physiological Load Replicating Phantoms'). The minimal immersion depth of the conductivity probe was 36 mm and measurements could be taken faster than 20 sec. Assuming a minimum sample area of 5 x 10 x 10 mm, the minimum sample volume was > 500 µl. 1 mol $^{23}$Na ions in 1 litre water possess a mass of 23 g and thus the effective accuracy of the conductivity meter method was ± 38 µg in a solution volume of 500 µl. In comparison, a quantification accuracy of < 10 mM in 1.2 µl voxel was achieved with qNa-MRI in 10 min acquisition time, corresponding to an effective quantification accuracy of ± 0.270 µg mass of $^{23}$Na nuclei in a solution volume of 1.2 µl. This demonstrates the high quantification accuracy of the developed method, which is $^{23}$Na-nuclei specific and spatially resolvable – an important advantage over the global and non-specific conductivity meter method. Taking into consideration the error in setting up a NaCl solution, which was < 3 mM, and the unknown error associated with the heating up of NaCl solutions/ agarose mixtures to form a gel, the quantification accuracy of < 10 mM was deemed to be an acceptable result that allowed for the measurement of *in vivo* TSC from a $^{23}$Na concentration of 45 mM in the normal brain to above 100 mM after stroke.

In a further experiment, the influence of the fast $T_2$-relaxation time on the quantification accuracy was tested. For this experiment, the relaxation time replicating phantom described in Section 7.3.1 was used. This phantom contained four vials filled with 500 mM NaCl and was made using varying agarose gel concentrations. $T_2$-weighted $^1$H MRI was performed to confirm the relaxation differences set up by the variations in gel concentrations. The $^{23}$Na concentration was quantified to 500 mM for all five gel concentrations as illustrated in Figure 7.9.

Variations remained due to reference gel artefacts in the lower sample regions. In the $T_2$-weighted $^1$H MR images, a clear $T_2$-weighting was observed for the solution (0 % gel concentration) and gels, confirming the correct experimental setup.

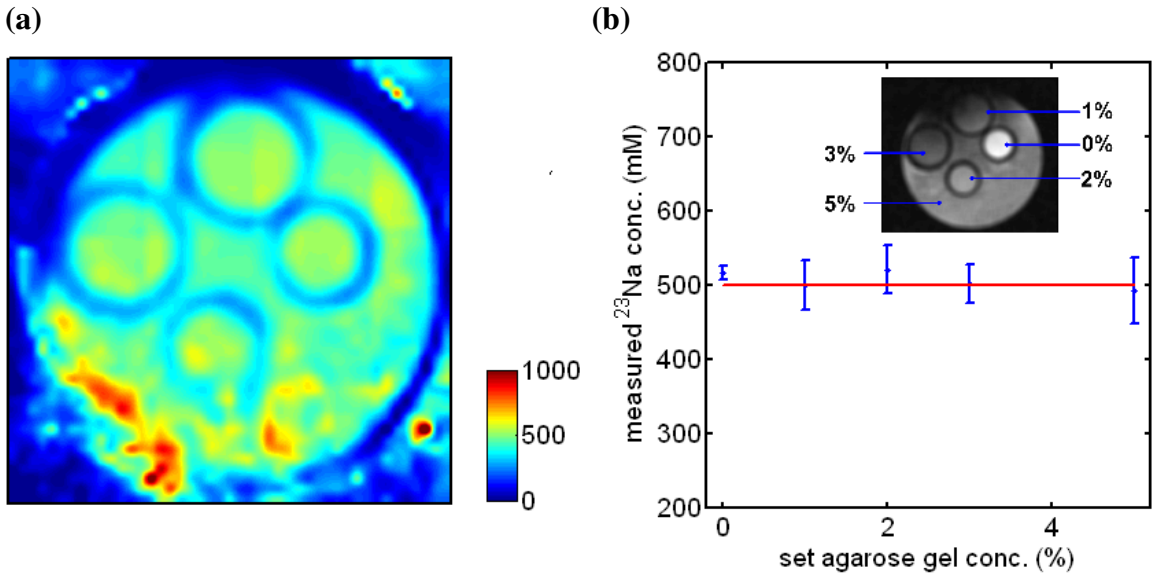


**Figure 7.9: (a) The $^{23}$Na concentration map for the $T_2$-relaxation times replicating phantom. (b) Measured $^{23}$Na concentrations as a function of set agarose gel concentration. The set $^{23}$Na concentration was 500 mM. Note the independence of the measured $^{23}$Na concentration from the gel concentration for 0 to 5 % gels. The dark parts in the inset $^{1}$H image are coil-related image artefacts. Note the $^{1}$H signal difference between solution and gel compartments.**

Estimated $^{23}$Na concentration differences for various gel concentrations and solutions were within the measured quantification accuracy of 10 mM, with slightly overestimated $^{23}$Na concentrations in solution and slightly underestimated $^{23}$Na concentrations in 5 % agarose gel. This was expected due to the employed reference material that was 1 % agarose gel. The differences in $T_2$-relaxation in different $^{23}$Na ion environments of solution and 5 % gel resulted in slightly over- and under- estimated $^{23}$Na concentrations, respectively. 1 % agarose gel concentration was chosen as the reference material to account for the different spin-spin relaxation properties in living tissue for the following reasons: Firstly, the dense cartilage environment was previously found to be best mimicked by 8 % agarose gel concentration [17]. Therefore, a brain tissue equivalent agarose gel concentration was expected to be below 8 %, consistent with a less solid $^{23}$Na ion environment.

Secondly, differences between short $T_2$-components in gels and solutions were expected to be large (< 5 ms for gels versus ~ 20 ms for solutions [99]). Thirdly, only minor relaxation time differences have been measured for gel concentrations from 1 % to 5 % agarose [108]. Consequently, a 1 % agarose gel concentration was believed to sufficiently replicate the expected range of *in vivo* $T_2$-relaxation times, falling between solution (i.e. blood) and an 8 % gel concentration (i.e. cartilage). In addition to the ultra-short TE used for the data acquisition, the reference gel concentration adjustment reduced remaining $T_2$-relaxation differences between tissue and reference material sufficiently.

The quantification accuracy for the employed 2D UTE sequence was validated on gel phantoms containing various NaCl and agarose concentrations (40 – 160 mM, and 0 - 5 % respectively). The quantification accuracy below 10 mM was achieved for a 1.2 µl voxel size and 10 min acquisition time. No comparable techniques exist, which allow for the non-invasive and localised *in vivo* quantification of TSC with the quantification accuracy achieved in the current study.

## 7.4 The Middle Cerebral Artery Occlusion (MCAO) Model

This section describes the Middle Cerebral Artery Occlusion (MCAO) model that was used to study the evolution of TSC in the rat brain after stroke. Ischaemia is physiologically modelled by arterial blockage, of which three approaches to model MCAO are described in the literature. The occlusion can be induced pharmacologically by a vasoconstrictive drug (such as endothylen), by diathermia, or by the intraluminal thread method. The pharmacological method is reversible, with drug and physiology dependent reversion times. The diathermia method requires highly invasive surgery to directly expose the MCA, which is subsequently cauterised using diathermy, and invariably causes oedema and bleeding near the expected stroke lesion, which can cause difficulties for imaging the lesion itself. Furthermore, due to the deliberate physical damage caused to the MCA, this model is irreversible, which limits its overall versatility, for example in performing a reperfusion experiment, which is potentially interesting for stroke work. The intra-luminal thread method, on the other hand, is minimally invasive in the region of the stroke lesion, but can cause additional damage due to brain swelling and an increased intra-cranial pressure. Nevertheless, surgery-related vessel damage near the stroke lesion is avoided with this model, which is particularly important for qNa-MRI when one considers that such damage typically involves haemorrhage in the ischaemic region which, given that blood has a TSC value in excess of three times that of brain tissue, would significantly hamper the direct measurement of stroke-related TSC changes. For these reasons, the intra-luminal thread model was used for all *in vivo* stroke experiments.

### 7.4.1 The Intra-luminal Thread Method

The focus of our experiments was to measure TSC after MCAO without reperfusion. Therefore, the intra-luminal thread model was preferred as the surgical technique to set up the stroke model (Figure 7.10).

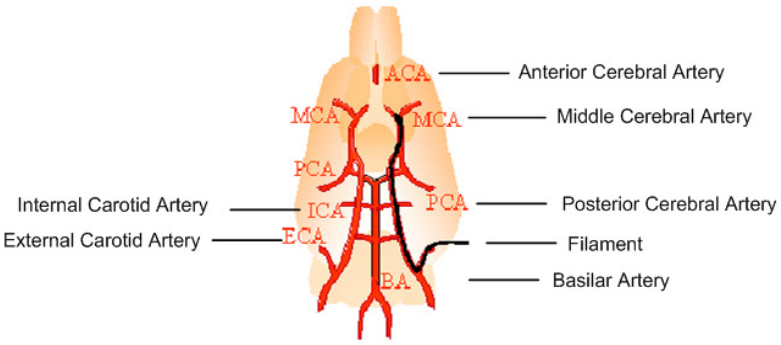


**Figure 7.10: The cerebral vascular system in a rat brain and the filament path used for the MCAO model.**

The surgical procedure was developed by the Glasgow University-based stroke research group lead by Prof. Mhairi Macrae (GEMRIC – Glasgow Experimental MRI Centre), with the actual stroke induced by their experienced animal senior technician, Lindsay Gallagher. The filament was inserted into the right external carotid artery where it was slid in to the beginning of the MCA. The final filament position was determined by the operator, relying on a tactile resistive threshold that was developed during long-term experience with the MCAO model. A sketch of the extracted vessel system and the surgical procedure is outlined in Figure 7.11. Surgery was supported by the use of a Carl Zeiss® S-21 surgical microscope (Jena, Germany) and all experiments were carried out under appropriate animal license and ethics approval. The following steps were carried out before the filament was inserted:

1. The common carotid artery was tied.

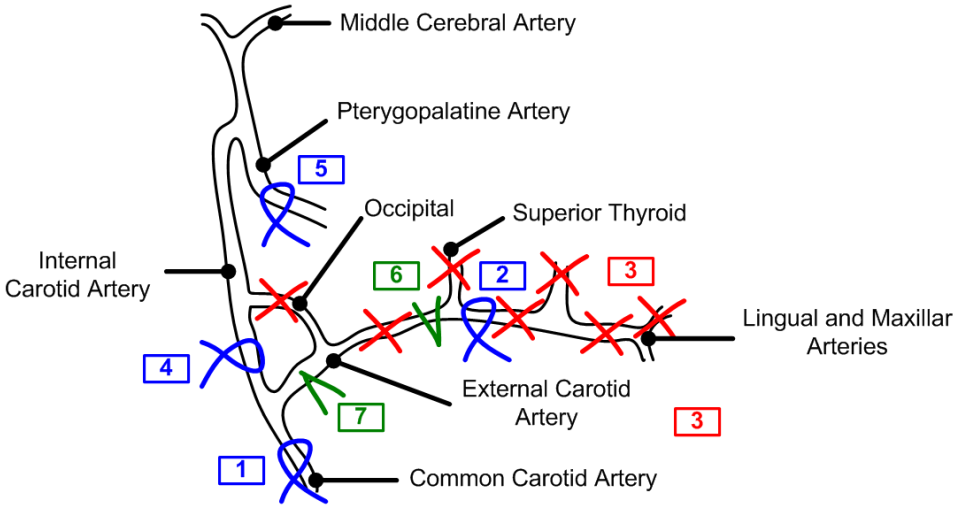


**Figure 7.11: Sketch of the surgical procedure in preparation for the filament insertion. Red crosses indicate points of diathermia, blue loops indicate ligature, and green tips indicate cuts.**

2. The external carotid artery was tied.
3. The superior thyroid max and lingual branches as well as parts of the external occipital artery were occluded via diathermia.
4. The internal carotid artery was loosely tied so that the filament could still pass through it. This was to fixate and stabilise the filament during the experiment.
5. The pterygopalatine artery was tied.
6. The external carotid artery was cut to free the vessel.
7. The external carotid artery was cut on one side above the bifurcation to insert the filament.

The final filament insertion is illustrated in Figure 7.12.

### 7.4.2 Monitored Physiological Parameters

The continual real-time monitoring of the physiological parameters of the rats was critically important in order to maintain the stability of the animal during the long duration (typically ~ 7 h) of the experiments. The monitored parameters and their respective physiological ranges are given in the following paragraphs.

#### 7.4.2.1 Electro Cardio Gram (ECG)

Two electrodes were placed across the chest and one reference electrode was fixed at the right leg. The contact areas were shaved and freed of hair to increase the conductivity between tissue and electrode.

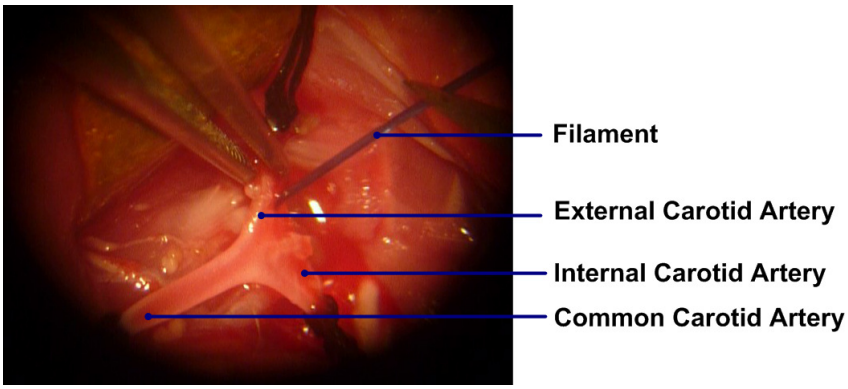


**Figure 7.12: Photograph of the filament insertion taken through the surgical microscope.**

The heart rate was monitored as extracted from the ECG signal and stabilised between 300 and 450 beats per minute (bpm). For comfort, the heart rate was ideally maintained between 350 and 400 bpm.

#### 7.4.2.2 Respiration

A small pressure transducer attached to the abdomen served as respiration measuring probe. The respiration was set by the respirator at 60 bpm. The qualitative respiration curve gave an indication of the breathing abilities of the animal. One third of the respiration cycle was supposed to correspond to inspiration. An A-shaped cycle indicated tracheal blockage.

The positioning of the animal on its belly complicated the stabilisation procedure and occasionally caused the occlusion of the tracheal respiration path. Such blockage was cleared by disconnecting the respiration tube from the respirator and blowing through it by mouth. The proper respiration of small animals was furthermore challenging because their lung volumes were very small compared to the tube length dependent volumes and its system compliance (1 l/min was delivered into a 1.5 ml lung volume).

#### 7.4.2.3 Temperature

The temperature was monitored by the signal given from a thermo-resistive rectal probe. The temperature was maintained through a temperature-controlled water bath that supplied a heat blanket with water which in turn was covering the rat's body. The physiological temperature ranged from 36.6° C to 38.0° C with an ideal temperature at 37.7° C. A temperature above 39° C indicated a severe problem with the state of the animal's health. However, this case never occurred throughout the experimental series.

#### 7.4.2.4 Blood Pressure Line

An invasive blood pressure line was set up with a glass catheter introduced into the left leg's femoral artery. The blood pressure was maintained within the range of 80 to 85 mmHg. A blood pressure-related heart rate was also computed from these measurements to compare to the ECG related heart rate. By these means the blood pressure could be monitored, even when the ECG signal was corrupted by the changing magnetic fields during the MRI experiment.

#### 7.4.2.5 Blood gases analysis

The invasive blood pressure line was also used to withdraw blood samples for later blood gases analysis. The $O_2$, $CO_2$ concentrations, and pH values were monitored. The $O_2$ concentration was maintained within the range of 80 to 100 mmHg, the $CO_2$ concentration was maintained within the range of 35 to 45 mmHg, and the pH value was maintained within 7.35 to 7.45.

The reduction in $CO_2$ concentration could have been caused by an excess of $O_2$ blood gas content. By decreasing the air gases volume supplied to the lungs, the $CO_2$ concentration was stabilised. The observation of $O_2$-saturation in % was also important, because values below 98 % changed the blood gases and may have indicated a possible blockage of the trachea.

#### 7.4.2.6 Anaesthetic

The animal was kept anesthetised via a facial breathing mask that delivered the anaesthetic as a gaseous mix of 2 - 3.5 % isoflurene in 1 l/min air gases that were composed of 30 % oxygen and 70 % nitrogen. A reduction in blood pressure indicated a possibly too high anaesthetic gas supply.

### 7.4.3 Experimental Workflow

In preparation for the MRI experiment, the rat was anesthetised and positioned on an animal support cradle, which could be moved in and out the bore of the magnet. The rat was kept warm by a blanket which was connected to warm water circulation. The ECG electrodes and the rectal temperature probes were fixed. The rat was transferred into the magnet room, where the various electric and fiberoptic cables were connected to the monitoring system; blood samples were withdrawn via a glass catheter. The receive-only surface coil was placed on the rat's head, with the rat's head positioned underneath and one fiducial vial above the coil. The coil system was tuned and matched on site using the Bruker system's facility. $^{1}$H automatic adjustments were started before a TriPilot was scanned to verify correct sample and coil positioning inside the magnet. Manual adjustments were performed using a $^{23}$Na FID experiment. $^{23}$Na MRI data was acquired for up to 7 h followed by one $T_2$-weighted $^{1}$H RARE anatomical scan. Blood gases were measured every hour; while heart rate, blood pressure, breathing rate, and temperature were continuously monitored. The physiological parameters were stabilised by variations in anaesthetic gases, blanket temperature, and air gases supply during the entire length of the experiment.

Ten rats were scanned, with eight strokes and two sham surgical operations performed. Stroke 1 and 2 served as pilot studies and were not further analysed, because the first measurement was taken later than 1 h after MCAO. Stroke 6 suffered from arterial bleeding and had to be sacrificed at 2 h after MCAO. Thus stroke 3, 4, 5, 7, and 8 were analysed as stroke models for the Chapters 7 and 8, and the two sham surgical animals were analysed to test for a proper model setup referred to as sham 1 and 2 in Chapter 7. The analysed stroke animals are henceforth referred to as Stroke 1, 2, 3, 4, and 5.

### 7.4.4 Histology

After the experiment (approximately 8 h post MCAO), the animal was removed from the magnet and sacrificed. The brain was removed from the skull and frozen in before further processing. The processing involved cutting the frontal cerebral hemisphere into 40 µm thick slices that were then stained with haematoxylin and eosin, a double stain used to identify ischaemic neurons. The haematoxylin served as neuronal and the eosin as cytoplasmic stain. This gave a good contrast between healthy and vulnerable cells.

Histology is the current state-of-the-art to find the exact ischaemic stroke volume after MCAO, because the state of the neuron (round/ shrunken) can be exactly assessed under the microscope (Figure 7.13). If the animal is allowed to survive for 24 h the boundary between stained infarct and normal tissue becomes much clearer, which allows identifying infarct regions on the basis of brighter and darker stained areas on the histology sections (Figure 7.14). One representative histology slide was picked for each of the eight levels of the stereotaxic atlas.

**(a)** **(b)**

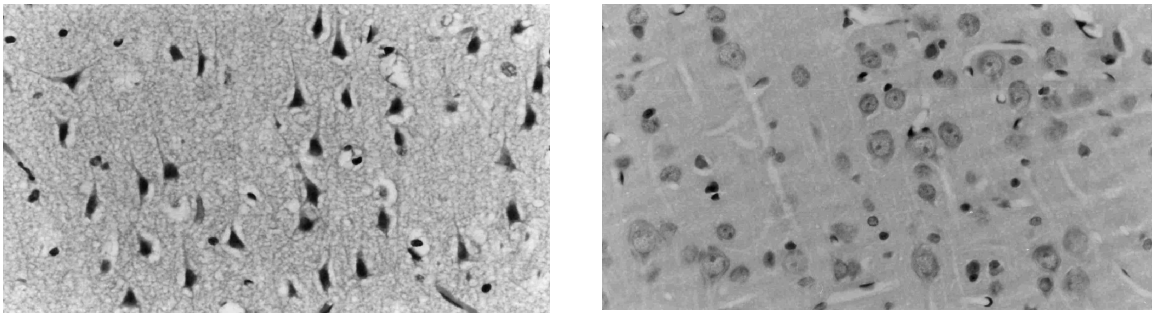

**Figure 7.13: Haematoxylin and eosin staining in striatum at 4 hours post-stroke. (a) Ischaemic tissue: neuron cell bodies are shrunken, triangulated and darkly stained with condensation of chromatin and a spongy neuropil (matrix surrounding neurons). (b) Normal tissue: neurone cell bodies are round with pale staining and have a regular shape, with a large nucleus and smaller cytoplasmic volume (these are representative microscopy images, which were included by courtesy of Prof. Mhairi MacRae, Glasgow University).**

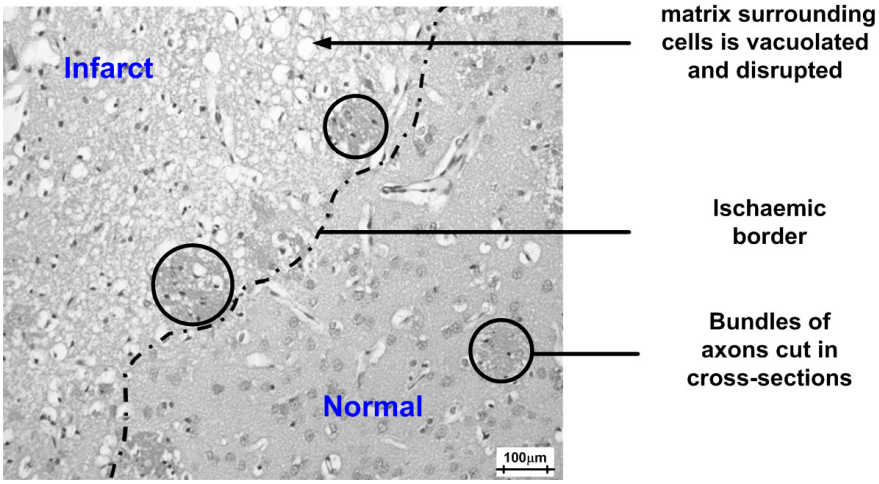


**Figure 7.14: Differences in the shape and staining intensity of neurones are apparent, when viewed through a microscope, which allows one to draw a boundary between histologically normal tissue and irreversibly damaged tissue (infarct). Normal: Neuropil (matrix surrounding cells) staining is much more homogeneous. Ischaemic: Neuropil is disrupted and vacuolated. Left upper corner shows ischaemic area, dashed line indicates ischaemic border evident following MCAO. Right lower corner represents normal neurons/ healthy tissue. This type of infarct border was evident in all subjects and aided in transcription of the infarct area across sections examined (this is a representative microscopy image, which was included by courtesy of Prof. Mhairi MacRae, Glasgow University).**

Where the eight levels cover the entire area of the frontal lobe, with Level 1 beginning at the frontal cortex through to Level 8 - central brain.

Photographs were taken of the eight sections for each brain, which were used for a qualitative assessment of the stroke extension. For an exact volumetric lesion measurement, the ischaemic border had to be manually transcribed into line diagrams, based on the stereotaxic atlas. The MSET® software was then used to digitise the line diagrams with the marked area of infarct. The PRISM® software package was employed to compute the actual lesion volume. The volume of the contralateral hemisphere was assumed to be constant at 575 $mm^3$ for every rat. Correction factors for the hemispheric swelling were incorporated into the computational procedure. The error of the volumetric measurement was given to be below 5 %.

## 7.5 Results

### 7.5.1 Histology

The area of infarct was identified by being the paler one in the right hemispheres at a macroscopic level (Figure 7.15). The digitalised photographs were saved in TIFF format scaled in 256 integer gray scale values.

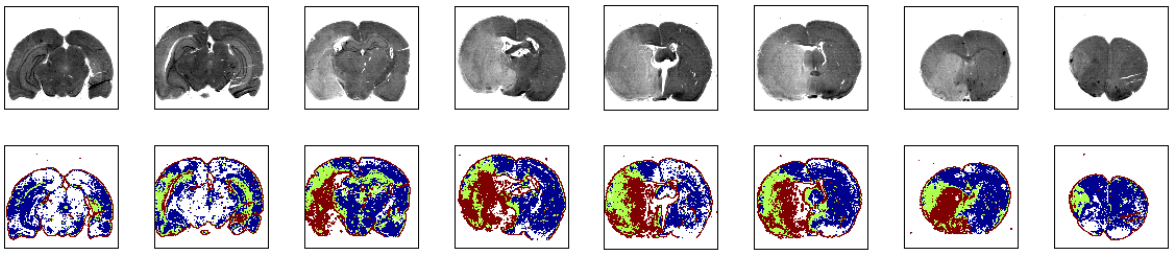

**Figure 7.15: Histology results after MCAO for each of the 8 levels encompassing the brain from one representative stroke brain (stroke 2) as black and white photographs (upper row), and threshold contour maps of the same black and white photographs (lower row). The lesion was clearly marked by brighter areas in the photographs and green and blue coloured areas in the contour maps. The lesion was extended across parts of caudate-putamen (brown) and cortex (green) in the right hemisphere (left brain side in the image).**

For the contour map plots and an easier qualitative assessment of the lesion area, the greyscale values in infarcted and normal areas were extracted from a cross section plot of the level 4 slide. The normal tissue was well represented by greyscale values of 122 (coloured blue in Figure 7.15). The infarcted tissue was represented by greyscale value 128 (brown) for cortex, and 133 (green) for caudate-putamen in the histology photographs taken of stroke 2. It was difficult to ascertain the exact greyscale value, which distinguished infarcted from viable neuronal tissues. Thus, a microscopy-based lesion delineation of the histology images and an exact infarcted volume computation was carried out at Glasgow University. The results are tabulated in conjunction with the qNa-MRI results in Table 7.2.

### 7.5.2 TSC Measurements after MCAO Sham Surgical Operation

To test for surgery-related TSC changes other than stroke, two MCAO sham surgical operations were performed and the MRI scanning protocol applied. $^{23}$Na MR images were acquired from 0.5 to 4.5 h after the sham MCAO procedure. TSC was quantified and the TSC maps were co-registered with the $^{1}$H images (Figure 7.16). The brain was manually selected from the $^{1}$H images and brain masks were computed. The TSC maps were masked and the maps were smoothened by a two-dimensional convolution kernel. No change in TSC was observed in the right cerebral hemisphere over time as was expected after the sham surgical operation.

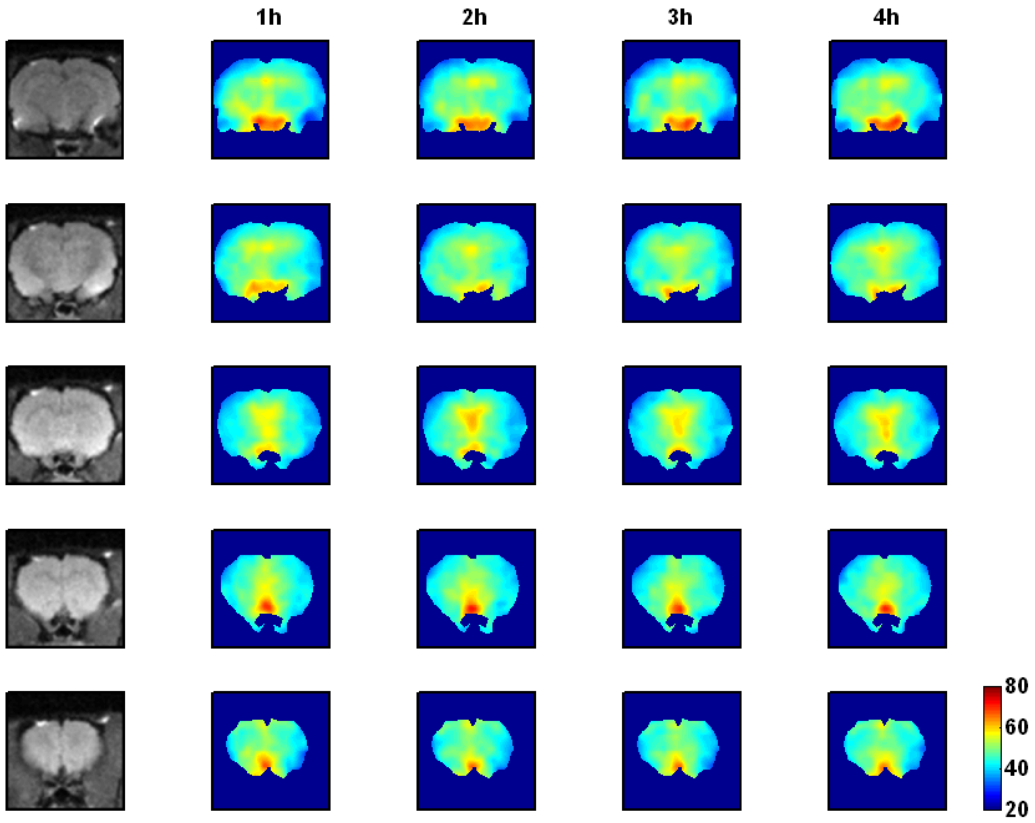


**Figure 7.16: The evolution of TSC after the sham surgical MCAO operation. Rows 1 to 5: five slices across the rat brain (2 mm slice thickness); Column 1: $^{1}$H anatomical images; Column 2 to 5: TSC maps from 1 to 4 h after MCAO. The measurement time points are labelled above the TSC maps and the colour bar indicates TSC in units of mM. Note that cerebral TSC remained constant in the right hemisphere (left brain side in the TSC map) over time after the sham surgical operation.**

### 7.5.3 TSC Measurements after MCAO

Five Sprague Dawley rats (~ 300 g) were set up according to the previously described stroke model and $^{23}$Na images were acquired from 0.5 to 8 h post MCAO. The internal reference of the contralateral normal brain hemisphere and the fiducial reference vial were manually marked for co-registration and quantification purposes. The TSC was quantified and the TSC maps were co-registered with the anatomical $^{1}$H images. The brain was manually selected from the $^{1}$H images and brain masks were computed. The masks were superimposed on the TSC maps that were initially smoothened by a two-dimensional convolution kernel. Increasing TSC was measured in the right hemisphere of the frontal cortex including regions of cerebral cortex and caudate-putamen (Figure 7.17). TSC values of up to 140 mM were measured in stroke tissue. For a quantitative temporal TSC map analysis, linear regression was computed for TSC in every voxel *j* over time.

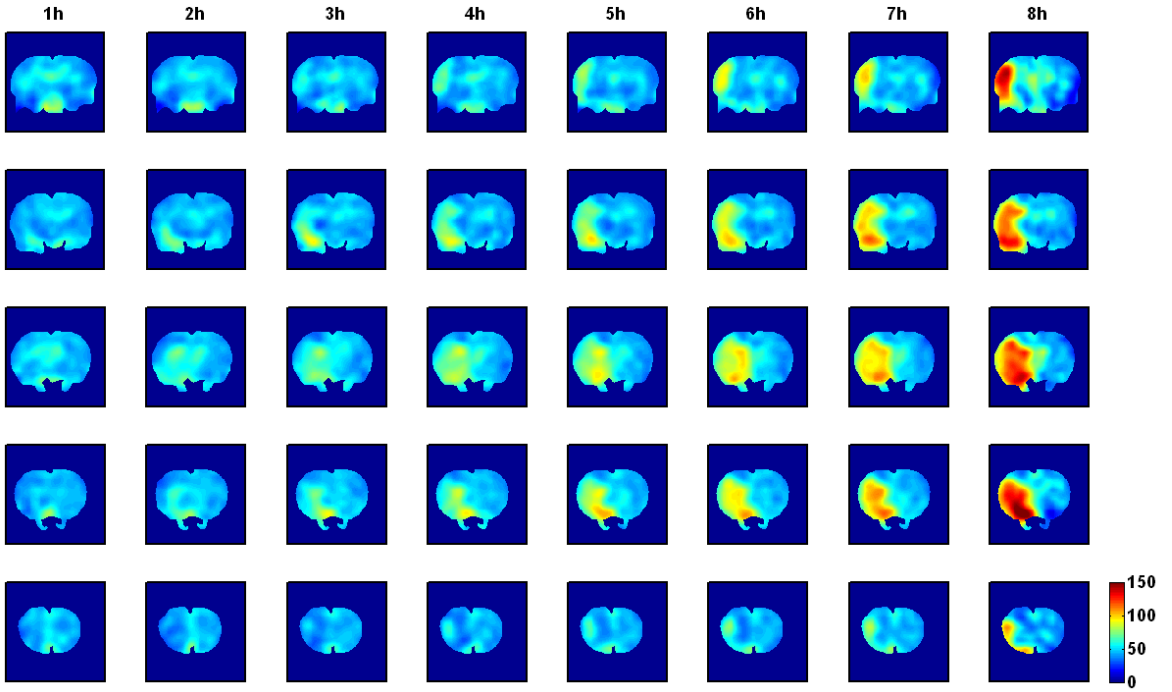


**Figure 7.17: The evolution of TSC after MCAO for 5 slices across one representative brain (stroke 2). Times after MCAO are labelled above each column and the colourbar indicates TSC in mM. Note that TSC changed in the ischaemic lesion on the right hemisphere (left brain side in the TSC map) after MCAO.**

The TSC was assumed to increase linearly with time post MCAO, $t_{pMCAO}$, allowing for the derivation of the slope constant $c_{slo,j}$ and $c_{off,j}$ in voxel $j$:

$$TSC_j(t_{pMCAO}) = c_{slo,j} \cdot t_{pMCAO} + c_{off,j} \qquad \text{(Equation 7.19).}$$

The assumption of a linear increase in TSC during the acute phase of stroke was derived from published data suggesting such linear increase in similar stroke model [5, 12, 13]. The linear slope maps for the five brain slices through the stroke lesion are presented in Figure 7.18 together with TSC maps, $^1$H $T_2$-weighted images, and histology contour maps. Note that the maximum slope was measured with similar values in peripheral cortex and core caudate-putamen regions. To determine the average TSC slope for the stroke lesion, other studies employed the TSC slope threshold method [5, 12], where the stroke lesion was determined as the amount of voxels exhibiting TSC slopes above the TSC slope threshold (e.g. > 90 % of the maximum TSC slope). The maximum slope was determined for each rat and two thresholds were set to 60 and 90 %. Thus the amount of voxels with TSC slopes above 90% was smaller compared to the amount of voxels with TSC slopes above 60 %. The RoIs with slopes > 90 % and > 60 % are henceforth referred to as 90 % and 60 % maximum TSC slope RoIs, respectively. The mean and standard deviation was computed for the 90 % and 60 % maximum TSC slope RoIs for all five stroke experiments and are tabulated in Table 7.2.

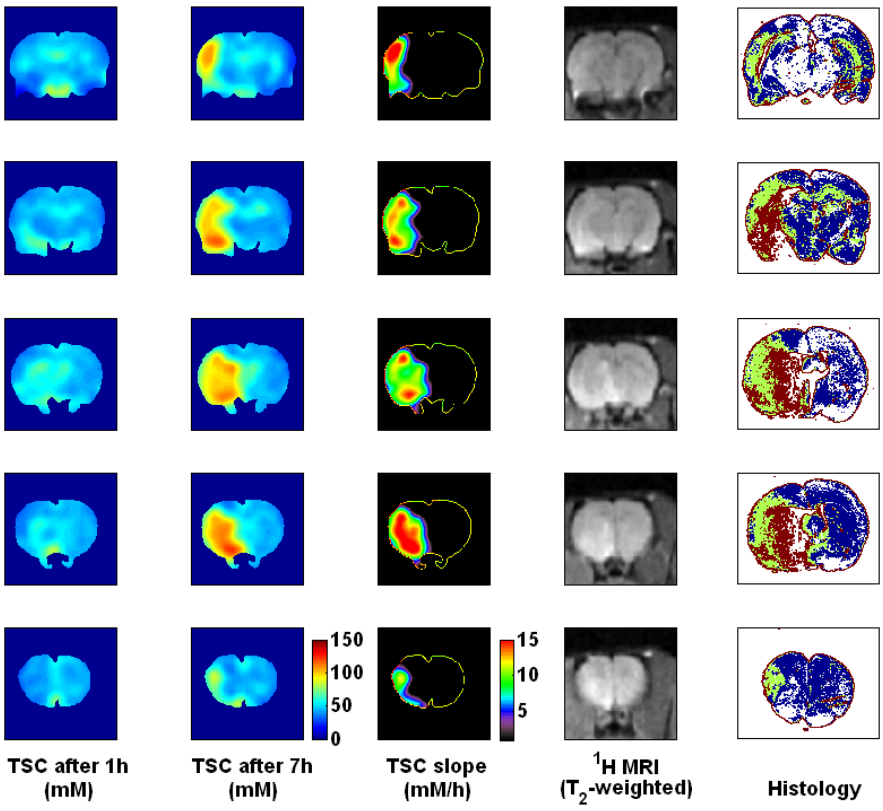


**Figure 7.18: Analytic results for one representative brain (stroke 2). The stroke lesion could be delineated by increased TSC in the left hemisphere and by a significant TSC slope during the 7 h measurement period. These $^{23}$Na-MRI lesion delineations correlated well with the corresponding histology-delineated lesions, as indicated by the green and brown coloured histology images in the last column. Only slight $T_2$-weighted signal intensity changes were observed in the $^{1}$H MR images measured at 7 h after MCAO, demonstrating their lack of diagnostic usefulness at this early time point.**

The histology-defined stroke lesion correlated closely with the boundaries of the 60 % maximum TSC slope RoI in all five rats. The large stroke size, coupled with the high spatial resolution achieved in the current study, allowed for a qualitative analysis of TSC over time in various regions of expected core and penumbral areas. The averaged TSC values over core, periphery, and contralateral normal tissue were extracted from respective RoIs in the TSC maps and graphed in Figure 7.19. In contralateral normal tissue, TSC remained constant over the entire scanning time, whereas increasing TSC was measured in both the periphery and the core stroke regions. Major regional differences were observed in the onset time of TSC increases, with delay times approaching 2 h measured in the peripheral regions.

**Table 7.2: Slopes for TSC measurements in stroke tissue from 0.5 to 8 h after MCAO.**

| | *Brain Areas with 60 % maximum TSC slope* | *Volume determined from histology slides ($mm^3$)* | *90 % maximum TSC slope (mM/h)* | *60 % maximum TSC slope (mM/h)* |
|---|---|---|---|---|
| ***Stroke 1*** | ***CP and Cortex*** | ***290 ± 15*** | **9.6 ± 0.3** | **7.6 ± 0.9** |
| ***Stroke 2*** | ***CP and Cortex*** | ***260 ± 13*** | **11.5 ± 0.3** | **9.8 ± 1.3** |
| ***Stroke 3*** | ***CP and Cortex*** | ***340 ± 17*** | **12.6 ± 0.2** | **10.6 ± 1.3** |
| ***Stroke 4*** | ***CP*** | ***184 ± 9*** | **12.6 ± 0.4** | **10.2 ± 1.5** |
| ***Stroke 5*** | ***CP*** | ***110 ± 6*** | **14.1 ± 0.4** | **11.9 ± 1.6** |
| ***Population Mean*** | | ***237 ± 91*** | **12.1± 1.7** | **10.0 ± 1.6** |

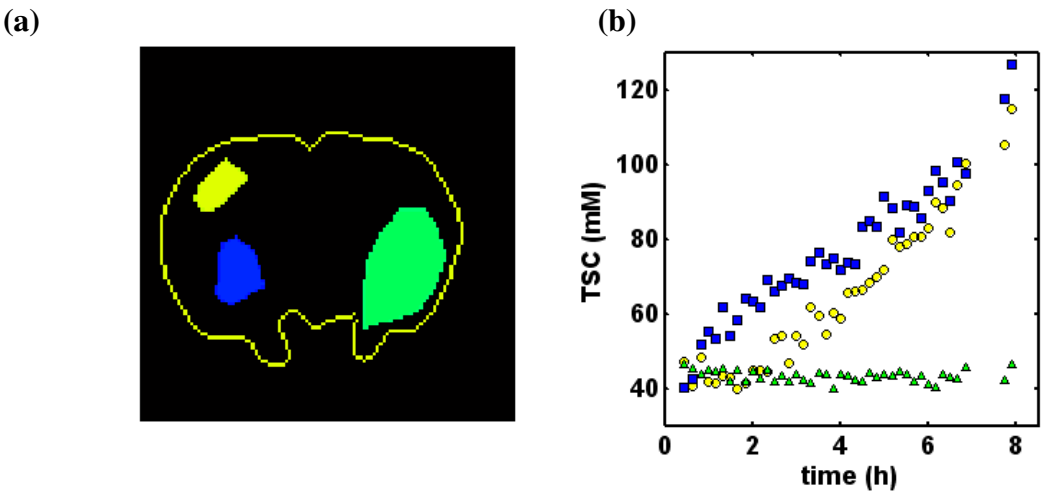


**Figure 7.19: (a) RoIs corresponding to regions of caudate-puatamen (blue), cortex (yellow), and contralateral normal tissue (green). (b) The TSC in these RoIs as a function of time in the hours after MCAO. Note that TSC increased within 1 h after MCAO in caudate-putamen tissue (blue squares), whereas TSC increase was delayed by up to 2 h in cortex tissue (yellow circles). The TSC in contralateral normal tissue (green triangles) remained constant.**

## 7.6 Discussion

The analysis of the measured TSC data sets using a linear regression model allowed for the comparison of the TSC slope results in this study with the TSC slopes published by others. Jones *et al*. computed an average TSC slope of 25 ± 5 %/h in four rats [5], and Yushmanov *et al*. computed an average TSC slope of 22 ± 4 %/h over eight rats [12], both employing a comparable MCAO model to the model used for the current work. In the current study, TSC was quantified in rat brain after MCAO with high spatio-temporal resolution. The TSC slope averaged at 22 ± 4 %/h over five rats in the infarcted stroke tissue volume.

Thus the TSC slope values in the here presented study corresponded well with the TSC slope values published by the others [5, 12].

In addition to the quantitative results, the current study provided an early acquisition of the TSC time course data after MCAO, from as early as 26 min out to 8 h after stroke onset time in five rats. The first data point after MCAO was sampled significantly earlier than in previously reported MCAO rat studies [5, 13]. For instance, Jones *et al*. measured TSC in four rats with the first acquisition time point being delayed by 2 to 4 h after MCAO [5]. In a more recent study involving eight rats, the earliest time point at which the TSC was measured was 1.1 h after MCAO in one rat, and although the mean starting time was not mentioned, the acquisition time window of 2 to 4 h at 1.1 to 7.3 h after MCAO suggests that much later start times (> 2 h ) were used for the other seven rats [13]. As a result, the evolution of the TSC in the crucial early phase after MCAO was not measured which may have lead to erroneous conclusions about regional TSC changes in these studies.

Yushmanov *et al*. [13] reported on higher TSC slopes in the periphery (22 %/h) than in the core (15 %/h), which was attributed to a better collateral perfusion than in caudate-putamen [12]. Nevertheless, in the current study the TSC slope was found to be maximal in both the peripheral (cortex) and the core (caudate-putamen) stroke tissue contradicting the principle findings by Yushmanov *et al*.. Three of five strokes extended across the caudate putamen and cortex regions (stroke 1, 2, and 3). The maximal slope was always found to be centrally located in the core of the caudate-putamen and the cortex stroke tissue. To explain the variations in TSC slopes measured in the different RoIs of the stroke lesion, one must discuss the TSC time course data in these tissues.

The quantitative analysis of the TSC time course data in two different RoIs of cortex and caudate-putamen resulted in two main observations:

1. TSC increase was delayed by up to 2 h in the cortex tissue, whereas this delay was measured < 1 h in caudate-putamen, and
2. The rate of TSC increase was the highest immediately after the TSC increase started and levelled off approximately 2 h later.

These observations were evident in all five strokes and could only be made due to the early measurement of the regional differently changing TSC after MCAO. Hence, the local TSC increase after MCAO is non-linear and consequently a non-linear curve fit is necessary to appropriately analyse the measured TSC time course data.

Moreover, the non-linear TSC increase explains the discrepancies of the measured TSC slopes in cortex and caudate-putamen tissue in earlier studies (e.g. [12]), where the acquisition window started later than 1 h after MCAO. As a result, fitting a line to the measured time courses from 2 h to 7 h post MCAO would result in different TSC slopes measured in the cortex and caudate-putamen regions, as was erroneously reported by the authors. A non-linear TSC increase ultimately leads to lower TSC slopes in caudate-putamen tissue, where TSC was in fact observed to level-off at 2 h after MCAO after an early onset (< 1 h after MCAO) of TSC increase. On the other hand, higher TSC slopes could have been measured from 2 to 7 h after MCAO in cortex tissue, with the onset of the measured TSC increase delayed by up to 2 h. Thus, the initially high rate of TSC increase and the delay to TSC increase led to an overestimated TSC slope in the cortex tissue compared to an underestimated TSC slope in the caudate-putamen tissue, when the measurement was started later than 1 h after MCAO. Therefore, it is felt that the higher TSC slopes for periphery compared to core regions reported elsewhere [13] are an artefact of the data fitting employed and the lack of data in the early phase after the MCAO.

Regarding the delay time, several recent publications reported on a similar delayed TSC increase. Bartha *et al*. found a 11 % ± 8 % decrease in $^{23}$Na MR signal intensity for the initial 40 min followed by a 20 % $^{23}$Na signal intensity increase in rabbit brain tissue over the last 200 min of their 240 min long experiment [3]. In another study conducted by LaVerde *et al*., where $^{23}$Na concentration increases were measured in stroke brain tissue of a non-human primate [41], stroke onset time was estimated with up to 0.45 h delay before TSC increase. Thulborn *et al*. recorded TSC evolution after MCAO in one monkey brain [86]. TSC was analysed in cortex core and cortex periphery. Relatively small slopes of only 1.2 mM/h were reported in cortex periphery regions out to 400 min after MCAO, whereas TSC was found to increase immediately in the core region of the cortex (5.0 mM/h). The TSC slope in the peripheral cortex region was > 5 mM/h at time points later than 400 min after MCAO. However, the significance of the low TSC slope values reported in cortex periphery (1.2 mM/h) for the initial 400 min after MCAO must be considered in relation to the experimental quantification error. Although the authors did not quote the quantification error in their study, it is reasonable to suggest that it may have been strongly degraded by swapping the $^{1}$H and $^{23}$Na resonators, which was required for interleaved $^{1}$H and $^{23}$Na imaging (which was, in fact, performed four times during the course of the experiment). The quantification error could be further estimated from a similar TSC study, where a zero-slope in normal tissue of the monkey brain was found to vary by ± 2.2 %/h (± 1 mM/h) and the resonators were not swapped during the course of

the experiment [41]. This variation might have been similar in Thulborn's experiment. Thus, including the resonator changing, the measured slope of 1.2 mM/h was most likely insignificant. The hypothesis of the authors was that TSC increases in all stroke regions from the very first moment after stroke onset and could be reversed through tissue reperfusion as long as TSC was below a certain threshold, proposed to be 70 mM [8]. Thus, the apparent discovery of a slightly increasing TSC in peripheral tissue supported their TSC threshold hypothesis, where still viable tissue can have TSC levels < 70 mM. If one considers the time over which this low slope behaviour was exhibited rather as a delay time, their results correspond qualitatively well with the results found in this thesis.

Fitting a line to the measured TSC data was the first approach taken to analyse the measured data and followed the example given by other groups working in the field of $^{23}$Na-MRI and MCAO models. However, since the measured time course data exhibited a strong non-linear time course, it was necessary to develop a non-linear model to match the TSC time course data more appropriately and extract parameters, which would allow for the determination of the infarcted stroke tissue volume.

In conclusion, linear TSC slopes compared well with TSC slopes reported by other studies. For the first time it was found that TSC increase was delayed across the lesion, while TSC increased immediately in core (caudate-putamen), the TSC increase was delayed by approximately 2 h in the periphery (cortex). Chapter 8 describes the development of a non-linear TSC model to enable the quantitative analysis of TSC rate and delay time after MCAO in all five rats.

# 8 The Development of a Non-Linear Model for TSC Increase after MCAO

The measurement of TSC from a very early time point after MCAO and a linear model fit to the TSC time course data was described in Chapter 7. However, upon closer examination of the time course data in core and peripheral regions of the stroke lesion, it was concluded that a linear fit was inappropriate. The aim of the work presented in this chapter was to develop and describe a more suitable non-linear model for temporal TSC increase after MCAO and to re-analyse the time course data with this model in order to achieve novel insights about the progression of infarction after stroke onset time.

## 8.1 Introduction

Various TSC time course data after stroke have been reported in the literature. In addition to linear fits to the TSC increase after stroke onset time, delayed increases in TSC and initially decreases in TSC have been reported.

A linear increase in TSC was measured by Jones *et al*. who reported on a data set acquired between 2 and 7 h after direct surgical transsection of the MCA (MCAT) in rats [5]. The same group further reported a linear TSC increase within the 1 to 7 h period after MCAO [12, 13]. The former paper furthermore claimed that stroke onset time could be estimated from the linear TSC evolution with an onset time error (OTE) ranging from -6 to13 min [5]. Nevertheless, in a more recent study in non-human primate brains by LaVerde *et al*., the OTE had a quoted accuracy of 27 min after physical stroke induction [7].

Non-linear TSC curves were moreover reported by Bartha *et al*., who measured an initial decrease in TSC before observing a subsequent linear increase in seven rabbit brains after embolic occlusion of the MCA [3], and Thulborn *et al*. who measured a slightly increasing TSC during the first 1.6 h (1.2 mM/h) and a faster increasing TSC for the next

6 h (5.7 mM/h) after embolic occlusion of the MCA in one non-human primate brain [8]. These variable results reveal an underlying uncertainty about the initial evolution of TSC after stroke, which might also be lesion size and location dependent. This was indicated by a recently published study on human stroke and the measurement of TSC, which found that TSC increased by 68 % from normal TSC at 48 h after stroke onset time [110].

A comprehensive delayed-exponential model was therefore developed to fit the measured TSC time course data after MCAO, which was then used to compute pixel-based parameter maps. From these maps, a measure of the infarcted tissue volume as a function of time was inferred.

## 8.2 The delayed-exponential TSC Model

The non-linear model was derived from the measured TSC time course data and the known physiological extra- and intra-cellular $^{23}$Na concentration values. In Chapter 7, the TSC time course data was analysed for two different RoIs, which were manually defined to cover either the cortex or the caudate-putamen regions. The major difference between these time courses was that the TSC increase was temporally delayed in the cortex, whereas TSC increased immediately in the caudate-putamen. It was necessary for the non-linear model to replicate this delay time to TSC increase. Furthermore, the measurable TSC must level off at a physiologically sensible value, which is obviously not taken into account with a simple linear fit. Although the limited measurement time range of up to 8 h after MCAO in the current study prevented the experimental confirmation of the maximum achievable TSC value, it can be assumed to be limited by the extra-cellular $^{23}$Na concentration value of 140 mM [30]. Moreover, since $^{23}$Na ions migrate along a $^{23}$Na concentration gradient until an equilibrium state is achieved and also taking into account the measured exponential TSC time course for caudate-putamen, it was hypothesised that the maximum TSC is approached in an exponential rather than linear manner. Consequently, a non-linear model was developed, based on a delayed-exponential time course concept, comprising a linear section, typically with zero or close to zero slope, followed by an exponentially increasing section. The TSC in the exponential section was modelled as follows:

$$TSC_j(t) = \quad c_{init,j} + (140mM - c_{init,j}) \cdot \left(1 - e^{\frac{t - t_{del,j}}{\tau_j}}\right) \qquad \text{(Equation 8.1).}$$

where the $TSC_j(t)$ in voxel $j$ at time $t$ depends on the initial TSC, $c_{init,j}$, the delay time $t_{del,j}$ and the time constant $\tau_j$. The linear and exponential TSC time course sections were

separated by the delay time. The delay time characterises the duration of the linear description of the TSC time course, and the delay time value marks the point at which the TSC actually increases with respect to the time of MCAO. The following algorithm for fitting the discontinuous delayed-exponential function was developed:

1. The TSC time course data for a single voxel was extracted from the quantified TSC maps.
2. To determine whether the extracted voxel was located within the stroke lesion, a linear fit to the entire TSC time course data for that voxel was performed, and a resulting slope > 2.4 mM/h (over the measurement window of 8 h) was presumed to qualify as stroke tissue. Note that the quantification accuracy for the experiment was < 10 mM. Thus a TSC change > 20 mM (twice 10 mM) after 8 h could be considered as a significant TSC difference; resulting in a TSC slope threshold of 2.4 mM/h.
3. The initial TSC was estimated as the average of the first three data points.
4. If the initial TSC was measured to be > 55 mM, the TSC was assumed to have already increased, and consequently the initial TSC was assigned to a value of 45 mM and the delay time was set to 20 min. The delay time was more accurately determined after the later exponential least square fit to within ± 20 min.
5. If TSC was measured to be ≤ 55 mM, the first derivative of the TSC time course data with time, d*(TSC)*/d*(t)*, was computed starting with the determined initial TSC value and including consecutive sampling points one after the other in order to determine the amount of data points which corresponded to the linear section of the delayed-exponential model.
6. The absolute TSC slope was considered to be zero, when measured below 2.4 mM/h. The latest time point after MCAO at which the TSC slope was measured < 2.4 mM/h was assigned to the delay time. See Figure 8.1 for a graphical interpretation in a single voxel example for the delay time pre-estimation.
7. The exponential least squares problem was solved for the TSC data points which corresponded to an exponential TSC increase, beginning with the first data point sampled at the delay-time until the final acquired data point. The parameter boundaries were set to ± 1 mM for the initial TSC, and the TSC offset, to between 0.1 and 24 h for the time constant, and to ± 20 min for the delay time.

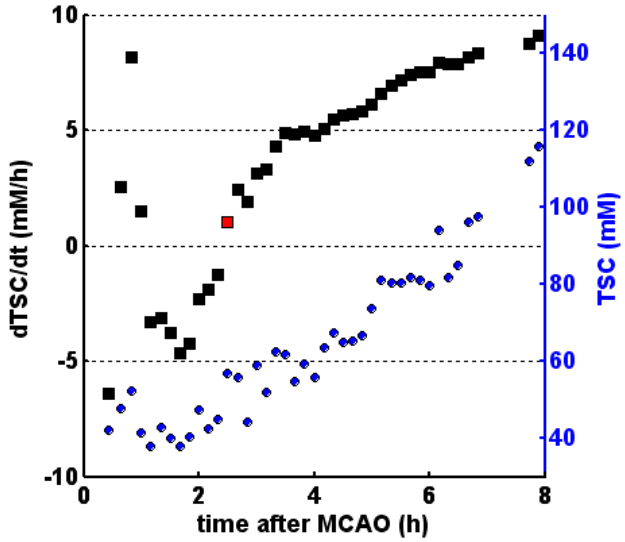


**Figure 8.1: The derivation of the delay time from the measured single voxel TSC time course data (blue circles) and the temporally evolving TSC slope, which was computed as the first derivative of the TSC with time (black squares). The delay time corresponded to the latest time after MCAO at which the absolute TSC slope remained below 2.4 mM/h (this is indicated by the red square). The initial TSC was derived from the average of the first three TSC values, at approximately 45 mM in this case. The data points acquired after the delay time (i.e. after the red square) were extracted for exponential curve fitting. The delay time estimate was further refined by the exponential least square fit within a ± 20 min time window.**

The delay-time and time constant parameters were computed for every pixel within the stroke lesion and parameter maps displaying the spatial distribution of the exponential time constant and delay time were generated. For a better understanding of the parameter map computation and their meanings, the delayed-exponential model that was computed for one slice (slice 3) of stroke 2 is illustrated in Figure 8.2. This illustration focuses on four particular voxels extracted from different regions within the stroke lesion, and serves to investigate possible variations in $^{23}$Na nuclei accumulation between core and peripheral tissue with regards to delay-time and time constant. From this model, an approximate 2 - 3 h difference in delay time was determined between periphery and core in both cortex and caudate-putamen. The voxel coordinates given above each graph in Figure 8.2 can be used to localise the respective stroke tissue region in the accompanying delay-time and time-constant maps, in order to relate the measured TSC time course data to the spatial location within the stroke lesion.

The rate of TSC increase, which is inversely related to the derived exponential time constant, was measured to be higher in the central region of each brain area (i.e. caudate-putamen and cortex) compared to the periphery of each area.

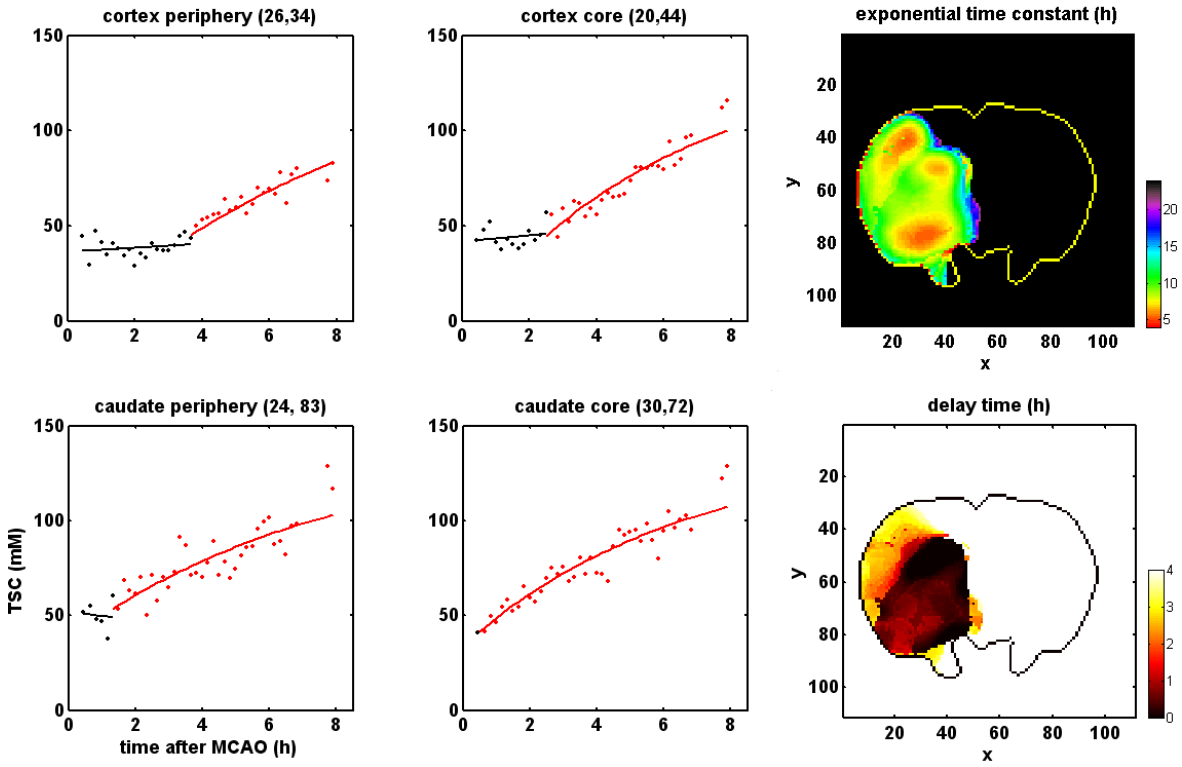


**Figure 8.2: The delayed-exponential model fit to the TSC data measured in single voxels of caudate-putamen and cortex. Note the differences in delay time between cortex and caudate-putamen as well as between cortex periphery and cortex core. The voxel locations can be extracted from the TSC slope and delay time maps by the coordinates (x,y) given above each graph.**

Furthermore, caudate-putamen was clearly differentiable from cortex tissue in both the time constant and the delay time maps. By contrast, these regions were not separable from each other in the linear TSC slope maps computed in Chapter 7.

## 8.3 The Physiological Interpretation of the Delayed-Exponential Model

The measurement of a delayed TSC increase after MCAO in this study suggests that the current biological model, which assumed an immediate linear TSC increase after MCAO must be modified. Previous models assumed an immediate TSC increase after MCAO, due to an increase in the intracellular $^{23}$Na concentration. Indeed Jansen *et al*. measured such an intracellular $^{23}$Na concentration increase [93]. However, this measurement depended on the amount of intracellular $^{23}$Na nuclei in the tested voxel rather than only in the one part of this voxel – the intracellular volume. Therefore, the assumption that TSC increases after MCAO due to an increase in the amount of $^{23}$Na nuclei inside cells holds true only as long as there is no variation in the intracellular volume.

The results of the TSC measurements after MCAO presented herein suggest that TSC remained constant for up to 2 h after MCAO in specific brain regions which were

found to comprise still-viable tissue in previous studies using an identical MCAO model [109]. Moreover, a slight TSC decrease (~ 10 mM) was measured in the cortex region at 1 h after MCAO, confirming that the vessel blockage-related underperfusion commenced at the time of MCAO and not later. A similar TSC-related decrease was previously measured by Bartha *et al*. in the rabbit brain [3]. Thus, a different biological model of TSC increase may be required to explain the measured differences in TSC time course data in different stroke tissue regions. This model includes volumetric compartment variations as well as intracellular $^{23}$Na concentration variations. The following model for TSC increase in ischaemic stroke tissue is suggested:

1. Immediately after MCAO, the $Na^+/K^+$-pump efficiency is degraded.
2. The intracellular $^{23}$Na concentration increases.
3. Water is attracted into the intracellular compartment by an increased metabolite concentration inside the cells subsequently diluting the intracellular $^{23}$Na concentration back to its normal concentration value.
4. The intracellular compartment volume increases (i.e. cell swelling occurs as has been measured by DWI measurements immediately after stroke).
5. The extracellular compartment volume decreases, which holds high $^{23}$Na nuclei content and thus contributes significantly to the TSC in brain tissue.
6. As a result, the TSC, which is the average $^{23}$Na concentration across the intra- and extra-cellular compartments, decreases (this decrease has been measured to be ~ 10 mM in the cortex at 1 h after MCAO).
7. As soon as the cell membrane ruptures (i.e. membrane integrity loss and tissue infarction), the intracellular compartment reduces to the extracellular compartment.
8. The TSC increases rapidly.

Thus, it can be hypothesised that the delay-time parameter could serve as a marker of cell membrane integrity loss and tissue infarction after stroke onset time.

## 8.4 The Detection of Infarcted Stroke Tissue during the Acute Phase

The delay-time maps were further analysed in order to compute the volume of tissue exhibiting an increase in TSC at various time points after MCAO. The infarcted tissue volume was computed at various observation time points after MCAO, which were spaced by 30 min. Any voxels which had delay-times less than the respective observation time point were counted as infarcted tissue voxels. As an example of this method, the observation time point was selected in one brain slice to be at 2 h after MCAO. The RoIs

exhibiting delay times below and above the observation time point were automatically defined from the TSC time course data, and are illustrated in Figure 8.3 (a) and (b) respectively. The difference in delay time to TSC increase for these RoIs is easily distinguishable in the TSC time course data, where each time course represents the average across the respective RoI. In this case, selecting a delay time of 2 h separated the cortex from the caudate-putamen TSC time course data which, following prior experience with the stroke model, were expected to represent the expected penumbral and core regions at this observation time point. The same difference had already been observed in Chapter 7 for manually chosen RoIs in similar brain areas. This demonstrates the power of the delay time parameter in its ability to distinguish the core and penumbral regions automatically.

The last computational step involved the determination of the infarcted tissue volume over time, which was done by summing the number of voxels across the five measured brain slices which exhibited an increasing TSC at various time points after MCAO. In this way voxels exhibiting increasing TSC were classified by the delay time parameter rather than a fixed TSC threshold. Thus, from the delay time map, voxel with delay times smaller than the observation time point were assumed to represent infarcted tissue and were included into the lesion volume calculation.

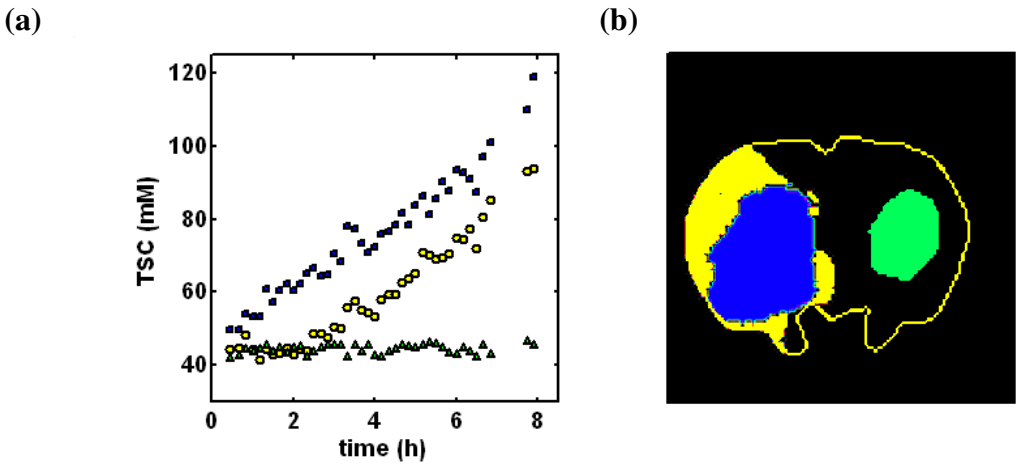


**Figure 8.3: (a) The average TSC time course data for two automatically upon their delay times chosen RoIs and one manually chosen RoI of contralateral tissue. The two RoIs in the stroke lesion were selected due to their different delay times < 2 h (blue) and between 2 to 6 h (yellow circles). The contralateral tissue was chosen as reference RoI (green triangles). (b) the automatically chosen RoIs cover core (exclusively in the caudate-putamen), and penumbra (mostly in the cortex).**

Despite the fact that the lesion size was different for all five animals, the comparison of the infarct volume evolution over time was rendered possible through the use of a relative volume measure, whereby the final lesion volume in each rat was set to 100 % and the measured volumes at earlier time points were normalised to this maximum volume. In this way, a percentage temporal evolution of infarcted tissue volume over time could be determined, as illustrated in Figure 8.4 for the brain slice discussed previously (i.e. slice 3 in stroke 3). The tissue volume increase during the first 2 h mainly corresponded to the evolution of stroke in the caudate-putamen, whereas the contribution of infarct volume after 2 h was mainly due to an onset of TSC increase in the cortex region. This method was then used to compute the infarct volume for all five slices through the rat brain and for each of the five investigated strokes.

## 8.5 Results

The five acquired stroke data sets, of which the measurements were described in Chapter 7, were re-analysed with the delayed-exponential model approach. The delay time maps were computed for five brain slices in each of the five rats and the results are presented in Figure 8.5. The lesion size and delay times could thus be compared between every animal. The delay times were higher in cortex than in caudate-putamen tissue for all five animals.

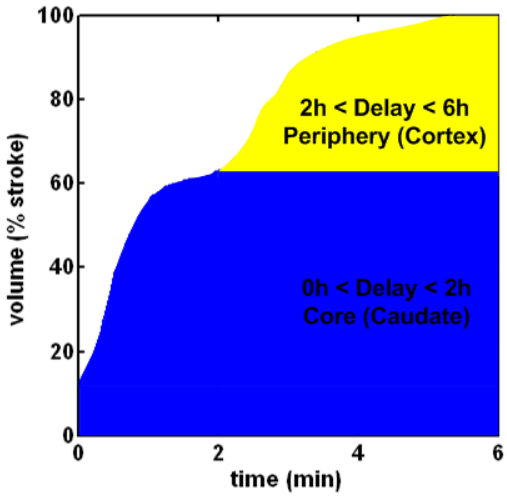


**Figure 8.4: Infarcted stroke tissue volume normalised to the infarcted tissue volume at 6 h after MCAO as a function of time for slice 3 in stroke 2 (colours yellow and blue correspond to RoIs in previous Figure 8.3).**

A large variation in lesion sizes was observed in the delay time maps, with stroke 1, 2, and 3 extending across both caudate-putamen and cortex, and stroke 4, and 5 only covering caudate-putamen and small areas of the cortex. Stroke 8 was the smallest stroke measured for all five animals. From the delay time maps, the tissue volume with increased TSC at various time points after MCAO was computed for each stroke and normalised to the final volume size at the end of the experiment. The averaged temporal evolution of tissue volume for the five rats is plotted in Figure 8.6, showing the mean and standard deviation at 30 min steps after MCAO.

For the purpose of comparing the exponential time constants with the linear TSC slopes in Chapter 7, the exponential time constant was converted into TSC slope. The exponential time constant of the delayed-exponential model describes the duration over which the TSC increases by 63.21 % (equal to $1\text{-}e^{-1}$) of the total $^{23}$Na concentration offset.

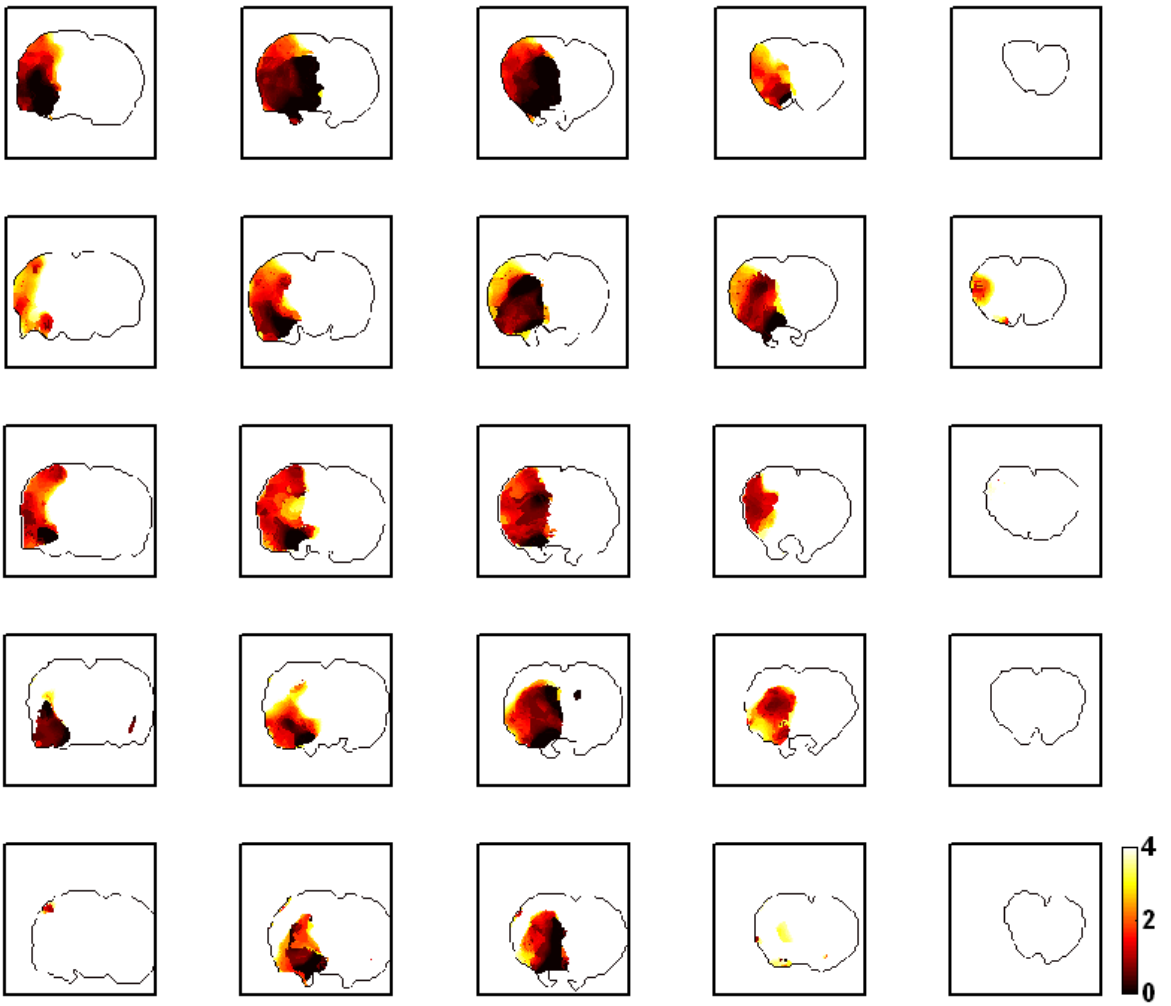


**Figure 8.5: Delay time maps (colour bar units in hours) for stroke 1, 2, 3, 4, and 5 (from top to bottom row) and five slices across the brain respectively (left to right column).**

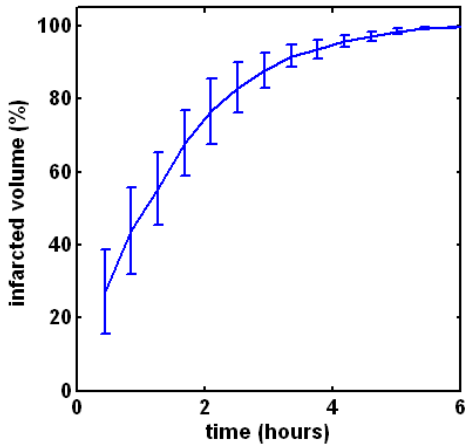


**Figure 8.6: The percentage of the infarcted tissue volume at various observation time points after MCAO normalised to the infarcted tissue volume at 8 h after MCAO averaged across all five rats.**

Under the assumption that the TSC increase can be approximated by a line over the duration of one time constant, the exponential time constant can be converted to TSC slope for every voxel *j* using the following equation:

$$\left(\frac{\Delta TSC}{1h}\right)_j = \frac{\left(140mM - c_{ini,j}\right)\cdot\left(1 - e^{-1}\right)}{\tau_j} \qquad \text{(Equation 8.2).}$$

The TSC slope maps thus calculated for all five rats are illustrated in Figure 8.7. The TSC slopes were maximal for the smallest stroke size in stroke 8. No regional TSC slope differences were observed between cortex and caudate-putamen. The 90 % and 60 % maximum TSC slopes were computed from the TSC slope maps for the five strokes and the mean and standard deviations were tabulated in Table 8.1.

**Table 8.1: Exponential time constants for stroke 1, 2, 3, 4, and 5 that were fit to the corresponding TSC time courses and averaged across the final lesion size.**

| | *90 % maximum TSC Slope (mM/h)* | *60 % maximum TSC Slope (mM/h)* |
|---|---|---|
| ***Stroke 1*** | **10.6 ± 0.3** | **8.2 ± 1.0** |
| ***Stroke 2*** | **13.1± 0.4** | **10.1 ± 1.3** |
| ***Stroke 3*** | **17.4± 0.5** | **12.7± 1.5** |
| ***Stroke 4*** | **13.9± 0.4** | **11.1± 1.5** |
| ***Stroke 5*** | **19.0± 0.5** | **14.8± 1.8** |
| ***Population Mean*** | **14.8± 3.4** | **11.4± 2.5** |

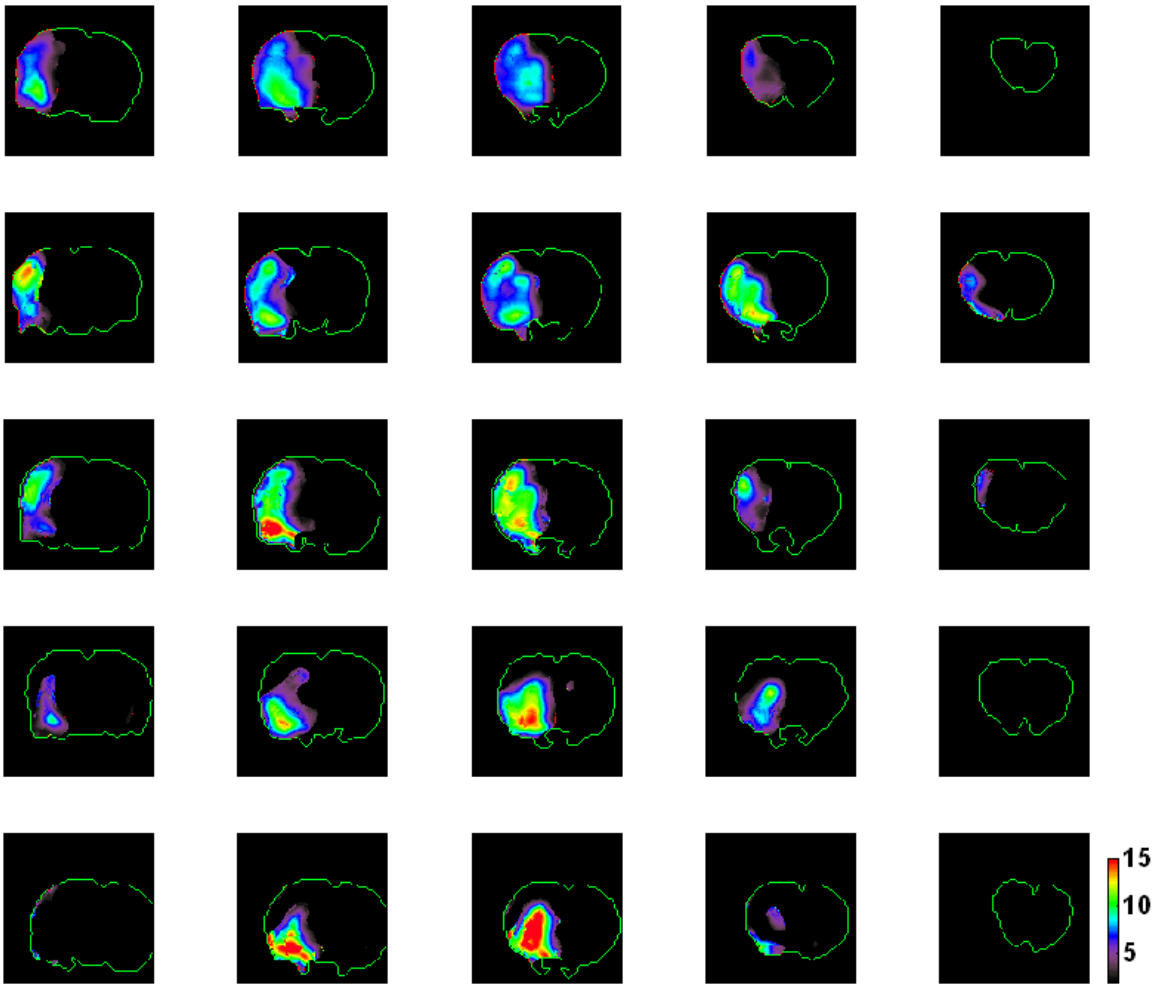


**Figure 8.7: TSC slopes (colourbar units in mM/h) for stroke 1, 2, 3, 4, and 5 (from top to bottom row) and five slices across the brain, respectively (left to right column).**

Nevertheless, the TSC slopes between the five strokes varied strongly as indicated by a higher standard deviation for the population mean compared to the single stroke TSC slopes.

## 8.6 Discussion

The TSC time course data, which was analysed in Chapter 7 using a linear regression model, was re-analysed with a non-linear regression model in this Chapter. The delayed-exponential model fit allowed for the quantitative assessment of two parameters:

1. the time after MCAO before TSC increased (the delay time), and
2. the rate of TSC increase after tissue infarction (TSC slope).

The TSC slopes computed with the delayed-exponential model averaged higher than the TSC slopes based upon the linear regression model (Table 8.2).

**Table 8.2: Comparison of the averaged TSC slopes for two different models, the linear regression model used in Chapter 7 and the herein described delayed-exponential model.**

| | *90 % maximum TSC Slope (mM/h)* | *60 % maximum TSC Slope (mM/h)* |
|---|---|---|
| ***Linear Regression*** | **12.1± 1.7** | **10.0 ± 1.6** |
| ***Delayed-Exponential Regression*** | **14.8± 3.4** | **11.4± 2.5** |

Since, the TSC slope computed from the exponential time constants represented the period of rapidly increasing TSC, rather than the entire measurement window period used for the linear slope fit as the TSC slopes resulting from the former were expected to be higher compared to the latter. For instance, the delay times before the actual TSC increase were not taken into account by the linear regression model, which consequently resulted in over- and underestimated TSC slope values.

The 60 % maximum TSC slopes measured with the delayed-exponential model varied between 8.2 and 14.8 mM/h between stroke 1 to 5, the maximum TSC slope being measured for the smallest stroke size of stroke 5. These variations in the measured TSC slopes for the different strokes may be explained by the phenomenon of the $^{23}$Na nuclei accumulation after stroke onset time. In the case of infarction, the cell membranes disintegrate and the swollen intracellular space with its low intracellular $^{23}$Na concentration (~ 10 mM) abruptly passes into extracellular space. This abrupt change in cellular environment creates a $^{23}$Na concentration gradient in the extracellular compartment, from the edge to the centre of the infarct. For each animal, it is assumed that the extracellular $^{23}$Na concentration was similarly high (~ 140mM) at the infarct edge and low (~ 45 mM) in the infarct centre.

Thus, the $^{23}$Na concentration gradient from the edge to the centre of the stroke lesion created by the cell membrane rupture may vary in dependency of the overall lesion size. This consideration may explain why the TSC slope was higher in smaller lesions compared to larger lesions. Nevertheless, further experiments are necessary to prove this hypothesis, since the number of animals ($N = 5$) in this study was insufficient to draw an exact conclusion from the lesion sizes to the TSC slopes. The extracellular $^{23}$Na concentration difference, $\Delta[Na^+]_e$, relative to the lesion radius $r$, determines the velocity with which $^{23}$Na ions diffuse to the centre of the infarct. Consequently, TSC slope ought

to be proportional to the diffusion velocity $v_{Dif}$ of $^{23}$Na ions, and inversely proportional to lesion size defined by its radius $r$:

$$\frac{\Delta TSC}{\Delta t} \propto \quad v_{Dif} \cdot \frac{\Delta [Na^+]_e}{\Delta r} \qquad \text{(Equation 8.3).}$$

It may therefore take longer to accumulate the same amount of $^{23}$Na ions inside the core for larger lesions under the assumption of an identical pool of $^{23}$Na nuclei contained in each rat's body. This hypothesis, rather than differences in metabolic rates between individuals, may explain the lower TSC slopes which were measured in previous studies (these ranged from 2.4 to 2.9 %/h in human brains [110], 5.4 to 7.2 %/h in monkey brains [41], up to 20 %/h in rabbit brains [3], and 33 ± 9%/h in rat brains in this study).

Moreover, the hypothesis of a (TSC slope)-to-(lesion size) dependency also suggests that TSC slope is independent of tissue viability after MCAO. The maximum slopes were measured (with only minor differences) in the centre of both the cortex and the caudate-putamen, which could be clearly separated from each other in the TSC slope maps due to the decreased TSC slopes measured around the edges of these brain regions. The fact that TSC slope was nearly similar in cortex and caudate-putamen in every animal suggests that TSC slope is tissue-independent and cannot serve as a marker for tissue viability after MCAO.

However, the delay time was found to differ significantly between the cortex (presumed to be penumbra/ still-viable) and the caudate-putamen (core/ infarcted) tissue. Thus delay time could serve as a marker for infarcted tissue after MCAO in conjunction with the modified physiological interpretation given in Section 8.3. The accuracy of the delay time computation depended on the amount of sampled data points corresponding to the linear section of the delayed-exponential model, because the delay time was computed as the intersection of the linear and the exponential model sections. Thus, with only a few data points measured during the linear part of the model in tissue exhibiting short delay times, the intersection computation was difficult. This was rendered even more difficult in cases where the TSC had already increased and hence, the initial data points on the exponential section were also missing. Thus the delay time accuracy was strongly influenced by the time after MCAO at which the first TSC measurement was carried out, particularly in brain regions exhibiting a short delay time. Those inaccuracies could be avoided by either exactly determining the initial TSC before the experiments or by inducing the stroke in situ within the MRI scanner and measuring TSC immediately after MCAO, which has not proved possible using current stroke models. Indeed, the 26 mins

after MCAO for the first TSC measurement in the current study represents a significant improvement on the earliest time reported in the literature for similar studies (> 1 h in [5, 12, 13]).

To date it was believed that TSC increase was due to an increase in intra-cellular $^{23}Na$ concentration after a reduction in $Na^+/K^+$-pump efficiency [86]. Significant differences in TSC levels in tissue with a risk of infarction compared to infarcted tissue have been reported by others [8, 86]. Indeed, such differences have led to the hypothesis that there may exist a viability threshold, separating viable from non-viable tissue. The original idea of such a TSC viability threshold stems from Ito *et al.* in 1979 [2], who measured the evolution of the TSC after both permanent and temporary MCAO using the invasive technique of flame photometry. The $^{23}Na$ concentration was globally measured for the posterior two-thirds of the left cerebral hemisphere for several rats, which were sacrificed at various time points after MCAO and which underwent permanent stroke or which were re-perfusion at 30 min or 3 h after MCAO. The TSC values for the reperfusion and permanent stroke models were compared and revealed a lower TSC for tissue which was re-perfused at 30 min after MCAO, whereas TSC was measured higher in tissue which was re-perfused at 3 h after MCAO when compared to the temporally corresponding TSC results for the permanent MCAO model. From these results, Boada *et al.* [4] established a theory describing a three hour time window for small laboratory animals during which tissue could recover from elevated TSC levels if blood supply was reinstated; in 1999 Thulborn *et al.* [8] already suggested that a viability threshold of 70 mM may be appropriate to separate viable from non-viable stroke tissue. However, a recent study published by LaVerde *et al.* found that the increase in TSC values stopped after reperfusion [111], which was initiated in monkey brains within 5.4 h after MCAO. No subsequent decrease was measured, contradicting the hypothesis that TSC may recover in still viable tissue if perfusion is re-established. The latter finding challenges the existence of a TSC viability threshold at pathological TSC values in stroke tissue.

The physiological response to a degraded membrane pump function is cell swelling. Therefore, the change in TSC in this period before infarction occurs may be expected to be minimal. It is well known that cell swelling occurs immediately after MCAO due to an accumulation of water molecules inside cells, which has been confirmed via measurements of the Apparent Diffusion Coefficient during this period after stroke induction in various studies [31, 87]. The consequence of a volumetric compartment change on the TSC value is perhaps reflected in the measured TSC time course data. The

rapid cell swelling which occurs in the acute phase after MCAO will invariably result in a decreasing volume of the extracellular compartment with its high $^{23}$Na concentration content, and hence result in a potential decrease in TSC. Such a reduction in TSC has been measured for up to 40 min after MCAO by Bartha *et al*. [3], although the authors attributed this TSC decrease to their use of a long TE of 3.2 ms: it was assumed that a possible reduction in $^{23}$Na MR sensitivity due to the nuclei passing from the extra- to the intracellular compartment may in turn have reduced the $T_{2f}$-relaxation times of these $^{23}$Na nuclei, thereby reducing the measured signal and hence the measured TSC. A similar TSC decrease was observed in cortex tissue during the first two hours after MCAO. In the study presented here, TSC could be quantified more accurately due to the use of short TE below 1 ms. Thus, the initial decrease in TSC may be attributed to an effective reduction in TSC in the respective stroke tissue. This effect has only been measured in three rats in the cortex region. Although Bartha's experiment may confirm our results, nevertheless more work is required to exactly quantify the TSC reduction during the cell swelling phase.

Despite the suggestion of a dip in TSC values in the acute phase after MCAO, in general the TSC across the different brain regions of the rats studied remained fairly constant during this period, before the increase in TSC values occurred for each brain region. The hypothesis of relatively constant TSC during the cell swelling phase, where tissue is considered as still viable and salvageable was confirmed by the results of this chapter:

1. A significant delay time of up to 3 h was measured before TSC increased in the peripheral cortex region.
2. The generated delay time maps represent the expected spatio-temporal evolution of infarction in the investigated MCAO model, which was expected to evolve from the caudate putamen to the cortex [109].
3. Assuming that the delay time characterises the onset of tissue infarction, the volume of infarcted tissue reached 90 % of its final volume at 3 h after MCAO, which supports the concept of a three hour time window within which stroke tissue could be salvaged in small animal brains, expounded in several studies [2, 4].
4. Regions with elevated TSC levels compared well with decreased staining values in histo-chemically analysed brain slices at 6 to 8 h after MCAO.

The correlation of stroke lesions defined by histology images and regions with elevated values in the TSC maps had been confirmed by several other studies [5, 12, 34]. Furthermore, the sudden increase in TSC at various time points after MCAO suggests a time-dependent and possibly viability-dependent dramatic change in cell homeostasis. Thus, the measured TSC increase, which was presented here, was believed to correspond to cell membrane integrity loss – a decomposition of the membrane characterised in microscopy images by shrunken cell structure. The delay time to TSC increase could hence serve as a direct marker for infarction after ischaemic stroke. This hypothesis was furthermore supported by recently published results from human $^{23}$Na-MRI and ADC measurements, which suggested that TSC increased in core, but not in peripheral stroke tissue [110, 112]. Although their theory had not been confirmed by biopsy measurements, the results found herein substantiated their suspicion of a tissue viability threshold that is identical to non-pathological TSC of approximately 45 mM.

Non-viable stroke tissue was spatio-temporally and non-invasively identified by the pathologically-elevated TSC levels from as early as 0.5 h after ischaemic stroke. After an extensive non-linear spatio-temporal TSC time course analysis, it can be concluded that *increased TSC levels identified non-viable (i.e. infarcted) stroke tissue*.

# 9 Conclusions and Outlook

In the present work, cerebral Tissue Sodium Concentration was spatio-temporally measured in a rodent stroke model by means of quantitative $^{23}$Na MRI (qNa-MRI).

The first part of the work focused on the MRI transmitter and detector system development in order to homogenise the $B_1$-transmit field and maximise the detected SNR per unit scan time at the $^{23}$Na channel. A validation method was developed, which allowed optimising the detector element on the work bench by measuring the respective coil profiles using the network analyser. It was found that surface coil detectors designed from 1.5 mm thick copper wire, wound in two windings with 20 and 30 mm i.d., and shaped over a cylindrical radius of 21 mm, achieved the maximum SNR at 12 mm sample depth at a measurement frequency of 79.4 MHz. As a result, a $^{1}$H/$^{23}$Na double-tuned transceiver surface coil was developed, which achieved a two-fold SNR increase in the $^{23}$Na channel at 12 mm sample depth when compared to a commercial $^{1}$H/$^{23}$Na double-tuned surface coil. The same coil design could serve to develop other $^{1}$H/X-nuclei transceiver surface coils, where X-nuclei comprises all NMR active non-$^{1}$H-nuclei, because it proved to be practical, stable, and maximises the X-nuclei SNR during the MRI scanning. Furthermore, a $^{1}$H/$^{23}$Na double-tuned dual coil system was developed, which was composed of a $^{1}$H/$^{23}$Na double-tuned birdcage resonator and a $^{23}$Na single-tuned surface coil both designed with an active decoupling circuit in the $^{23}$Na channel. This resonator system was designed in such a way that high $^{23}$Na $B_1$-homogeneity was achieved ($B_1$-field variations < 4.5 % across the rat brain) and that the detected SNR was maximised at the $^{23}$Na channel. A three-fold SNR increase was measured at 12 mm sample depth when the developed coil system was compared to a commercial $^{1}$H/$^{23}$Na transceiver surface coil with the 90° flip angle adjusted to the sample surface. The bench test evaluation method may prove useful in future X-nuclei-MRI coil development studies, where an accurate MRI evaluation is difficult and time consuming due to the low available SNR per unit scan time in the MR images.

In the second part of this thesis, a quantification method was developed in order to measure TSC in the diseased rat brain. To this end, a 2D multi-slice pulse sequence was optimised for $^{23}$Na MRI with short TE of 853 µs. The image artefacts caused by the filtered back-projection algorithm were reduced by using a nearest-neighbour regridding algorithm which was implemented in MATLAB®. Furthermore, a quantification method was developed for the dual coil system. Quantification accuracy tests on different $^{23}$Na- and gel-concentrations containing phantoms revealed a quantification accuracy of < 10 mM for images acquired using the following acquisition parameters: 10 min TA, 853 µs TE, 1.2 µl voxel resolution. Although the 853 µs TE proved to be sufficiently low for the measurement of TSC in brain tissue, future work must focus on further reducing the TE, which could for instance be achieved by employing a 3D radial sequence and faster switching gradient sets. Shorter TE would enable the quantification of TSC in cartilage or other structures, which exhibit very short $T_{2f}$ relaxation times.

In the third part, the TSC was measured in a rodent stroke model from as early as 0.5 h for up to 8 h after Middle Cerebral Artery Occlusion (MCAO). As a result, the TSC was found to increase non-linearly and with regional variations across the stroke lesion. Therefore, a novel delayed-exponential model was developed to fit the measured TSC data. A TSC slope value derived from this model-fit averaged at 11 ± 3 mM/h after MCAO, which was found to be similar in core and penumbra regions, but higher in smaller than in larger stroke lesions. By measuring the TSC in different regions of the stroke lesion at different time points after stroke induction, it was hoped to find a quantifiable parameter which would allow for the separation of infarcted core tissue and still-viable penumbra tissue. However, since the TSC slope was measured to be similar in both areas, it was concluded that the TSC slope cannot serve to distinguish between core and penumbra tissue after stroke.

In the last part of this thesis, a delay time parameter was defined as the time at which the TSC began to increase after MCAO. Delay time parameter maps were computed on which core tissue could be well separated from still-viable stroke tissue. From these maps one could observe that TSC increased earlier than 2 h after MCAO in the potential core region (i.e. the caudate-putamen) and later than 2 h after MCAO in the potential penumbra region (i.e. the cortex). The brain regions of potential core and penumbra tissue were well known from previous experiences with the same MCAO model [109].

The lesion sizes measured in the histology slides furthermore coincided well with the infarcted lesion sizes measured as the regions with elevated TSC levels at 8 h after

MCAO. Thus, qNa-MRI could potentially serve to perform temporally-resolved histology after MCAO and thus reduce the number of animals necessary for those studies drastically. The number of sacrificed animals in this MRI study was reduced to ten and represents an equivalent number of 330 sacrificed animals which would otherwise have been needed for a similar post-mortem-based stroke study. In addition to the reduced number of animals, the TSC time course data could be acquired non-invasively and spatially resolved in one and the same animal.

In conclusion, spatio-temporally-resolved TSC measurements may provide an accurate measure for tissue death and could replace the current gold standard of $T_2$-weighted $^{1}$H MRI, which detects the onset of regional ischaemic tissue damage not immediately, but later than 3 h after infarction. Future studies have to be performed to validate these findings. Such a validation could be performed by comparing the infarcted stroke tissue volumes measured with qNa-MRI to the volumes measured by means of histology at various time points after MCAO.

Future work will focus on the development of a $^{1}$H Perfusion Weighted Imaging (PWI)-to-$^{23}$Na-MRI mismatch to determine penumbra and core tissue in the stroke lesion. In conjunction with PWI, the ischaemic tissue under risk, could be determined accurately via a PWI/TSC or PWI/$^{23}$Na-MRI mismatch. The infarcted tissue measured by elevated TSC values could thus be determined as a percentage of the underperfused stroke lesion volume measured via PWI. This mismatch method could then be used in pre-clinical studies of stroke models. Since elevated TSC levels correlated well with brighter stained histology regions, non-invasive $^{23}$Na-MRI could replace the current-state-of-the-art (i.e. histology) to investigate stroke models over time in one and the same animal as opposed to a series of different animals sacrificed at different time points after stroke onset time. Thus, qNa-MRI could reduce the numbers of animals needed for such studies and could also benefit the development of novel pharmacological and surgical stroke treatments.

Furthermore, human stroke diagnosis could benefit from such a PWI/$^{23}$Na-MRI mismatch method. Firstly, the temporal evolution of infarcted tissue volume over time after stroke onset could be determined in a multiple subject study, where each subject is scanned once at arbitrary, but different time points after stroke onset time. This could open up the restrictive 3 h treatment window currently specified for current stroke patients and deliver a more quantitative foundation for effective treatment administration (e.g.: surgical revascularisation or pharmaceutical rt-PA administration).

Secondly, the PWI/$^{23}$Na-MRI mismatch method could evolve to a useful diagnostic tool in clinical MRI, because the stroke lesion could be functionally assessed by the extension of the tissue with elevated TSC levels as a percentage of the underperfused tissue region. Since every stroke is differently sized, this may deliver a possibility to apply surgical treatment (e.g. revascularisation) at individually varying time points after stroke onset time. The underperfused-to-infarcted-tissue-ratio may also allow for accurately estimating stroke onset time.

In conclusion, the results of this thesis lay the foundation on which the diagnosis and treatment of ischaemic stroke tissue in humans must be re-thought, because the infarcted tissue region may in future be separated from the underperfused tissue at any time point after stroke onset time with no delay in detecting the infarcted tissue using the irreversible TSC or TSC-related $^{23}$Na MRI intensity measure in conjunction with $^{1}$H-PWI.

# References


1. Bowman, J., et al., *National Audit of Stroke Care*. 2008, Irish Heart Foundation.
2. Ito, U., et al., *Brain Edema during Ischemia and after Restoration of Blood-Flow - Measurement of Water, Sodium, Potassium Content and Plasma-Protein Permeability.* Stroke, 1979. **10**(5): p. 542-547.
3. Bartha, R., et al., *Sodium T2*-weighted MR imaging of acute focal cerebral ischemia in rabbits.* Magn Reson Imaging, 2004. **22**(7): p. 983-91.
4. Boada, F.E., et al., *Triple/single quantum filtered sodium MRI of acute brain ischemia.* 2005 27th Annual International Conference of the IEEE Engineering in Medicine and Biology Society, Vols 1-7, 2005: p. 731-734.
5. Jones, S.C., et al., *Stroke onset time using sodium MRI in rat focal cerebral ischemia.* Stroke, 2006. **37**(3): p. 883-8.
6. LaVerde, G., et al., *Serial triple quantum sodium MRI during non-human primate focal brain ischemia.* Magnetic Resonance in Medicine, 2007. **57**(1): p. 201-205.
7. LaVerde, G.C., et al., *Sodium time course using 23Na MRI in reversible focal brain ischemia in the monkey.* J Magn Reson Imaging, 2009. **30**(1): p. 219-23.
8. Thulborn, K.R., et al., *Comprehensive MR imaging protocol for stroke management: tissue sodium concentration as a measure of tissue viability in nonhuman primate studies and in clinical studies.* Radiology, 1999. **213**(1): p. 156-66.
9. Tsang, A., et al. *Sodium Image Intensity Increases in Ischemic Core Tissue, but not Penumbra in Acute and Sub-acute Stroke*. in *Stroke Journal of the American Heart Association*. 2009. San Diego.
10. Wang, Y., et al., *Brain tissue sodium is a ticking clock telling time after arterial occlusion in rat focal cerebral ischemia.* Stroke, 2000. **31**(6): p. 1386-91; discussion 1392.
11. Hussain, M.S., et al., *Sodium imaging intensity increases with time after human ischemic stroke.* Ann Neurol, 2009. **66**(1): p. 55-62.
12. Yushmanov, V.E., et al., *Inhomogeneous Sodium Accumulation in the Ischemic Core in Rat Focal Cerebral Ischemia by Na-23 MRI.* Journal of Magnetic Resonance Imaging, 2009. **30**(1): p. 18-24.
13. Yushmanov, V.E., et al., *Sodium Mapping in Focal Cerebral Ischemia in the Rat by Quantitative Na-23 MRI.* Journal of Magnetic Resonance Imaging, 2009. **29**(4): p. 962-966.
14. Brown, M.A. and R.C. Semelka, *MRI Principles and Applications.* Wiley-Liss New York, 1999.
15. Weishaupt, D., V.D. Koechli, and B. Marincek, *How Does MRI Work?* . Second Edition ed. 2008: Verlag Springer Berlin Heidelberg

16. Woessner, D.E., *NMR Relaxation of Spin-3/2 Nuclei: Effects of Structure, Order, and Dynamics in Aqueous Heterogeneous Systems.* Concepts in Magnetic Resonance, 2001. **13(5)**: p. 294-325.
17. Shapiro, E.M., et al., *Sodium visibility and quantitation in intact bovine articular cartilage using high field (23)Na MRI and MRS.* J Magn Reson, 2000. **142**(1): p. 24-31.
18. Thulborn, K.R., et al., *Quantitative tissue sodium concentration mapping of the growth of focal cerebral tumors with sodium magnetic resonance imaging.* Magn Reson Med, 1999. **41**(2): p. 351-9.
19. Maril, N., et al., *Functional sodium magnetic resonance imaging of the intact rat kidney.* Kidney Int, 2004. **65**(3): p. 927-35.
20. Ouwerkerk, R., R.G. Weiss, and P.A. Bottomley, *Measuring human cardiac tissue sodium concentrations using surface coils, adiabatic excitation, and twisted projection imaging with minimal T2 losses.* J Magn Reson Imaging, 2005. **21**(5): p. 546-55.
21. Ouwerkerk, R., et al., *Tissue sodium concentration in human brain tumors as measured with 23Na MR imaging.* Radiology, 2003. **227**(2): p. 529-37.
22. Constantinides, C.D., et al., *Human skeletal muscle: sodium MR imaging and quantification-potential applications in exercise and disease.* Radiology, 2000. **216**(2): p. 559-68.
23. Constantinides, C.D., et al., *Noninvasive quantification of total sodium concentrations in acute reperfused myocardial infarction using 23Na MRI.* Magn Reson Med, 2001. **46**(6): p. 1144-51.
24. Constantinides, C.D., et al., *Superparamagnetic iron oxide MION as a contrast agent for sodium MRI in myocardial infarction.* Magn Reson Med, 2001. **46**(6): p. 1164-8.
25. Schepkin, V.D., et al., *Sodium magnetic resonance imaging of chemotherapeutic response in a rat glioma.* Magn Reson Med, 2005. **53**(1): p. 85-92.
26. Lee, R.F., et al., *A broadband phased-array system for direct phosphorus and sodium metabolic MRI on a clinical scanner.* Magn Reson Med, 2000. **43**(2): p. 269-77.
27. Lanz, T., et al. *An 8 Channel $^{23}$Na Heart Array for Application at 3 T*. in *ISMRM*. 2007. Berlin.
28. Gareis, D., et al., *Transmit-receive coil-arrays at 17.6T, configurations for H-1, Na-23, and P-31 MRI.* Concepts in Magnetic Resonance Part B-Magnetic Resonance Engineering, 2006. **29B**(1): p. 20-27.
29. Caplan, L.R., *Intracranial branch atheromatous disease: a neglected, understudied, and underused concept.* Neurology, 1989. **39**: p. 1246-50.
30. Faller, A., *Der Körper des Menschen: Enführung in Bau und Funktion.* Thieme Verlag, 1999.
31. Roberts, T.P. and H.A. Rowley, *Diffusion weighted magnetic resonance imaging in stroke.* Eur J Radiol, 2003. **45**(3): p. 185-94.
32. Rojas, S., et al., *Modest MRI signal intensity changes precede delayed cortical necrosis after transient focal ischemia in the rat.* Stroke, 2006. **37**(6): p. 1525-32.
33. Christensen, J.D., et al., *Quantitative tissue sodium concentration mapping of normal rat brain.* Magn Reson Med, 1996. **36**(1): p. 83-9.
34. Lin, S.P., et al., *Direct, longitudinal comparison of (1)H and (23)Na MRI after transient focal cerebral ischemia.* Stroke, 2001. **32**(4): p. 925-32.
35. Nielles-Vallespin, S., et al., *3D radial projection technique with ultrashort echo times for sodium MRI: clinical applications in human brain and skeletal muscle.* Magn Reson Med, 2007. **57**(1): p. 74-81.

36. Preston, E. and D.O. Foster, *Diffusion into rat brain of contrast and shift reagents for magnetic resonance imaging and spectroscopy.* NMR Biomed, 1993. **6**(5): p. 339-44.
37. Winter, P.M. and N. Bansal, *TmDOTP(5-) as a (23)Na shift reagent for the subcutaneously implanted 9L gliosarcoma in rats.* Magn Reson Med, 2001. **45**(3): p. 436-42.
38. Neuberger, T., et al., *23Na microscopy of the mouse heart in vivo using density-weighted chemical shift imaging.* Magma, 2004. **17**(3-6): p. 196-200.
39. Pekar, J., P.F. Renshaw, and J.S.J. Leigh, *Selective detection of intracellular sodium by coherence-transfer NMR.* J Magn Reson, 1987. **72**(159-161).
40. Kline, R.P., et al., *Rapid in vivo monitoring of chemotherapeutic response using weighted sodium magnetic resonance imaging.* Clin Cancer Res, 2000. **6**(6): p. 2146-56.
41. LaVerde, G.C., *Sodium MRI For Studying Ischemic Tissue In Acute Stroke.* PhD Thesis, 2006.
42. Winter, P.M., et al., *Quantitation of intracellular [Na+] in vivo by using TmDOTP5- as an NMR shift reagent and extracellular marker.* J Appl Physiol, 1998. **85**(5): p. 1806-12.
43. Borthakur, A., et al., *In vivo triple quantum filtered twisted projection sodium MRI of human articular cartilage.* J Magn Reson, 1999. **141**(2): p. 286-90.
44. Hughes, C.E., et al., *NMR Spectroscopy and Imaging of Sodium in Ordered Environments. The Return of the Central Transition.* J Magn Reson B, 1996. **111**(2): p. 189-93.
45. Hancu, I., F.E. Boada, and G.X. Shen, *Three-dimensional triple-quantum-filtered (23)Na imaging of in vivo human brain.* Magn Reson Med, 1999. **42**(6): p. 1146-54.
46. Hancu, I., J.R. van der Maarel, and F.E. Boada, *A model for the dynamics of spins 3/2 in biological media: signal loss during radiofrequency excitation in triple-quantum-filtered sodium MRI.* J Magn Reson, 2000. **147**(2): p. 179-91.
47. Tanase, C. and F.E. Boada, *Triple-quantum-filtered imaging of sodium in presence of B(0) inhomogeneities.* J Magn Reson, 2005. **174**(2): p. 270-8.
48. Goodman, J.A., et al., *Sodium ion apparent diffusion coefficient in living rat brain.* Magn Reson Med, 2005. **53**(5): p. 1040-5.
49. Mispelter, J., M. Lupu, and A. Briguet, *NMR Probeheads for Biophysical and biomedical experiments: Theoretical Principles & Practical Guidelines*. 2006, London: Imperial College Press.
50. Hugh D. Young, R.A.F., *Sears and Zemansky's University Physics with Modern Physics 11th Edition*. 2004: Addison Wesley
51. Viswanathan, R., et al., *Beyond Copper: MR Imaging with Carbon Nanotube Receiver Coils*, in *17th Scientific Meeting, International Society for Magnetic Resonance in Medicine*. 2009: Honolulu p. 503.
52. Miller, J.R., et al., *Superconducting receiver coils for sodium magnetic resonance imaging.* Ieee Transactions on Biomedical Engineering, 1996. **43**(12): p. 1197-1199.
53. Shen, G.X., F.E. Boada, and K.R. Thulborn, *Dual-frequency, dual-quadrature, birdcage RF coil design with identical B1 pattern for sodium and proton imaging of the human brain at 1.5 T.* Magn Reson Med, 1997. **38**(5): p. 717-25.
54. Carr, J.J., *Secrets of RF Circuit Design*. 2000: Technology & Engineering. 534.
55. Roemer, P.B., et al., *The NMR phased array.* Magn Reson Med, 1990. **16**(2): p. 192-225.

56. Hayes, C.E. and L. Axel, *Noise Performance of Surface Coils for Magnetic-Resonance Imaging at 1.5-T.* Medical Physics, 1985. **12**(5): p. 604-607.
57. Bottomley, P.A., C.H.L. Olivieri, and R. Giaquinto, *What is the optimum phased array coil design for cardiac and torso magnetic resonance?* Magnetic Resonance in Medicine, 1997. **37**(4): p. 591-599.
58. Wang, J.M., A. Reykowski, and J. Dickas, *Calculation of the Signal-to-Noise Ratio for Simple Surface Coils and Arrays of Coils.* Ieee Transactions on Biomedical Engineering, 1995. **42**(9): p. 908-917.
59. Prock, T., D.J. Collins, and M.O. Leach, *Numerical evaluation of shaped surface coil sensitivity at 63 MHz.* Physics in Medicine and Biology, 2001. **46**(7): p. 1753-1765.
60. Woo, D.C., et al., *Evaluation of the turn variation of spiral RF surface coils for MR microscopic imaging and spectroscopy.* Measurement, 2007. **40**(6): p. 615-622.
61. Giovannetti, G., et al., *Conductor geometry and capacitor quality for performance optimization of low-frequency birdcage coils.* Concepts in Magnetic Resonance Part B-Magnetic Resonance Engineering, 2004. **20B**(1): p. 9-16.
62. Rivera, M., et al., *MRI visualization of small structures using improved surface coils.* Magnetic Resonance Imaging, 1998. **16**(2): p. 157-166.
63. Redpath, T.W., *Signal-to-noise ratio in MRI.* British Journal of Radiology, 1998. **71**(847): p. 704-707.
64. Alecci, M., et al., *Practical design of a 4 Tesla double-tuned RF surface coil for interleaved 1H and 23Na MRI of rat brain.* J Magn Reson, 2006. **181**(2): p. 203-11.
65. Shields, L., *Evaluation of Detector Coils for use in 23Na Magnetic Resonance Imaging, at 7 T, using Bench Tests*, in *Physics (B.A. Moderatorship Thesis)*. 2009, Trinity College Dublin: Dublin.
66. Fitzsimmons, J.R., H.R. Brooker, and B. Beck, *A Transformer-Coupled Double-Resonant Probe for Nmr Imaging and Spectroscopy.* Magnetic Resonance in Medicine, 1987. **5**(5): p. 471-477.
67. Tomanek, B., et al., *Double-frequency birdcage volume coils for 4.7T and 7T.* Concepts in Magnetic Resonance Part B-Magnetic Resonance Engineering, 2005. **26B**(1): p. 16-22.
68. Hurlston, S.E., et al., *A high-temperature superconducting Helmholtz probe for microscopy at 9.4 T.* Magn Reson Med, 1999. **41**(5): p. 1032-8.
69. Hurlston, S.E., G.P. Cofer, and G.A. Johnson, *Optimized radiofrequency coils for increased signal-to-noise ratio in magnetic resonance microscopy.* International Journal of Imaging Systems and Technology, 1997. **8**(3): p. 277-284.
70. Gelb, R.A.a.A., *A Method to Reduce the Gibbs Ringing Artifact in MRI Scans While Keeping Tissue Boundary Integrity.* IEEE TRANSACTIONS ON MEDICAL IMAGING, 2002. **21**(4): p. 15.
71. Volotovskyy, V., et al., *Doubly tunable double ring surface coil.* Concepts in Magnetic Resonance Part B-Magnetic Resonance Engineering, 2003. **17B**(1): p. 11-16.
72. Schnall, M.D., et al., *A New Double-Tuned Probe for Concurrent H-1 and P-31 Nmr.* Journal of Magnetic Resonance, 1985. **65**(1): p. 122-129.
73. Augath, M., et al., *In vivo 39K, 23Na and 1H MR imaging using a triple resonant RF coil setup.* Journal of Magnetic Resonance, 2009. **In Press, Corrected Proof**.
74. Hayes, C.E., et al., *An efficient highly homogeneous radio frequency coil for whole-body NMR.* Journal of Magnetic Resonance, 1985. **63**(622-628).
75. Matson, G.B., P. Vermathen, and T.C. Hill, *A practical double-tuned 1H/31P quadrature birdcage headcoil optimized for 31P operation.* Magn Reson Med, 1999. **42**(1): p. 173-82.

76. Asfour, A. and V. Auboiroux, *A new dedicated double-tuned (100 MHz-27 MHz) volume RF coil actively-decoupled form a receive-only simple-tuned (27 MHz) coil: application to the MRF experiments of hyperpolarized Xe-129 in the rat brain.* 2008 Ieee Instrumentation and Measurement Technology Conference, Vols 1-5, 2008: p. 945-950.
77. Shen, G.X., et al., *Experimentally verified, theoretical design of dual-tuned, low-pass birdcage radiofrequency resonators for magnetic resonance imaging and magnetic resonance spectroscopy of human brain at 3.0 Tesla.* Magnetic Resonance in Medicine, 1999. **41**(2): p. 268-275.
78. Haase, A., et al., *NMR probeheads for in vivo applications.* Concepts in Magnetic Resonance, 2000. **12**(6): p. 361-388.
79. Chin, C.-L., et al., *BirdcageBuilder: Design of Specified-Geometry Birdcage Coils with Desired Pattern and Resonant Frequency.* Concepts in Magnetic Resonance, 2002. **15**(2): p. 156-163.
80. Hudson, A.M.J., W. Köckenberger, and R.W. Bowtell, *Dual resonant birdcage coils for1H detected13C microscopic imaging at 11.7 T* Magnetic Resonance Materials in Physics, Biology and Medicine 2000. **10**(2): p. 61-68.
81. Streif, J.U.G., et al., *A coil combination for magnetic resonance perfusion imaging of mice in vivo at 7 T.* Review of Scientific Instruments, 2003. **74**(5): p. 2843-2848.
82. Barberi, E.A., et al., *A transmit-only/receive-only (TORO) RF system for high-field MRI/MRS applications.* Magn Reson Med, 2000. **43**(2): p. 284-9.
83. Reykowski, A., S.M. Wright, and J.R. Porter, *Design of Matching Networks for Low-Noise Preamplifiers.* Magnetic Resonance in Medicine, 1995. **33**(6): p. 848-852.
84. Avdievich, N.T. and H.P. Hetherington, *4 T Actively detuneable double-tuned H-1/P-31 head volume coil and four-channel P-31 phased array for human brain spectroscopy.* Journal of Magnetic Resonance, 2007. **186**(2): p. 341-346.
85. Jamison, R. and W. Kriz, *Urinary concentrating mechanism*. 1982: New York/ Oxford: Oxford University Press, Inc.
86. Thulborn, K.R., et al., *Sodium MR imaging of acute and subacute stroke for assessment of tissue viability.* Neuroimaging Clin N Am, 2005. **15**(3): p. 639-53, xi-xii.
87. Pereztrepichio, A.D., et al., *Sensitivity of Magnetic-Resonance Diffusion-Weighted Imaging and Regional Relationship between the Apparent Diffusion-Coefficient and Cerebral Blood-Flow in Rat Focal Cerebral-Ischemia.* Stroke, 1995. **26**(4): p. 667-674.
88. Weber, R., P. Ramos-Cabrer, and M. Hoehn, *Present status of magnetic resonance imaging and spectroscopy in animal stroke models.* Journal of Cerebral Blood Flow and Metabolism, 2006. **26**(5): p. 591-604.
89. Lin, S.P., et al., *Investigation of mechanisms underlying transient T2 normalization in longitudinal studies of ischemic stroke.* Journal of Magnetic Resonance Imaging, 2002. **15**(2): p. 130-136.
90. Wang, Y., et al., *Hypoxic-ischemic brain injury in the neonatal rat model: Relationship between lesion size at early MR imaging and irreversible infarction.* American Journal of Neuroradiology, 2006. **27**(1): p. 51-54.
91. Miyasaka, N., et al., *Cerebral ischemic hypoxia: Discrepancy between apparent diffusion coefficients and histologic changes in rats.* Radiology, 2000. **215**(1): p. 199-204.
92. Ten Hove, M., et al., *Combined blockade of the Na+ channel and the Na+/H+ exchanger virtually prevents ischemic Na+ overload in rat hearts.* Molecular and Cellular Biochemistry, 2007. **297**(1-2): p. 101-110.

93. Jansen, M.A., et al., *Assessment of myocardial viability by intracellular Na-23 magnetic resonance Imaging.* Circulation, 2004. **110**(22): p. 3457-3464.
94. Yang, G.Y., et al., *Edema, Cation Content, and Atpase Activity after Middle Cerebral-Artery Occlusion in Rats.* Stroke, 1992. **23**(9): p. 1331-1336.
95. Boada, F.E., et al., *Fast three dimensional sodium imaging.* Magn Reson Med, 1997. **37**(5): p. 706-15.
96. Bernstein, M.A., K.F. King, and X.J. Zhou, *Handbook of MRI Pulse Sequences*. 2004: Elsevier Academic Press.
97. Nagel, A., *Natrium-Magnetresonanztomographie: Entwicklung einer 3D radialen Messtechnik mit optimierter k-Raum-Abtastdichte und hoher SNR-Effizienz.* 2009, PhD Thesis, Ruprechts-Karl-Univerität Heidelberg.
98. Haake, E.M., et al., *Magnetic Resonance Imaging - Physical Principles and Sequence Design.* Wiley & Sins, Inc., 1999.
99. Boada, F.E., et al., *Quantitative in-Vivo Tissue Sodium Concentration Maps - the Effects of Biexponential Relaxation.* Magnetic Resonance in Medicine, 1994. **32**(2): p. 219-223.
100. Atkinson, I.C., et al., *Safety of human MRI at static fields above the FDA ST guideline: Sodium imaging at 9.4T does not affect vital signs or cognitive ability.* Journal of Magnetic Resonance Imaging, 2007. **26**(5): p. 1222-1227.
101. O'Sullivan, J.D., *A Fast Sinc Function Gridding Algorithm for Fourier Inversion in Computer-Tomography.* Ieee Transactions on Medical Imaging, 1985. **4**(4): p. 200-207.
102. Jackson, J.I., et al., *Selection of a Convolution Function for Fourier Inversion Using Gridding.* Ieee Transactions on Medical Imaging, 1991. **10**(3): p. 473-478.
103. Beatty, P.J., D.G. Nishimura, and J.M. Pauly, *Rapid gridding reconstruction with a minimal oversampling ratio.* Ieee Transactions on Medical Imaging, 2005. **24**(6): p. 799-808.
104. Stobbe, R. and C. Beaulieu, *Advantage of sampling density weighted apodization over postacquisition filtering apodization for sodium MRI of the human brain.* Magnetic Resonance in Medicine, 2008. **60**(4): p. 981-986.
105. Ebel, A., W. Dreher, and D. Leibfritz, *Effects of zero-filling and apodization on spectral integrals in discrete Fourier-transform spectroscopy of noisy data.* Journal of Magnetic Resonance, 2006. **182**(2): p. 330-338.
106. Thulborn, K.R. and J.J.H. Ackerman, *Absolute Molar Concentrations by NMR in Inhomogeneous B1 - a Scheme for Analysis of Invivo Metabolites.* Journal of Magnetic Resonance, 1983. **55**(3): p. 357-371.
107. Ouwerkerk, R., et al., *Elevated tissue sodium concentration in malignant breast lesions detected with non-invasive (23)Na MRI.* Breast Cancer Res Treat, 2007.
108. Romanzetti, S., et al., *A comparison of three SPRITE techniques for the quantitative 3D imaging of the Na-23 spin density on a 4T whole-body machine.* Journal of Magnetic Resonance, 2006. **179**(1): p. 64-72.
109. Santosh, C., et al., *Potential use of oxygen as a metabolic biosensor in combination with T2*-weighted MRI to define the ischemic penumbra.* Journal of Cerebral Blood Flow and Metabolism, 2008. **28**(10): p. 1742-1753.
110. Hussain, M.S., et al., *Sodium MRI intensity evolves over time in human acute ischemic stroke.* Stroke, 2008. **39**(2): p. 580-580.
111. LaVerde, G.C., et al., *Sodium Time Course Using Na-23 MRI in Reversible Focal Brain Ischemia in the Monkey.* Journal of Magnetic Resonance Imaging, 2009. **30**(1): p. 219-223.
112. Tsang, A., et al., *Sodium Image Intensity Increases in Ischemic Core Tissue, but not Penumbra in Acute and Sub-acute Stroke.* Stroke, 2009. **40**(4): p. E199-E199.

# Publications and Awards

## Publications in Peer Reviewed Journals

**F. Wetterling**, M. Liehr, H. Liu, P. Schimpf, J. Haueisen, *The localization of focal heart activity via body surface potential measurements: tests in a heterogeneous torso phantom,* Physics in Medicine and Biology, **54** (18): p. 5395-5409, 21st August 2009. (Featured Article)

A.J. Fagan and **F. Wetterling**. *Development of sodium-MRI for stroke and tumour investigations in rodents*, in Irish Journal of Medical Science. Dublin, **177** (8): S271, 25th September 2008.

## Publications in Peer Reviewed Conference Proceedings

A. J. Fagan, **F. Wetterling**, L. Galagher, C. McCabe, M. I. MacRae , S. Junge, *Detection of regional variations in tissue sodium concentration changes in the acute phase of a rodent stroke model*, 15th Annual Meeting of the International Society for Magnetic Resonance in Medicine - British Chapter, Cardiff, UK (September 2009).

**F. Wetterling**, S. Junge, A. Nauerth, O. Gobbo, I. M. MacRae, and A. J. Fagan, *The Measurement of Spatially-Dependant Tissue Sodium Concentration Increase in a Rodent MCAO Stroke Model,* 17th Annual Meeting of the International Society for Magnetic Resonance in Medicine, Honolulu, Hawaii, USA (April 2009)

**F. Wetterling**, O. Gobbo, M. Tabbert, S. Junge and A.J. Fagan. *Sodium MRI Using a Two-Element Phased Array Coil: A Quantification Accuracy Study*. 25th Annual Scientific Meeting of the European Society for Magnetic Resonance in Medicine and Biology, Valencia, Spain (October 2008).

**F. Wetterling**, O. Gobbo, M. Tabbert, S. Junge and A.J. Fagan. *A Variable Inductively Coupled Two-Element Phased Array Coil for Rat Brain Na-MRI at 7T*, 25th Annual Scientific Meeting of the *European Society for Magnetic Resonance in Medicine and Biology*, Valencia, Spain (October 2008).

**F. Wetterling**, M. Tabbert, S. Junge, and A. J. Fagan, *Cerebral Sodium MRI with a Noise-Matched Surface Coil at 7T,* British Chapter of the International Society for Magnetic Resonance in Medicine, Newcastle, UK (September 2008)

## Awards and Grants

| | |
|---|---|
| Association of Physical Scientists in Medicine, Young investigator grant 2008 | 1500EUR |
| International Society for Magnetic Resonance Imaging in Medicine - British Chapter, 2009 AstraZeneca Price for Outstanding i*n vivo* work, shared with Dr. A. J. Fagan | 560EUR |
| Trinity College Dublin, Travel Grant 2008 | 400EUR |
| Association of Physical Scientists in Medicine, Best presentation prize 2008 | 300EUR |
| European Society for Magnetic Resonance in Medicine and Biology, Travel Grant 2008 | 200EUR |
| International Society for Magnetic Resonance in Medicine - British Chapter, student stipend 2008 | 200EUR |
| Institute of Physics in Ireland, student stipend 2008 | 200EUR |
| Institute of Physics in Ireland, student stipend 2009 | 100EUR |

## Invited Talks

**F. Wetterling**, A. Nauerth, S. Junge, M. I. Macrae, and A. J Fagan, *The Measurement of Tissue Sodium Concentration Changes in an In Vivo Stroke Model: Sodium MRI at 7T,* Centre for Computer Assisted Clinical Medicine, University of Heidelberg, Germany, October 2008

**F. Wetterling**, M. Liehr, P. Schimpf, H. Liu, and J. Haueisen, *The Ability of a Spatio-Temporal Dipole Localization Algorithm to Distinguish Correlated Sources: Tests in a Physical Phantom,* Max Planck Institute of Cognitive Neuroscience, Leipzig, Germany, (November 2005).

## Other Conference Contributions

**F. Wetterling**, Lindsay Gallagher, M. I. Macrae, S. Junge, and A. J. Fagan, *The Detection of Infarcted Stroke Tissue via Quantitative Sodium MRI: An In Vivo Study at 7T,* Bruker Scientific Users' Meeting, Ettlingen, Germany (October 2009).

**F. Wetterling**, S. Junge, L. Gallagher, I.M. Macrae, A.J. Fagan , *Monitoring of Brain Function with High Spatio-Temporal Resolution Using Quantitative Sodium Magnetic Resonance Imaging*, Institute of Physics Spring Meeting, 3-5th Apr, 2009

**F. Wetterling** and A. Fagan, *The Measurement of Tissue Sodium Concentration Changes during Cerebral Stroke Via Quantitative Sodium MRI*, APSM Annual Scientific Meeting

of the Association of Physical Scientists in Medicine, Kilkenny Hotel, Kilkenny, Ireland (February 2009).

**F. Wetterling**, A. Nauerth, S. Junge, M. I. Macrae, and A. J. Fagan, *Sodium MRI to Investigate In Vivo Stroke Models Using a 70/30 BioSpec System,* Bruker Scientific Users' Meeting, Karlsruhe, Germany (October 2008).

**F. Wetterling**, A.J. Fagan, *A dual RF resonator system for sodium MRI of small animals*, Institute of Physics Spring Meeting, Monaghan, Ireland, 7-9th March, 2008

**F. Wetterling** and A. J. Fagan, *A Dual RF Resonator System for Sodium MRI*, Joint Annual Scientific Meeting of the Irish Radiotherapy Physics Group and Association of Physical Scientists in Medicine, Croke Park Conference Center, Dublin, Ireland (February 2008).

**F. Wetterling**, M. Tabbert, S. Junge, and A. J. Fagan, *A Dual Coil System for Quantitative $^{23}$Na-MRI*, Bruker Scientific Users' Meeting, Karlsruhe, Germany, (October 2007).

**F. Wetterling** and A. J. Fagan, *Quantitative Sodium Magnetic Resonance Imaging: A Novel Detector Design for Improved Image Quality*, Annual Scientific Meeting of the Association of Physical Scientists in Medicine, Tallaght Hospital, Dublin (May 2007).

A. J. Fagan, **F. Wetterling**, *Development of $^{23}$Na MRI Techniques,* Annual Scientific Meeting of the Association of Physical Scientists in Medicine, Trinity College Institute of Neuroscience, Dublin, Ireland (May 2006).